CORA Cork Open Research Archive
Cartlann Taighde Oscailte Chorcaí

Title	Dynamically reconfigurable long-reach PONs for high capacity access
Authors	Carey, Daniel
Publication date	2019
Original Citation	Carey, D. 2019. Dynamically reconfigurable long-reach PONs for high capacity access. PhD Thesis, University College Cork.
Type of publication	Doctoral thesis
Rights	© 2019, Daniel Carey. - http://creativecommons.org/licenses/by-nc-nd/3.0/
Download date	2026-11-01 02:08:11
Item downloaded from	https://hdl.handle.net/10468/7924



UCC
University College Cork, Ireland
Coláiste na hOllscoile Corcaigh

Ollscoil na hÉireann, Corcaigh
National University of Ireland, Cork



Dynamically Reconfigurable Long-Reach PONs for High Capacity Access

A thesis presented by
Daniel Carey
for the degree of
Doctor of Philosophy

Photonic Systems Group,
Tyndall National Institute, Department of Physics,
University College Cork

Research Supervisor: Prof. Paul Townsend
Research Co-Supervisor: Dr. Giuseppe Talli
Head of Department: Prof. John McInerney

April 2019

Contents

Statement of Originality v
Acknowledgements vii
Abstract xi

1. Introduction 1

1.1 Context of the Study 1
1.2 Background 4
1.3 Research Objectives 7
1.4 Thesis Overview 8

2. Transmission Impairments and Performance Evaluation 11

2.1 Optical Fibre 12
2.2 Transmission Impairments 17
2.2.1 Linear Signal Distortions 18
2.2.2 Loss Compensation Through Optical Amplification 26
2.2.3 Non-Linear Signal Distortions 32
2.3 Noise Considerations 39
2.3.1 Receiver Noise Mechanisms: 42
2.4 Transmission Performance Evaluation 46
2.4.1 System Characterisation and Penalties 49
2.5 Summary 52

3. The Evolution of Optical Access 55

3.1 Driving Fibre-to-the-Premises 56
3.2 The Evolution of Optical Access Networks 60
3.2.1 Long-Reach PONs 63
3.2.2 Next-Generation PONs 65
3.3 Beyond Next Generation Access 72
3.3.1 Bridging the Digital Divide 73
3.3.2 EU FP7 Integrated Project DISCUS 77
3.3.3 Long-Reach Optical Access 79
3.3.4 Technology Evolution and Physical Layer Challenges 80

3.4 Summary . . . 85

4. Low-Cost Tuneable Transmitters for Wavelength Agile PONs . . . 87

4.1 Light Amplification by Stimulated Emission of Radiation . . . 88
4.2 Tuneable Semiconductor Lasers . . . 90
4.3 Wavelength Agile PONs . . . 92
4.4 Challenges Facing Low-Cost Tuneable Lasers for Optical Access . . . 95
4.5 Widely Tuneable MEMS-VCSELs . . . 97
4.5.1 Device Characterisation . . . 100
4.5.2 Wavelength Stability Under Fixed Bias Operation . . . 102
4.5.3 Performance Evaluation for Transmission at 10Gb/s: . . . 104
4.5.4 Overview of the MEMS-Tuneable VCSEL . . . 107
4.6 Single-Growth Monolithically Integrated Tuneable Transmitter . . . 108
4.6.1 Laser Section . . . 113
4.6.2 Modulator Section . . . 115
4.6.3 SOA Section . . . 119
4.6.4 Temperature Dependence and Inter-section Crosstalk . . . 124
4.6.5 Transmission Performance Evaluation . . . 127
4.6.6 Dynamic Wavelength Stability . . . 130
4.6.7 Overview of the Monolithically Integrated Transmitter . . . 139
4.7 Summary and Conclusions . . . 140

5. Physical Layer Design and Subsystem Analysis . . . 143

5.1 Physical Layer Design Strategy . . . 144
5.1.1 Urban Access: The 'Tree-Structured' LR-PON . . . 144
5.1.2 Rural Access: The 'Open-Ring' Architecture . . . 148
5.2 Optical Amplification Scheme . . . 153
5.2.1 Erbium-doped Fibre Amplifiers . . . 154
5.2.2 EDFA Gain Dynamics . . . 156
5.2.3 Gain Control Techniques . . . 158
5.3 Analysis of Residual Transients from Gain-Controlled EDFAs . . . 159
5.3.1 Evolution of Residual Transients in Chained EDFA Links . . . 166
5.4 10G Burst-Mode Subsystems . . . 169
5.4.1 Linear Burst-Mode Receiver . . . 170
5.4.2 Forward Error Correction . . . 173
5.4.3 FPGA Implementation of Burst-Mode FEC . . . 178
5.4.4 FEC Performance of Upstream Channels Impaired by Optical Transients . . . 180
5.5 Summary and Conclusions . . . 184

6. Demonstration of Dynamically Reconfigurable Long-Reach PONs 187

6.1 Experimental Testbed Configuration . . . 189
6.1.1 Single Amplifier Node ('Tree-Like') Architecture . . . 199
6.1.2 Chained Amplifier Node ('Open-Ring') Architecture . . . 203
6.2 Experimental Results . . . 206
6.2.1 10G TDM-PON and Fronthaul Channels . . . 206
6.2.2 Evaluating the FEC Performance in the 'Open-Ring' . . . 212
6.2.3 100G DP-QPSK Point-to-Point Overlay . . . 215
6.3 Integrated SDN Control Plane Services . . . 222
6.3.1 Link Protection and Resiliency . . . 224
6.3.2 Dynamic Wavelength Allocation . . . 226
6.4 Summary and Conclusions . . . 228

7. Conclusions and Future Work . . . 231

7.1 Overview of this Thesis Contribution . . . 231
7.2 Future Work . . . 237
7.2.1 Wavelength Referencing and Control . . . 237
7.2.2 Beyond 10G TDM-PONs . . . 238

Appendix A: Q-Factor in Power and OSNR-Limited Systems . . . 241

Appendix B: Time-Resolved Chirp Measurement . . . 245

Appendix C: Power Budget and OSNR Model . . . 247

Appendix D: Time-Dependent Gain Model for EDFAs . . . 253

Appendix E: Overview of the LBMRx Assembly . . . 259

Appendix F: ECOC Exhibition 2015 . . . 261

Acronyms and Abbreviations . . . 267

List of Figures . . . 271

List of Tables . . . 277

List of Publications . . . 279

References . . . 281

Statement of Originality

I hereby certify that I am the sole author of this thesis. Except where indicated, all the work presented in this thesis is solely attributed to the author. The author participated in the design and implementation of all experiments except where explicitly stated. Precise details of collaborators may be ascertained from the list of co-authors in the 'List of Publications'.

I certify that, to the best of my knowledge, my thesis does not infringe upon anyone's copyright nor violate any proprietary rights and that any ideas, techniques, quotations, or any other material from the work of other people included in my thesis, published or otherwise, are fully acknowledged in accordance with the standard referencing practices.

I declare that this is a true copy of my thesis and has not been submitted for another degree to any other University or Institution.

Signed: _____

Date: _____

Acknowledgements

This work would not have been possible without the support of many exceptional people, to whom I would like to express my sincere gratitude.

At the outset, I would like to wholeheartedly thank my supervisor Prof. Paul Townsend for giving me this opportunity. I will be forever grateful for his generosity, direction and time as his door was always open to me no matter how busy his schedule. I would also like to thank my co-supervisor Dr. Giuseppe Talli for his guidance, patience and support alongside his invaluable contribution to all aspects of this work. Furthermore, I am indebted to Dr. Cleitus Antony for his instruction on research methodology and his constructive criticism which helped me to focus on the technical aspects of my research topics. Moreover, I must thank Dr. Stefano Porto, Dr. Alan Naughton and Dr. Nicola Brandonisio; not only for their valued contribution to some of the experimental setups and results obtained during the course of this project but also for their ever-present support and friendship. Furthermore, I would also like to gratefully acknowledge Science Foundation Ireland (SFI) (grants 12/IA/1270, 12/RC/2276 and 10/CE/I1853) and the EU FP7 project DISCUS (grant CNECT-ICT-318137) for funding this work.

It has been an absolute privilege for me to work with the Optical Access Team within the Photonic Systems Group (PSG) of the Tyndall National Institute; a Cork-based, international team of experts who continue to maintain a global influence in the field of optical communications. With this in mind, I would like to express my gratitude to all present and past members of PSG, especially Dr. Peter Ossieur, Dr. Fatima Gunning, Dr. Bob Manning, Dr. Rod Webb and Prof. Andrew Ellis for their encouragement and assistance. Furthermore, I must also mention the valuable contributions and advice from Dr. Naoise MacSuibhne, Dr. Mark Power, Dr. Marco Dallasanta, Dr. Robert Sheehan and Dr. David Goulding. In particular, a special thanks must also be extended to Ms. Martina Connolly for her help and guidance throughout my time in Tyndall.

I would also like to extend a note of appreciation to Dr. Aidan Daly (formerly of the III-V Materials and Devices Group, Tyndall) for his assistance during our collaborative research efforts to evaluate the surface micro-machined MEMS-VCSELs developed within the EU FP7 project 'SUBTUNE'. In addition, I must acknowledge the invaluable contribution from Mr. Prasanna Ramaswamy, Dr. Brendan Roycroft and Mr. Brian Corbett of the III-V Materials and Devices Group within the Tyndall National Institute for designing and fabricating the monolithically integrated transmitter based on the discretely tuneable slotted Fabry-Pérot laser that was developed as part of DISCUS. Moreover, I must take this opportunity to recognise the substantial contribution from our DISCUS project partners, especially those from the CONNECT research center in Trinity College Dublin. In particular, Mr. Frank Slyne, Dr. Christian Blümm, Dr. Séamus McGettrick and Dr. Marco Ruffini who developed the control plane and the software-defined networking (SDN) platform that were integrated with the physical layer of the experimental testbed. Lastly, a special note of thanks must also be extended to Dr. René Bonk of Nokia Bell Labs in Stuttgart, Germany for his assistance with the design and characterisation of the SOA-based amplifier node.

On a personal level, above all, I want to thank my beautiful wife Niamh for her love and ever-present support; she is my guiding light and I am truly blessed to have her in my life. I must also convey my utmost gratitude to my parents Maurice and Kathleen for giving me the foundation on which I have built my life; they have encouraged and supported me in all of my endeavors.



Daniel M. Carey,
Photonic Systems Group,
Tyndall National Institute,
University College Cork,
Ireland.
14/04/2019

"I shall be telling this with a sigh
Somewhere ages and ages hence:
Two roads diverged in a wood, and I—
I took the one less traveled by,
And that has made all the difference."

- "The Road Not Taken", Robert Frost.

Abstract

Fibre-to-the-Premises (FTTP) is currently seen as the ultimate in high-speed transmission technologies for delivering ubiquitous bandwidth to customers. However, as the deployment of network infrastructure requires a substantial investment, the main obstacle to fibre deployment is that of financial viability. With this in mind, a logical strategy to offset network costs is to optimise the infrastructure in order to capture a greater amount of customers over larger areas with increased sharing of network resources. This approach prompted the design of a long-reach passive optical network (LR-PON) in which the physical reach and split of a conventional PON is significantly increased through the use of intermediate optical amplification. In particular, the LR-PON architecture effectively integrates the metro and access networks enabling the majority of local exchange sites to be bypassed resulting in a substantial reduction in field equipment requirements and power consumption. Furthermore, the extension in physical reach and split can be coupled with an increased information capacity through the use of time- and wavelength division multiplexing (TWDM) which serve to exploit the large bandwidth capabilities offered by single-mode fibre.

In this project, reconfigurable TWDM LR-PON architectures which dynamically exploit the wavelength domain are proposed, assembled and characterised in order to establish an economically viable 'open access' environment that is capable of concurrently supporting multiple operators offering converged services (residential, business and mobile) to support diverse customer requirements and locations. The main investigations in this work address the key physical layer challenges within such wavelength-agile networks. In particular, a range of experimental analysis has been carried out in order to realise the critical component technologies which include low-cost, 10G-capable, wavelength-tuneable transmitters for mass-market residential deployment and the development of gain-stabilised optical amplifier nodes to support the targeted physical reach ($\geq$ 100km) and split ($\geq$ 512). Finally, the feasibility of the proposed dynamically reconfigurable LR-PON configurations as a flexible and cost-effective solution for future access networks is verified through full-scale network demonstrations using an experimental laboratory test-bed.

I would like to dedicate this work to my wife Niamh, my parents Maurice and Kathleen and my late grandfather Christopher O'Sullivan.

"...Let there be light..." - Genesis 1:3

1

Introduction

"The fundamental problem of communication is that of reproducing at one point either exactly or approximately a message selected at another point."
- Claude E. Shannon (1948)[1]

We live in an age of information. Just as the industrial revolution of the 19th century saw the transition to remarkable new manufacturing processes, the digital revolution which began at the end of the twentieth century has seen a radical shift from analogue to digital electronics which has redefined global telecommunications and technology. In particular, four years after the first report of laser action in a semiconductor by Robert Hall and his team at General Electric [2], the introduction of optical fibre by Charles K. Kao and George Hockham of Standard Telecommunication Laboratories Ltd. in 1966 launched a new era for fixed-line communications infrastructure [3]. Today, over fifty years later, optical fibre has been deployed throughout the world as the primary transmission medium in core and metropolitan (metro) networks connecting businesses and communities while long-haul and submarine fibre cables connect countries and continents as shown in Fig. 1.1 [4].

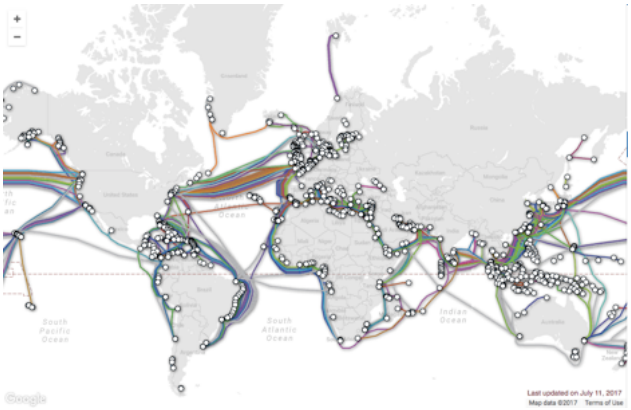


Figure 1.1: Global submarine fibre-optic cable map [4].

Information is now a resource comparable in value to that of oil having become a cornerstone of global economics. Over the last decade, the increasing demand for bandwidth is primarily due to an ever-growing level of online services such as high-definition TV, video conferencing, online gaming, social media and cloud computing. In fact, as shown in Fig. 1.2, the Cisco Visual Networking Index (VNI) has forecasted that global internet-protocol (IP) traffic will nearly triple from 96 exabytes[1] per month in 2016 to 278 exabytes in 2021 [5]. As a result, the efficiency and speed of information transfer from source to destination has become of critical importance. In particular, the bandwidth that can be delivered to customers at the edge access network is one of the most fundamental performance parameters as it correlates directly with productivity and wealth creation [6, 7].

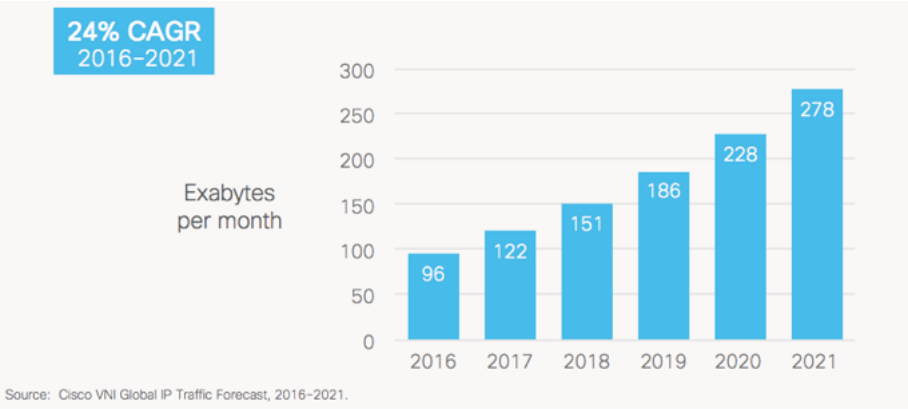


Figure 1.2: Compound annual growth rate forecast for internet protocol traffic according to the Cisco visual networking index, 2016 [5].

Fibre-to-the-Premises (FTTP) is currently the ultimate in high-speed transmission technologies for delivering ubiquitous bandwidth to customers, and when installed has the potential to deliver the envisaged bandwidth requirements for all users irrespective of geographic location for the foreseeable future [8]. Notably, standards for multi-gigabit speed passive optical networks (PONs) are now nearly 10 years old [9, 10], with new standardisation and research efforts focussed on developing next generation access solutions with increased capacity through the aggregation of wavelength channels [11] each supplying a higher bandwidth (>10Gb/s) to a larger amount of customers over wider areas using a longer physical reach [12, 13].

[1] 1 exabyte $= 1 \times 10^{18}$ bytes

Recent Growth in Fibre-to-the-Premises Deployment:

As shown in Fig. 1.3, the latest figures obtained from the Organisation for Economic Co-operation and Development (OECD) indicate that the deployment of FTTP is now actively underway in many countries around the world with governments and network operators investing in optical access infrastructure to ensure economic viability for the future.

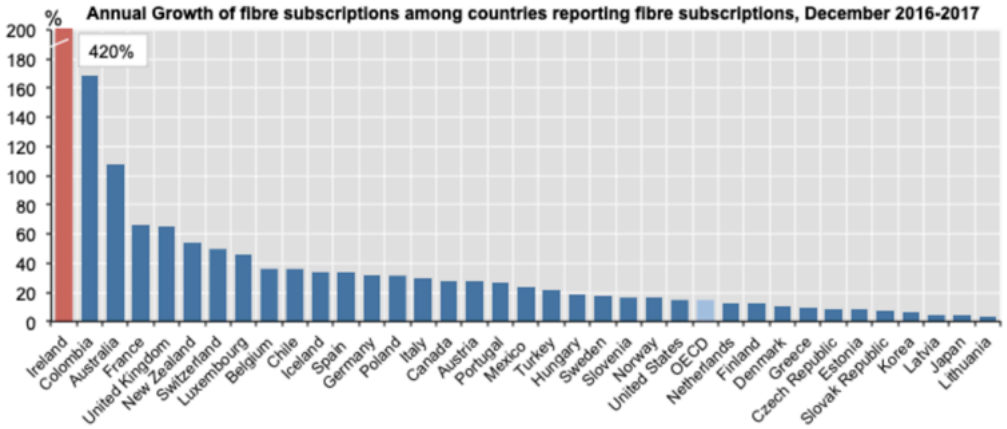


Figure 1.3: OECD: Annual growth of fibre subscriptions, December 2016-2017 [14].

Despite the recent annual growth of fibre subscriptions, the transfer of communication services to a fully end-to-end optical network has progressed more slowly than expected as major financial investment is required with considerable time needed to complete the necessary work. As a result, many countries have chosen to incrementally update their communications infrastructure using intermediate configurations such as Fibre-to-the-Cabinet (FTTC) which reduces deployment costs by utilising copper or wireless technologies as a interim solution [15]. In addition, the deployment of digital subscriber line (DSL) services such as asymmetric DSL (ADSL) and very-high-bit-rate DSL (VDSL) has extended the lifetime of twisted-pair copper cables, however, with a limited bandwidth-distance product only those close to the cabinets can be guaranteed a decent quality of service (QoS). This physical media limitation has led to the creation of a digital divide, where broadband services are severely limited for rural communities in remote areas served by long cables. Consequently, the implementation of future access networks should now be focussed on the efficient use of fibre infrastructures and network resources rather than just the simple increase of the available bandwidth per customer.

1.2 Background

Historically, the most effective way to reduce operational and capital expenditure (OPEX, CAPEX) in telecommunications networks is to maximally share the infrastructure and information capacity among as many customers as possible. Using this approach, the most effective configuration for FTTP is the passive optical network (PON); a point to multi-point tree-like topology which uses passive optical splitters to enable a single 'feeder' fibre to serve multiple customers via an optical distribution network (ODN).

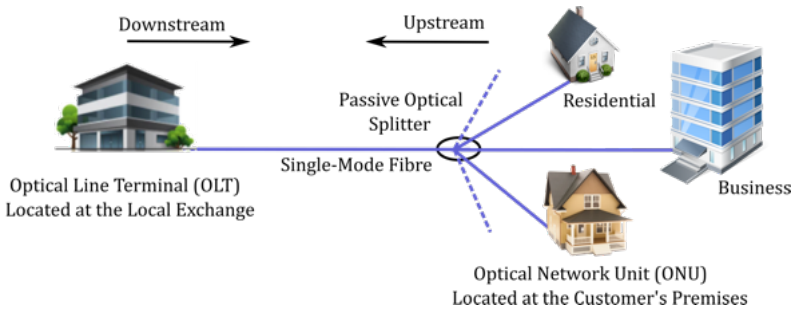


Figure 1.4: Conventional structure of a passive optical network (PON).

One of the main advantages offered by the PON architecture is the ability to share network costs among the end users; however, the growth in bandwidth resulting from increased online services is such that traditional price decline (which occurs in every industry as product volumes increase) may not be sufficient to keep the costs of network growth in line with the revenue required by operators [16]. The financial margins are further restricted by the current high-cost of optical components and the expensive, power-hungry electronic equipment located in the local exchange (LE) sites. Nevertheless, a logical strategy to further offset network costs is to optimise the infrastructure in order to capture a greater amount of customers over larger areas with increased sharing of network resources. This approach prompted the design of an alternative architecture known as a long-reach PON (LR-PON) in which the physical reach and/or the split of a conventional PON is significantly increased through the use of intermediate optical amplification [12]. Notably, the LR-PON architecture effectively combines the access and metro networks into a single all-optical system enabling the majority of LE sites to be bypassed resulting in a substantial reduction in the number of required equipment interfaces and

network elements thus providing a cost-effective access solution with a lower power consumption. Furthermore, the extension in physical reach and split can be coupled with an increased information capacity through the use of hybrid multiplexing techniques such as time-division multiplexing and dense wavelength-division multiplexing (TDM-DWDM) which exploit the large bandwidth capabilities offered by single-mode fibre [17].

Motivation

In the past, large scale optical communication projects such as 'PIEMAN' [18] have successfully demonstrated the advantages of increasing the physical reach, split and capacity of access networks through in-line optical amplification and hybrid multiplexing schemes (i.e. TDM-DWDM). However, the physical layer design was centred around what has become known as the "lollipop" or "tree-structured" LR-PON model. This configuration typically maintains a long feeder fibre (up to 90km) between the metro/core (M/C) node and the amplifier node (AN) located at the old local exchange (LE) or central office (CO) site and then a relatively short (up to 20km) optical distribution network (ODN). This configuration has been shown to work well for urban areas where the customer base is densely distributed; however, in sparsely populated rural areas, the communities to be served can be much smaller than the achievable LR-PON split, hence, the conventional tree-structured LR-PON would be considerably underutilised leading to a direct increase in the cost per customer. To this end, new architectures must now be identified, which are advantageous for establishing economically viable and energy-efficient optical access solutions to ensure the future economic viability of rural communities.

A further issue in today's networks is that of 'stranded capacity' in which network bandwidth cannot be used for reconfigurable service provision because the physical layer effectively blocks access to it. Notably, this issue can be directly addressed through the dynamic exploitation of the wavelength domain; however, this requires the realisation of low-cost remotely tuneable sources and receivers which are supported by a wavelength-agile physical layer and efficient bandwidth allocation algorithms. Nonetheless, the introduction of reconfigurable optical access networks will be a revolutionary step that will enable different wavelengths to be dynamically allocated to various service providers or even to heterogeneous services (i.e. residential, business, wireless fronthaul). Moreover, while the capacity of each wavelength

channel could be shared among multiple optical network units (ONUs) as in conventional TDM-PONs, any channel could also remain unshared, being modulated in any format with assignment to a single ONU, thus enabling the provision of dedicated point-to-point services over a shared fibre infrastructure. However, it should be noted that these considerations require a 'clean-slate' approach to the architectural design by universal application of optical technologies throughout the fixed network eliminating traditional demarcations of core, metro and access. Thus the essential concept is to establish a complete end-to-end architecture exploiting the bandwidth and flexibility offered by wavelength agile LR-PONs and a flat optical core to produce an economically viable and energy efficient optical network which will be the foundation for communications for the long term future.

In this work, we study and successfully demonstrate the physical layer feasibility of two distinct DWDM-TDM LR-PON configurations capable of simultaneously delivering all currently foreseen and future services including 10Gb/s residential, 100Gb/s business and wireless fronthaul to all users independent of their geographical location [19, 20]. A high-level illustration of these architectural configurations is presented in Fig. 1.5. These new architectures far exceed the capability of currently deployed optical access networks in many ways. Firstly, the physical reach was increased significantly compared with the typical distance of 20km for today's widely deployed G-PON systems to over 100km. Additionally, the realisation of dynamically reconfigurable DWDM channels dramatically increases the capacity and bandwidth efficiency when compared to single wavelength systems. Finally, as demonstrated in Chapter 6, a single LR-PON system will serve at least 512 ONUs rather than the 32 (or 64) of today's optical access systems.

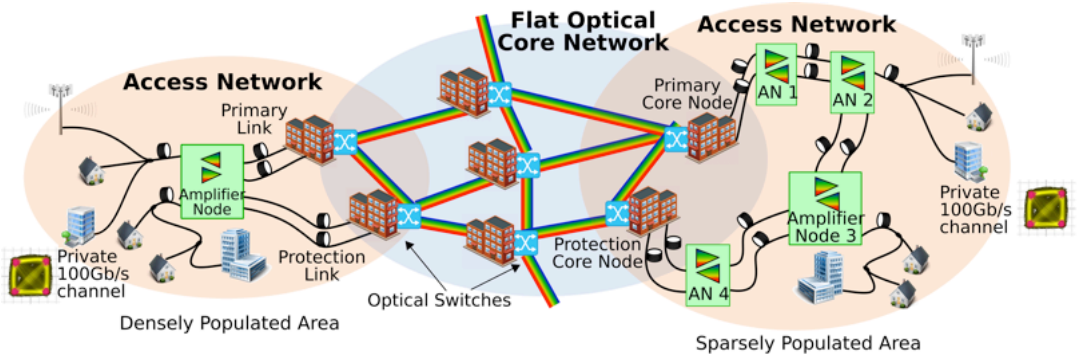


Figure 1.5: High-level network concept proposed for urban and rural deployment.

1.3 Research Objectives

The main objective of this project was to study and solve the critical physical layer challenges facing the realisation of cost-effective dynamically reconfigurable DWDM-TDM LR-PON architectures. In particular, the research tasks addressed in this work include:

- Analysis of innovative low-cost tuneable lasers targeted for mass deployment in customer premises equipment.
- Investigation of high gain, low-noise optical amplifiers capable of supporting dynamic multi-channel traffic over the targeted physical reach and split.
- Assembly and evaluation of an advanced experimental testbed to demonstrate the feasibility of dynamically reconfigurable LR-PONs for future high capacity access networks.

With respect to the tuneable transmitters required for the customers premises equipment, a consequence of the strict tolerance placed on the accuracy and precision of the transmission wavelength within DWDM systems coupled with the need for a wide tuning range (>10nm) demands a greater design and fabrication complexity for tuneable diode laser technologies, hence, cost becomes a critical factor [21]. Consequently, to maintain the feasibility of the proposed network strategy, innovative tuneable laser technologies must be investigated which have been driven by the potential for appreciable cost savings through an increased yield, a lower power consumption and a simplified fabrication processes.

Furthermore, in order to support the targeted reach and split ratio of the proposed LR-PON physical layer, the amplifier nodes (ANs) must be carefully designed. For instance, erbium-doped fibre amplifiers (EDFAs) have emerged as suitable candidates for deployment in optical access networks due to their ability to provide a high gain and a relatively low noise figure across a wide band of channels [22]. However, their relatively slow gain dynamics attributed to a long upper state lifetime (~ 10ms) indicates the potential for saturation induced gain transients. This behavior can have a negative impact on the determination of the decision threshold at the receiver leading to unrecoverable errors in received data; therefore, devices

with active gain stabilisation controls must be studied in order to optimise the link performance.

Finally, the feasibility of the proposed LR-PON configurations must be verified through a physical layer demonstration. This requires the assembly of an experimental testbed within which all of the required technologies are present. These include the integration of 10G-capable burst-mode subsystems such as forward error correction (FEC) operating in conjunction with an innovative linear burst-mode receiver (LBMRx) and the overlay of a dedicated point-to-point 100G channel for business customers. Moreover, for the first time, the physical integration of software defined networking (SDN) to manage access and core network is targeted to enable two service use cases which include the provision of an end-to-end service restoration in the case of a primary link failure and the realisation of dynamic bandwidth allocation through wavelength assignment.

All of the work contained in this thesis was carried out within the Photonic Systems Group of the Tyndall National Institute, University College Cork, Ireland. The activities were funded by Science Foundation Ireland (SFI) (grants 12/IA/1270, 12/RC/2276 and 10/CE/I1853) and the European Union large-scale integrated project DISCUS (grant CNECT-ICT-318137).

1.4 Thesis Overview

Chapter two presents the fundamental physical concepts, properties and limitations of fibre-optic transmission systems alongside the methods by which the performance of these systems are evaluated. This is followed by a detailed synopsis outlining the evolution of optical access networks is presented in **chapter three**. In particular, the network configurations standardised by organisations such as the International Telegraph Union Telecommunication Standardisation Sector (ITU-T) and the Institute of Electrical and Electronic Engineers Standards Association (IEEE-SA) are presented and discussed before the proposal of a new end-to-end architecture aimed at bridging the 'digital-divide' based on the combination of a flat optical core and a LR-PON.

Chapter four motivates the main challenges facing the realisation of low-cost tuneable lasers for use within the optical network units of wavelength agile PONs. In

particular, driven by the potential for appreciable cost savings through an increased yield, the potential for a lower power consumption and simplified fabrication processes, two progressive tuneable laser technologies including a MEMS-VCSEL and a 10G-capable monolithically integrated transmitter based on a single-growth slotted Fabry-Pérot laser are presented and investigated in detail.

Chapter five presents the physical layer design strategy and subsystem analysis of two distinct TDM-DWDM LR-PON topologies. These include a 'tree-structured' topology with a single amplifier node which is suitable for deployment in densely populated urban areas and a novel chained amplifier node ('open-ring') architecture for deployment in sparsely populated rural regions. Specifically, the feasibility of each design is examined through a link power and OSNR budget in order to ensure the performance of the upstream and downstream links are within the operating range of the corresponding transceivers. Subsequently, the optical amplification requirements are investigated in order to design the amplifier nodes with a particular emphasis on erbium-doped fibre amplifiers (EDFAs) due to their desirable performance parameters. However, their relatively slow gain dynamics can result in saturation-induced crosstalk in multi-channel systems, hence, devices with active gain stabilisation circuitry are studied in order to ensure the integrity of the high-dynamic range burst-mode traffic.

In **chapter six**, the reconfigurable LR-PON architectures proposed in Chapter 5 are assembled and investigated through comprehensive network demonstrations using an advanced experimental test-bed. Both configurations use EDFAs as in-line amplifiers, however, through a collaboration with researchers from Nokia Bell Labs in Stuttgart, an alternative tree-structured configuration using SOAs was also investigated in an attempt to extend operation outside the C-band. Notably, the work presented in this chapter substantially extends previous demonstrations of evolutionary optical access networks in relation to the size of the system demonstrated, the level of reconfigurability and integration with the higher control and service layers. The findings obtained from the work presented in Chapters four, five and six resulted in the publication of a number of high impact conference and journal articles which are catalogued within the 'List of Publications'.

Finally, **chapter seven** concludes this thesis with an overview of the main research contributions alongside suggestions for future work.

2

Fibre-Optic Transmission Impairments and Performance Evaluation

'Sand from Centuries Past: Send Future Voices Fast'
- Charles K. Kao., Nobel Lecture, 2009.

This chapter presents an overview of the main physical phenomena associated with optical fibre communication systems alongside a description of the transmission performance evaluation techniques used throughout this work.

In section 2.1, the chapter begins with a brief overview of the development of optical fibre before moving on to discuss the primary sources of linear (loss, dispersion, crosstalk) and non-linear (Kerr nonlinearities, inelastic scattering) signal distortions acquired during transmission in section 2.2. In particular, to compensate for the fibre propagation loss in long distance links and branching losses in access networks, in-line optical amplifiers can be used in order to avoid costly optical-electrical-optical (OEO) regeneration. For these reasons, general concepts common to all optical amplifiers, such as gain saturation and signal degradation due to amplifier noise, are described in section 2.2.2. This is followed by a detailed discussion on the implications of optical receiver noise mechanisms in section 2.3, with an emphasis on shot, thermal and beat-noise. Finally, section 2.4 presents an overview of the main performance evaluation methods used to investigate the feasibility of an optical transmission link through bit error rate analysis. For instance, the difference in behavior between a power-limited system and an OSNR-limited system is also discussed in section 2.4.1.

2.1 Optical Fibre

Today the majority of the world's long-distance voice and data traffic is carried over optical fibre cables [23]. Unlike, traditional copper cables which utilise electrical impulses to transmit information, optical fibres transfer data that has been encoded in light. To motivate the concept of optical communications, the following sections present a brief outline of the structure and development of optical fibre which has revolutionised global telecommunications.

Structure:

In essence, an optical fibre is a cylindrical dielectric waveguide fabricated using low-loss materials such as silicon dioxide, SiO_2, also known as silica. Within an optical fibre, light captured from an optical source is guided within the core of refractive index, n_1, which is surrounded by a cladding layer of lower refractive index, n_2. The cladding layer is typically covered in a protective acrylate buffer coating that is applied during the manufacturing process in order to provide physical and environmental protection. For field deployment, further shielding is provided by a strengthening material contained within an outer covering known as a jacket which is typically made from polyvinyl chloride (PVC). For instance, Fig. 2.1 presents an image of a fibre-optic patch cord which is equipped with connectors at either end to enable convenient connectivity between telecommunication equipment.

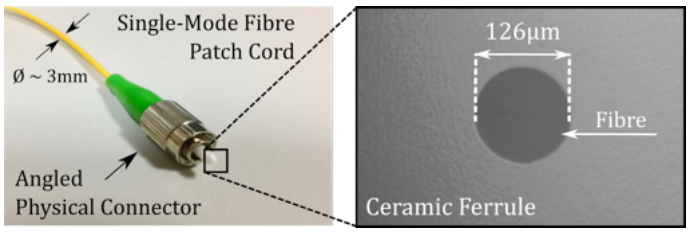


Figure 2.1: Single-mode fibre patch cord with magnified ceramic ferrule showing the fibre cross section.

Development:

The foundations for the development of optical fibre can be traced to the mid-1850s when Irish physicist John Tyndall's famous 'light-pipe' experiment demonstrated that light could be confined within a falling stream of water through the physical

phenomenon known as total internal reflection (TIR). Based on Tyndall's work, Kapany and Hopkins of Imperial College London invented the first actual fibre optical cable in 1952 using unclad glass which was then used to develop a fibrescope to convey optical images along a flexible axis [24]. A decade later, Charles Kao and George Hockham working with Standard Telephones and Cables discovered that the main source of attenuation in optical fibre was caused by impurities in manufacturing [3]. Kao and Hockham also identified a critical and theoretical specification for long-range optical communication devices requiring no more than 20dB of optical loss per kilometre which prompted the need for a purer form of glass to help reduce light loss. This target was overcome by Kapron, Keck and Maurer of Corning Glass Works in 1970 who successfully developed a fused glass fibre with a loss of ≤20dB/km [25] by doping titanium into the fibre core. From this point, fibre optic research progressed rapidly and by 1985 single-mode glass fibres made from highly purified silicon dioxide (also known as silica, SiO_2) derived largely from sand were routinely produced with extremely low losses (≤ 0.2dB/km).

Optical Carrier Propagation:

Optical fibres are typically classified as multi-mode or single-mode fibres, where the concept of a 'mode' typically refers to the spatial distribution of light which is localised in the vicinity of the core through the process of total internal reflection and which propagates through the fibre in the z-direction with a well-defined phase velocity ($v_p = \omega/\beta$). That is, where the z and time dependence of the optical carrier are given by the phase condition $e^{i(\beta z - \omega t)}$, where ω is the angular frequency and β is the effective propagation constant which is ultimately determined from the boundary conditions defined by the fibre geometry [26].

$$\beta(\omega) = \frac{\omega}{v_p} = \frac{\omega}{c} n_{eff}(\omega) \tag{2.1.1}$$

where, n_{eff} is the effective index which accounts for the refractive index of both the core and cladding. It should be noted that an optical mode will cease to be guided within the core when $n_{eff} \leq n_2$; therefore, the mode is said to reach a cut-off when $n_{eff} = n_2$. In practice, optical fibres for telecommunications are designed to satisfy the weakly guiding approximation using a step-index (top hat) profile, where

$(n_1 - n_2)/n_1 \ll 1$ which implies that $n_{eff} \approx n_1$ [27].

The multi-mode fibre (MMF) variant of telecommunications fibre has a relatively large core diameter ($\approx 50\mu$m) which results in the propagation of multiple spatial modes. This larger core size simplifies connections by making it much easier to capture light from a transmitter thus allowing source costs to be reduced. However, due to the frequency dependent characteristics of the core material, the propagation of multiple modes exhibits varying group velocities and different group delays which results in modal dispersion during transmission [28]. Consequently, over long distances a substantial delay can develop between the fastest and slowest mode which ultimately limits the bandwidth capability. Despite this inherent limitation, MMF can be applied in short reach communications with an attenuation co-efficient of approximately 3.5dB/km and a typical bandwidth-distance product of 500 MHz.km at 850nm with the ability to achieve 10Gb/s per fibre up to 300m [29].

Alternatively, single-mode fibre (SMF) has a core diameter between 8 and 10.5μm which facilitates the transmission of a single fundamental spatial mode. As this type of fibre is free from modal dispersion, the fidelity of each light pulse can be maintained over much longer distances compared with MMF; therefore, it is more suitable for long-reach communication applications. Low-loss, step-index silica SMF (also known as standard SMF) is the most common fibre variant deployed throughout the world; its physical specifications are documented by the International Telecommunications Union (ITU) within the G.652 recommendations for the purpose of standardisation [30]. An illustrated cross-section of a step-index single-mode optical fibre is presented in Fig. 2.2.

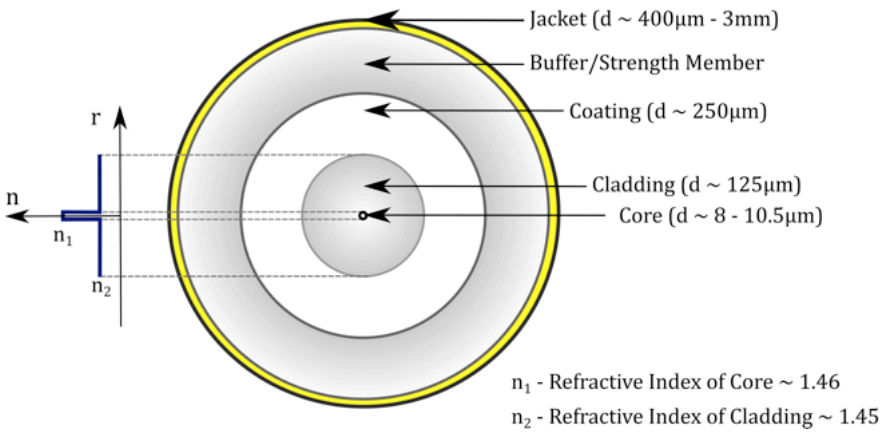


Figure 2.2: Illustrated cross section of a step-index single-mode fibre.

The Information Signal:

In practice, the digital information signal can be encoded onto the optical carrier in the transmitter by varying the carriers intensity (I), frequency (ω_c) or phase (ϕ) to represent a '1' or a '0' using a technique known as *modulation* [31].

Intensity (or amplitude) modulation (IM/AM) is the most-common format in fibre-optic communications as it is one of the most straightforward ways of encoding a carrier signal with information. In turn, the simplest form of IM is known as on-off keying (OOK) in which the information is represented by the carrier as a sequence of high and low light intensities which are represented by a train of optical pulses. In general, a high intensity (pulse) represents a '1' while a low intensity (no pulse) signifies a '0'. At the receiver side, the process of demodulation is also relatively straightforward requiring a photodetector to convert the optical signal back into an electrical signal through direct detection (DD) where a decision circuit then identifies bits as either '1' or '0' by comparing the amplitude of the electric signal with respect to a decision threshold as illustrated in Fig. 2.3.

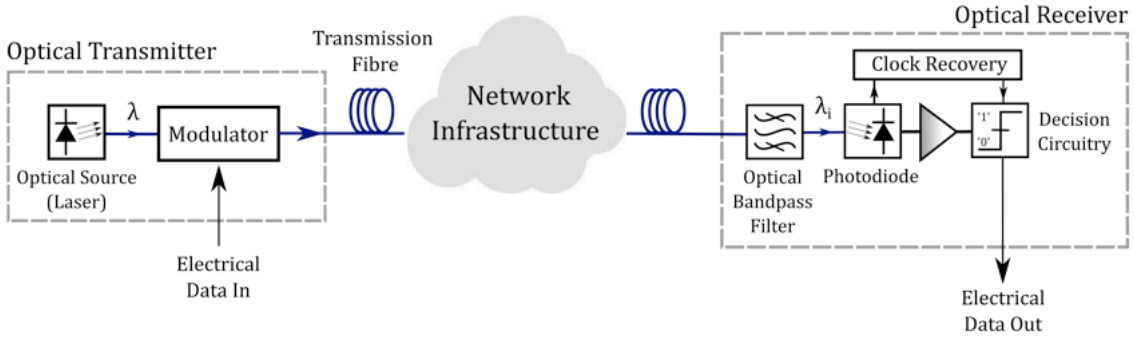


Figure 2.3: Conceptual block diagram of a basic optical communication system using intensity modulation and direct detection.

In this thesis, the primary modulation format of interest is non-return-to-zero on-off-keying (NRZ-OOK), where the optical power does not return to zero between two successive '1' bits. Instead, it occupies the full timeslot, $T = 1/B$, where B signifies the bit-rate and both '1' and '0' symbols occur with equal probability (50%) regardless of the state of the preceding bit. An illustration of the NRZ-OOK modulation waveform is presented in Fig. 2.4.

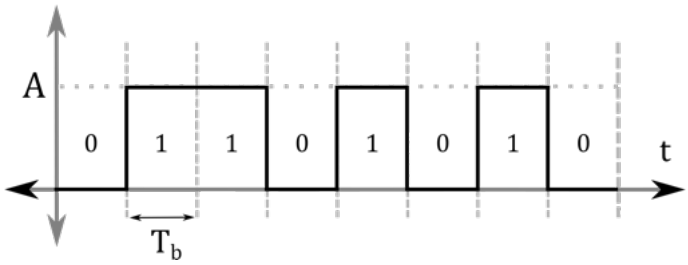


Figure 2.4: Illustration of an NRZ-OOK modulation signal.

For system performance evaluation, a pseudorandom binary sequence (PRBS) is typically used as a general-purpose test pattern. PRBS is can be denoted as $2^n - 1$ or PRBS-n, where n indicates the shift register length used to create the pattern. Each PRBS pattern contains every possible sequence of n bits, except the state which corresponds to all zeros. Consequently, each NRZ-OOK PRBS test pattern has an associated power spectral density (PSD) that indicates the frequency distribution of the power in the pattern. In particular, for NRZ-OOK, by assuming an ideal rectangular modulating signal with amplitude, A, and bit rate B; the normalised PSD envelope of a monochromatic optical carrier with a frequency f_c encoded with NRZ-OOK can be determined as [32]:

$$S_c^{NRZ}(f) = \frac{A^2}{8B}[sinc^2(\frac{f - f_c}{B}) + sinc^2(\frac{f + f_c}{B})] + \frac{A^2}{8}[\delta(f - f_c) + \delta(f + f_c)] \quad (2.1.2)$$

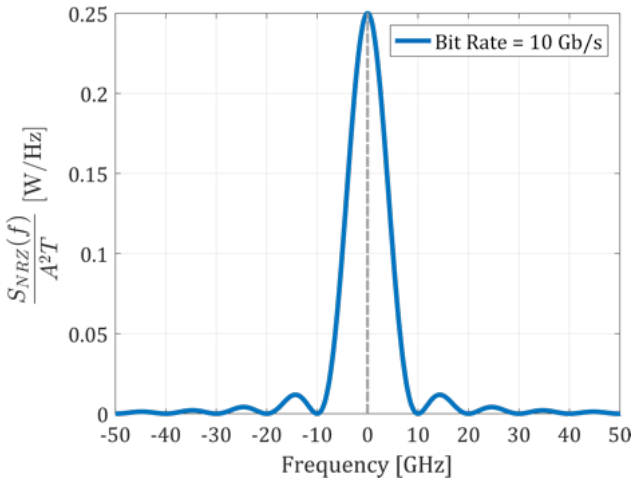


Figure 2.5: Spectral envelope of a monochromatic optical carrier modulated at 10Gb/s with NRZ-OOK.

Knowledge of the spectral profile of a modulated signal ultimately leads to improvements in system design. For instance, the result shown in Fig. 2.5, indicates that the spectrum of a modulated optical carrier contains many frequency components with most of the energy contained within the spectral region $f_c \pm B$. Consequently, even in the ideal case of a monochromatic optical carrier, the signal will have an appreciable spectral width. Furthermore, it is clear that there is substantial low-frequency content that can be attributed to long sequences of consecutive identical digits (CIDs) in the data signal. These features introduce significant challenges for clock and data recovery (CDR) units located at the receiver which must extract timing information in order to process the data synchronously. In practice, further encoding or scrambling is often used to increase the transition frequency in order to format the data into a more manageable form.

2.2 Transmission Impairments

Optical fibre offers several distinct advantages over alternative transmission media, including a superior bandwidth capability, low-loss and high link reliability through immunity to moisture and external electromagnetic interference (EMI). However, as with any transmission medium apart from a vacuum, the propagation of light through optical fibre is beset with several limitations which become more evident as the transmission distance is increased.

Fibre-optic transmission impairments can be categorised into three groups: linear, non-linear and noise. These impairments can accumulate within the fibre and any interaction between these processes can lead to deterministic (predictable) or stochastic (random) outcomes. The main sources of linear impairment include attenuation (or loss), chromatic dispersion (CD), polarisation mode dispersion (PMD) and adjacent channel crosstalk. Alternatively, the main source of non-linear impairments in optical fibres are a consequence of Kerr nonlinearities which include self-phase modulation (SPM), cross-phase modulation (XPM) and four-wave mixing (FWM) in addition to inelastic scattering processes such as stimulated Brillouin scattering (SBS) and stimulated Raman scattering (SRS).

2.2.1 Linear Signal Distortions

In a dielectric† medium such as optical fibre, the electric polarisation, $\vec{P}$, is frequency dependent and does not respond instantaneously to an applied electric field [26]. This inherent delay results in the dissipation of the electromagnetic energy within the medium which manifests as a loss of signal power at the waveguide output. Consequently, the relative permittivity, ϵ_r, of a 'lossy' dielectric is generally given as a complex function which is dependent on frequency;

$$\epsilon_r(\omega) = \epsilon_r^{Real}(\omega) + i\epsilon_r^{Im}(\omega) \tag{2.2.1}$$

where, ϵ_r^{Real} is the real part of the dielectric permittivity, $\epsilon_r^{Im}(\omega)$ represents the imaginary part of the dielectric permittivity and $i = \sqrt{-1}$.

This phenomenon also has consequences for the refractive index of the dielectric material, n, as both quantities are related through the following expression:

$$n = \frac{c}{v} = \frac{1}{\sqrt{\mu_0\epsilon_0}}.\frac{\sqrt{\mu\epsilon}}{1} = \sqrt{\frac{\mu_0\mu_r\epsilon_0\epsilon_r}{\mu_0\epsilon_0}} = \sqrt{\epsilon_r(\omega)}, \quad \text{where, } \mu_r = 1 \tag{2.2.2}$$

where, μ_0, μ_r, ϵ_0, ϵ_r represent the free-space and relative magnetic permeability and electric permittivity respectively.

In turn, Eqn. 2.2.2 implies that the refractive index can also be considered as a complex function which is dependent on frequency according to:

$$\mathbf{n}(\omega) = n(\omega) + i\kappa(\omega) \equiv \sqrt{\epsilon_r(\omega)} \tag{2.2.3}$$

where, n signifies the real part of the refractive index ($= c/v$) and κ represents the imaginary part of the refractive index which is often termed the *extinction coefficient*. In practice, the complex nature of the frequency dependent refractive index has implications for the propagation constant (β) which is used to describe the phase of the guided carrier wave as it propagates through the fibre.

$$\beta(\omega) = \frac{\omega}{c}\mathbf{n}(\omega) = \frac{\omega}{c}(n(\omega) + i\kappa(\omega)) \tag{2.2.4}$$

†Insulator that can be polarised by an E-field

Attenuation in Silica-Based Optical Fibre:

As with any physical medium apart from a vacuum, the dielectric fibre waveguide demonstrates an intrinsic loss of power when an optical signal is transmitted through it. By minimising extrinsic factors such as bending losses [33], the main sources of attenuation within glass optical fibre for low intensity operation can be attributed to material absorption and elastic scattering. Notably, pure silica glass has two intrinsic absorption mechanisms in the ultraviolet (α_{UV}) and infrared (α_{IR}) regions which leave a low absorption window between 800 and 1700nm.

A major source of extrinsic absorption in optical fibre is due to the presence hydroxyl (OH^-) ions from water vapour which is bonded to the glass structure during the manufacturing process (α_{OH^-}) producing absorption peaks at ~ 1383nm, 950nm while combination of the overtones with the fundamental silica resonance result in visible peaks at 1240nm, 1130nm and 880nm. These peaks can be seen in the attenuation spectrum of low-loss optical fibre presented in Fig. 2.6. An additional source of extrinsic loss in silica fibre is due to transition metal ion impurities (α_{Im}) which include iron (Fe^{2+}), copper (Cu^{2+}) and chromium (Cr^{3+}) which are also dissolved within the glass during the manufacturing process. Consequently, the total absorption coefficient of the fibre (α_{Abs}) is given by the sum of the intrinsic and extrinsic absorption contributions:

$$\alpha_{Abs} = \alpha_{UV} + \alpha_{IR} + \alpha_{OH^-} + \alpha_{Im} \tag{2.2.5}$$

For low intensity operation, optical scattering is best described in terms of elastic phenomena where photons interact with spatial variations in the material dielectric constant (ϵ_r), such that the photons alter their propagation direction, phase, and polarisation, without energy loss such that the photon frequency after scattering remains the same. Linear scattering can be categorised into two major types: Rayleigh and Mie scattering; both resulting from non-ideal physical properties of the manufactured fibre.

Rayleigh scattering is the dominant intrinsic loss mechanism in the low-absorption window of the fibre between the UV and IR absorption regions. It results from random inhomogeneities in the material density which are much smaller than the wavelength of the light. The subsequent elastic scattering produces an attenuation, α_R, proportional to the inverse fourth power of wavelength ($\propto 1/\lambda^4$) which significantly

impacts shorter wavelengths [34, 35]. Alternatively, Mie scattering can occur for material inhomogeneities that are comparable in size to the wavelength of the light (i.e > $\lambda/10$). Such irregularities include fibre diameter fluctuations, the presence of air bubbles and appreciable index variations in the core-cladding interface. Fortunately, due to a well-established and carefully controlled manufacturing process, conventional silica-based glass fibres are largely free of such material instabilities; therefore, attenuation due to Mie scattering is typically negligible (i.e. $\alpha_{Mie} \approx 0$) with the total attenuation due to the elastic scattering contribution, α_R, attributed to Rayleigh scattering. As a result, the total attenuation coefficient within silica optical fibre which is attributed to the combination of material absorption and linear scattering can be expressed as,

$$\alpha_{Tot} = \alpha_{Abs} + \alpha_R \tag{2.2.6}$$

The first low-loss optical fibre was manufactured by the Nippon Telegraph and Telephone (NTT) Public Corporation, Japan in 1979 [36]. Figure 2.6 presents the attenuation spectrum for a low-loss single mode fibre with the wavelength transmission bands for single-mode fibre as specified by the International Telecommunications Union (ITU) within supplement 39 of the G Series recommendations [37].

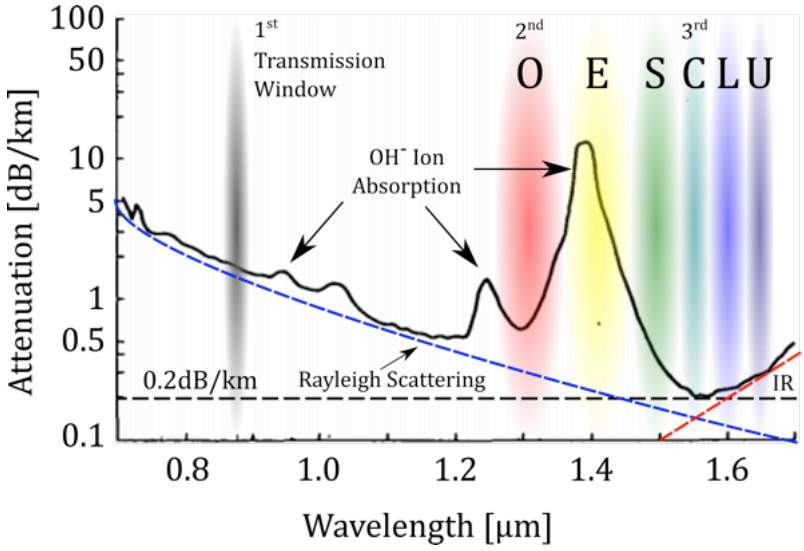


Figure 2.6: Attenuation spectrum of the first low-loss single-mode fibre (1979) with highlighted transmission bands for optical communications (Reproduced from [36]).

A description of the six ITU wavelength bands (O,E,S,C,L and U) which comprise the spectrum between 1260nm to 1675nm are presented in Table 2.1. It should be noted that long-haul transmission initially took advantage of the O and C-bands with subsequent extension into the L-band in order to take advantage of the dispersion and low-loss properties of the fibre respectively. In this thesis, the experiments and simulations utilise the C-band (1535 - 1565nm), unless otherwise stated, where a minimum loss of $\alpha^{dB} < 0.2$dB/km can be achieved when appropriate manufacturing processes are employed.

Band	**Description**	**Range**	**Bandwidth**
O-Band	Original	1260 - 1360nm	100nm (17.5THz)
E-Band	Extended	1360 - 1460nm	100nm (15.1THz)
S-Band	Short-Wavelength	1460 - 1530nm	70nm (9.4THz)
C-Band	Conventional	1530 - 1565nm	35nm (4.4THz)
L-Band	Long-Wavelength	1565 - 1625nm	60nm (7.1THz)
U-Band	Ultra-Long Wavelength	1625 - 1675nm	50nm (5.5THz)

Table 2.1: Wavelength transmission bands for single-mode fibre communications [37]

Propagation Loss:

The overall throughput of an optical fibre can be quantified in terms of the input optical power, $P(0)$, and the output power, $P(L)$ observed after light propagates a distance, L, along the fibre length:

$$P(L) = P(0)e^{-\alpha L} \tag{2.2.7}$$

where, α is the total attenuation coefficient for the fibre which has units of Neper per meter $[Np/m]$. The Neper is a logarithmic unit which uses the base e; however, it is usually more convenient to express the fibre attenuation coefficient in decibels per kilometre [dB/km] which uses a logarithmic unit to the base 10 and is related to the linear scale according to the following expression:

$$\frac{\alpha_{dB}}{\alpha} = 10log_{10}e \approx 4.343 \tag{2.2.8}$$

In optical communications, optical signal power is generally represented using the logarithmic decibel scale which is referenced to a value of one milliwatt ($1mW$). Absolute power measurements referenced to $1mW$ are denoted by the unit dBm.

$$P_{dBm} = 10log_{10}(\frac{P_{mW}}{1_{mW}}) \tag{2.2.9}$$

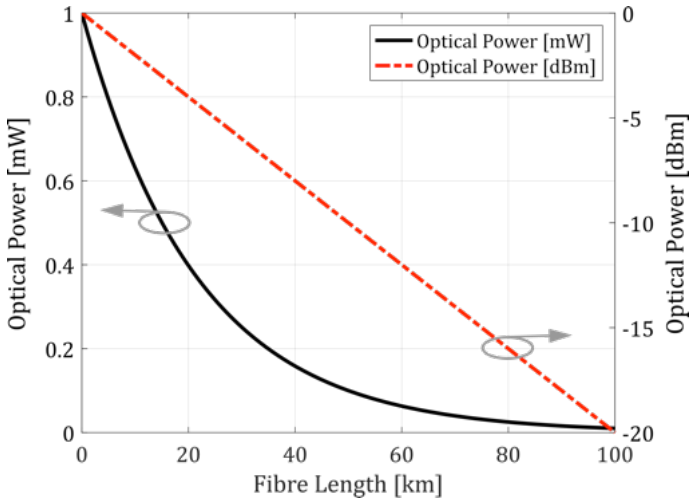


Figure 2.7: Propagation Loss in Optical Fibre for an Attenuation Coefficient of 0.2dB/km (~ 0.046 Np/km) Corresponding to Transmission around 1550nm Using a Launch Power of 1mW (0dBm).

Dispersion in Optical Fibres:

As demonstrated in Eqn. 2.2.4, when an optical signal is launched into a fibre, the frequency components of the signal will propagate with different speeds due to the frequency dependence of the refractive index, this effect is known as dispersion. In an amplitude modulated system, dispersion leads to the temporal broadening of the optical pulses which ultimately limits the achievable transmission bandwidth and physical reach due to intersymbol interference (ISI) where adjacent pulses interfere with each other up to a point where they are indistinguishable from each other.

The primary sources of pulse broadening in fibre-optic communications include intermodal dispersion, chromatic dispersion and polarisation-mode dispersion. Notably, the main advantage of single-mode fibre is that intermodal dispersion is absent as only the fundamental mode is allowed to propagate. Moreover, the experiments in this thesis were carried using bit rates ~ 10Gb/s and transmission distances ~ 100km which are far below the threshold for which the impact of polarisation-mode dispersion becomes appreciable [26]; hence, its contribution to pulse broadening is assumed to be negligible. Consequently, the primary source of pulse broadening considered in this work is a result of chromatic dispersion which is a consequence of the frequency dependence of the refractive index.

Chromatic Dispersion:

Chromatic dispersion (CD) refers to the temporal broadening of an optical pulse during propagation due to the frequency dependence of the refractive index, $n(\omega)$, as discussed previously. This property causes different spectral components of an optical pulse to propagate along the fibre with slightly different group velocities, v_g. In practice, the amount of CD can be determined through the derivative of the relative group delay, τ_g, with respect to the vacuum wavelength, λ, which is typically specified in units of picoseconds per nanometer $[ps/nm]$:

$$CD = \frac{d\tau_g}{d\lambda} = \frac{d}{d\lambda}\left(\frac{L}{v_g}\right) \quad [ps/nm] \tag{2.2.10}$$

where, the relative group delay, τ_g, is the time taken for the constituent wavelengths of the optical pulse to propagate through a distance L with a group velocity, v_g, which represents the propagation speed of the pulse envelop.

As $v_g^{-1} = d\beta/d\omega$, by definition, where $\beta(\omega)$ is the frequency dependent propagation constant; Eqn. 2.2.10 can be re-written as,

$$CD = L\frac{d}{d\lambda}\left(\frac{d\beta}{d\omega}\right) = -\frac{2\pi cL}{\lambda^2}\frac{d}{d\omega}\left(\frac{d\beta}{d\omega}\right) = -\frac{2\pi cL}{\lambda^2}.\beta_2 \tag{2.2.11}$$

where, $\beta_2 = d^2\beta/d\omega^2$ is known as the group velocity dispersion (GVD) parameter.

In fibre-optic communications, it is usually more convenient to define a dispersion parameter, D_λ, which is expressed in units of picoseconds per nanometer per kilometre [ps/(nm.km)]:

$$D_\lambda = \frac{d}{d\lambda}\left(\frac{d\beta}{d\omega}\right) = \frac{d}{d\lambda}\left(\frac{1}{v_g}\right) = -\frac{2\pi c}{\lambda^2}\beta_2 \quad [ps/(nm.km)] \tag{2.2.12}$$

For practical purposes, the dispersion parameter, D_λ, of optical fibre is usually extrapolated using the following well-known expression [38, 39]:

$$D_\lambda = \frac{S_0}{4}\left(\lambda - \frac{\lambda_0^4}{\lambda^3}\right) \quad [ps/(nm.km)] \tag{2.2.13}$$

where, S_0 signifies the dispersion slope ($S_0 = dD_\lambda/d\lambda$) which governs higher-order dispersion effects and λ_0 is the zero-dispersion wavelength. For standard single mode fibre, λ_0 lies around 1310nm and S_0 is approximately 0.092 $ps/(nm^2 \cdot km)$ [40]. The dispersion parameter for standard SMF as specified in Eqn. 2.2.13 is presented in Fig. 2.8.

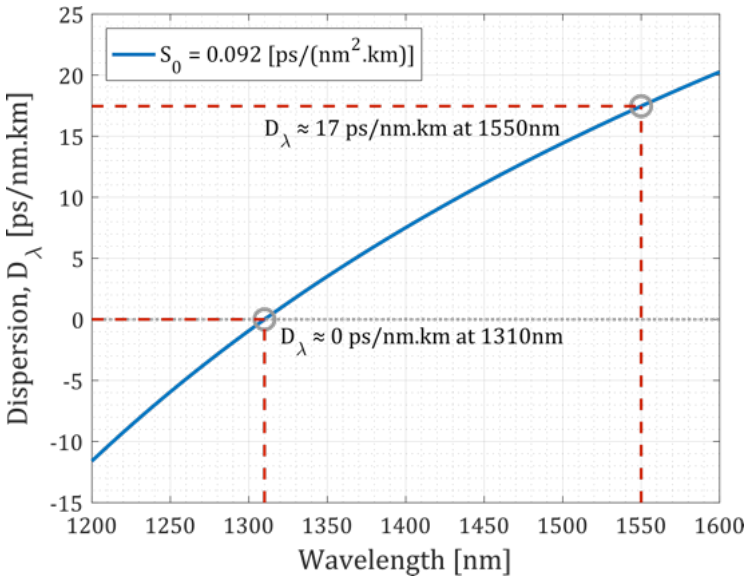


Figure 2.8: Dispersion parameter as a function of transmission Wavelength for Standard Single-Mode Fibre.

Ultimately, chromatic dispersion in optical fibre places a limit on the maximum distance that a signal can be transmitted before requiring regeneration. This limit can be estimated by determining the transmission distance at which a pulse has broadened by one bit interval, T_b. For instance, the amount of temporal pulse broadening, ΔT, accumulated over a fibre length, L, can be determined by considering the optical spectral width ($\Delta\lambda$),

$$\Delta T = |D_\lambda|.\Delta\lambda.L \tag{2.2.14}$$

For transmission at a bit rate, B, if an optical pulse has been broadened by one bit period (i.e. $\Delta T = T_b = 1/B$), the corresponding transmission distance known as the *dispersion length* can be determined as:

$$B.\Delta T = B.(|D_\lambda|.\Delta\lambda.L) = 1 \quad \Rightarrow \quad L = \frac{1}{B.|D_\lambda|.\Delta\lambda} \tag{2.2.15}$$

For an externally modulated NRZ-OOK signal, the spectral width, Δf, can be estimated as $\sim 1.2B$ [41]. By converting this relation into the wavelength domain[†] the dispersion length for 10Gb/s transmission at 1550nm in a standard single mode fibre where $|D_\lambda| \approx 17$ [ps/(nm.km)] can be estimated as,

$$L_D = \frac{c}{1.2B^2|D_\lambda|\lambda^2} \quad \approx \quad 61.21km \tag{2.2.16}$$

This estimated limit is close to the 70km observed in practice for a 1dB power-penalty which indicates the increase in optical power required to maintain the same signal quality as that in the absence of dispersion [41]. It should also be noted that the dispersion limit is inversely proportional to the square of the bit rate. Consequently, as the bit rate is increased, not only will the frequency content of the signal increase but the timeslots will become narrower resulting in an increased sensitivity to broadening of adjacent pulses. This feature indicates that chromatic dispersion is one of the most significant performance limiting phenomena in fibre-optic communications.

[†] $f = \frac{c}{\lambda} \Rightarrow \Delta f = |-\frac{c}{\lambda^2}.\Delta\lambda|$

Out-of-band Crosstalk and Filter-Induced Signal Distortions:

In WDM systems, wavelength selective components such as demultiplexers and optical bandpass filters are used to isolate channels for re-routing or detection. While the insertion losses (IL) of these wavelength selective components can be kept relatively low, narrow channel spacing coupled with poor channel isolation can result in power from an adjacent channels being present in that of the target channel. This leaked power effectively acts as noise on the target channel and is known as out-of-band (or inter-channel) linear crosstalk [42]. Alternately, filter-induced signal distortions can arise if the signal passes through a chain of wavelength selective components which may narrow the bandwidth enough to produce clipping of the signal spectrum. However, as this work concentrates mainly on wavelength agile access network applications where the overall number of employed filters/multiplexers is limited to a few (i.e. <5), such impairments do not represent a major issue and for this reason they are no longer taken into account. However, for further information on these topics the reader is referred to [43], [44] and [45].

2.2.2 Loss Compensation Through Optical Amplification

As discussed in section 2.2.1, inherent attenuation in optical fibre leads to propagation loss which ultimately limits the achievable physical reach of fibre-optic transmission links. To overcome this inherent attenuation, in-line optical amplification can be employed within the system to boost the power of the transmitted signals in order to ensure that they are above the detectability threshold of the associated optical receivers. Notably, one of the main advantages of optical amplification is that it avoids signal regeneration through optical-electrical-optical (O-E-O) conversion which is not financially or practically viable for WDM applications in which multiple channels are transmitted over the fibre. Moreover, optical amplifiers offer several advantages over regenerators which include insensitivity to the bit rate or signal formats alongside the ability to amplify multiple WDM channels simultaneously; hence, a system using optical amplifiers can be more easily upgraded.

The various utilisation strategies for optical amplifiers within a fibre-optic link [46] are demonstrated within Fig. 2.9. For instance, at the transmitter side, a booster amplifier can be used to ensure a sufficiently high launch power while in-

line amplifiers compensate for loss in the field deployed fibre. Lastly, at the receiver side, a pre-amplifier can be used to exploit the sensitivity of the optical detector. In the following section, the main aspects of optical amplification are discussed with respect to their impact on the transmission performance.

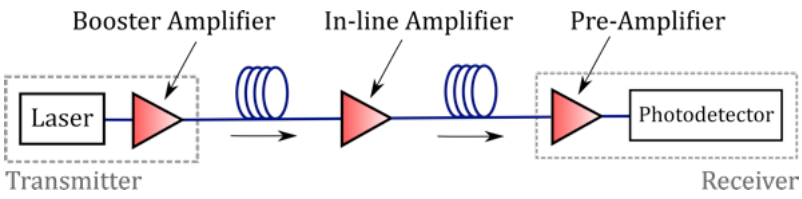


Figure 2.9: Illustration of the utilisation strategy for optical amplifiers within a fibre-optic link.

Optical Gain and Saturation:

The large-signal gain provided by an optical amplifier is defined as the ratio of the output power, P_{out}, to the input power, P_{in}, of the propagating continuous-wave signal:

$$G = \frac{P_{out}}{P_{in}} \tag{2.2.17}$$

where, the equivalent relation in decibel units is given by,

$$G_{dB} = P_{out}\,[dBm] - P_{in}\,[dBm] \tag{2.2.18}$$

In general, the gain provided by a particular active material can be determined through the evolution of optical power through that material.

$$\frac{dP}{dz} = g(\omega)P(z) \tag{2.2.19}$$

where, P is the optical power at a distance z from the input ($z = 0$) and $g(\omega)$ is the frequency and power dependent material gain coefficient per unit length which can be modelled as a homogeneously broadened two-level system [47]:

$$g(\omega) = \frac{g_0}{1 + (\omega - \omega_0)^2 T_2^2 + P/P_{sat}} \tag{2.2.20}$$

with the peak gain, g_0, frequency of incident signal, ω, transition frequency, ω_0, dipole relaxation time, T_2 and input saturation optical power, P_{sat} which in the steady state leads to a reduction in the gain to half of its small-signal value.

When the incident optical frequency is tuned to the gain peak (i.e. $\omega = \omega_0$), the gain co-efficient is then given by,

$$g(\omega) = \frac{g_0}{1 + P/P_{sat}} \tag{2.2.21}$$

Substituting Eqn 2.2.21 into Eqn. 2.2.19, the evolution of power along the amplifier is then given by

$$\frac{dP}{dz} = \frac{g_0 P(z)}{1 + P/P_{sat}}$$

This equation can be solved by separating the variables and integrating over the length of the gain medium as follows,

$$\int_{P(0)}^{P(L)} (\frac{1}{P(z)} + \frac{1}{P_{sat}}) dP = g_0 \int_0^L dz \tag{2.2.22}$$

By recognising that $P(0) = P_{in}$, $P(L) = P_{out} = GP_{In}$ and $G_0 = e^{g_0 L}$ (unsaturated gain); the solution to Eqn. 2.2.22 is given by,

$$\frac{P_{out}}{P_{Sat}} = \frac{G}{G-1} log_e(\frac{G_0}{G}) \tag{2.2.23}$$

$$\Rightarrow P_{out} = \frac{G}{G-1} log_e(\frac{G_0}{G}).P_{sat} \tag{2.2.24}$$

In contrast to the input saturation power, P_{Sat}, the output saturation power of optical amplifiers, P_s^{Out}, is typically specified by the output power for which the gain has dropped by a factor of 2 (i.e. $G = G_0/2$).

$$\Rightarrow P_s^{Out} = \frac{G_0 log_e(2)}{G_0 - 2}.P_{sat} \tag{2.2.25}$$

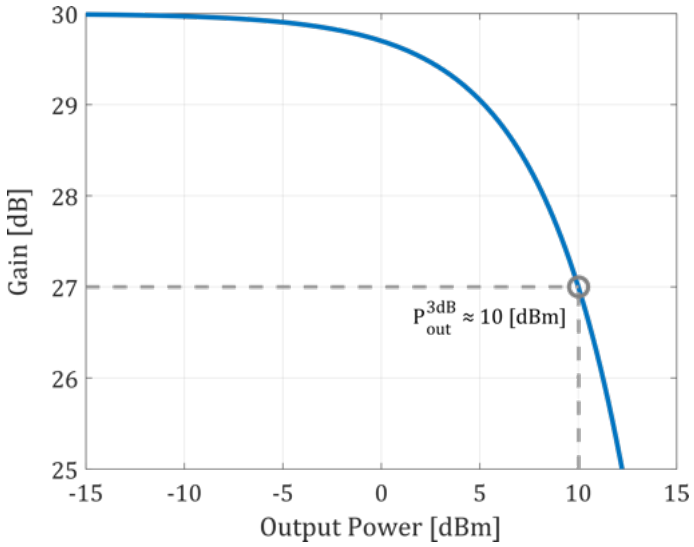


Figure 2.10: Optical gain as a function of the output power for $G_0 = 30$dB and $P_s^{Out} \approx +10$dBm.

Noise Contribution from Optical Amplifiers:

The main disadvantage of optical amplification is the generation of optical noise due to amplified spontaneous emission (ASE). ASE is the product of a quantum effect known as *spontaneous emission* which is attributed to the spontaneous decay of excited states of atoms or ions within an active material; therefore, it is an unavoidable effect. When ASE appears outside the wavelength region of the signal, it can be filtered out using an optical filter; however, when it lies within the wavelength region of the signal, it constitutes noise which cannot be separated from that signal. Consequently, if multiple amplifiers are concatenated within a fibre-optic link, the ASE contribution can accumulate within the link and result in serious degradation of the optical signal-to-noise ratio (OSNR) which can dictate the signal quality at the receiver. The total ASE power at the output of an optical amplifier within an optical bandwidth, B_{ref}, considering both possible polarisation modes for a given value of gain, G, is given by the following relation [48]

$$P_{ASE} = 2S_{ASE}B_{ref} = 2.n_{sp}(G-1)h\nu B_{ref} \tag{2.2.26}$$

where, $S_{ASE} = n_{sp}(G-1)h\nu$ represents the ASE power spectral density $[W/Hz]$ for a single polarisation mode which incorporates Planck's constant ($h \approx 6.626 \times 10^{-34}\,[Js]$), the optical frequency, ν, for which the product $h\nu$ gives the energy of one photon at the signal frequency, the amplifier gain, G, and the spontaneous-emission factor, n_{sp}, which is a function of the atomic populations of the ground, N_1, and excited states, N_2, of a two-level system as demonstrated in Eqn. 2.2.27.

$$n_{sp} = \frac{N_2 - N_1}{N_1} \tag{2.2.27}$$

Subsequently, the OSNR at the output of an optical amplifier is defined as the ratio of the average optical signal power, P_{out}, to the ASE power, P_{ASE}, which is typically measured within an optical reference bandwidth, B_{ref}, of 0.1nm (~ 12.5GHz for wavelengths in the region of 1550nm).

$$OSNR = \frac{P_{out}}{P_{ASE}} = \frac{GP_{in}}{2.n_{sp}(G-1)h\nu B_{ref}} \tag{2.2.28}$$

In practice, a common way to characterise the performance of an optical amplifier is through its associated *noise figure*, NF, which is a measure of the amount of optical noise added to the signal following amplification [48]:

$$NF \approx \frac{P_{ASE}}{2h\nu B_{ref}G} + \frac{1}{G} \equiv 2n_{sp}\frac{G-1}{G} + \frac{1}{G} \approx 2n_{sp}, \quad when\ G \gg 1 \tag{2.2.29}$$

From Eqn. 2.2.29, it should be noted that in the case of an ideal amplifier ($n_{sp} = 1$), the NF maintains a minimum value of 2 which suggests that although an optical amplifier improves the signal strength it will also degrade the signal-to-noise ratio, SNR, by at least a factor of 2 (i.e. 3dB); this feature of phase insensitive amplifiers in the region of high gain is known as the quantum limit [49]. In practice, the noise figure of optical amplifiers depends on the technology used and typically exhibit

values above this quantum limit, i.e. $n_{sp} > 1$. For instance, semiconductor optical amplifiers (SOAs) providing 20dB gain typically demonstrate values in the region of 6.5dB as demonstrated in Fig. 2.11.

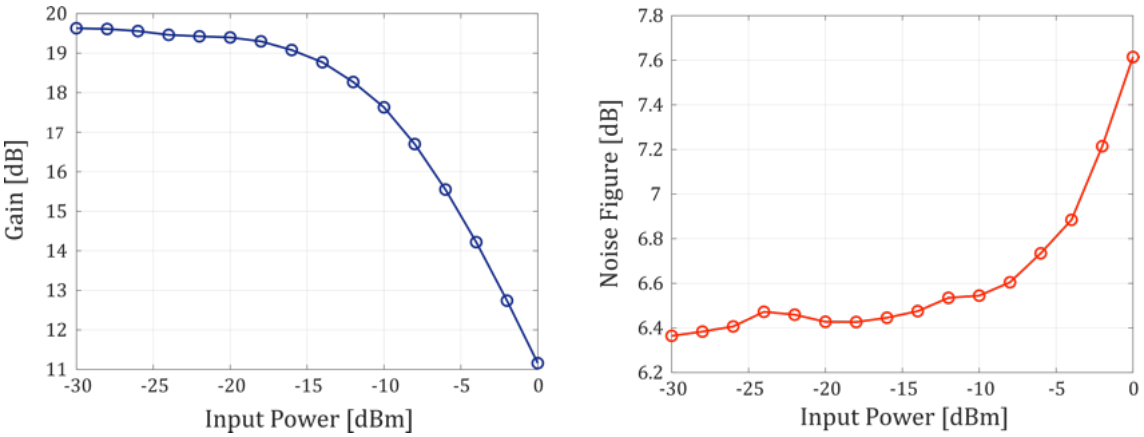


Figure 2.11: Measured gain and noise figure as a function of the input power to a CIP SOA-S-C-14-FCA using a wavelength at 1550nm.

For practical purposes, the gain and NF values of commercial amplifiers are typically specified within the product datasheet. Using the expression for NF presented in Eqn. 2.2.29, the OSNR at the output of an optical amplifier (given by Eqn. 2.2.28) can be re-written as:

$$OSNR = \frac{GP_{in}}{(NF\,G-1)2h\nu B_{ref}} \approx \frac{P_{in}}{NF\,h\nu B_{ref}},\ for\ G \gg 1 \tag{2.2.30}$$

As both OSNR and NF are typically specified in decibel (dB) units; it is usually convenient to re-write Eqn. 2.2.30 as,

$$\begin{aligned} OSNR\ [dB] &= 10log_{10}(OSNR) \\ &\approx \underbrace{P_{in}\,[dBm]}_{10log_{10}(P_{in}[W])} + 30 - \underbrace{NF\,[dB]}_{10log_{10}(NF)} - 10log_{10}(h\nu B_{ref}) \end{aligned} \tag{2.2.31}$$

Notably, Eqn. 2.2.31 indicates that for a given signal frequency, ν, the OSNR at the output of an optical amplifier for an optical reference bandwidth, B_{ref}, can

determined from the input power, P_{in}, and the associated NF. Consequently, in order to improve the OSNR, the launch power must be increased or the length of the fibre span has to be reduced; however, it should be noted that the fibre launch power is ultimately limited by degradations due to nonlinear impairments which are briefly discussed in the following section.

2.2.3 Non-Linear Signal Distortions

Fundamentally, the origin of nonlinearity lies in the anharmonic motion of bound electrons under the influence of an intense electric field. Consequently, the electric polarisation, $\vec{P}$, has a general relation which is comprised of a linear component, $\vec{P}_L$, and a nonlinear component, $\vec{P}_{NL}$, as defined in Eqn.2.2.3.

$$\vec{P} = \underbrace{\epsilon.\chi_e^{(1)}\vec{E}}_{\vec{P}_L} + \underbrace{\epsilon.\chi_e^{(2)}\vec{E}.\vec{E} + \epsilon.\chi_e^{(3)}\vec{E}.\vec{E}.\vec{E} + ...}_{\vec{P}_{NL}}$$

In practice, the dominant contribution to $\vec{P}$ is provided by the linear dielectric susceptibility, $\chi_e^{(1)}$, it's value determines the refractive index, n, and the attenuation coefficient, α. Moreover, the second order susceptibility, $\chi_e^{(2)}$, is responsible for Pockels effect and second harmonic generation in materials which lack inversion symmetry at the molecular level [50]. However, as silica is composed of symmetric O-Si-O molecules, $\chi_e^{(2)} \longrightarrow 0$; hence, optical fibres do not tend to exhibit nonlinear effects related to second order susceptibility [50]. Nonetheless, electric quadrupole and magnetic dipole moments as well as defects within the fibre core can contribute to second harmonic generation in optical fibre under certain conditions. As these processes are beyond the scope of this work they will not discussed further; however, for additional information the reader is referred to [51] and [52].

Notably, the lowest-order nonlinear effects observed in optical fibre are primarily attributed to the third order susceptibility, $\chi_e^{(3)}$ which is responsible for third harmonic generation (THG), four wave mixing (FWM) and non-linear refraction. As the processes that produce THG and FWM in optical fibres have a relatively low efficiency, the majority of nonlinear effects are a result of non-linear refraction which is a consequence of the intensity dependence of the refractive index which is also known as *the Kerr-effect* defined in Eqn. 2.2.32 [53].

$$n(\omega, I) = n_L + n_{NL}.I = n_L + n_{NL}.\frac{P}{A_{eff}} \tag{2.2.32}$$

where, n_L is the linear refractive index, n_{NL} is the nonlinear refractive index which is $\approx 2.63 \times 10^{-20}$ $[m^2/W]$ for silica fibres in the region of 1550nm [54], I is the optical intensity $[W/m^2]$, P $[W]$ is the optical power and A_{eff} $[m^2]$ is the effective area of the fibre core over which the optical power is assumed constant ($A_{eff} \sim 85\mu m^2$ for standard SMF). Furthermore, as the propagation of light within optical fibre is limited by attenuation, the majority of the nonlinear interactions take place within the initial region of the fibre link. For convenience, this region, known as the *effective length*, L_{eff}, is modelled as a the distance over which the power is assumed to be approximately constant [55].

$$L_{eff} = \frac{\int_0^L P(z)dz}{P_{in}} = \frac{1}{P_{in}} \int_0^L P_{in} e^{-\alpha z} dz$$
$$= \int_0^L e^{-\alpha z} dz = \frac{1 - e^{\alpha L}}{\alpha} \approx \frac{1}{\alpha}, \quad for \ L >> 10km \tag{2.2.33}$$

where, L represents the physical length of the fibre and α gives the fibre loss in Neper per kilometre [Np/km]. For instance, a fibre link with a loss coefficient of 0.2dB/km and a physical length of 100km has a corresponding effective interaction length of ~ 21.5km.

Kerr Nonlinearities:

The intensity dependence of the refractive index presented in Eqn 2.2.32 gives rise to multiple non-linear effects which include self-phase modulation (SPM), cross-phase modulation (XPM) and four-wave mixing (FWM).

The intensity dependent refractive index causes an induced phase shift in the propagating pulse that is proportional to the temporal variation of its own intensity; this process is known as *self-phase modulation* (SPM). Consequently, the various wavelength components within the pulse will undergo different phase shifts which in turn gives rise to a frequency chirp (i.e. a temporally varying instantaneous

frequency across the pulse).

In practice, for an unchirped input pulse, the SPM-induced chirp is inherently positive in that the leading edge causes the refractive index to increase resulting in a shift to lower frequencies (red-shift) while the falling edge causes a decrease in refractive index producing a shift towards longer frequencies (blue-shift). This self-induced frequency chirp affects the propagating pulse through GVD [50]; hence, transmission over long distances ($\gg$ 10km) can produce substantial pulse broadening which ultimately limits the achievable bit rate. Moreover, unlike chromatic dispersion, the nonlinear SPM induced chirp cannot be easily compensated as these amplitude distortions are dependent on the signal power. However, in an anomalous dispersion regime ($\beta_2 < 0, D_\lambda > 0$), the interplay between SPM and GVD can produce a lower level of pulse broadening than in the case of GVD alone, therefore, a certain level of SPM can actually be advantageous for fibre-optic communications [56]. Nonetheless, SPM is ultimately a power limiting nonlinear process in single-mode fibres for long distance transmission [57], hence, in order to prevent appreciable pulse broadening and distortion attributed to SPM for a given length of fibre the launch power must be controlled.

Alternatively, in a multichannel system, the intensity dependence of the refractive index can also produce a non-linear phase shift which depends not only on the power of an individual channel but also on the power of the other channels propagating within the fibre; this nonlinear phenomenon is known as *cross-phase modulation* (XPM) [58]. In standard SMF, the XPM-induced nonlinear phase modulation is translated into intensity fluctuations through chromatic dispersion which can result in a severely degraded channel performance; thus, XPM is exhibited as an inter-channel crosstalk mechanism which effectively limits the number of wavelength channels that can be transmitted simultaneously through a single fibre.

It is important to recognise that chromatic dispersion also causes different wavelength channels to propagate with different group velocities such that their relative position changes along the fibre, that is to say the channels *walk-off* from each other as they propagate. However, as XPM can only occur when pulses overlap in the time domain, the difference in group velocity for channels with a wide spectral separation will be large enough such that the temporal overlap of optical pulses is short and the impact of XPM is negligible. Nonetheless, as the channel spacing is decreased the difference in group velocity between adjacent channels may become low enough such

that the overlap is long enough to enable the XPM effects to accumulate; hence, a higher value of dispersion can be beneficial to suppress XPM-induced crosstalk [59]. In practice, the *walk-off* length, L_w, given in Eqn. 2.2.34 can be used to provide an indication of the XPM efficiency; it signifies the length of fibre required for interacting pulses separated by a channel spacing, $\Delta\lambda$, to walk-off from each other [60] as demonstrated in Fig. 2.12.

$$L_{wo} \approx \frac{\delta t}{D_\lambda \Delta\lambda} \quad [m] \tag{2.2.34}$$

where, D_λ is the fibre dispersion parameter and δt represents the time duration that characterises the intensity changes in the propagating optical signals. In the case of NRZ-OOK signals, the changes in optical intensity correspond to distinct rising or falling edges, therefore, δt represents the edge duration.

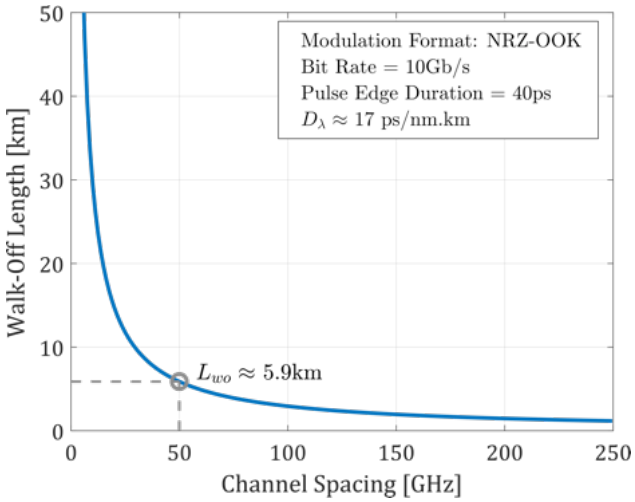


Figure 2.12: The walk-off length [km] for NRZ-OOK transmission at 10Gb/s as a function of the channel spacing for wavelengths within the low-loss spectral region of standard single-mode fibre [$D_\lambda \approx 17$ ps/(nm.km), $\lambda_c \sim 1550$nm].

It should be noted that the validity of Eqn. 2.2.34 relies on the assumption that the wavelength spacing between channels, $\Delta\lambda$, is sufficiently larger than the bandwidth of the individual channels (a factor of 4 between the two is typically large enough for this purpose [61]) and that the portion of the fibre length which is not dispersion compensated, is sufficiently larger than the walk-off length, L_{wo}. Nonetheless, it

is clear that the impact of XPM induced-crosstalk is more substantial for systems employing narrow channel spacing and/or fibre with a low dispersion parameter.

For a fixed number of channels operating at the same bit rate in standard single-mode fibre, the impact of XPM can be reduced by increasing the channel spacing and/or reducing the per-channel launch power. In practice, it is difficult to analytically estimate the impact of XPM due to the number and nature of the variables involved; therefore, complex numerical simulations are required which must consider the signal envelopes of all channels propagating in the fibre. As this analysis is beyond the scope of this thesis it will not be discussed further; however, for more information the reader is directed to [62], [63] and [50].

An additional consequence of refractive index modulation induced by high intensity light during multichannel transmission involves the induction of a phase modulation on all transmitting channels which can provoke beating between the signals based on certain phase matching conditions [64, 65]. This process results in the generation of sidebands at new frequencies and a reduction of power in the original channels. A further damaging consequence of this process involves the generation of light at a frequency which coincides with one or more of the allocated transmission channels; these mixing products manifest as noise and lead to a greater degradation of the signal quality. This nonlinear phenomenon is generally known as *Four-Wave Mixing* (FWM) as it accounts for the parametric interaction of four photons with angular frequencies, ω_1, ω_2, ω_3 and ω_4 within a non-linear medium. Moreover, as the quantum states of the molecules are unchanged with respect to the beginning and end of this process, the conservation of energy and momentum holds between the annihilated and created photons. Notably, in standard SMF, chromatic dispersion decreases the FWM efficiency considerably as the difference in phase velocity causes the phase matching condition to be satisfied only over a short transmission distance. As a result, FWM only becomes significant for small WDM channel spacing, i.e. less than 50GHz, and low dispersion fibre [66], neither of which are utilised within this work.

Stimulated Inelastic Scattering:

A second class of non-linear interactions are governed by stimulated inelastic scattering where the optical field transfers some of its energy to the transmission medium. In particular, this phenomenon refers to stimulated Brillouin scattering (SBS) and

stimulated Raman scattering (SRS).

Stimulated Brillouin scattering (SBS) is a well-known non-linear process that occurs when the electric field of a high-intensity transmitted signal interacts with the acoustic vibrational modes of the fibre material to generate an acoustic wave via *electrostriction* [67] which in turn modulates the refractive index and scatters the incident light. The scattered (Stokes) light is reflected backwards with respect to the incident (pump) light with a downshifted frequency as energy and momentum must be conserved during each scattering event. This change in frequency for the Stokes wave is known as the *Brillouin shift* which attains a value of approximately 11GHz for transmission in the region of 1550nm [50]. Notably, as the Brillouin shift is significantly smaller than the typical DWDM channel spacing (50GHz), SBS should not produce an appreciable amount of interchannel cross-talk; however, above a critical power threshold (which depends on the chosen modulation format), the reflected power no longer increases linearly with launch power and a significant amount of the transmitted light is redirected back towards the transmitters; hence, SBS serves to limit the per-channel power that can be launched into the fibre [68].

In practice, SBS is a narrowband effect and the spontaneous Brillouin gain has an intrinsic bandwidth, $\Delta\nu_{SBS}$, of less than 100MHz in silica fibre [69]; hence, the SBS threshold strongly depends on the linewidth of the carrier. While directly modulated lasers will exhibit linewidths much greater than $\Delta\nu_{SBS}$, the induced frequency chirp may interact with the chromatic dispersion to produce undesired signal distortions, hence, external modulation is generally preferred for dense WDM (DWDM) systems. Notably, in this work, the primary modulation format used is non-return-to-zero on-off keying (NRZ-OOK) for which the spectrally broadened sidebands contribute negligibly to SBS; however, the carrier component which contains half of the total signal energy will readily undergo SBS. Moreover, it should be noted that commercially available narrow-band DFB lasers that are traditionally used in DWDM network experiments have continuous-wave linewidths in the region of 10MHz which is well within $\Delta\nu_{SBS}$. Consequently, in order to mitigate the effect of SBS, the linewidth of the laser is typically broadened by applying a frequency sinusoidal dither to the bias supplied of the laser in order to induce a low-frequency phase modulation [70]. This dither frequency is usually set below the low frequency cut-off of the photodiode in order to ensure it is outside the receiver bandwidth. Nonetheless, it should also be noted that dithering cannot infinitely increase SBS

threshold without additional penalties since at some point induced phase modulation of the signal will be converted to amplitude modulation by fibre dispersion.

Unlike SBS, which generates an acoustic pressure wave due to electrostriction, *stimulated Raman scattering* (SRS) occurs in an optical fibre when a high-intensity incident (pump) wave having exceeded an associated power threshold is inelastically scattered by the silica molecules. This phenomenon converts the pump photons to a lower frequency (Stokes photons) with the energy difference transfered to an optical phonon which describes the quantised energy of a molecular vibration. As the SRS-induced frequency shift is dictated by the band of vibrational energy states of the silica molecules within the fibre; scattering can occur in both propagation directions. For standard SMF, the Raman gain bandwidth which exceeds 10THz (≈80nm) with the maximum gain occurring when the frequency downshift is approximately 13THz (~104nm) while there is another gain peak near 15THz (~120nm) [71].

The power threshold associated with SRS is defined as the input pump power at which the Stokes power becomes equal to the pump power at the fibre output. Assuming a Lorentzian gain spectrum, this critical power threshold has been analytically determined by Smith et al. [68] for the worst-case scenario, where the polarisation of the pump and Stokes waves (which both propagate in the forwards direction) have been maintained along the length of the fibre. For instance, the SRS power threshold for a single channel launched into a span of 100km is approximately +30dBm (~1W); hence, it is clear that SRS is not a limiting factor for single-channel systems as launch powers are typically below +10dBm (10mW). However, in a WDM system, SRS can severely degrade the link performance by transferring energy from shorter wavelength channels to higher wavelength channels within the Raman gain bandwidth as the fibre itself acts as an amplifier. As a consequence of this process, the shortest transmission wavelength is the most depleted as it can contribute gain to multiple channels at higher wavelengths. For the network architectures considered in this project, the input power per channel is much lower than the SRS threshold, and the total bandwidth of the WDM channels in each transmission direction is approximately 13nm. Moreover, the channels were not co-polarised as they originated from different uncorrelated sources, hence SRS-induced impairments are not present.

2.3 Noise Considerations

Aside from distortions induced by the physical properties of the transmission medium; undesired random fluctuations in the signal (*noise*) can corrupt the fidelity of the information content, especially at low amplitude levels where the receiver has a greater difficulty in decoding the signal information. Consequently, as the noise level rises there is a increasing probability that bits may be misinterpreted which produces errors in the received data. In order to understand the impact of noise and distortion on the design of fibre-optic communication systems, it is crucial to understand the process of signal detection and receiver performance quantification.

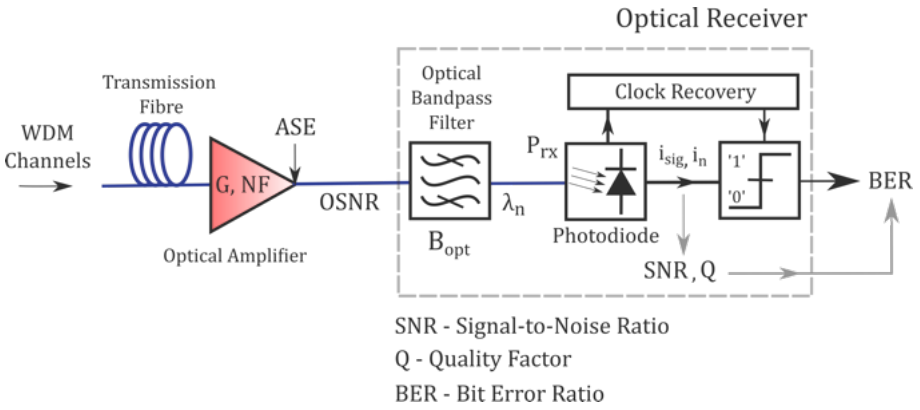


Figure 2.13: Illustration of the direct detection and decision process within a WDM system whose channels are impaired by ASE following optical amplification.

The first element of an optical receiver is the photodetector which is used to convert the transmitted optical signal back into the electrical domain prior to amplification and processing. As the optical signal is typically weakened during transmission through the fibre, the photodetector must have very high performance requirements which include a high sensitivity at the wavelength range of interest, a minimal noise contribution and a sufficient bandwidth (i.e. a suitable response time) to handle the desired data rate. In practice, it is also favourable for a photodetector to maintain a relative insensitivity to temperature over a wide operating range, a low-power consumption and manufacturing cost with a form factor that is compatible with fibre optic packaging.

Photodetectors are primarily comprised of light sensitive semiconductor materials known as photodiodes. Photodiodes are *square-law detectors* whose output is proportional to the square of the electric field ($\propto |E^2|$); hence, the electrical output is directly proportional to the power of the incident light with no direct dependence on the phase or polarisation.

$$\langle i_{sig}(t)\rangle \propto P_{in} \quad \Longrightarrow \quad \langle i_{sig}(t)\rangle = R.P_{in} \tag{2.3.1}$$

where, $\langle i_{sig}(t)\rangle$ is the time averaged current [A] generated by a steady state incident optical power, P_{in} [W] and R is the wavelength-dependent responsivity of the photodiode [A/W] which is given as [26]:

$$R = \frac{\langle i_{sig}(t)\rangle}{P_{in}} \equiv \frac{\eta q}{h\nu} \approx \eta \frac{\lambda_{\mu m}}{1.24} \tag{2.3.2}$$

with η signifying the quantum efficiency of the material which is dependent on the bandgap, q is the magnitude of the charge carried by a single electron $\approx 1.602 \times 10^{-19}$ [C], h is Planck's constant $\approx 6.626 \times 10^{-34}$ [Js] and ν is the frequency of the incident light [Hz] where $h\nu$ gives the energy [J] of one incident photon.

As the interaction of photons with the semiconductor material of the photodiode is a statistical process, the linear relation presented in Eqn 2.3.1 is only valid for time averaged quantities as it does not account for the undesired random fluctuations (noise) in the photocurrent present around the mean value. For noise processes that can be described using Gaussian statistics, the variance of the photocurrent noise, σ_n^2, can be estimated through the autocorrelation function of $\langle i_n(t)\rangle$ which is related to the noise spectral density, $S_n(f)$, by the Wiener-Khinchin theorem [26]:

$$\langle i_n(t) i_n(t+\tau)\rangle = \int_{-\infty}^{\infty} S_n(f) e^{2\pi i f \tau} df$$

$$\xrightarrow[\tau \to 0]{} \quad \langle i_n^2(t)\rangle = \int^{B_e} S_n(f) df = \sigma_n^2 \tag{2.3.3}$$

If the noise is measured just after the photodiode, the equivalent noise bandwidth of the receiver, B_e, is equal to the intrinsic bandwidth of the photodiode whose

value depends on the design. However, if the noise is measured at the output of the receiver, the transfer function of the entire receiver module, $H(f)$, must be considered to account for other components such as amplifiers and the low-pass filter which is used to remove high frequency electrical noise. It is also worth noting that the value of B_e is generally different to the 3dB bandwidth, B_{3dB}, which is typically quoted in the receiver specifications. For instance, in this analysis, the electronic circuitry is assumed to have a first-order low-pass characteristic as given by the following transfer function, $H(f)$ [72]:

$$H(f) = \frac{1}{1 + i\frac{f}{B_{3dB}}} \tag{2.3.4}$$

The relationship between B_e and B_{3dB} for the low-pass filter response can then be determined as,

$$B_e = \int_0^\infty |H(f)|^2 df = \frac{\pi}{2} B_{3dB} \tag{2.3.5}$$

In general, the value of σ_n^2 depends on the associated noise mechanism. However, if multiple noise sources are present, each exhibiting Gaussian statistics, the total noise contribution can be determined as the sum of all the individual noise mechanisms.

$$\sigma_{tot}^2 = \sum_{n=1}^{N} \sigma_n^2 \tag{2.3.6}$$

The performance of an optical receiver is dependent on the electrical signal-to-noise ratio (SNR) which is defined as the ratio of the peak electrical power for the detection of a '1' bit to the associated noise variance which serves as a measure of the signal quality [73].

$$SNR = \frac{\langle i_{sig,1}(t) \rangle^2}{\sigma_{tot}^2} \tag{2.3.7}$$

It is important to recognise that Eqn. 2.3.7 is only valid for signals whose extinction ratio (ER), $P_{sig,1}/P_{sig,0}$, is large enough such that $i_{sig,1}(t) \gg i_{sig,0}(t)$. In general, the quality-factor (Q-factor) gives a more accurate analysis of the signal quality as it

includes the noise statistics for the '0'-bit; this parameter will be discussed later in section 2.4.

2.3.1 Receiver Noise Mechanisms:

The inherent noise mechanisms in optical receivers are shot noise and thermal noise; however, it is important to note that optical noise such as amplified spontaneous emission (ASE) accumulated within the transmission link of optically amplified systems can further degrade the signal quality following conversion to electrical beat-noise at the receiver; therefore, the signal performance also has a dependence on the received OSNR.

Shot Noise:

The generation of electron-hole pairs within a photodiode is a statistical process due to the discrete quantum nature of photons which arrive at the receiver in a random fashion. For instance, within any given time interval, there will be random fluctuations in the number of charge carriers generated as photons impact the surface of the photodiode; these fluctuations produce undesired variations in the photocurrent known as *quantum noise* or shot noise which was first studied by Walter Schottky in 1918 [74]. Notably, due to the random nature of these independent reception events, shot noise is generally described using Poisson statistics; however, a Gaussian distribution can be used as a valid approximation considering the large number of photons ($10^2 \sim 10^3$ photons/pulse) involved in the process. As the spectral density of shot noise is practically constant over a wide frequency band ($< 100GHz$), it approximates white noise; therefore, Eqn. 2.3.8 holds for the majority of integrated circuit designs of practical interest [75],

$$S_{shot}(f) = q\langle i_{sig}(t)\rangle \tag{2.3.8}$$

Using Eqn. 2.3.3, the noise variance can then be determined as

$$\sigma^2_{shot} = \int^{B_e} q\langle i_{sig}(t)\rangle df = 2q\langle i_{sig}(t)\rangle B_e \tag{2.3.9}$$

with the corresponding SNR for a shot-noise limited system given by

$$SNR = \frac{\langle i^2_{sig,1}(t)\rangle}{\sigma^2_{shot}} = \frac{\langle i_{sig,1}(t)\rangle}{2qB_e} = \frac{\eta P_{sig,1}}{2h\nu B_e} \tag{2.3.10}$$

which utilises the definition of responsivity from Eqn. 2.3.2 to demonstrate that SNR increases linearly with the received optical signal power.

Thermal Noise:

In an electric conductor at a finite temperature, the random thermal agitation of electrons appears as an electronic noise commonly known as thermal noise; however, it is also known as *Johnson noise* or *Nyquist noise* in honour of the scientists who first studied it [76, 77].

In optical receivers, thermal noise can be modelled as a stationary Gaussian process with a spectral density, $S_{th}(f)$, which is added by a load resistor, R_L, connected to the photodiode in the receiver front-end. For all bandwidths of interest,the two-sided spectral density, $S_{th}(f)$ approximates a white noise process for a given temperature (T) with a frequency independence up to ~ 1THz [26] given by

$$S_{th}(f) = \frac{2k_BT}{R_L} \tag{2.3.11}$$

where, k_B is the Boltzmann constant which has a value of $\approx 1.3806 \times 10^{-23}$ [J/K]. The corresponding thermal noise variance is determined using Eqn. 2.3.3,

$$\sigma^2_{th} = \langle i^2_{th}\rangle = \int^{B_e} \frac{2k_BT}{R_L} df = \frac{4k_BT}{R_L} B_e \tag{2.3.12}$$

Equation 2.3.12 presents an interesting result in that it does not depend on the signal; hence, it is the same for both '1' and '0' levels. In practice, an optical receiver contains many electrical components such as amplifiers which contribute to the thermal noise variance; therefore, Eqn. 2.3.12 can be modified to include the corresponding noise factor, F_n, which represents the level of noise added to the

signal from the additional receiver components.

$$\sigma_{th}^2 = \frac{4k_BT}{R_L} B_e.F_n \tag{2.3.13}$$

For a system dominated by thermal noise, the SNR can be estimated as

$$SNR = \frac{\langle i_{sig,1}^2(t)\rangle}{\sigma_{th}^2} = \frac{\langle i_{sig,1}^2(t)\rangle R_L}{4k_BTB_eF_n} = \frac{(R^2P_{sig,1}^2)R_L}{4k_BTB_eF_n} \tag{2.3.14}$$

where the performance varies as P_{sig}^2; however, it should be recognised that the SNR can also be improved by increasing R_L; hence, most receivers use a high-impedance front end.

Beat-Noise in Optically Amplified Systems:

As outlined in section 2.2.2, optical amplification is used to compensate for the inherent attenuation, α_{dB}, within optical fibre; however, it also degrades the OSNR through the addition of amplified spontaneous emission (ASE) which represents a source of Gaussian optical noise generated by quantum fluctuations in the gain medium. Subsequently, at the receiver, square-law (direct) detection results in the co-polarised ASE field, $E_{ASE,\parallel}(t)$, beating with the field of the optical signal, $E_{sig}(t)$, and the beating of the ASE with itself producing undesired fluctuations in the photocurrent which serves to further degrade the SNR. For instance, when only the contribution of ASE noise is considered, the photocurrent generated by the receiver can be written as,

$$\begin{aligned} i_{rx}(t) &= R(|E_{sig}(t) + E_{ASE,\parallel}(t)|^2 + |E_{ASE,\perp}(t)|^2) \\ &= \underbrace{R|E_{sig}(t)|^2}_{\substack{\text{Information}\\ \text{Signal}}} + \underbrace{2R.Re\{E_{sig}(t).E_{ASE,\parallel}^*(t)\}}_{\substack{\text{Signal-ASE}\\ \text{Beat Noise}}} + \underbrace{R(|E_{ASE,\parallel}(t)|^2 + |E_{ASE,\perp}(t)|^2)}_{\substack{\text{ASE-ASE}\\ \text{Beat Noise}}} \end{aligned} \tag{2.3.15}$$

where, $Re\{\}$, indicates the real part of a complex quantity, * signifies the complex conjugate, R is the responsivity of the photodiode [A/W] and $E^{\perp}_{ASE}(t)$ represents the orthogonally polarised portion of the ASE which does not beat with the signal.

If the bandwidth of the optical filter, B_{opt}, preceding the photodiode significantly exceeds both the signal bandwidth and the electrical bandwidth of the receiver, B_{3dB}, the signal-ASE and ASE-ASE beat noise variances can be approximated as [26]

$$\sigma^2_{sig-ASE} = 4R^2 P_{sig,1} S_{ASE} B_e \tag{2.3.16}$$

$$\sigma^2_{ASE-ASE} = 4R^2 S^2_{ASE} B_{opt} B_e \tag{2.3.17}$$

where, R is the responsivity of the receiver [A/W], G is the gain of the optical amplifier, S_{ASE} represents the power spectral density of the ASE which is co-polarised with the signal (as specified in Eqn. 2.2.26), B_e is the noise equivalent bandwidth of the receiver and B_{opt} is the bandwidth of the optical filter centred on the signal wavelength. In practice, the ASE-ASE beat noise generated by wavelengths outside the region of the signal can be suppressed using an optical bandpass filter, as evident in Eqn. 2.3.17; therefore, in a beat-noise limited system, the inherent signal-ASE beat noise is considered as the dominant optical contribution to the SNR degradation. In this scenario, the receiver's noise performance can be fully characterised by the OSNR as shown in Eqn. 2.3.18

$$SNR = \frac{\langle i^2_{sig,1}(t) \rangle}{\sigma^2_{sig-ASE}} = \frac{R^2 P^2_{sig,1}}{4R^2 P_{sig,1} S_{ASE} B_e} = \frac{P_{sig,1}}{4 S_{ASE} B_e} = OSNR(\frac{B_{ref}}{B_e}) \tag{2.3.18}$$

where,

$$OSNR = \frac{P_{sig,avg}}{P_{ASE}} = \frac{P_{sig,avg}}{2 S_{ASE} B_{ref}} = \frac{P_{sig,1}}{4 S_{ASE} B_{ref}} \tag{2.3.19}$$

in accordance with Eqn. 2.2.26 and 2.2.28; with $P_{sig,1} = 2.P_{sig,avg}$.

Accounting for Multiple Noise Contributions:

Equations 2.3.10, 2.3.14 and 2.3.18 have considered scenarios for which a certain noise mechanism (shot, thermal and beat) is dominant; however, in some practical cases all of the noise sources discussed in this section are contributing to the overall degradation of the signal. Since these noise mechanisms have been approximated as statistically independent Gaussian functions, the overall noise can be determined through the summation of the contributing current variance values; hence, the total SNR is given by

$$SNR_{tot} = \frac{\langle i^2_{sig,1}(t)\rangle}{\sigma^2_{tot}} = \frac{RP_{sig,1}}{\sigma^2_{shot} + \sigma^2_{th} + \sigma^2_{signal-ASE} + \sigma^2_{ASE-ASE}} \tag{2.3.20}$$

However, the shot noise current variance specified in Eqn. 2.3.9 must be modified to account for the received ASE power (P_{ASE}) as follows,

$$\sigma^2_{shot} = 2q[R(P_{sig,1} + P_{ASE})]B_e \tag{2.3.21}$$

2.4 Transmission Performance Evaluation

As the SNR only accounts for the statistics of the '1'-bit level, an alternative metric known as the quality factor (Q-factor, Q) is commonly used to include the current noise variance associated with the '0' level under the conventional approximation of Gaussian noise statistics with an optimised decision threshold (I_d) [78].

$$Q = \frac{I_1 - I_0}{\sigma_1 + \sigma_0} = \frac{R(P_1 - P_0)}{\sigma_1 + \sigma_0} \tag{2.4.1}$$

where, $P_{1,0}$ and $I_{1,0}$ are the noise-free average optical powers and signal currents for the '0' and '1' bits respectively, and $\sigma_{0,1}$ are the associated noise standard deviations.

Under the assumption that the signal has a high extinction ratio (i.e. $P_{sig,1}/P_{sig,0} \gg 1$) using NRZ-OOK modulation, the relation between Q and SNR for a systems limited by thermal-noise and beat-noise can be determined:

Thermal Noise Limited: $\sigma_1 = \sigma_0 = 2\sigma_{th}$

$$Q \approx \frac{I_1}{2\sigma_{th}} \quad \Rightarrow \quad Q^2 \approx \frac{I_1^2}{4\sigma_{th}^2} \approx \frac{SNR}{4} \quad \Rightarrow \quad Q \approx \sqrt{\frac{SNR}{2}} \tag{2.4.2}$$

Beat-Noise Limited: $\sigma_{sig-ASE} = \sigma_1 \, (\gg \sigma_0)$

$$Q \approx \frac{I_1}{\sigma_{sig-ASE}} \approx \sqrt{SNR} \approx \sqrt{\frac{OSNR.B_{ref}}{B_e}} \tag{2.4.3}$$

where Eqn. 2.3.7 and 2.3.18 have been used to establish the relationship between Q and SNR, with $I_1 = \langle i_{sig,1}(t) \rangle$. Furthermore, if the system noise is Gaussian, the Q-factor can be used as a convenient way of expressing the *bit error rate* (BER) which constitutes the ultimate measure of transmission performance in communication systems. Notably, the BER is statistically defined as the time-averaged fraction of misinterpreted bits (errors) contained in a stream of n bits. Moreover, for long averaging times, as the number of transmitted bits increases, the quality of the estimate improves and the BER approaches the true probability of having a detection error for an individual bit, $P(e)$. However, while it is important to transmit enough bits through the systems such that the BER is an accurate estimate of $P(e)$, the practicalities of such a measurement for a high performance transmission link can be unreasonable. For instance, in order to measure a BER of 1×10^{-15} with a 95% confidence level by counting the generated errors at a bit rate of 10Gb/s requires a measurement time of approximately 3.5 days [79]. As a result, the Q-factor is a representation of system performance based on the observation of the mean and standard deviation of the electrical signal at the receiver rather than counting individual errors. It should also be noted that the reliability of a transmission system is not achieved by maintaining the BER at an extremely low level in order to avoid all bit errors. Instead, if the data rate can be kept below a tolerable BER threshold, the use of forward error correction (FEC) through digital signal processing (DSP) can to ensure that the system performs virtually error-free, i.e. reaching a BER $\leq 1 \times 10^{-12}$ [80].

$$BER = \frac{1}{2}[P(1/0) + P(0/1)] \approx \underbrace{\frac{1}{2}\text{erfc}\left(\frac{Q}{\sqrt{2}}\right)}_{\substack{\text{Gaussian Noise} \\ \text{Statistics}}} \tag{2.4.4}$$

where, $P(1/0)$ represents the probability of deciding a '1' when a '0' is received, $P(0/1)$ signifies the probability of deciding a '0' when a '1' is received where the factor of 1/2 accounts for equal probability of either a '1' or '0' to occur and $erfc(z)$ is the complimentary error function = $(2/\sqrt{\pi})\int_z^\infty e^{-t^2}dt$.

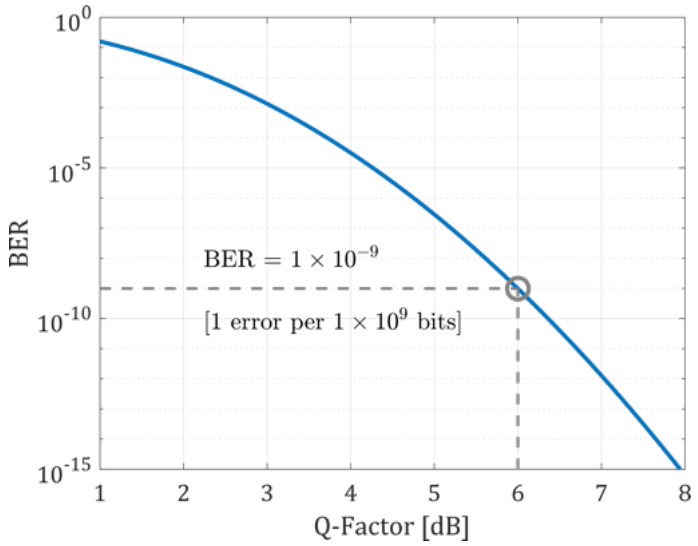


Figure 2.14: Bit error rate as a function of the Q-factor.

As demonstrated in Fig. 2.14, the Q-factor is generally represented in decibel units, [dB], using, $Q_{dB} = 20log_{10}(Q)$, where the factor of 20 is used as Q is defined with respect to the mean and standard deviation of the electric signal (i.e. current or voltage) at the receivers decision block as opposed to the electrical power used in the SNR calculations. In practice, the BER is generally measured using a bit error rate tester (BERT) as a function of the average received optical power (P_{rx}); however, for links limited by beat-noise it can be more meaningful to measure the BER with respect to the received OSNR. With this in mind, Eqn. 2.4.4, 2.4.2 and 2.4.3 can

be used to establish the relationship between BER, Q and SNR for systems limited by thermal noise and beat-noise respectively:

$$\underline{\textit{Thermal Noise Limited:}} \qquad BER \approx \frac{1}{2}\text{erfc}\left(\frac{\sqrt{SNR}}{2}\right) \tag{2.4.5}$$

$$\underline{\textit{Beat-Noise Limited:}} \quad BER \approx \frac{1}{2}\text{erfc}\left(\sqrt{\frac{OSNR.B_{ref}}{2B_e}}\right) \tag{2.4.6}$$

At this point, it is important to recognise that the exact relationship between BER, Q and SNR is ultimately dependent on the detection scheme with the preceding analysis assuming direct detection governed by Gaussian noise mechanisms with an optimised decision threshold and a high signal extinction ratio. As a consequence, should these conditions be violated the performance analysis may be estimated inaccurately.

2.4.1 System Characterisation and Penalties

The performance of a fibre optic communication link is typically characterised by deliberately stressing the receiver in order to manipulate the Q-factor by inducing the effects attributed to the various noise mechanisms presented in section 2.3.1; this concept is illustrated in Fig. 2.15. For instance, when the received signal maintains a relatively high value of OSNR ($\sim 30dB$), the channel performance is ultimately determined by the level of thermal noise which is intrinsic to the receiver. As such a system is effectively power-limited, characterisation is achieved by monitoring the BER as the average received optical power, P_{Rx}, is adjusted through the application of a controlled amount of attenuation. Alternatively, for systems employing optical pre-amplification, P_{Rx} is generally well above the minimum receiver sensitivity; therefore, the performance of the signal is governed by the level of beat-noise which depends on the amount ASE power, P_{ASE}, present at the receiver. These OSNR-limited systems are generally characterised by recording the BER in response to the addition of a controlled amount of ASE in order to manipulate the received OSNR.

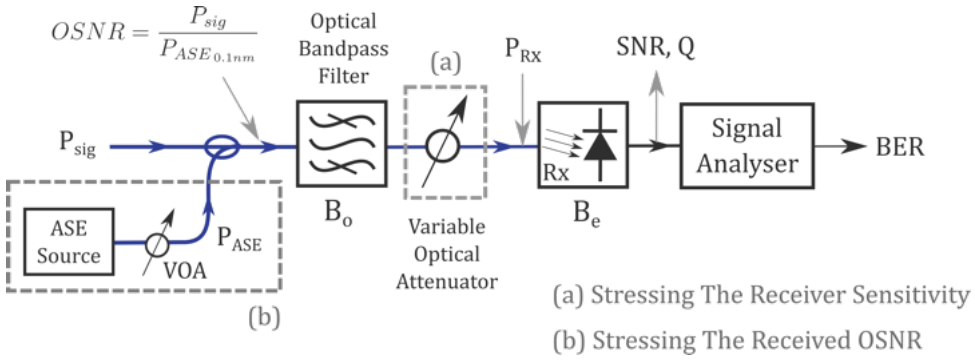


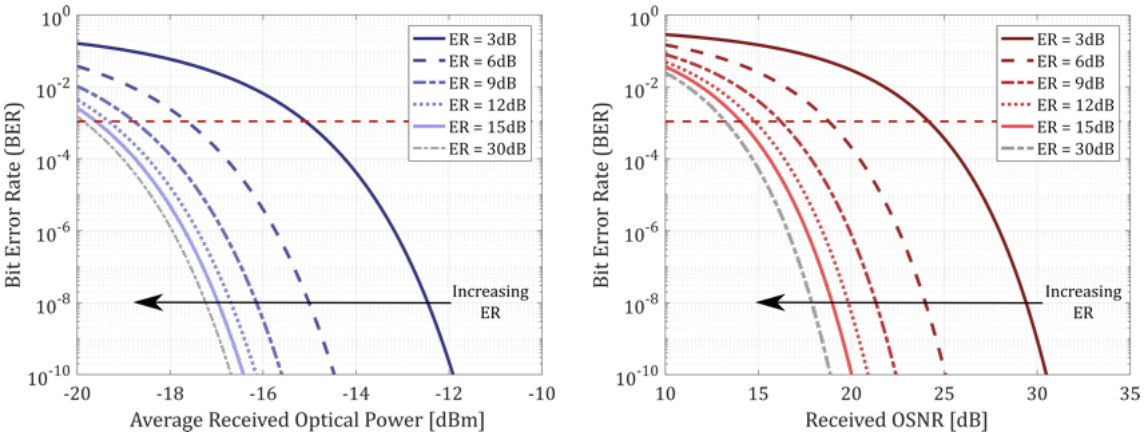
Figure 2.15: Illustration of the main fibre-optic system characterisation processes: (a) stressing the receiver sensitivity, (b) Stressing the received OSNR.

As outlined within the previous sections of this chapter, optical signals can suffer from multiple sources of impairment including loss, dispersion during transmission through a given fibre-optic link. Subsequently, following reception, these impairments are evident through a power or OSNR penalty which represents a horizontal displacement of the BER curve (without alteration of its shape) with respect to the equivalent 'back-to-back' measurement which only considers the combined performance of the transmitter and the receiver. For example, the concept of a performance penalty is presented in Fig. 2.16 which presents the analytically simulated BER as a function of (a) the average received optical power, P_{Rx}, and (b) the received OSNR for a power-limited and OSNR-limited system respectively using different values of the transmitter ER which describes the extent of digital modulation on the optical carrier through the ratio of the optical power at the '1'-bit level ($P_{sig,1}$) to the optical power at the '0' bit level ($P_{sig,0}$).

$$ER = \frac{P_{sig,1}}{P_{sig,0}} \quad \Rightarrow \quad P_{sig,1} = ER.P_{sig,0}, \quad P_{sig,0} = \frac{P_{sig,1}}{ER} \tag{2.4.7}$$

In comparison to the effects of other system impairments such as chromatic dispersion and non-linear distortions the effects of extinction ratio (ER) are relatively simpler to describe analytically; hence, it is used here for convenience in order to demonstrate the system characterisation concepts; however, in principle, the same methods can also be applied to any of the above impairments with no difference

whatsoever. It is also important to note that Eqn. 2.4.2 and 2.4.3 which describe the BER for thermal and beat-noise limited systems cannot be used here as their derivation assumed an infinitely high extinction ratio, which does not hold in practice; therefore, the Q-factor was re-calculated in both cases to account for the statistics of the '0'-bit level. These calculations are presented in Appendix A.



(a) (b)

Figure 2.16: Analytical simulation of the BER performance for a (a) power limited and an (b) OSNR limited transmission link for various values of extinction ratio (ER).

Using the data presented in Fig. 2.16, the corresponding power and OSNR penalties were calculated with respect to a target BER value of 1.1×10^{-3} using the curve generated with the highest extinction ratio (30dB) as a reference. This value of BER was chosen as it represents the required performance threshold of the Reed-Solomon RS(248,216) FEC algorithm that has been selected for use within the DISCUS experimental test-bed in accordance with recent 10G PON standards [81]. The associated penalty curves are presented in Fig. 2.17.

For high values of ER (i.e. ≥15dB), both system types perform similarly with a negligible penalty (<1dB) observed with respect to the reference value. On the other hand, when the ER is reduced to values representative of those achieved by the modulators employed within this work (≤ 15dB), the penalty curves differ significantly. In particular, it is evident that OSNR penalty rises much faster than the power-limited case. This behavior can be attributed to the fact that the noise

variances and the associated Q-factor for both cases have very different characteristics. In particular, for the power limited case the Q-factor is linearly proportional to the received power, P_{rx}. In other words, if the Q-factor needs to be increased by a certain amount in order to compensate for the effect of a given impairment, it should be sufficient to increase the received input power P_{Rx} by an equivalent amount. Alternately in the case of an OSNR-limited system, the Q-factor exhibits a more complex relation to the received OSNR. For instance, it can be seen that the numerator is linearly proportional to the OSNR while the denominator depends on the square root of the OSNR. In short, this is the fundamental reason behind the different penalty profile exhibited in Fig. 2.17. Consequently, it is important to note that the concept of penalty could be deceptive if the associated system noise-limitation is not specified.

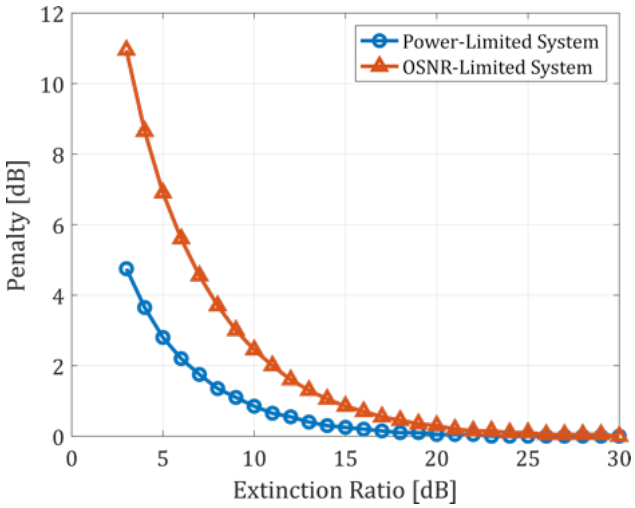


Figure 2.17: Performance penalty measured at a BER value of $\approx 1.1^{-3}$ for a power limited system and an OSNR-limited system for various values of extinction ratio.

2.5 Summary

This chapter has presented the fundamental transmission impairments of a fibre-optic communication link alongside the main techniques used to evaluate the signal performance. For instance, the primary sources of signal deterioration have been presented and classified as linear (attenuation, chromatic dispersion etc.), non-linear

(Kerr effects, stimulated scattering) and noise. In addition, optical amplifiers are presented as a regeneration-free solution to compensate for the inherent attenuation of the signal power, with details presented on the general concepts of optical gain, G, and saturation alongside the associated noise figure, NF, attributed to the generation of amplified spontaneous emission (ASE) which can lead to signal degradation though a reduction in the optical-signal-to noise ratio (OSNR).

Following reception, the main noise mechanisms which contribute to the degradation of the electrical signal-to-noise ratio (SNR) signal are presented and discussed followed by the introduction of a parameter known as the signal quality factor (Q) which accounts for the impact of the noise statistics on both bit ('1' and '0') levels.

Finally, the bit error rate (BER) was shown to represent the ultimate measure of system performance evaluation where link characterisation is achieved by deliberately stressing the receiver over its range of operation in order to induce the associated system defining noise mechanisms, namely thermal and beat-noise for power and OSNR-limited systems respectively. This process enables the impact of signal degradation to be captured through a performance penalty which is determined with respect to a back-to-back BER measurement; however, in order to avoid inconsistencies, it has been shown that it is crucial to include information on the type of system being considered (i.e. power or OSNR-limited) as the same penalty value can have a significantly different impact and interpretation. For these reasons, it is crucial to incorporate a performance margin when designing an optical communications system in order to account for any unforeseen penalties and the possibility of incremental upgrades such as increasing the physical reach or split.

3

The Evolution of Optical Access

"The day will come when the man at the telephone will be able to see the distant person to whom he is speaking" - Alexander Graham Bell (1906)

This chapter presents an overview of the development history of optical access networks alongside the technology requirements facing the realisation of dynamically reconfigurable long-reach passive optical networks (LR-PONs) which target a cost-effective Fibre-to-the-Premises (FTTP) solution capable of supporting multiple service scenarios (residential, business) and a wide-range of geo-types (urban, rural).

In section 3.1, the chapter begins by highlighting the increasing demand for bandwidth in the access portion of the network while motivating the need for Fibre-to-the-premises (FTTP) technologies. Subsequently, section 3.2 outlines the evolution of optical access networks and the corresponding standardisation efforts, beginning with a description of the widely deployed gigabit-capable PONs. This is followed in section 3.2.2 by an overview of the 'next-generation' (NG) PON configurations which target line rates of 10Gb/s; these include the IEEE 10GE-PON, the FSAN/ITU-T XG-PON and the recently standardised NG-PON2 which has introduced WDM to the access network. By considering the limitations in today's access solutions, section 3.3 motivates the concept of a dynamically reconfigurable long-reach PON (LR-PON) which employs time- and wavelength-division multiplexing to increase the information capacity and bandwidth efficiency alongside in-line optical amplification which extends the physical reach and split far beyond that of current access configurations in order to maximise sharing of network resources (i.e. infrastructure and bandwidth). Finally, section 3.3.4 highlights the key enabling technologies required to establish such a system. These include, low-cost tuneable transmitters, high dynamic range burst-mode optical amplifier nodes and the realisation of innovative 10G burst-mode subsystems such as forward error correction (FEC).

3.1 Driving Fibre-to-the-Premises

Present day communication networks are facilitated by a hierarchical structure consisting of core, metropolitan (metro) and access networks as illustrated in the simplified model presented Fig. 3.1. The core network represents the central or backbone portion of the infrastructure which carries traffic between cities, countries and continents in order to interconnect the primary distribution points known as nodes. Subsequently, wide-ranging regional systems known as metro networks provide interconnectivity between the core nodes and the central office (CO) or local exchange (LE) sites which connect the customers to service providers through the access network.

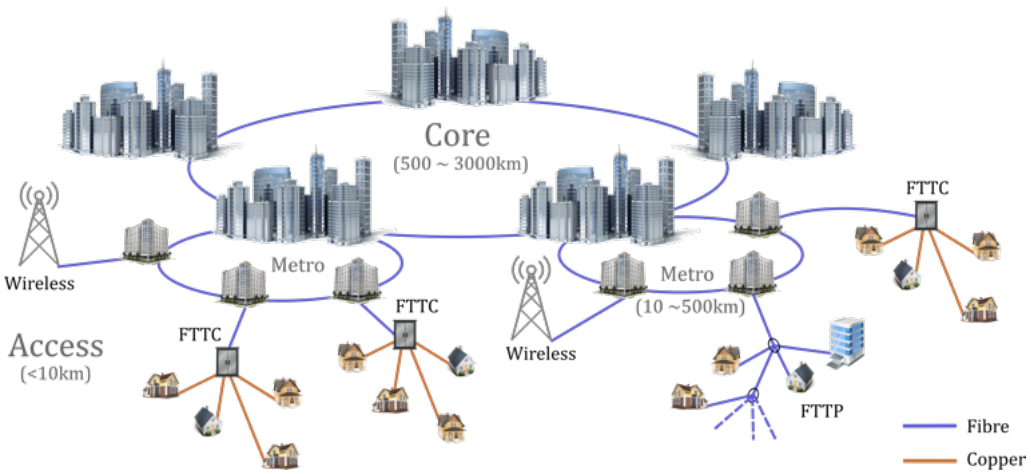


Figure 3.1: Illustration of a modern telecommunication network hierarchy.

In recent years, the development of online services such as video conferencing, video-on-demand (VoD), high-definition television (HDTV), voice-over internet protocol (VoIP), e-learning and online gaming have necessitated the continual upgrade of access network technologies in order to keep up with the increasing bandwidth demands presented in Table 3.1. For instance, residential customers now require an access solution that can provide high-speed broadband offering 'triple-play' services (i.e. voice, data and video) while corporate users require a high-capacity, low-latency infrastructure through which they can connect their local access networks (LANs) to the core. With this in mind, it is clear that efficient high-speed broadband communication networks are essential for thriving modern communities. In fact, whether

it is for social or business purposes, our lives now revolve around devices (e.g. computers, smart phones, televisions, tablets, smart watches, game consoles, e-readers. etc.) which expect a continual and seamless connection to the internet. This thirst for data is pushing the physical media dependent limitations of traditional copper-infrastructure and driving network operators to consider optical access networks in an attempt to meet the growing demands from both business and private customers.

Online Service	**Required Bandwidth [Mb/s]**
Telephone (VoIP)	< 0.5
Music Streaming (High Quality)	< 0.5
Standard Definition (SD) Video	3 - 4
High Definition (HD) Video	5 - 8
Ultra-High Definition (UHD) Video	25
Video Calling (SD/HD)	0.5/1.5
HD Teleconferencing (Group)	6
HD Online Gaming (Multiplayer)	5-10
Web Browsing and Email	1
Social Media (excl. video content)	3

Table 3.1: Estimated bandwidth requirements of typical broadband services [82].

It is important to note that the current level of worldwide interconnectivity would not have been possible without the development of optical fibre which is now the dominant transmission medium within the metro and core networks. In fact, according to Corning Incorporated, one of the worlds leading innovators in materials science, more than 2 billion kilometres of optical fibre is now deployed around the world, linking businesses, communities, countries and continents together [83]. Moreover, as shown in Fig. 3.2, the latest results from the Organisation for Economic Co-operation and Development (OECD) indicate that fibre-based access infrastructures including the Gigabit PON (G-PON) [84] and the Ethernet PON (E-PON) [85] are now a significant presence, particularly in Asia where Japan and Korea report deployment figures >75%.

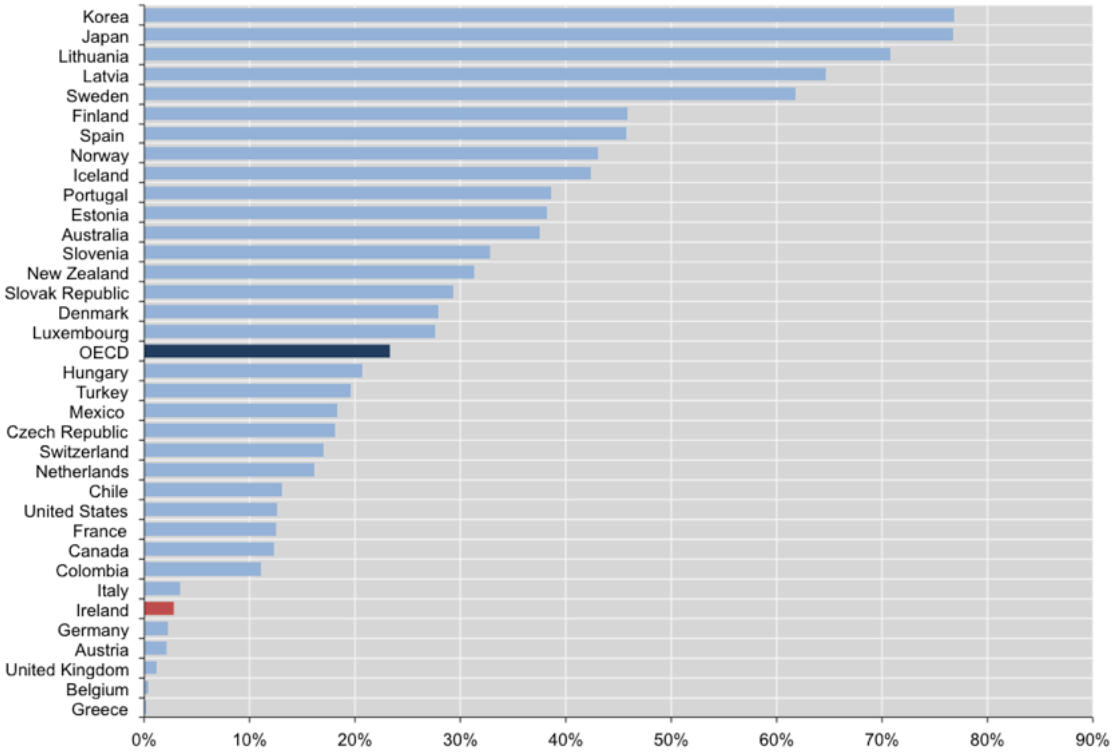


Figure 3.2: Percentage of fibre connections in total broadband subscriptions, December 2017 [14].

As outlined in Chapter 1, the deployment of optical fibre requires a substantial investment, hence many countries have opted for an incremental upgrade to their existing legacy infrastructure while some still lack applications to take full advantage of the bandwidth offered by optical fibre. As a consequence, the demand for a short-term upgrade to an all-fibre network cannot justify the financial investments required; hence, a fibre-to-the-cabinet (FTTC) access configuration utilising a copper-based 'last-mile' infrastructure providing DSL services is still a dominant presence globally. However, as indicated in Fig. 3.3, using DSL technology to support the delivery of high-speed broadband (≥30Mb/s) requires the costly installation of fibre terminals within hundreds of meters from the subscribers.

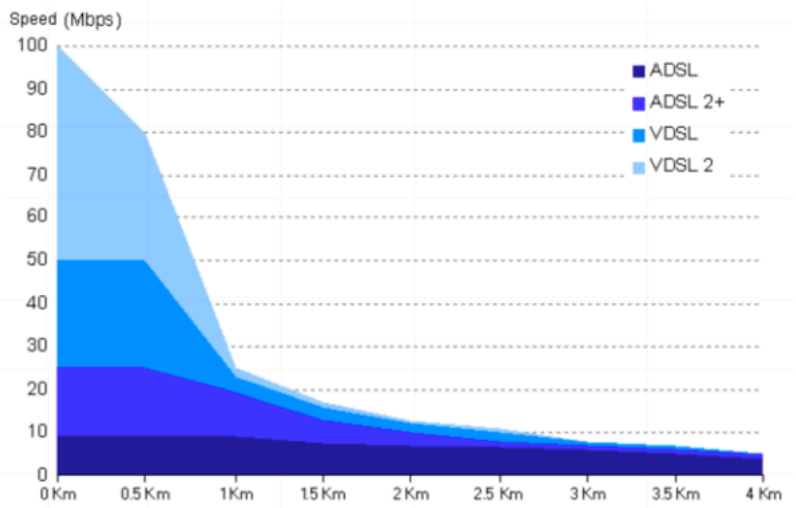


Figure 3.3: Theoretical performance of DSL technologies (Reproduced from [15]).

To avoid the expense and time required for cable installation, a number of wireless technologies including WiMax (Worldwide Interoperability for Microwave Access) [86] and Long-Term Evolution (LTE) [87] have been proposed to provide broadband services alongside satellite solutions [88]. However, it should be noted that in order to make the deployment of terrestrial wireless technologies feasible, base stations must be strategically located in order to capture a sufficiently large number of customers. This inevitably leads to more remote areas with less effective coverage than more densely populated regions with reduced bandwidth capability and quality of service. Moreover, even within areas of good coverage, wireless bandwidth availability can be dependent on the number of active users and the spectrum available in that particular area. Alternatively, despite the extensive coverage capabilities, satellite-enabled broadband requires a considerable investment to cover the equipment and installation costs. In addition, it is subject to congestion limitations and appreciable latency issues due to the long transmission distances involved (i.e. ~36,000km for a geostationary orbit) making it unsuitable for certain broadband services such as business applications and online gaming.

To demonstrate the capabilities of the main access technologies in use today, the maximal line rates and reach are presented in Table 3.2. It should be noted that due to physical media limitations and network congestion, the peak bit-rates may not be achievable at the maximum range; hence, the reported values are purely indicative of the maximum specified within the respective standards. Nonetheless, from these

figures, it is evident that copper and wireless access solutions will not be capable of supporting the increasing demand for higher bit-rates or bridging the digital divide that exists between dense urban areas and sparse rural communities. Consequently, in order to address the current access bottleneck and facilitate the efficient delivery of ubiquitous high-speed broadband for the foreseeable future, network operators must focus on the delivery of Fibre-to-the-Premises (FTTP).

	Technical Maximum Values			
Technology	**Downstream [Mb/s]**	**Upstream [Mb/s]**	**Reach [km]**	**Connection**
ADSL2+	24	1	5	Twisted Pair
VDSL2[3]	100	40	1	Twisted Pair
G.fast	1000	1000	0.1	Twisted Pair
CATV[4]	200	100	2-100	Coaxial Cable
WiMax	70	30	60	Wireless
LTE	100	30	3-6	Wireless
Satellite	30	10	~36,000	Wireless
E-PON	1250	1250	20	FTTP
G-PON	2500	1250	20	FTTP

Table 3.2: Comparison of various access technologies [89].

3.2 The Evolution of Optical Access Networks

The initial concept for a PON emerged in the 1980's when single-mode fibre (SMF) technology was seen as the new way forward for optical communications through the many significant advantages it offered over multi-mode fibre (MMF) including lower-loss, dispersion and bandwidth [90, 91, 92]. Subsequently, over the last two decades various iterations of the PON have been standardised by the Institute of Electrical and Electronic Engineers (IEEE) alongside a collaborative effort between the Full Service Access Network (FSAN) a customer driven working group and the International Telecommunications Union standardisation sector (ITU-T).

[3] with vectoring [93]

[4] Cable Television/Cable Modem

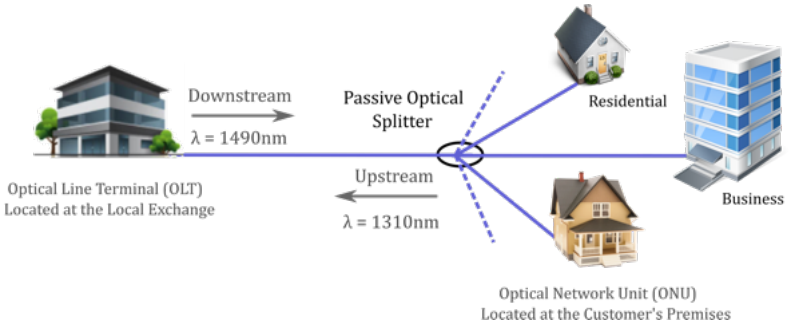


Figure 3.4: The baseline configuration of G-PON and E-PON.

Today, the G-PON and the E-PON are the most widely deployed optical access technologies with G-PON currently the dominant choice in North America while Asia has seen significant E-PON deployment in countries such as Japan and Korea. Moreover, in the last decade, a large-scale deployment using a mix of E-PON and G-PON has been undertaken in China which is recognised as the worlds largest FTTP market [94].

	G-PON	**E-PON**
Standard	ITU-T G.984 [84]	IEEE.802ah [85]
Downstream (DS) [Gb/s]	1.24416 or 2.48832	1.25
Upstream (US) [Gb/s]	1.24416 or 2.48832	1.25
Multiplexing Method	US: TDMA DS: TDM	US: TDMA DS: TDM
Protocol	Ethernet over ATM/IP or TDM	Ethernet
Linecode	Non-Return-to-Zero (NRZ)	8B/10B
Wavelength Plan [nm]	US: 1260-1360 DS: 1480-1500	US: 1260-1360 DS: 1480-1500
ODN Loss Budget	Min Loss: 10dB[3] Max Loss: 25dB	Min Loss: 10dB[4] Max Loss: 24dB
Split	64	32
Reach [km]	20	20
Average Bandwidth per User	19.5Mb/s or 39Mb/s	39Mb/s
Transmission Structure	Asymmetric	Symmetric

[3]Class B (Attenuation Range) [4]1000BASE-PX20

Table 3.3: Comparison of current-generation PON standards

Although G-PON and E-PON possess underlying technological differences, they have both drawn a strong influence from the FSAN/ITU-T broadband PON (B-PON) recommendations [95] with respect to wavelength plan and framework of the optical distribution network (ODN). In particular, their performance is primarily governed by time-division multiplexing (TDM) in order to optimise sharing of the fibre infrastructure. The basic strategy of a TDM-PON involves the use of a single wavelength communication channel in each transmission direction. These wavelengths are combined through wavelength division multiplexing (WDM) to enable single-fibre operation as illustrated in Fig. 3.5. In the downstream (DS) direction, the optical line terminal (OLT) located at the head end of the network broadcasts encrypted data in continuous-mode (CM) which is received by every optical network unit (ONU) at the access edge. Each ONU then accepts or rejects the data based on the identifier (ID) contained within the received frame header. Conversely, in the upstream (US) direction, the ONUs cannot transmit data in CM as the signals would converge and overlap at the splitting locations; therefore, to avoid data collision a time division multiple access (TDMA) scheduling protocol is used which assigns transmission windows to each ONU. In this way, a given ONU only transmits when it is allocated a timeslot and it needs to transmit; this process is known as burst-mode (BM) transmission. The size and frequency of the allocated timeslots are based on the traffic volumes required across all ONUs; hence, the available upstream bandwidth is distributed fairly among all end users depending on their requests.

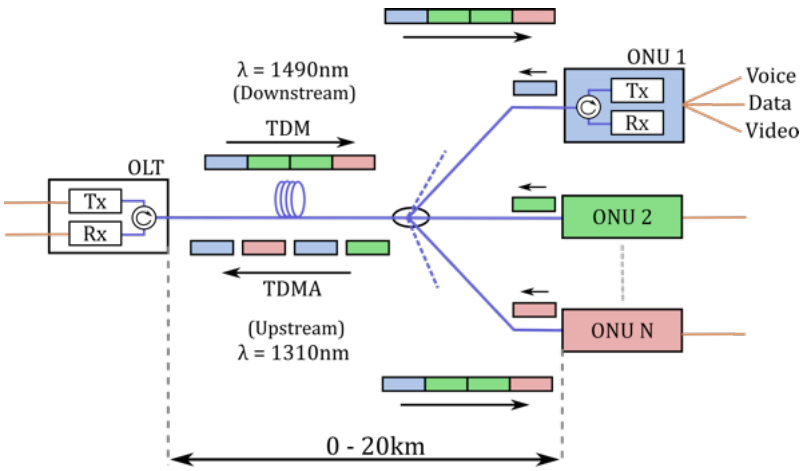


Figure 3.5: Illustration of TDM and TDMA operation [Tx - transmitter, Rx - receiver].

3.2.1 Long-Reach PONs

One of the main advantages offered by PONs is the ability to share network costs among the end users (subscribers); however, the growth in bandwidth demand resulting from increased online services is such that the price decline of electronics and optical technology alone will not be sufficient to keep the costs of network growth in line with the revenue required by operators; therefore, radical new architectures may be necessary to change the end-to-end cost structure of networks and massively reduce the cost of bandwidth provision [96, 97].

A logical strategy to further offset network costs is to optimise the infrastructure in order to capture a greater amount of customers over larger areas with increased sharing of network resources. This concept has been of interest since the 1990's [98] with more recent efforts focussed on expanding the physical reach of G-PON and E-PON via mid-span optical amplifiers [99]. Notably, this concept has since been standardised by ITU-T within the G.984 series of recommendations [100, 101] which specify a maximum logical reach of 60km using a configuration commonly known as a long-reach (LR) PON. It is important to note that in this context the term passive does not strictly mean unpowered, but is related to the absence of active electronic routing elements within the deployed field infrastructure. In practice, the achievable transmission distance of a LR-PON depends on a number of factors which include the wavelength plan, the transmitter (Tx) and receiver (Rx) specifications and the targeted split-ratio; however, advanced network configurations have demonstrated a total physical reach up to 100km and beyond through integration of the metro and access networks [12].

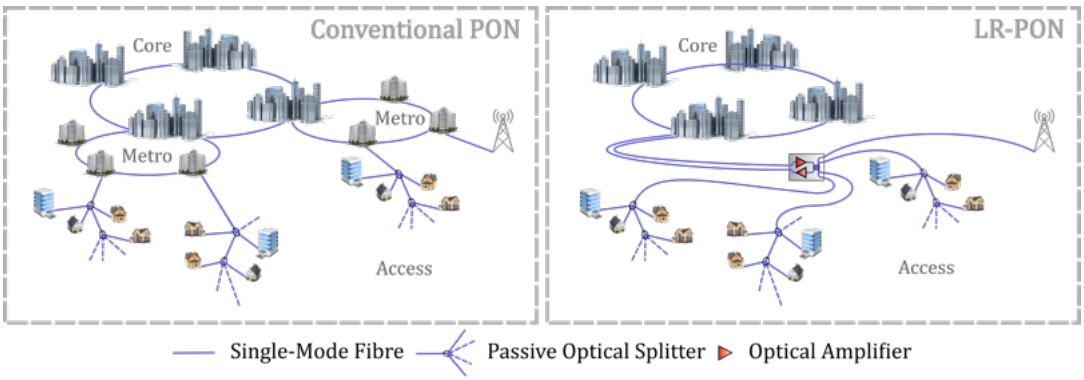


Figure 3.6: Illustration of network simplification through node consolidation using a long-reach PON to integrate the metro and access networks.

Optical Amplifier Technologies:

To facilitate the increased physical reach and split targets of LR-PONs, several optical amplifier technologies have been proposed which utilise optical fibre or semiconductor material as their active media. Notably, for operation in the C-band (1530 - 1565nm), Erbium-doped fibre amplifiers (EDFAs) offer a key solution due to their overall performance quality in terms of low noise figure (NF), high gain, high achievable output power and the ability to provide these characteristics in a system with a large number of WDM channels within the low-attenuation spectral region of SMF. They also have the added advantage of being a mature technology in optical networks making them attractive for deployment in an access architecture [102]. Although, the majority of fibre-amplifiers deployed to date are EDFAs; alternative fibre technologies have been investigated to realise operation outside of the C-band. For instance, to enable reach extension in legacy PON technologies such as G-PON, Praseodymium-Doped Fluoride fibre amplifiers (PDFAs) have shown potential to support upstream signal amplification as their gain spectrum lies within the O-band (1260 - 1360nm) [103] while Thulium-doped fluoride fibre amplifiers (TDFAs) offer the ability to amplify wavelengths within the S-band (1460-1530nm) which is compatible with the downstream transmission window [104]. These novel technologies are not taken into account in this work; however, for further information the reader is referred to [105].

Alternatively, semiconductor optical amplifiers (SOAs) are a promising cost-effective amplifier technology based on mature III-V material technologies and fabrication techniques suitable for mass production with commercial devices readily available from multiple vendors worldwide. Unlike doped-fibre amplifiers (DFAs) and Raman amplifiers, SOAs are pumped electronically via an applied current; therefore, a separate pump laser is not required. Notably, Indium-Phosphide (InP) based SOAs can be designed to provide gain within any wavelength window of SMF (1200nm - 1700nm) by varying the composition of the active material [106]. Although, SOAs do not provide the same gain, saturation output power or noise-figure as fibre-based amplifiers they present a significantly lower physical footprint with low power consumption, potential for monolithic integration with other components and short excited state lifetimes (~100ps) making them highly suitable for burst-mode applications. Based on these properties, SOAs have been considered for deployment within reach extenders for single-channel G-PON systems [107, 108].

In this thesis, the capabilities of EDFAs and SOAs will be examined as potential technologies to support LR-PON operation. In particular, within Chapter 4 an SOA has been monolithically integrated with a modulator and a discretely tuneable three-sectioned slotted Fabry-Pérot (3s-SFP) laser is examined and presented as a potential candidate for deployment in low-cost, wavelength-agile ONUs. Furthermore, within Chapter 5, the dynamics of commercial EDFAs which employ active gain-stabilisation via dynamic pump control will be examined as candidates to support high-dynamic range burst-mode transmission.

3.2.2 Next-Generation PONs

With the continuous increase in bandwidth demand generated by consumer and business applications over the last decade, the need for a new, higher capacity access architecture is more than obvious. For instance, while it is expected that technologies such as G-PON and E-PON will meet the broadband requirements for residential customers in the short-to-medium term; in the long-term, they will struggle to deliver emerging bandwidth heavy multimedia services such as UHD TV, 3D TV, cloud computing and multi-player HD online gaming. Moreover, it is anticipated that the highest bandwidth demands will come from business users and mobile backhaul which are expected to require sustained, symmetric and low-latency data rates of 1Gb/s and beyond. As a result, the higher bandwidth capabilities of optical access networks represents an attractive, lower cost option compared to a leased line or dedicated point-to-point Ethernet connection [109]. Consequently, network operators must now consider which optical access platform will allow them to adapt most cost effectively as future bandwidth demand and applications evolve. In particular, they expect next-generation PON technologies to enhance bandwidth and service support capabilities while supporting coexistence with their existing equipment and outside plant. With this in mind, the IEEE and the FSAN/ITU-T collaboration began work on the next-generation of PON technologies which targeted bit rates of 10Gb/s and beyond. Both organisations focussed a smooth evolution from existing technologies to converged optical access networks capable of supporting residential, business and mobile backhaul. Notably, since the ODN infrastructure represents approximately 70% of total investments in FTTP networks, it was crucial that the next-generation of IEEE and FSAN/ITU-T standards were backwards compatible, enabling operators to re-use their existing infrastructure [110].

10G-EPON

The standardisation of the IEEE 10Gb/s Ethernet PON (10G-EPON) began in September 2006 following a call for interest (CFI) [111] and ended in late 2009 with the publication of the IEEE 802.3av-2009 specifications [9]. In addition to increasing the channel bandwidth from 1Gb/s to 10Gb/s, a primary objective of the IEEE 802.3av task force included the realisation of backwards compatibility with the mass-deployed legacy 1G-EPON systems (including the RF video overlay) in order to ensure a return on investment (ROI) for the network operators. Further system upgrades include the implementation of a new line coding technique with a lower overhead (~ 3.125%), upgraded DBA mechanisms, specifications for 10G burst-mode transmission, forward error correction (FEC) and new security considerations [112].

To enable the coexistence of 10G-EPON with legacy E-PON systems, the 1Gb/s and 10Gb/s downstream channels are separated through wavelength division multiplexing, with 1Gb/s transmission limited to 1480–1500nm band (λ_{DS} = 1490nm) and 10Gb/s transmission using 1575–1580nm band (λ_{DS} = 1557nm). In the upstream direction, the 1Gb/s and 10Gb/s wavelength bands overlap; the 1Gb/s band spreads from 1260 to 1360nm (λ_{US} = 1310nm) while the 10Gb/s band lies between 1260 and 1280nm (λ_{US} = 1270nm). It is important to note that the upstream channels of 10G-EPON and E-PON have been strategically allocated to take advantage of the low-chromatic dispersion region of SMF. However, as different ONUs may have different line rates (1Gb/s or 10Gb/s) both upstream channels must be separated in the time domain using a technique known as dual-rate TDMA. The 10G-EPON wavelength allocation scheme is illustrated within Fig. 3.7.

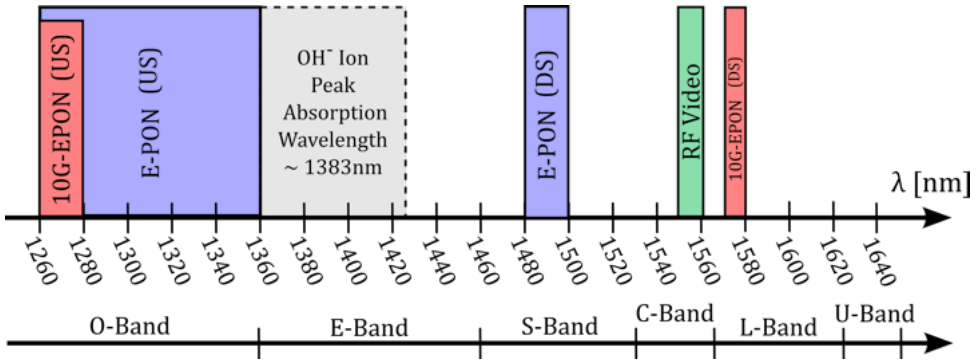


Figure 3.7: Wavelength map of 10G-EPON and legacy E-PON systems.

Alongside the work being undertaken by the IEEE taskforce, the FSAN/ITU-T collaboration established a road map for the evolution optical access technologies with next-generation PONs (NG-PONs) separated into a medium and long-term solutions known as NG-PON1 and NG-PON2 [113]. The first working group was tasked with an evolutionary upgrade of the G-PON standard with a primary focus on increasing the bit rates to 10Gb/s using technologies capable of coexisting with the deployed G-PON systems over the legacy fibre infrastructure. The objective of the second group involved the investigation of all other systems capable of out performing NG-PON1 in terms of ODN compatibility, bandwidth, capacity and cost-efficiency [110]. This included the realisation of new ODNs and technologies that were not available in the expected time horizon which were completely independent of G-PON standards [114].

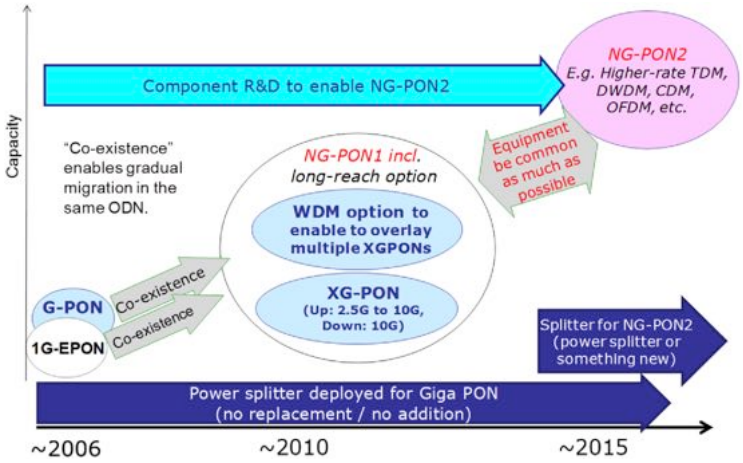


Figure 3.8: The FSAN/ITU roadmap for the standardisation of next-generation optical access networks (Reproduced from [114]).

NG-PON1 (XG-PON)

The FSAN group began to gather options for NG-PON1 in early 2008; these candidates are explained further in [115]. Of the technologies considered for standardisation, the emerging system known as XG-PON (or XG-PON1), utilised an asymmetric 10Gb/s DS, 2.5Gb/s US configuration which was considered the optimum compromise between cost and complexity. Notably, at the time of investigation, the development of a 10Gb/s burst-mode capable Tx for deployment in the ONUs

located at the customers premises posed a substantial financial obstacle. Moreover, a burst-mode OLT Rx capable of operating at 10Gb/s presented a significant technological challenge with an unknown time-frame for commercialisation; hence, the asymmetric configuration was selected for standardisation.

Similar to the design of 10G-EPON, a primary requirement for XG-PON included the realisation of co-existence with the widely deployed G-PON technology in order to enable a seamless upgrade of individual customers without the need to introduce any changes in the ODN or disrupt services for existing customers. To facilitate this coexistence strategy, the recommendations for XG-PON included an updated wavelength plan which utilised WDM to facilitate two wavelength bands; this updated wavelength plan is identical to the plan proposed for 10G-EPON systems shown in Fig. 3.7. Notably, the physical layer convergence of FSAN/ITU-T and IEEE specifications allows for the shared and convergence of 10G technologies including chips, optics and hardware platforms with the aim of driving cost reductions. In this way, carriers have a choice of 10G PON technologies with the advantage of a single physical layer [116]. A side-by-side comparison of the IEEE and FSAN/ITU-T next-generation 10G PON technologies is presented in Table 3.4.

	10G-EPON	**XG-PON**
Standard	IEEE 802.3av [9]	ITU-T G.987 [10]
Downstream [Gb/s]	10.3125	9.95328
Upstream [Gb/s]	1.25 or 10.3125	2.48832
Multiplexing Method	US: TDMA DS: TDM	US: TDMA DS: TDM
Linecode	64B/66B	Scrambled NRZ
Wavelength Plan [nm]	US: 1260-1280 DS: 1575-1580	US: 1260-1280 DS: 1575-1580
ODN Loss Budget	Min Loss: 15dB[6] Max Loss: 29dB	Min Loss: 16dB[7] Max Loss: 31dB
Split	64	64
Reach [km]	20	20
Average DS Bandwidth per User	161 Mb/s	155 Mb/s
Transmission Structure	Symmetric or Asymmetric	Asymmetric

[6]High Power Budget (PR30/PRX30), [7]Nominal2 Class

Table 3.4: Comparison of next-generation PON standards.

The ITU-T published the standards for XG-PON within the G.987 series of recommendations in 2010; this was followed by the world's first XG-PON field trial by Verizon and Huawei Technologies Ltd. in Taunton, MA. [117]. It should also be noted that the 10G symmetric XG-PON variant (known as XG-PON2 or XGS-PON) has recently been standardised within the ITU-T G.9807 series recommendations [118]. Interestingly, this approach was initially considered as too complex with respect to delivering cost-effective component technologies for US transmission; however, the standardisation was strongly motivated by business users who require a sustained, low-latency symmetric bandwidth [119].

NG-PON2: TWDM-PON

Following the development of the XG-PON standard, FSAN began work on the second iteration of the next-generation PON strategy (i.e. NG-PON2) which involved the consideration of new fibre architectures that could take advantage of the maturing WDM technologies in order to further enhance capabilities of the access network and address the anticipated market [120]. For instance, the original NG-PON2 strategy considered the deployment of passive wavelength splitters such as arrayed waveguide gratings (AWGs) within the ODN instead of the traditional power splitters [121]. However, it soon became clear that the NG-PON2 should be backwards compatible with legacy PON systems due to the substantial investments made to date in power splitter based fibre infrastructure. Furthermore, network operators requested that NG-PON2 must be able to co-exist with previously deployed systems such as G-PON and XG-PON in order to facilitate progressive migration of existing subscribers and the addition of new subscribers with minimal disruption of services. Subsequently, in April 2012, the time and wavelength division multiplexed (TWDM) PON configuration was chosen as the primary solution for NG-PON2 as it was most compatible with the preferential high-volume residential application. It should be noted that the proposed system also enables extensive re-use of XG-PON technology by effectively stacking multiple XG-PONs through WDM. Moreover, in an attempt to mitigate the operational expenditure, network operators requested a limitation on the number of equipment variants resulting in the need for 'colourless' ONUs which incorporate tuneable transceivers in order to reduce inventory costs and establish flexibility with respect to service provision [122].

The NG-PON2 standards were finally published in 2015 within the ITU-T G.989 series of recommendations [11]. An overview of the main physical layer specifications is presented in Table 3.5. In particular, the baseline architecture, uses four wavelength channels with a fixed 100GHz spacing between 1596 and 1603nm to achieve an aggregated capacity of 40Gb/s (4 × 10Gb/s) in the DS direction. Alternately, in the US direction, four wavelengths with a bit rate of 2.5Gb/s or 10Gb/s can be used to establish an aggregated capacity of 10Gb/s or 40Gb/s respectively. Notably, to address the wavelength control capabilities of the various ONU-Tx technologies currently available, the US wavelength band for the TWDM-PON is specified using three distinctions: wide (1524 - 1544nm), reduced (1528 - 1540nm) and narrow (1532 - 1540nm) where channel spacings of 200GHz, 100GHz and 50GHz are supported.

	NG-PON2	
Standard	ITU-T G.989 [11]	
Downstream [Gb/s]	4 × 2.48832 or 9.95328	
Upstream [Gb/s]	4 × 2.48832 or 9.95328	
Multiplexing Method	US: TDMA DS: TDM	Point-to-Point WDM
Linecode	Scrambled NRZ	Vendor Specific
Wavelength Plan [nm]	US: 1524-1544[7] DS: 1596-1603	1524 - 1625[8] 1603 - 1625[9]
ODN Loss Budget	Min Loss: 20dB[10] Max Loss: 35dB	Min Loss: 20dB[10] Max Loss: 35dB
Split	64	64
Reach [km]	40	40
Average Bandwidth per User	39Mb/s or 156Mb/s	1.25Gb/s - 10Gb/s
Transmission Structure	Symmetric or Asymmetric	Symmetric

[7]Wideband Option, [8]Expanded Spectrum, [9]Shared Spectrum, [10]Class E2 (Optical Path Loss)

Table 3.5: Overview of the NG-PON2 specifications.

It should be noted that to facilitate the demanding bandwidth requirements for business and backhaul services, the NG-PON2 recommendations also include a point-to-point (PtP) WDM overlay allowing access to unshared bandwidth. In practice, the ONUs for PtP WDM require similar low-cost tuneable Tx and Rx elements

as for TWDM-PON with the main difference being the continuous-mode operation for PtP WDM as opposed to burst-mode for the TWDM-PON. Notably, within the proposed baseline architecture, eight PtP channels between 1603 and 1625nm are considered to allow full coexistence with legacy PON technlogies. However, depending on demand, a network operator may choose to support additional WDM channels via unused spectrum anywhere between 1524nm and 1625nm as shown in Fig. 3.9.

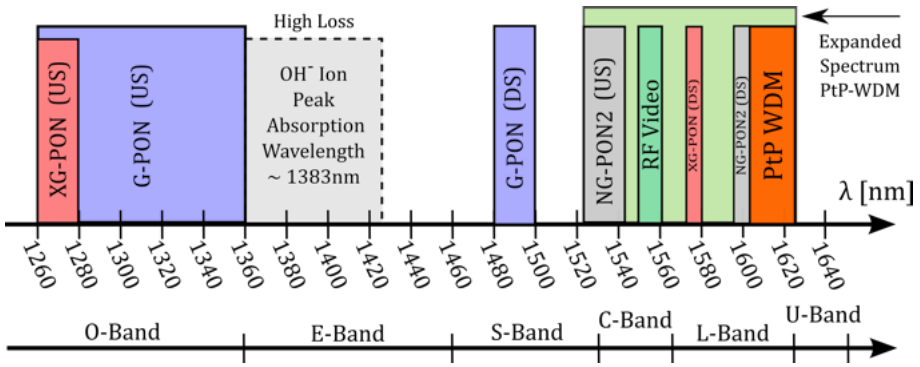


Figure 3.9: NG-PON2 wavelength map (Note: Coexistence with legacy PON systems).

At present, one of the most challenging aspects of the NG-PON2 configuration is the realisation of low-cost wavelength agile technologies with precise tuning and control functionality for deployment within the customers premises equipment. While tuneable transceivers are widely used in carrier networks, current modules don't necessarily meet all of the NG-PON2 performance specifications and are too expensive for mass-market residential deployment. In fact, according to [123], the ONU technology accounts for approximately 20% of the total PON investment costs; therefore, the development of such components is of critical importance in order to maintain the financial viability of the proposed configuration. This issue is currently being addressed by photonic systems research groups worldwide with investigations currently focussed on directly modulated tuneable lasers (DMLs) [124] and photonic integrated circuits (PICs) which have demonstrated advantages with respect to potentially low-cost fabrication techniques [125]. In addition, to compliment the introduction of tuneability in the physical layer, the transmission convergence (TC) layer must be modified in order to specify the techniques required to manage and control the multiple wavelengths present in the system [126].

The introduction of WDM within the recent NG-PON2 standard offers a significant innovation with respect to legacy PON systems offering an appreciably higher capacity with options available depending on the use case (i.e. residential, business). However, on closer inspection, this system represents an incremental step forward rather than a revolutionary one. This rate of progression is largely attributed to the compelling need for network operators to drive down equipment and operational costs for new systems in order to stimulate the market and allow the new technology to establish itself without adding confusion to the landscape. Furthermore, since there is limited short or medium term demand for 10Gb/s residential services it is expected that in the long-term there will be a minor amount of XG-PON deployment followed by more extended deployments of NG-PON2 as its capabilities best match the need to upgrade G-PON networks; hence, it is expected that most network operators are expected to go directly to NG-PON2 and skip XG-PON [127].

3.3 Beyond Next Generation Access

As 10G PON has matured commercially in recent years and TWDM-PON has been standardised for NG-PON2, the bandwidth offered by a PON system has increased immensely. Nonetheless, network operators concerns have now turned towards efficient utilisation of PON resources (infrastructure, bandwidth), value-added service provisioning, and return-on-investment improvement [128]. For instance, a number of large-scale EU research projects (e.g. PIEMAN [129] and SARDANA [130]) have established the feasibility of innovative FTTP architectures which extend the physical reach (≥ 100km) and split (≥ 512) alongside a significantly increased information capacity (32$\lambda\times$ 10Gb/s) through the use of hybrid time and wavelength multiplexing techniques [13, 131]. Nonetheless, the implementation of a static wavelength assignment strategy within these systems ultimately restricts the dynamic provision of bandwidth to end users; hence, the resulting concept of 'stranded capacity' presents a major limitation of current optical access solutions. Furthermore, the 'tree-structured' physical layer proposed by the PIEMAN project employs a long backhaul ($\sim 90km$) to support a relatively short distribution network (~10km). It should be noted that this strategy is only suitable for urban deployment where a dense distribution of subscribers is required in order optimise infrastructure utilisa-

tion and minimise the cost per customer. Consequently, when FTTP is rolled out on a large scale the architecture must be as economically viable as possible for the wide range of geo-types that occur in a typical country-wide networks.

3.3.1 Bridging the Digital Divide

Ideally, all users and all communities should have equal access to high speed broadband so that there is no division of service availability due to customer location. However, many countries still exploit old copper transmission technology and have created a digital divide between those with good copper access close to the operator's electronic infrastructure and those located in more remote areas connected via much longer copper lines. Moreover, despite the recent annual growth of fibre subscriptions detailed within the latest report on broadband coverage published by the European Union (EU) [132], rural areas continue to be sparsely covered as they are not considered a viable business case by network operators. The resulting lack of infrastructure and connectivity in these regions has lead to repercussions for businesses, schools, healthcare providers and government agencies with many countries now experiencing a significant growth in urbanisation as a result. Furthermore, the recent growth of teledensity in urban areas, fueled by mobile technology has further increased the digital divide. To illustrate this point, the latest figure demonstrating level of rural broadband coverage in Europe using next-generation access (NGA) technologies is presented in Fig. 3.10. The data shown encompasses VDSL, DOCSIS 3.0 and FTTP technologies capable of supplying download speeds of at least 30Mb/s. The latest information indicates that by mid-2017, 92.4% of rural EU homes were passed by at least one fixed broadband technology; however, less than 50% (46.9%) had access to high-speed next generation services.

The main challenges for the provision of telecommunication services to rural communities are driven by technological and economic considerations. For example, a lower population density will require network coverage over a larger geographical area in order to capture a sufficient number of customers and optimise resource utilisation; this has direct implications on the required infrastructure and the cost per customer. In addition, unreliable or complete lack of energy sources still presents a significant barrier in remote areas while the requirement to maintain a sufficient backup system raises the operational costs significantly.

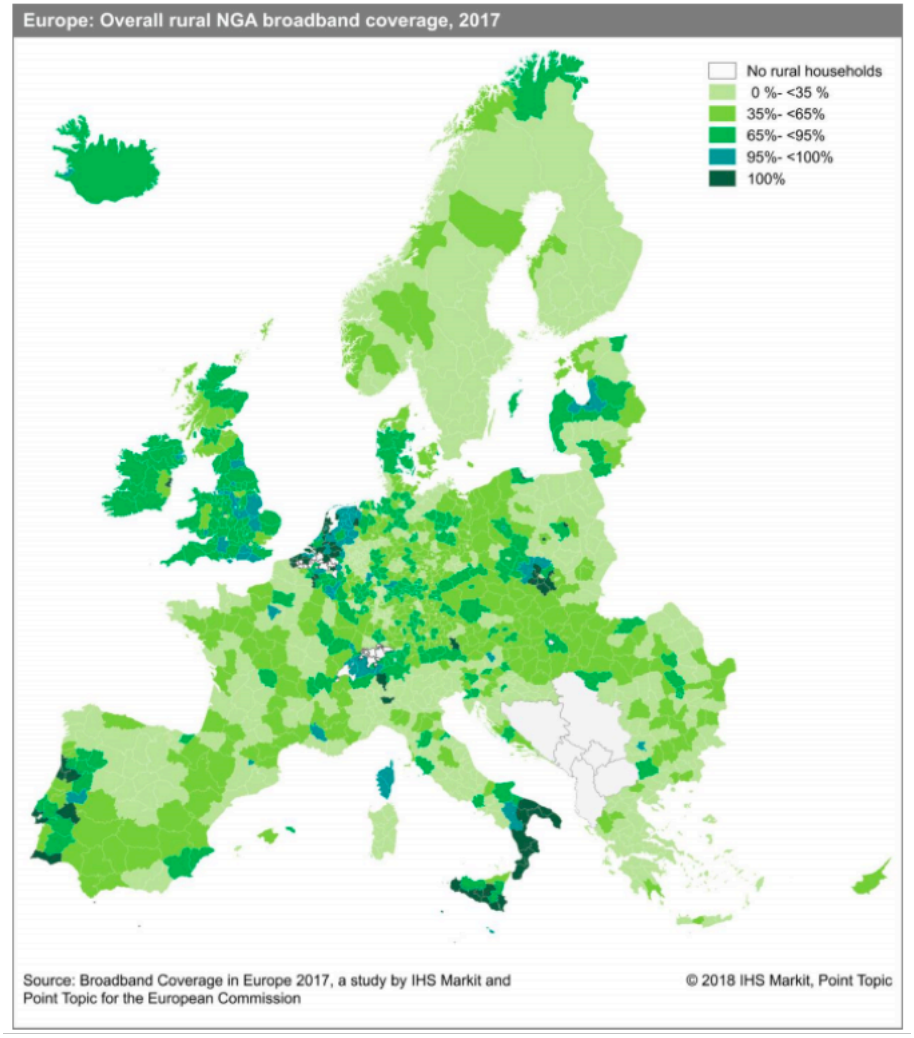


Figure 3.10: Rural High-Speed Broadband Coverage, Europe, 2017 (Reproduced from [132])

The disparity between rural and urban connectivity in the Republic of Ireland is evident from Fig. 3.11 which illustrates the availability of high-speed broadband (≥30Mb/s) in the second quarter of 2017. As of September 2017, just 65% of the 2.3 million premises around the country have access to high-speed broadband. However, by the end of 2018 it is expected that 77% will be covered with 90% coverage forecast for 2020. The image and corresponding data presented within Fig. 3.11 are taken from the Department of Communications, Climate Action and Environment which presents the data as part of the National Broadband Plan (NBP) [133]. The NBP is a government driven initiative that targets download speeds of 70Mb/s per user with a

minimum of 40Mb/s generally available and 30Mb/s in harder to reach rural areas in accordance with the Digital Agenda for Europe (DAE)[134]. The DAE was outlined by the European Commission in 2010 and it is aimed at boosting Europe's economy by delivering sustainable economic and social benefits from a digital single market. The main objectives of the DAE include the provision of universal download speeds of 30Mb/s for all citizens with 50% of European Union (EU) households subscribing to speeds of 100Mb/s by 2020.

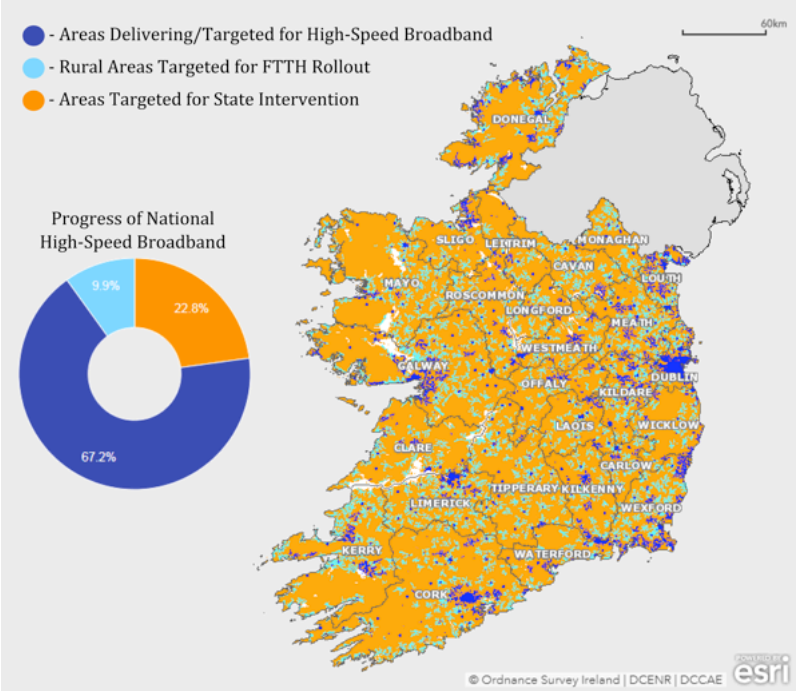


Figure 3.11: Status of High-Speed Broadband in the Republic of Ireland, 2017 (Reproduced From [133])

With particular respect to FTTP deployment, the latest data for coverage by country within the EU is presented in Fig. 3.12 [132]. The EU average for FTTP coverage reached 26.8% as of mid-2017, with eleven countries (incl. Ireland) reporting coverage levels below the EU average. Moreover, the EU average for rural FTTP availability is just above 10%, with coverage in Ireland at 1.2% as fixed-line and wireless technologies such as VDSL and LTE continue to be preferred due to the substantial economical and technological requirements for the deployment of a rural fibre infrastructure.



Figure 3.12: Comparison of (a) National and (b) Rural Fibre-to-the-Premises Coverage Within the EU as of Mid-2017 (Reproduced from [132])

The implementation of future access networks should now be focussed on the efficient utilisation of fibre infrastructures and network resources rather than just the simple increase of the available bandwidth per customer. To this end, new architectures must now be identified, which are advantageous for establishing economically viable and energy-efficient optical access solutions. In particular, to ensure the future economic viability of rural communities, the development of an alternative fibre architecture with improved infrastructure utilisation is essential to facilitate the delivery of high-speed broadband (≥30Mb/s) and mobile telephony to sparsely

populated areas in accordance with the DAE [134]. To this end, the fundamental concept adopted by the EU FP7 project DISCUS was to exploit the two fundamental advantages of optical technology: (i) the potential to offer a large bandwidth and (ii) the ability to supply this over long distances to all parts of the network. In particular, when this strategy is applied to the access network, the outome specifies an architecture that is long enough to directly reach the core nodes.

3.3.2 EU FP7 Integrated Project DISCUS

In 2012, the large-scale integrated project DISCUS (DIStributed Core for ubiquitous bandwidth supply to all Users and Services) was funded by the 7^{th} EU framework program for Research and Innovation (2007 - 2013) in the field of information and communication technologies for future networks (ICT-2011.1.1). Projects funded from this category of the framework targeted the development of future broadband (fixed and mobile) networks with an energy efficient, secure and robust infrastructure that will use the available spectrum flexibly and efficiently in order to meet the objectives set by the digital agenda for Europe in 2010 [134].

The main goal of the DISCUS project was to define and develop a new radical architectural concept through a 'clean-slate' approach to enable an integrated optical access network which addresses the primary challenges (i.e. financial viability, power consumption, capacity scaling etc.) arising from an FTTP enabled future. These objectives demanded an innovative end-to-end design in order to establish an 'open access' environment capable of concurrently supporting multiple operators offering converged services (i.e. residential, business and mobile) in order to account for diverse customer requirements and geographic locations [8, 135]. In particular, the physical layer strategy focussed on substantially reducing the number of required electronic systems such as signal regenerators through the realisation of an optically amplified fibre infrastructure while at the same time minimising the cost per customer through optimal sharing of the network resources (i.e. infrastructure and bandwidth). As a result, the baseline DISCUS architecture presented in Fig. 3.13 involves the amalgamation of a dynamically reconfigurable time- and wavelength-division multiplexed LR-PON with a flat optical core which is arranged into islands of transparency. The primary constraint placed on this architecture is that it needs to evolve from today's network solutions and be capable of adopting

new technologies as they become available. While the starting point is a generic reference architecture, the design strategy must be capable of evolving according to the insights gained throughout the duration of the project; these include technological developments and results from cost and business models, power consumption models, service and traffic models, and regulatory and policy studies.

Two distinct LR-PON configurations, namely the 'tree-structured' (urban) and 'open-ring' (rural) systems which will be described further in later chapters, were conceived as potential candidates for the network demonstration. However, in the remainder of this chapter, the preliminary access configuration is motivated alongside the technology required to overcome the foreseen physical layer challenges. It is important to note that the design and demonstration of the DISCUS architecture was carried out in collaboration with several project partners: *Trinity College Dublin (Ireland), Nokia Bell Labs (Stuttgart, Germany), Huber+Suhner Polatis Ltd. (UK), Aston University (UK), III-V Labs (France), Telefonica (Spain), Telecom Italia (Italy) and KTH (Sweden).*

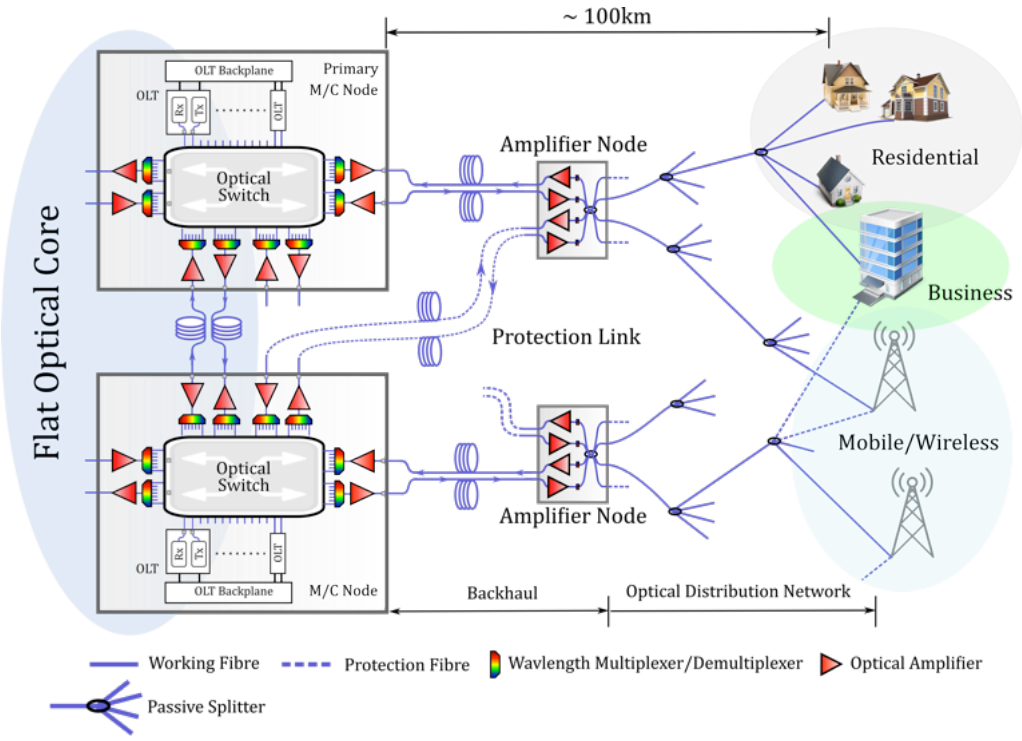


Figure 3.13: DISCUS: High-level physical layer concept based on a flat optical core and a dynamically reconfigurable LR-PON.

3.3.3 Long-Reach Optical Access

Considering Fig. 3.13, the enhanced physical reach afforded by th LR-PON architecture enables the majority of LE sites to be bypassed with fibre terminations (i.e. OLTs) concatenated into a small number of metro/core (M/C) nodes, each covering large areas. This approach can produce significant cost savings on infrastructure and equipment but it also has the potential to significantly reduce the power consumption, hence, the economic requirements compliment the sustainability drivers. Moreover, as a reduction of cost from the backhaul and core networks can also help to balance the cost required for the ODN deployment, traffic can be kept the optical domain using in-line optical amplification in order to bypass the intermediate electronic switching and processing units traditionally located at the LE sites. When this strategy is coupled with the inclusion of a reconfigurable optical switch within the M/C nodes, the resulting system offers the potential to enable a congestion-free, wavelength transparent network interface where the aggregated data from the far-reaching access network (≥ 100km) can be processed by the OLTs and redirected back towards the access section or it can be handed over to the core.

Recent studies have shown that the proposed DISCUS architecture has the potential to reduce the number of nodes carrying out electronic switching and processing by almost two orders of magnitude [136]. For instance, a test scenario undertaken for the U.K. core network demonstrated that the number of exchange sites could be reduced from ~5,600 to approximately 75 [137]. A similar study for the Irish network demonstrated that 1100 exchange sites could be reduced to around 18, this result is illustrated in Fig. 3.14 [138].

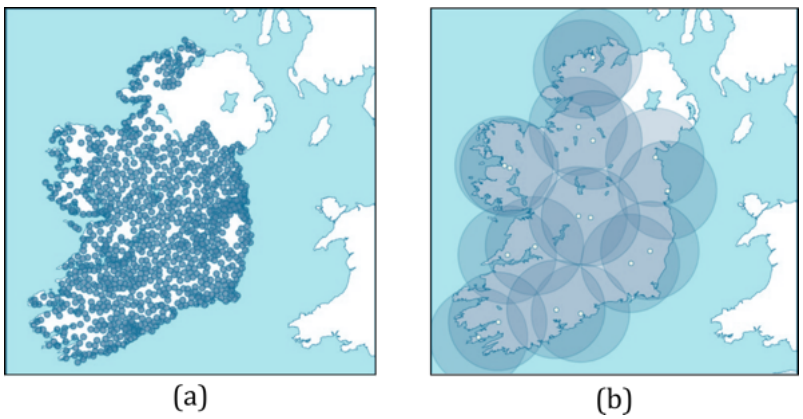


Figure 3.14: (a) Ireland with all 1100 exchange sites, (b) Ireland with 18 M/C nodes.

3.3.4 Technology Evolution and Physical Layer Challenges

In order to support the proposed network architecture, innovative technologies will be required. In this thesis, the technology evolution focuses on the following areas: low-cost tuneable transmitters, high dynamic range burst-mode optical amplifier nodes, 10G-capable burst-mode subsystems and the convergence of heterogeneous wavelength services over the PON infrastructure.

Low-Cost Wavelength-Agile Transmitters:

A critical component technology required to realise wavelength-agile ONUs are tuneable lasers. However, the strict tolerance placed on the accuracy and precision of the transmission wavelength coupled with the need for a wide tuning range (>10nm) and a relatively high output power (> +3dBm) ultimately demands a greater design and fabrication complexity. As a result, the primary challenge facing the mass-deployment of tuneable lasers in the access network is that of cost. With this in mind, DISCUS has selected a tuneable laser design based on a multi-section Fabry-Pérot cavity with integrated slots [139]. Notably, this slotted Fabry-Pérot (SFP) laser only requires a single epitaxial growth stage and uses feature sizes that can be reached with standard deep-UV optical lithography. This relatively simple fabrication process offers major advantages over alternative structures by greatly reducing the fabrication complexity while also increasing the potential yield. Moreover, as these lasers do not explicitly need cleaved facets to form the laser cavity they can be employed to integrate monolithically with other electro-optical devices. For instance, in this project, a tuneable three-sectioned SFP laser has been integrated with an electro-absorption modulator (EAM) and an SOA, thus creating a single device capable of providing a tuneable light source with the potential for high-speed, low-chirp modulation alongside a boosting/gating function to facilitate the generation of optical bursts. A detailed investigation of this device which was developed and fabricated by researchers in the III-V Materials and Devices Group of the Tyndall National Institute is presented in Chapter 4.

High Dynamic-Range Optical Amplifier Nodes:

The amplifier nodes (ANs) represent a critical feature of the DISCUS architecture as they extend the optical power budget of the physical layer to realise a longer physical reach (≈100km) and higher split (≤512). This approach effectively integrates the metro and access portions of the network enabling the fibre infrastructure to bypass the majority of LE sites required for todays networks thus reducing both power consumption and equipment costs significantly [13]. As in conventional metro DWDM network design, the preferred option to further minimise cost is to use a single multichannel amplifier within the AN for each transmission direction; however, it must be noted that the choice of amplifier technology will ultimately dictate the wavelength plan. For example, to support operation in the C-band (1530 - 1565nm), Erbium-doped fibre amplifiers (EDFAs) offer a key solution due to their overall performance quality in terms of low noise figure (NF), high gain, high achievable output power and the ability to provide these characteristics in a system with a large number of channels. From a practical perspective, using a C-band wavelength plan for the DISCUS architecture has a significant advantage with the wide availability of mature components and technologies such as optical amplifiers and wavelength multiplexers. With respect to the wavelength allocation between the transmission bands, interleaving of the US and DS channels can be considered; however, in this work the short wavelength side of the C-band (1528.77 - 1544.53nm) has been allocated to the DS channels and the long wavelength side (1548.51 - 1564.27nm) has been allocated to the US channels.

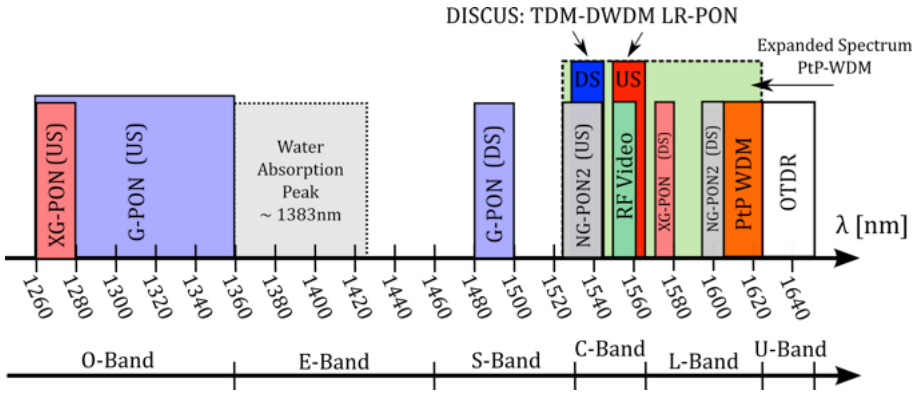


Figure 3.15: Wavelength plan of legacy PON systems alongside the proposed transmission bands for the DISCUS TDM-DWDM LR-PON [140].

Notably, due to their relatively slow gain dynamics, EDFAs are typically designed to operate with continuous traffic in conventional metro and core networks. Moreover, as illustrated in Fig. 3.16, the fast input power variation ($< \mu s$) produced by high dynamic range burst-mode traffic ($\geq 15dB$) can generate significant burst envelope distortions due to saturation-induced gain transients that can be attributed to the lengthy excited state lifetime of the Er^{+3} dopant ions ($\sim 10ms$) [141].

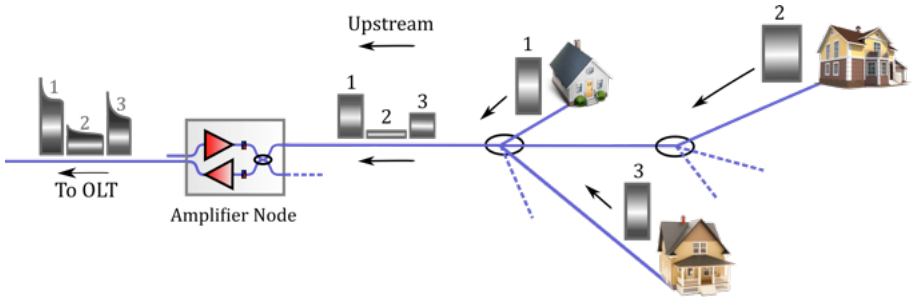


Figure 3.16: Illustration of saturation-induced optical gain transients from an EDFA-based amplifier node.

Unless suitable mitigation strategies are employed, these signal distortions ($\sim \mu s$) can result in significant performance degradation and/or sync loss, or even damage to the OLT-based burst-mode receiver (BMRx) which typically sets its gain and extracts a decision threshold from a short (tens of nanoseconds) preamble. In recent years, the development of reconfigurable optical add and drop multiplexers (ROADMs) to support dynamic WDM systems has driven the evolution of EDFA transient control circuitry that may also provide a solution for supporting burst mode traffic in the long-reach, high-split architectures proposed within DISCUS. For instance, a number of gain stabilisation techniques have been reported for burst-mode operation of EDFAs by using electro-optic feedback [142, 143]. The suitability of commercial gain-stabilised EDFAs for deployment within the optical amplifier nodes of dynamically reconfigurable TDM-DWDM LR-PON architectures is evaluated within Chapter 5.

10G Burst-Mode Subsystems:

A critical aspect of the upstream link is the implementation of an efficient time-division multiple access (TDMA) protocol in order to share the available bandwidth

between the users assigned to a specific wavelength. Here, each user generates bursts of data during the allocated timeslots which are scheduled by the PON protocol [81].

Within a LR-PON, the varying propagation distances between each ONU and the assigned OLT suggest that if the same average optical power was launched from each ONU at the access edge, the bursts arriving at the OLT will exhibit different levels of transmission impairments including loss, OSNR, chromatic dispersion and bit-phase. Consequently, to support the envisaged architecture, the OLT-based BMRx must offer a high optical sensitivity alongside the ability to adjust the electronic gain and dc-offsets within a guard interval of a few tens of nanoseconds before synchronising the phase of the signal within a short preamble at the start of each burst. It is important to note that throughout this thesis, a 'loud' packet (LP) represents the burst arriving at the OLT with the highest power while the incident burst with the lowest power is referred to as a 'soft' packet (SP).

At present, the majority of existing OLTs employ BMRx technology consisting of a limiting amplifier. This approach uses an limiting amplifier to make a hard decision whether the input signal represents a 0 or 1 through comparison against a threshold and the resulting output signal takes on two corresponding levels. Alternatively, a linear burst-mode receiver (LBMRx) linearly amplifies its input such that the average or peak amplitude equals a reference. This results in equalisation of the burst amplitudes with preservation the signal shape which is critical for the implementation of signal processing functions such as electronic dispersion compensation (EDC) [144] and forward error correction (FEC) [145] as illustrated in Fig. 3.17.

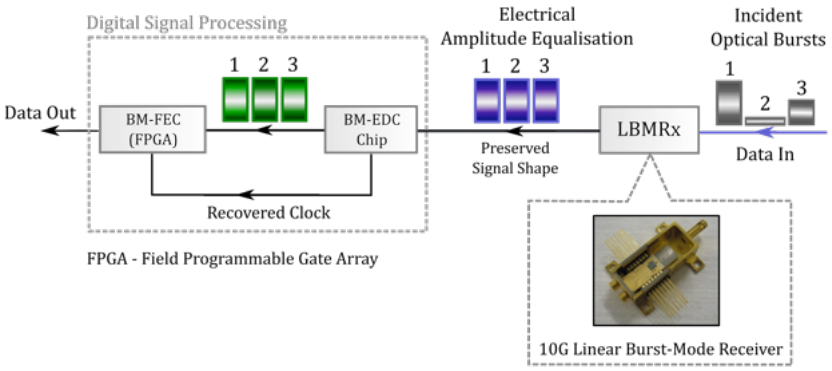


Figure 3.17: Linear burst-mode receiver concept with electronic dispersion compensation (EDC) and forward error correction (FEC).

For this project, an innovative 10G-capable AC-coupled LBMRx prototype developed by researchers in Tyndall's Photonic Systems Group (PSG) [146] was integrated with a field-programmable gate array (FPGA) incorporating a custom PON protocol and the Reed-Solomon (RS) FEC decoding functions. In Chapter 5, the resiliency of an RS(248, 216) error correction algorithm realised within the OLT-Rx is evaluated through a collaborative research effort which uses emulated optical transients imparted on bursts transmitted from two time-division multiplexed ONUs to introduce strongly correlated and localised errors [147]. Moreover, the transmission performance of the 10G burst-mode link for two distinct TDM-DWDM LR-PON variants designed and assembled for the DISCUS physical layer testbed are presented in Chapter 6 [19].

Point-to-Point Overlay of 100Gb/s DP-QPSK:

The development of future access networks will be driven by the need to dynamically provide access to core capacities (i.e. 100Gb/s or higher) to any point within the network [148]. In turn, this requires that the LR-PON must have the capability to offer such capacities without disrupting the on-going (TDM) traffic to and from the conventional (i.e. residential) customers attached to that network. While various encoding systems have been studied for 100Gb/s optical transmission signals [149], dual-polarisation phase shift keying (DP-QPSK) was chosen for deployment within the DISCUS architecture as it is the most commonly adopted solution for 100G in long haul and metro optical channels [150]. In particular, DP-QPSK is an advanced phase-modulation format that transmits 2-bit signals represented by four phases on two orthogonally polarised light beams at the same carrier frequency. In other words, it enables allows four bits of data to be encoded and sent as one optical symbol. Notably, the DP-QPSK signaling scheme reduces the effective symbol rate to one quarter of the system bit rate. While a DP-QPSK transmitter and coherent receiver are relatively complex and costly to implement, the lowered symbol rate permits the use of electrical and optical components with lower operating bandwidths (i.e. 25GHz as opposed to 100GHz) and improves the system immunity to factors that significantly limit transmission including chromatic dispersion.

In this work, a commercial DP-QPSK transponder was used to generate and receive 100G point-to-point traffic sent over the LR-PON physical layer. As service

demonstration over this channel is beyond the scope of this project, the task is limited to studying the performance of the channel at the physical layer. Notably, in this converged service scenario, the performance of phase modulated signals can be heavily influenced by non-linear crosstalk from co-propagating on-off keying (OOK) channels [151]. The results of this analysis are presented as part of the network demonstrator characterisation in Chapter 6.

3.4 Summary

This chapter reviews the evolution of optical access networks from the widely deployed single channel E-PON and G-PON systems to the next-generation 10G-capable configurations which include 10G-EPON, XG-PON and the recently standardised NG-PON2. From this study, it is evident that despite the incremental steps taken by these standards to address the ever-growing demand for bandwidth, network operators will be forced to look beyond this current range of access architectures in order to find a cost-effective, 'future-proof' solution capable of delivering ubiquitous bandwidth over larger areas to a higher number of customers. In fact, these requirements have already prompted the design of an alternative configuration known as a 'long-reach' (LR) PON which supports a physical reach $\geq$ 100km and a split $\geq$ 512 while also reducing capital and operational expenditure through node consolidation.

While large-scale research projects such as PIEMAN [18] have successfully demonstrated the physical layer feasibility of LR-PONs whose information capacity has been increased significantly through hybrid time- and wavelength-division multiplexing (32 x λ x 10Gb/s); the proposed physical layer is only suited to urban deployment where customers are densely distributed to achieve maximum utilisation while the static use of the wavelength domain restricts bandwidth efficiency by introducing stranded capacity. With this in mind, the EU FP7 integrated project DISCUS was funded to address the current physical layer limitations and technology gaps by embracing innovative architectures and emerging industry trends. In particular, the main objective of DISCUS was to exploit the two fundamental advantages of optical technology: (i) the potential to offer a large bandwidth and (ii) the ability to supply this over long distances to all parts of the network. It is important to

note that when this strategy is applied to the access network, the outcome specifies an architecture that is long enough to directly reach the core nodes. However, in order to realise the proposed configuration, several technological challenges must be addressed, these include the development of low-cost tuneable transmitters for deployment in mass-market residential ONUs and the realisation of burst-mode capable optical amplifier nodes to support multichannel, heterogeneous traffic. These technologies will be investigated further in the following chapters with the results of the DISCUS physical layer experimental testbed presented in Chapter 6.

4

Low-Cost Tuneable Transmitters for Wavelength Agile PONs

This chapter presents an investigation into the development of two innovative tuneable laser technologies targeted for mass deployment in the customer premises equipment of wavelength-agile PONs.

In section 4.1, the chapter begins with a brief history of the laser and an overview of the basic structure of semiconductor diode lasers before moving on to discuss the main wavelength tuning mechanisms in section 4.2. Subsequently, section 4.3 motivates the concept of reconfigurable optical access networks which require wavelength-agile transmitters to dynamically exploit the substantial information capacity offered by optical fibre through wavelength division multiplexing. This is followed by an outline of the performance requirements and development challenges facing the realisation of low-cost tuneable lasers for mass-market access deployment in section 4.4. Consequently, driven by the potential for appreciable cost-savings, the main technologies of interest examined in this chapter include a novel vertical cavity surface emitting laser (VCSEL) which achieves tuneability through thermal actuation of a curved top mirror and a monolithically integrated transmitter based on a discretely tuneable slotted Fabry-Pérot ridge waveguide laser. In particular, the tuneable VCSELs presented in section 4.5 employ a short cavity structure in conjunction with a flexible surface micro-machined Bragg reflector in order to increase the free-spectral range and achieve wide-band continuous tuning (i.e. $\geq$ 40nm) through electronic manipulation of the cavity length. Alternatively, the edge-emitting 10G-capable integrated transmitter introduced in section 4.6 uses an 'off-the-shelf' multi-quantum well (MQW) wafer structure with a single epitaxial growth process alongside standard photolithography techniques to achieve appreciable cost savings when compared with commercial grating-based solutions.

4.1 Light Amplification by Stimulated Emission of Radiation

The term 'laser' is an acronym of the words Light Amplification by Stimulated Emission of Radiation. In fact, having been postulated by Albert Einstein in his 1917 paper entitled '*On the quantum theory of radiation*' [152], stimulated emission describes the process by which an incoming photon of a specific frequency interacts with an excited atomic electron (or other excited molecular state), causing it to drop to a lower energy level with the creation of an additional photon that matches the input photon in wavelength, phase, and polarisation in accordance with the well-known relation,

$$\Delta E = E_2 - E_1 = hf \tag{4.1.1}$$

where, ΔE is the difference in energy between the upper, E_2 and lower E_1 , f is the frequency of the emitted photon and h is Planck's constant which has a value of approximately 6.626×10^{-34} [Js].

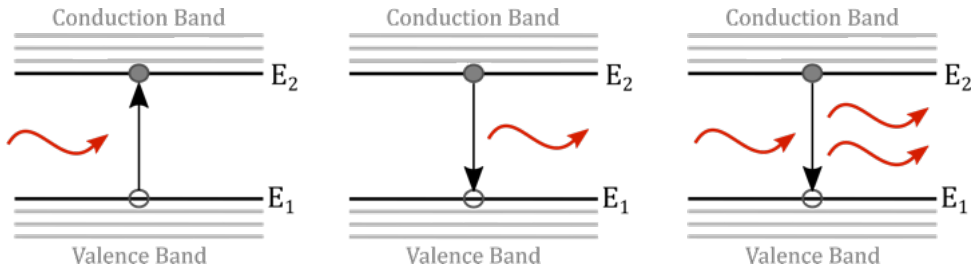


Figure 4.1: Electronic transitions between the conduction and valence bands: (a) excitation via absorption, (b) spontaneous emission, (c) stimulated emission.

Four decades after Einstein's work, the first laser was constructed by Theodore H. Maiman at Hughes Research Laboratories in Malibu, California, using a cylinder of synthetic ruby whose ends were silver-coated to make them reflective and able to serve as a Fabry-Pérot resonator while photographic flashlamps were used as the laser's pump source [153]. From here, research and development on lasers grew exponentially and by 1962, the first stimulated emission from a Gallium-Arsenide

(GaAs) diode at 840nm was reported by R. N. Hall et al. [2] as well as by some other groups. By 1970, at the dawn of fibre-optic communications, Zhores Alferov had developed and fabricated more sophisticated laser structures with optical and electrical confinement layers. Moreover, he achieved continuous-wave lasing at room temperature from an Aluminium-Gallium-Arsenide (AlGaAs) diode laser [154]. Following this work, optical fibre communications became the primary driving force behind diode laser development, particularly in the second half of the 70s and at the beginning of the 80s, where attention began to focus on emission in the region of 1310nm and 1550nm using Indium Phosphide (InP) based structures to address the zero-dispersion and low-loss spectral regions of single-mode fibre respectively.

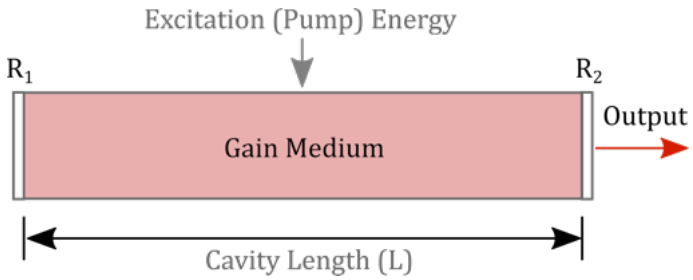


Figure 4.2: Basic laser configuration based on a Fabry-Pérot cavity.

The Lasing Mechanism

On a fundamental level, all lasers are comprised of a resonant cavity of length, L, which is bounded by facets with reflectivities of R_1 and R_2 respectively. These cavities are inherently passive with a loss of α per unit length. However, the cavities also contain an active region which is capable of providing optical gain, g, through stimulated emission induced by confined photons that have been generated spontaneously following the external excitation of the material. Within such a cavity, the change in optical power after one complete round trip, ΔP_{rt}, can be written as

$$\Delta P_{rt} = R_1 R_2 e^{(\Gamma g - \alpha)2L} \tag{4.1.2}$$

where Γ signifies the confinement factor of the guided optical mode. In practice, due to optical leakage at both end facets alongside scattering and absorption within the cavity, the power of the confined light will eventually decrease as photons leave the

cavity through emission or absorption. However, if enough optical gain is available to compensate for the round-trip losses (i.e. $\Delta P_{rt} \geq 1$) the laser is said to be above threshold, g_{thr}, and the intensity of the light oscillation in the cavity can begin to build up with the emission of highly coherent light.

$$g_{thr} = \Gamma g = \frac{1}{2L} log_e(\frac{1}{R_1 R_2}) + \alpha \tag{4.1.3}$$

4.2 Tuneable Semiconductor Lasers

Following the development of InP single-mode laser diodes capable of emission around 1310nm and 1550nm in the late 1970's and early 1980s [155, 156], the development of wavelength-tuneable laser diodes was primarily driven by the increasing demand on information capacity within optical communications systems where the application of advanced transmission techniques such as WDM are essential [157, 158].

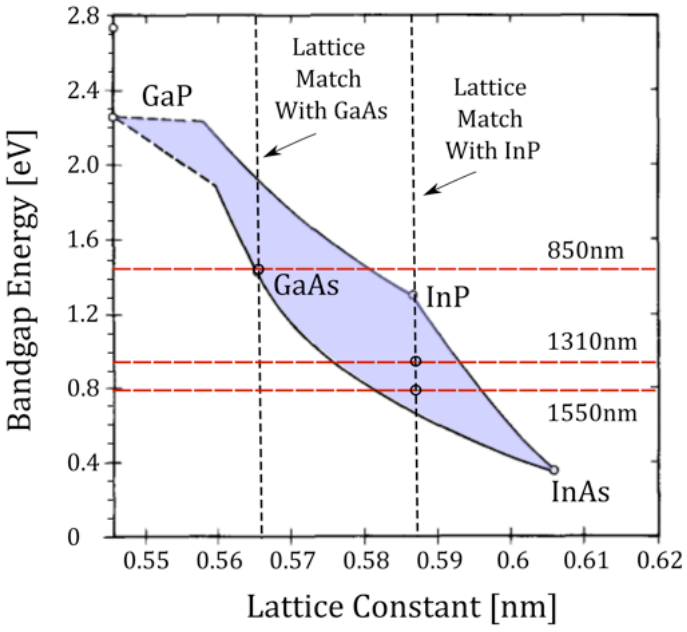


Figure 4.3: InGaAsP bandgap energy as a function of the lattice constant with various binary III-V compound semiconductors (Reproduced from [159])

A schematic of a generic tuneable laser is presented in Fig. 4.4 in order to demonstrate the main elements which must be aligned and translated in order to produce a wavelength-tuneable, single (longitudinal) mode laser. In practice, these elements can be combined in different ways to create unique physical structures, each possessing their own advantages and disadvantages [160]. At present, the main tuneable semiconductor laser assemblies include distributed feedback (DFB) laser arrays [161], distributed Bragg reflector (DBR) [162], external-cavity lasers (ECLs) [163] and vertical-cavity surface-emitting lasers (VCSELs) tuned via micro electro-mechanical systems (MEMS) [164].

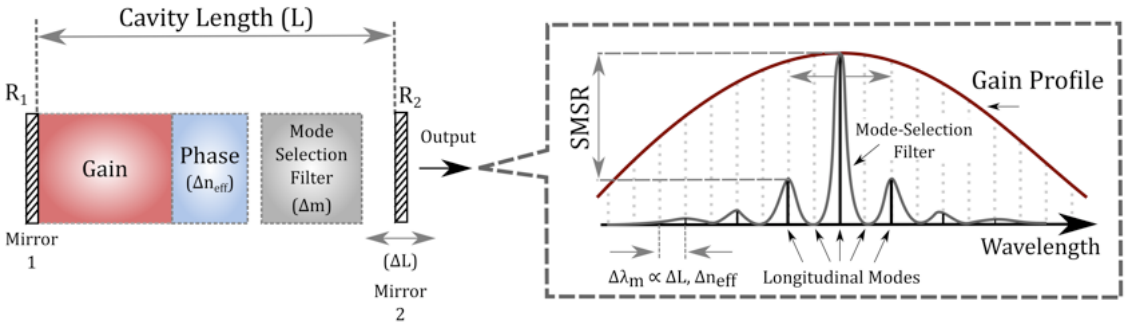


Figure 4.4: Schematic of a generic tuneable laser illustrating the main tuning mechanisms alongside a single-mode lasing spectrum defined by the achievable side-mode suppression ratio (Reproduced from [160]).

Tuning Mechanisms

In general, laser tuneability can be achieved electronically, thermally or mechanically where the mode number (m) and wavelength (λ) depend on the effective index (n_{eff}) and the effective cavity length (L) as shown in Eqn. 4.2.1.

$$\frac{m\lambda}{2} = n_{eff}L \tag{4.2.1}$$

with the fractional variation of one or all of these parameters contributing to the adjustment of the lasing wavelength:

$$\Rightarrow \quad \frac{\Delta\lambda}{\lambda} = \frac{\Delta n_{eff}}{n_{eff}} + \frac{\Delta L}{L} - \frac{\Delta m}{m} \tag{4.2.2}$$

With respect to the first two terms on the right hand side of Eqn. 4.2.2, electronic, thermal or mechanical tuning may apply; however, depending on the device in question, appreciable variations in either of these processes may disturb the lasing resonance conditions by influencing the mode selection mechanism causing abrupt mode jumps (or mode-hops). It is also important to note that these wavelength-tuning mechanisms generally affect the optical cavity gain, so that the optical power varies during tuning. Equally, the optical power control by the laser current affects the device temperature and thus the emission wavelength. Moreover, for telecommunication applications such lasers are often packaged with a thermoelectric cooler (TEC), a monitoring photodiode (MPD) and a wavelength locker (WL) in order to facilitate temperature, power and wavelength control respectively. Furthermore, as the tuneability of many devices may require the precise and simultaneous adjustment of multiple tuning currents [165], the handling convenience with respect to device packaging is drastically influenced.

4.3 Wavelength Agile PONs

With the introduction of wavelength division multiplexing (WDM) to the access network through the ITU-T NG-PON2 standard [11] attention has turned to the development of "colourless" components to reduce the manufacture and stockpiling of wavelength specific linecards. In particular, this approach has highlighted two feasible options for ONU transmitters: reflective devices or tuneable lasers. As shown in Fig. 4.5, the former case involves reflective semiconductor amplifiers (R-SOAs) [166] or hybrid R-EAM-SOAs [167] which can be seeded through carrier distribution using spectrally sliced ASE or centrally located laser banks. However, as the same fibre path is typically used for the unmodulated carrier and the upstream signal, hence, interference with Rayleigh backscattered or Fresnel reflected signals at the same transmission wavelength can give rise to the interferometric conversion of laser phase noise to intensity noise thus degrading the signal quality at the receiver

[168, 169, 170]. Furthermore, as these reflective devices will typically have a residual polarisation dependance, the inherent birefringence in optical fibre may compromise the carrier conditions at the input. Moreover, the differential loss incurred from the passive splitters in the optical distribution network (ODN) can result in differing levels of gain saturation within the SOA sections as well as an increased power ratio (or dynamic range) between optical bursts in the upstream direction [171].

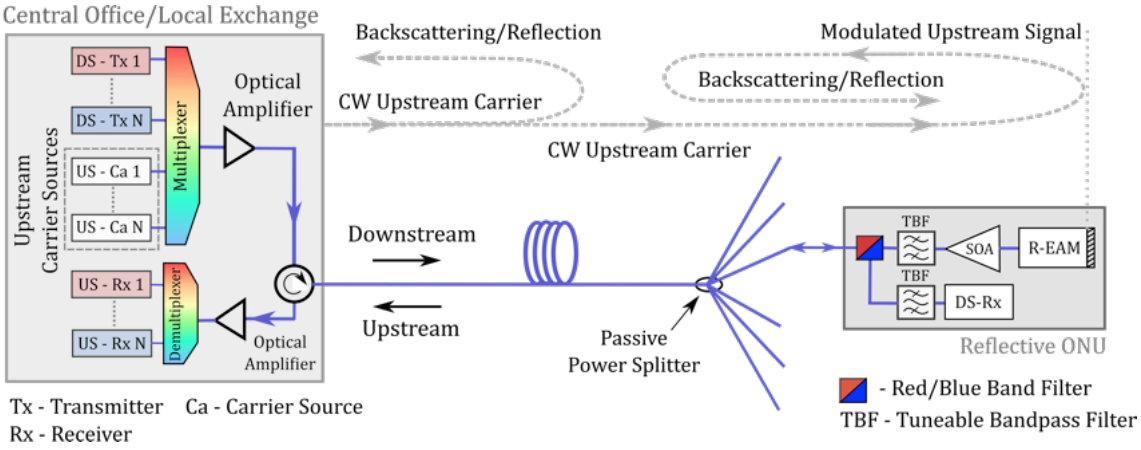


Figure 4.5: Illustration of the backscattering and reflection mechanisms in a carrier distributed PON.

While reflective transmitter solutions might be applicable in standard reach WDM-PONs, it is widely recognised that the wavelength layer of future access networks should be based on tuneable lasers. In particular, the envisaged physical reach (≥100km) and split ratios (≥ 512) of LR-PONs will require lasers with a relatively high output power and low linewidth to address the increased loss and dispersion attributed to such systems. Furthermore, these lasers will require a high-level of tuning precision and wavelength stabilisation in order to maintain the integrity of the set transmission channel thus avoiding inter-channel crosstalk.

To demonstrate the typical requirements for these tuneble lasers, the main optical interface parameters for tuneable ONU transmitters deployed within a reconfigurable point-to-point (PtP) wavelength-division multiplexed (WDM) PON in accordance with the recent ITU-T G989.2 (NG-PON2) recommendations are presented in Table

4.1. Notably, the channel tuning time has been divided into three classes: (1) < 10μs, (2) 10μs – 25ms, (3) 25ms – 1s; this approach is taken in order to define different use cases with respect to the employed wavelength control scheme. In particular, two wavelength control mechanisms are allowed; these include centralised control through OLT-ONU interactions and self-control in which the ONU is completely responsible for the control of the transmission wavelength. It is also important to note that the specifications outlined in Table 4.1 must be met through the tuning process to avoid any rogue behavior which may cause the wavelength to drift outside the allocated spectral window and interfering with neighboring channels.

Item	**Unit**	**Value**
Operating Wavelength Band	[nm]	1524 - 1544 (Wideband) 1528 - 1540 (Reduced Band) 1532 - 1540 (Narrow Band)
Minimum Channel Spacing ($\Delta\lambda$)	[GHz]	50
Maximum Channel Spacing ($\Delta\lambda$)	[GHz]	200
Maximum Spectral Excursion	[GHz]	$\pm$12.5 ($\Delta\lambda$ = 50GHz) $\pm$25 ($\Delta\lambda$ = 200GHz)
Wavelength Channel Tuning Time	-	Class 1: < 10μs Class 2: 10μs - 25ms Class 3: 25ms - 1s
Maximum Tuning Granularity	[GHz]	ChannelSpacing/20 $\approx$ 2.5
Mean Channel Launch Power (Max)	[dBm]	+9.0 (Unamplified OLT-Rx)
Mean Channel Launch Power (Min)	[dBm]	+4.0 (Unamplified OLT-Rx)
Minimum Extinction Ratio	[dB]	6
Minimum Side-mode Suppression Ratio	[dB]	30

Table 4.1: The Main Optical Interface Parameters for an ONU Transmitter in a TWDM-PON PON for a Linerate of 9.95328 Gbit/s in the Upstream Direction in Accordance with the ITU-T G989.2 (NG-PON2) Recommendations [172].

4.4 Challenges Facing Low-Cost Tuneable Lasers for Optical Access

From the specifications provided in Table 4.1, the strict tolerance placed on the accuracy and precision of the transmission wavelength coupled with the need for a wide tuning range (>20nm) and a relatively high output power (> $+3dBm$) ultimately demands a greater design and fabrication complexity. Therefore, at present, the primary challenge facing the mass-deployment of tuneable lasers in the access network is that of cost. In practice, monolithic integration has successfully addressed the challenging design processes necessary for tuneable transmitter assemblies by achieving the desired multicomponent functionality on a single chip resulting in a reduced form factor, power consumption and packaging complexity. Nonetheless, the main disadvantage of these devices (which are typically variants of the DBR laser) is their intricate fabrication processes which require multiple epitaxial growths with narrow tolerance steps in order to create the grating structures which have lead to high production costs. Currently, the price of 10G-capable tuneable transceivers for optical communications is somewhere in the three-digit US dollar range which is far too high, especially for mass-market residential deployment where the current price bench-mark has been set by G-PON with ONUs typically ≤ $100 [173] employing well-established distributed feedback (DFB) lasers with a cost in the region of $10-20. Consequently, to achieve economic feasibility, the price of tuneable lasers would have to drop below 10% of their current price [21].

In order make tuneable lasers more affordable for deployment in optical access networks, the most logical step is to remove sub-components from the laser package where possible. For instance, as illustrated in Fig. 4.6, one option would be to remove the thermistor and the thermo-electric cooler (TEC). Not only would this action significantly reduce the packaging costs, but it would also mitigate the power consumption considerably as in a typical design it may consume up to ~1W. Notably, uncooled operation of five-section SG-DBR and DS-DBR lasers has been successfully demonstrated in [174] and [175] respectively. However, in addition to their relatively complex fabrication processes which include multiple epitaxial growths with strict tolerance steps, these devices require advanced material substrates that are capable of stable operation over a wide temperature range (≤ 90°) [176].

An additional cost-saving option involves the removal of the wavelength locker

from each laser package, however, in its absence, appreciable thermal variations may lead to rogue wavelength behaviour in which the set value drifts outside the allocated channel window and interferes with adjacent channels through interferometric crosstalk. Consequently, the use of an open-loop control scheme would require extensive calibration efforts on a device-by-device basis in order to realise the full tuning map which must consider all currents and temperatures. However, as effects associated with laser-aging may compromise the validity of the associated calibration table [177], this approach is currently viewed as cost-prohibitive. On the other hand, a closed-loop wavelength control could be realised on a systems level using a centrally located wavelength referencing tool alongside an appropriate protocol adaptation in order to provide dynamic feedback to each active ONU through the downstream channels. It should be noted that this technique has been successfully demonstrated in [178] where a tuning accuracy of $\leq \pm 5$GHz has been achieved.

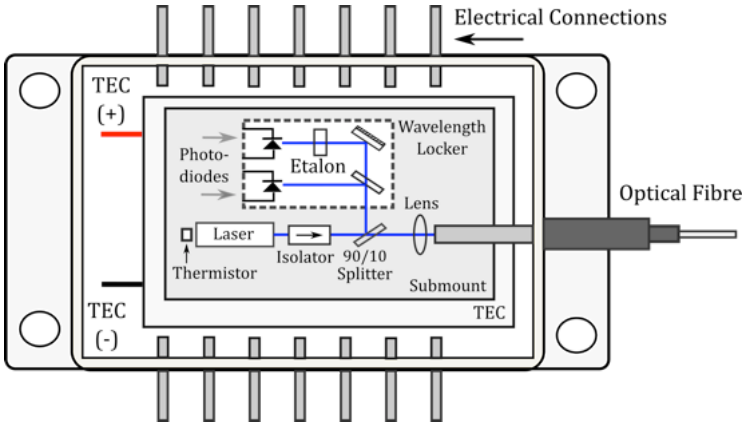


Figure 4.6: Illustration of a typical tuneable laser 'butterfly' package highlighting the various sub-components required.

To further mitigate fabrication costs, certain optical parameters (i.e. linewidth) could be relaxed depending on the application (i.e. direct or coherent detection) while attempts could also be made to reduce the costly calibration efforts through utilisation of device specific current injection equations as demonstrated in [162]. These generic equations can be extracted from a fully detailed device characterisation before being applied to different laser chips of the same device structure. While it is clear that the use of these equations cannot offer the high-end perfor-

mance offered by calibrated lasers due to the small differences from chip-to-chip which can be attributed to imperfect manufacturing techniques, the resulting operation may still be suitable for PON applications if used alongside an appropriate closed-loop wavelength control scheme. Nonetheless, to address the cost challenges currently facing the realisation of tuneable transmitters for mass-deployment in optical access networks, research has begun to focus on more innovative solutions which utilise alternative structures and low-cost fabrication techniques. With this in mind, the following sections present an investigation into the feasibility of two such devices including a vertical-cavity surface emitting laser (VCSEL) which incorporates a flexible surface micro-machined Bragg reflector and a novel monolithically integrated transmitter that is comprised of a discretely tuneable slotted Fabry-Pérot ridge waveguide laser, an absorptive modulator and an SOA whose main advantage lies in its low-cost,re-growth free fabrication process.

4.5 Widely Tuneable MEMS-VCSELs

Lead by Technische Universität Darmstadt in Germany, the specific targeted research project (STREP) 'SUBTUNE' (widely tuneable VCSELs using sub-wavelength gratings) was sponsored in 2008 by the European Commission under the 7th EU Framework Programme (FP7) [179]. The primary goal of this project was to target the development of innovative vertical cavity surface emitting lasers (VCSELs) which incorporate a micro-machined movable Bragg-mirror to achieve wide tuneability alongside a high output power and a high suppression of lateral and longitudinal sidemodes for application in communication and sensing systems. In particular, the main contribution of this work involved characterising these devices and assessing their suitability for use in fibre-optic communication systems. The results of this investigation are presented in the following sections.

VCSEL Concept and Design

By considering the lasing resonance condition and the free-spectral range, $\Delta\lambda_{FSR}$, of a typical laser cavity as shown in Eqn. 4.5.1 and 4.5.2 respectively; it is evident that the continuous tuning capabilities become much larger as the cavity length (L) is minimised such that the mode integer, m, is as small as possible.

$$\frac{m\lambda}{2} = n_{eff}L \tag{4.5.1}$$

$$\Delta\lambda_{FSR} = \lambda_m - \lambda_{m+1} = \frac{\lambda_c^2}{2n_{eff}L} \tag{4.5.2}$$

where, λ_c represents the centre wavelength of the tuning range. This 'short-cavity' concept is exploited in VCSELs where the direction of the light emission is vertical rather that parallel to the substrate as is the case for conventional 'edge emitting' diode lasers. This vertical emission structure is highly advantageous as it maintains a smaller footprint while facilitating on-wafer testing and production of two dimensional arrays which offer the potential of an increased yield alongside an improved packaging flexibility with respect to edge emitters.

While fixed-wavelength VCSELs have been successfully demonstrated at wavelengths of 1.3μm [180], 1.55μm [181] and 2μm [182], novel concepts for tuneable VCSELs incorporating micro-electro-mechanical systems (MEMS) targeted for operation within the C-band (1530 - 1565nm) have been primarily influenced by the work of Prof. Connie J. Chang-Hasnain [183]. As shown in Fig. 4.7, the MEMS-VCSEL structure studied in this work is comprised of an electrically pumped semiconductor cavity (also known as a 'half-VCSEL') which is embedded between two highly reflective (>99%) distributed Bragg reflectors (DBR) forming a plane-concave resonator geometry. It should be noted that a high reflectivity is necessary for these devices as the thin active region provides a relatively small round trip gain. The half-VCSEL is fabricated with two n-type InP heat and current spreading layers, each with a thickness of approximately 800nm, sandwiching the compressively strained active region with AlGaInAs quantum wells alongside a buried tunnel junction (BTJ) containing two highly doped lattice matched layers p+ AlGaInAs and n+ GaInAs for current confinement and a flat dielectric DBR which is embedded in a gold (Au) electroplated substrate. In practice, the Au-substrate not only acts as the bottom electrical contact but it also serves as a surface for heat extraction. The second DBR is then deposited on top of the wafer with tailored strain gradients using low temperature plasma enhanced chemical vapour deposition (PECVD) which assumes a concave shape after etching a sacrificial layer beneath the mirror. As these micromachined mirror membranes are fabricated directly on top of the half-VCSEL, these

devices offer the potential for high-efficiency mass production in contrast to other two step processes that required wafer-bonding [184] or gluing [164]. Notably, the radius of curvature of the top DBR is a critical parameter which must be carefully designed in conjunction with the diameter of the BTJ and the flat DBR at the bottom of the structure. in order to create a stable semi-confocal cavity of length L, The resulting resonant cavity, based on a 'two-chip' VCSEL concept, supports only a single longitudinal mode with a high side-mode suppression ratio (SMSR) within the VCSELs free-spectral range (FSR) [185, 186]. As the intricacies of the design and fabrication processes are beyond the scope of this thesis, the reader is referred to [179] and [187] for further details.

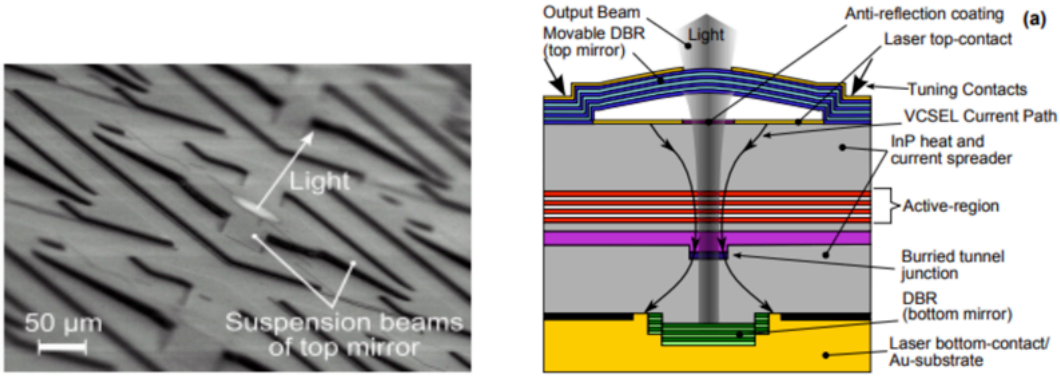


Figure 4.7: (L) Scanning electron microscope image and (R) a schematic of the MEMS tuneable VCSELs developed during the EU STREP SUBTUNE (Reproduced from [187] and [188]).

The Electro-Thermal Tuning Mechanism:

A fully fabricated MEMS-VCSEL, as schematically shown in Fig. 4.7, has an optical cavity length of

$$L = L_{DBR,b} + L_{SC} + L_{air} + L_{DBR,t} \tag{4.5.3}$$

where, $L_{DBR,b}$ and $L_{DBR,t}$ are the penetration depth into bottom and top DBR sections respectively, L_{SC} is the semiconductor section and L_{air} is the air gap. Notably, sending a current through the flexible top DBR membrane induces a thermal expansion via Joule heating (P_{Heat}) and thus an extension of the air gap, ΔL_{air}, and the total cavity length, ΔL, proportionally to the heating power which shifts the lasing wavelength to longer values, $\Delta\lambda_{ET}$, in accordance with Eqn. 4.5.1.

$$\Delta\lambda_{ET} \propto \Delta L_{air} \propto P_{Heat} = I^2_{MEMS} R_{MEMS} \tag{4.5.4}$$

where R_{MEMS} is the electrical resistance of the electrode deposited on top of the membrane ($\approx 20\Omega$). It should also be noted that the threshold current and the maximum output power of the VCSEL are influenced by the deflection of the top DBR membrane as it adjusts the gain conditions associated with the relative overlap of the antinode of the electric field with the quantum wells in the active region.

4.5.1 Device Characterisation

The tuneable VCSELs were provided (on-chip) by the Walter Schottky Institut and TU-Darmstadt in Germany. As the VCSELs were provided unpackaged, the chip was placed on a temperature controlled sub-mount that was maintained at 25°C during operation while two pairs of carefully placed electrical probes supplied the injection currents to the half-VCSEL and the flexible DBR membrane respectively. The optical output from the VCSEL was then captured using a lens-ended fibre whose position was manipulated using an XYZ translational stage and passed to an power meter or optical spectrum analyser (OSA) for analysis. The resulting fibre-coupled power-voltage-current (LVI) curves at different tuning currents (I_{MEMS}) are presented in Fig. 4.8.

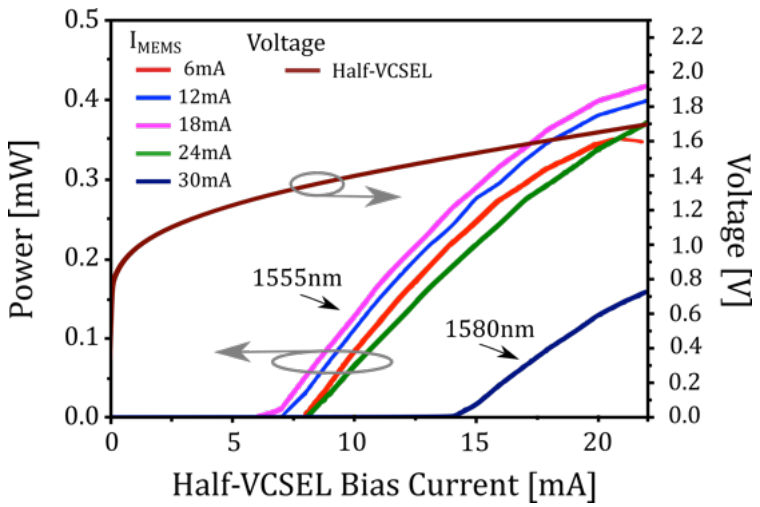


Figure 4.8: L-I-V curves measured for various MEMS tuning currents

For the chosen device, the half-VCSEL demonstrated a threshold voltage of approximately 0.8V for the entire range of MEMS bias currents; however, the threshold current was observed to vary by approximately 8mA across the VCSELs tuning range, dropping from 14mA at a tuning current of 30mA (~ 1580nm) to a minimum of 6mA for a tuning current of 18mA (~1555nm) where the corresponding mirror deflection provides a maximum fibre-coupled output power of 0.4mW (~ -4dBm) at the thermal rollover. This variation in threshold current is attributed to the detuning of the MEMS-DBR, the spectral distribution of the material gain, and the shift of the optical standing wave relative to the QW active region [189].

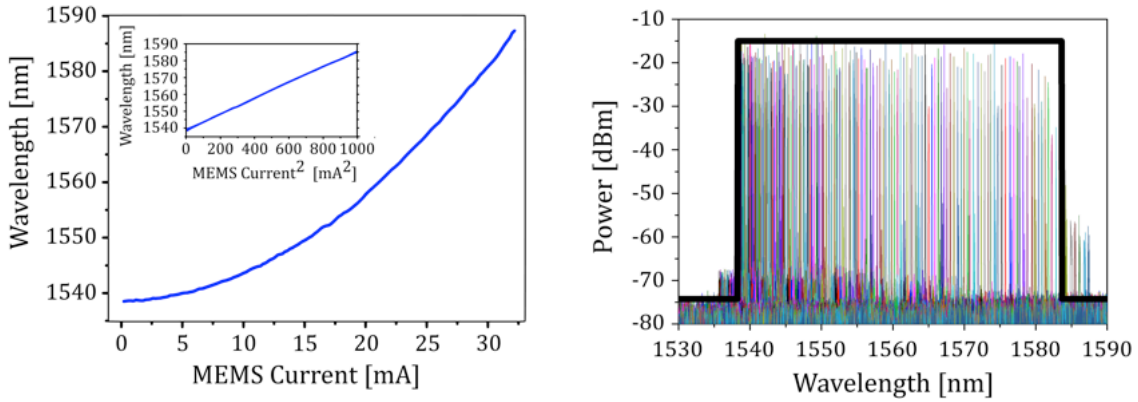


Figure 4.9: (L) Evolution of the peak wavelength as a function of MEMS tuning current showing linear behaviour as a function of the square of the tuning range. (R) Optical spectra captured across the tuning range for a half-VCSEL bias of 16mA, showing continuous single-mode operation.

As shown in Fig. 4.9, a bias current of 16mA supplied to the half-VCSEL was observed to provide a good compromise between output power and the achievable tuning range. In this case, lasing was achieved when the tuning current was varied between 0mA and 32mA with a corresponding single-mode, mode-hope free tuning range of approximately 45nm (1540nm - 1585nm) where the output wavelength was directly proportional to the square of the tuning current as shown in Fig. 4.9 in accordance with Eqn. 4.5.4. Two sample lasing spectra are provided in Fig. 4.10 to demonstrate the side-mode suppression ratio (SMSR) with respect to the higher-order transverse modes which attains values between 30 and 50dB cross the achievable tuning range. Furthermore, it can be inferred that there are slight ge-

ometric asymmetries in the plane-concave resonator as the eigenfrequencies of the orthogonal transverse-electric (TE) states of the axial mode have split. This frequency separation is primarily attributed to a variation in the radius of curvature on the flexible DBR membrane [190]. Nonetheless, the laser maintains a sufficiently high polarisation-mode suppression ratio (PMSR) ≥30dB. Furthermore, from the greatly suppressed transverse modes we can also infer that the phase fronts of the fundamental mode have an effective match to the resonator structure. However, with an appropriately engineered radius of curvature for the membrane through a higher precision controlling the parameters of the PECVD, a better match can be ensured to achieve values similar to those reported in [187].

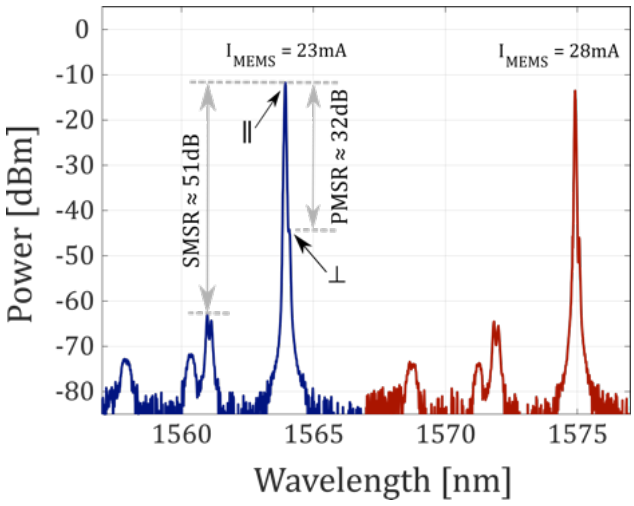


Figure 4.10: Sample optical spectra (with indicated polarisation modes) produced by two different MEMS tuning currents when the bias current supplied to the half-VCSEL is fixed at 16mA.

4.5.2 Wavelength Stability Under Fixed Bias Operation

A critical observation made during the initial characterisation of the device was that the output wavelength and power from the unpackaged VCSEL varied considerably with time, even under temperature control. This prompted a further investigation into the wavelength stability of the VCSEL under fixed bias operation from which an overall wavelength drift of up to 2nm (≈ 250GHz) was observed over the course of 60 minutes as depicted by the black curve in in Fig.4.11(a).

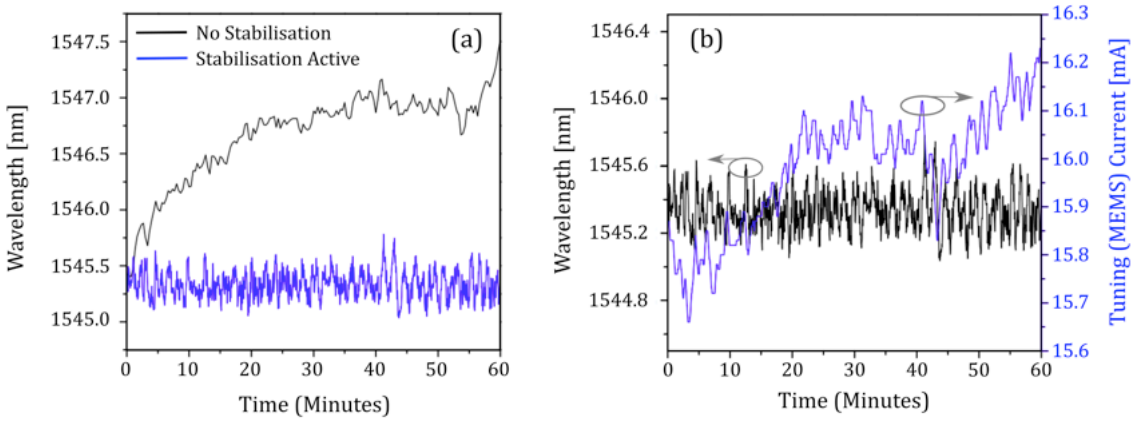


Figure 4.11: Analysis of the VCSEL wavelength stability with time. (a) comparison of the wavelength drift with and without the wavelength control loop. (b) change in tuning current required to maintain the VCSEL within the set wavelength tolerance of ±0.15nm (≈ 18.5GHz).

Notably, the wavelength exhibited instabilities on two timescales: a steady drift to longer wavelengths on the order of minutes and sub-second oscillations around the lasing wavelength. These variations are attributed to multiple sources including (i) resonance oscillations from residual air currents (ii) release of material stress and (iii) significant mechanical vibrations passing through the contact probe tips [191]. In particular, environmental reverberations can severely impact on device operation creating an effect referred to as 'optical microphoning'. As the top DBR needs a relatively large displacement range (on the order of micrometers) in order to achieve wide wavelength tuneability, it requires a certain amount of flexibility in the support beams. Consequently, adjusting the beam stiffness to reduce these instabilities may be possible with material design considerations done on a per-application basis. However, as the VCSEL was characterised in an unpackaged state, proper packaging using wire bonds to deliver the current and packaging of the devices in a fibre coupled configuration could also aid stability. In order to actively compensate for drifts in the set peak wavelength during this characterisation, a computer controlled feedback loop was designed using the instrument control software 'LabVIEW'. As illustrated in Fig. 4.12, the custom program actively tracked the peak emission wavelength by interacting with an OSA before numerically comparing it with a target value and adjusting the tuning current accordingly in order maintain the wavelength peak within a predefined tolerance of ±0.15nm (≈ ± 18.5GHz). This

value was chosen to accommodate the relatively slow speed of feedback loop and the resolution bandwidth of the OSA (0.1nm). However, in a real deployment scenario, a control loop based on a wavelength locker could be utilised to provide faster feedback and more accurate control [192]. The temporal wavelength variation of the tuneable VCSEL with active stabilisation is compared to the case without the feedback control loop in Fig. 4.11(a) while the changes in tuning current required to maintain the wavelength within the set tolerance is shown in Fig. 4.11(b).

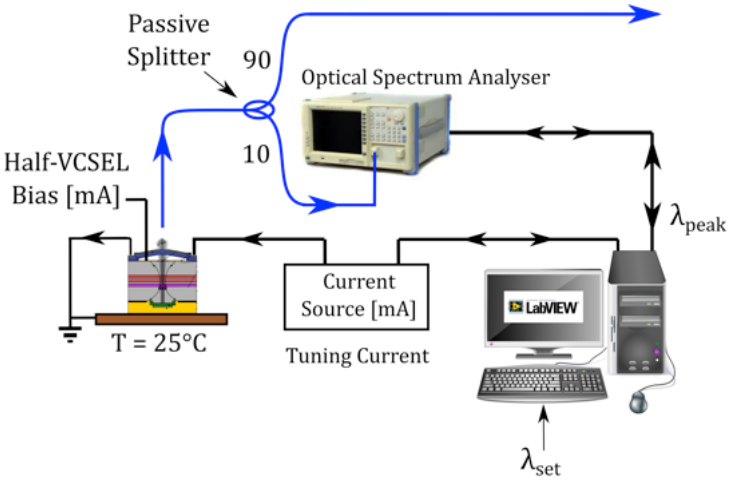


Figure 4.12: Illustration of the control loop used to maintain the lasing wavelength within a specified tolerance around a target peak value.

4.5.3 Performance Evaluation for Transmission at 10Gb/s

To evaluate the suitability of the MEMS-tuneable VCSEL for fibre-optic communications, the temperature controlled continuous-wave (CW) output from the VCSEL was externally modulated at 10.3125Gbit/s with non-return to-zero on-off keying (NRZ-OOK) using a reflective electro-absorption modulator monolithically integrated with a semiconductor optical amplifier (R-EAM-SOA) as shown in Fig. 4.13. An external modulator was required for this work as a previous study on these VCSELs found that the generated heat could not dissipate fast enough for high modulation frequencies resulting in a low-pass behavior with a characteristic cut-off frequency $f_{3dB} \approx 215$Hz [187]. Nonetheless, the modulation signal was produced using the pulse-pattern generator (PPG) from an Agilent N4901B Serial Bit Error

Rate Tester (BERT) with a $2^7 - 1$ pseudo-random binary sequence (PRBS) that was superimposed on a reverse DC bias which was subsequently adjusted for both wavelength and transmission distance in order to optimise the frequency chirp and achieve the minimum BER. In a real deployment scenario, adjusting the modulator bias for the exact distance may not be feasible for cost and complexity reasons; therefore, this analysis simply serves to examine the optimum performance capabilities of the system.

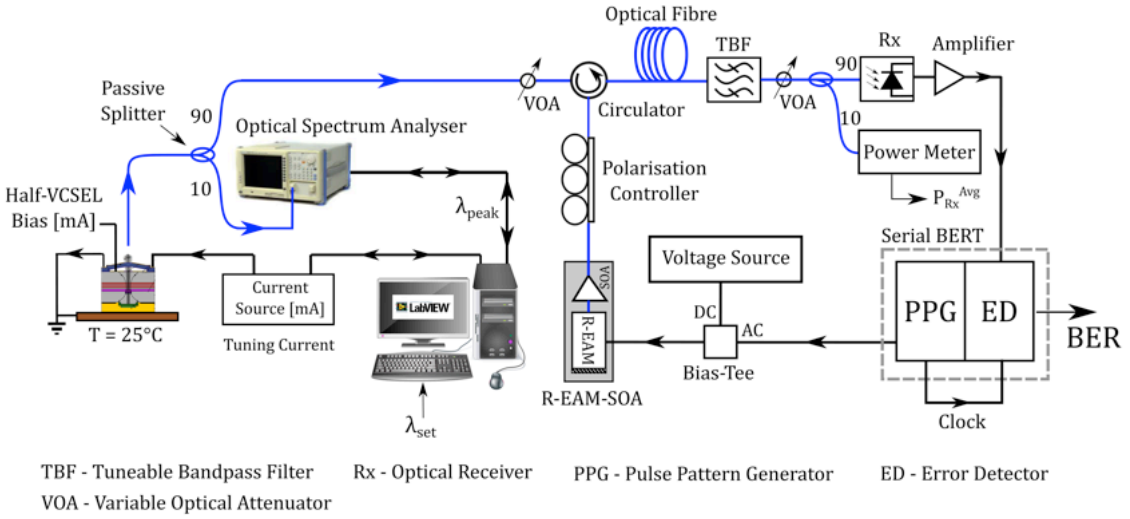


Figure 4.13: Experimental setup used to determine the capability of the MEMS-tuneable VCSEL as a 'colourless' transmitter within an optical network.

In order to avoid the generation of overshoots and unwanted patterning on the optical eye [171], a variable optical attenuator (VOA) was used to optimise the optical input power to the R-EAM-SOA which had a net round-trip gain of approximately 14dB. Subsequently, at the receiver (Rx) side, a tuneable optical bandpass filter (TBF) with a 3dB passband of approximately 0.5nm (≈ 62.5GHz) was used to remove the excess out-of-band ASE produced by the SOA while a VOA was used to adjust the average power, P_{Rx}^{Avg}, entering the commercial 12.5GHz PIN-based optical Rx. Following reception, a linear electrical amplifier with an effective gain of 14dB was used to increase the voltage swing of the electrical signal for use with the error detector (ED) which had a minimum sensitivity of 50mV peak-to-peak.

The BER performance of the system was investigated for back-to-back (BtB) and transmission over 50km of standard single-mode fibre using the internal clock recovery of the BERT where the optimum decision threshold and delay with respect to the received signal were found at each measurement step. In addition, a commercially available ECL (ANDO AQ8201-13) was used to determine the optimum EAM bias at the chosen test wavelengths while it also provided a reference from which the performance of the MEMS-tuneable VCSEL could be compared.

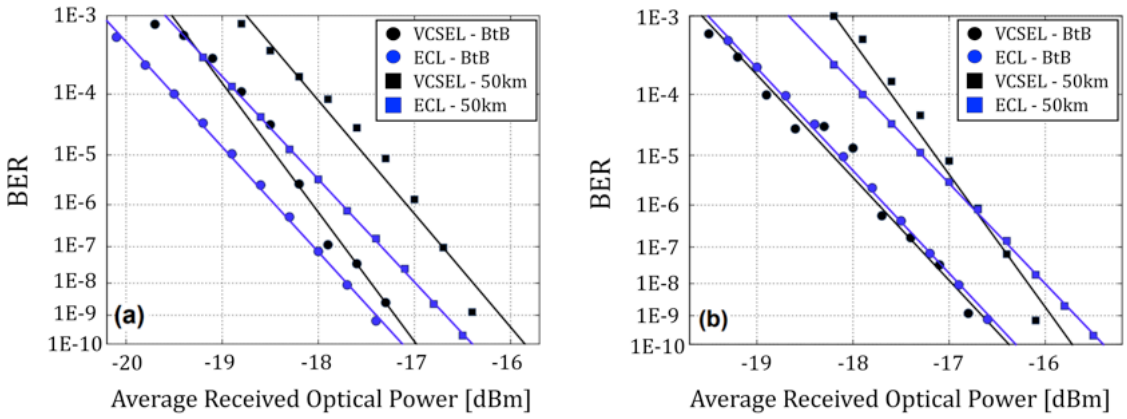


Figure 4.14: BER analysis for the externally modulated MEMS-VCSEL compared to a reference ECL for both back-to-back and over 50km of single-mode fibre at a wavelength of (a) 1540 nm and (b) 1570 nm.

The data presented in Fig. 4.14 demonstrates that the externally modulated MEMS-VCSEL consistently achieved bit error rates less than 10^{-9} (i.e. ≤ 1 error per $1x10^9$ bits transmitted) across a 30nm wavelength tuning range (1540 - 1570nm) with a minimum power penalty of approximately 0.2dB observed between the VCSEL and the ECL in both the back-to-back and 50km cases. However, it is evident that the VCSEL data has a slight scatter around the applied fit. These performance deviations are primarily attributed to intensity noise from the unpredictable sub-second variations in the output of the VCSEL due to the instability of the DBR membrane. While this behaviour averages to some extent, it is clear that there is still an appreciable discrepancy between the experimental VCSEL structure and a commercial continuous-wave laser. Nonetheless, the random variations were not large enough to prevent successful transmission (BER $\leq$ 1x10^{-9}) at 10Gb/s.

4.5.4 Overview of the MEMS-Tuneable VCSEL

The MEMS-tuneable VCSELs developed during the course of the EU funded project SUBTUNE successfully demonstrated a noteworthy continuous tuneability which encompassed the entire C-band (1530 - 1565nm) with a transmission capability of at least 50km at 10Gb/s through external intensity modulation which is compatible with the targets of the latest PON standards [140]. Moreover, as the performance of the un-packaged devices demonstrated in this work was so promising, some of the project partners continued their collaborative efforts in an attempt to further enhance the performance capabilities of these devices. It should be noted that based on the results demonstrated in this work, further device iterations have since been developed which have altered the half-VCSEL structure which has been encapsulated with low dielectric constant (k) polymer material Benzocyclobutene (BCB) in order to reduce the parasitic capacitance and enable direct modulation at speeds of up to 10Gb/s across a continuous-tuning range of 85nm (1522 - 1607nm) [193, 194].

The main advantages of these VCSELs compared to conventional edge-emitting distributed feedback (DFB) and distributed Bragg reflector (DBR) lasers include the potential for a higher yield per-wafer, a smaller threshold and driving currents which correspond to lower power consumption, a smaller footprint, wafer-level testing, efficient fibre coupling (due to the circular-symmetric Gaussian beam profile) and a much shorter cavity length enabling a substantially larger FSR. However, it is important to note that without any external mechanism these lasers are only thermally tuneable over a few nanometers. Moreover, a significant concern with using MEMS is that their long-term mechanical reliability has yet to be proved, hence, many manufacturers are now involved in these reliability tests, both at their own labs and in trials with systems manufacturers. Nonetheless, a significant challenge facing these devices prior to commercialisation is the development of a reliable cost-effective packaging strategy that will suppress the excessive DBR membrane vibrations which became apparent during the course of the detailed characterisation process undertaken in this work. Furthermore, to guarantee the signal fidelity in optical networks employing a narrow channel spacing (i.e. $\leq$ 50GHz), the integration of a wavelength locker will provide tighter control, which, as outlined earlier, will result in increased development costs.

4.6 Single-Growth Monolithically Integrated Tuneable Transmitter

As outlined earlier in this chapter, monolithic integration eliminates the challenging design and fabrication processes necessary for hybrid transmitter assemblies by achieving the desired multicomponent functionality on a single chip resulting in a reduced form factor, power consumption and cost. Today, monolithically integrated tuneable lasers are typically variants of the distributed Bragg reflector (DBR) laser, such as the sampled grating [195], super structure grating [196] and digital supermode DBR lasers [197]. Other types of tuneable laser such as the modulated grating Y-branch (MG-Y) laser are based on interferometric principles using Y-couplers [198]. Alternatively, various types of tuneable external cavity lasers (ECLs) have been designed [163], while a promising device based on a vertical-cavity surface emitting laser (VCSEL) using a surface micro-machined, electro-thermally actuated upper mirror has been shown to achieve a continuous single-mode tuning range of 102nm [187]. Nonetheless, the main disadvantage of these devices is their complex fabrication process which includes multiple epitaxial growths requiring high tolerance steps for creating the grating structures which can lead to high production costs. However, by taking inspiration from the cleaved coupled-cavity (C3) lasers demonstrated in [199] and the Y-laser presented in [200], designs for potentially low-cost discretely tuneable lasers have been developed over the course of last decade by etching slots into Fabry-Pérot (FP) ridge waveguide lasers [201]. In particular, the slots are etched through the upper waveguide in order to introduce reflections within the laser cavity which serve to perturb the primary longitudinal mode. This strategy results in mutually coupled FP cavities for which the effective mode spacing is given by:

$$\Delta\lambda_i = \frac{\lambda^2}{2n_g L_i}, \quad i = 1,\ 2,\ 3, \ldots \tag{4.6.1}$$

where n_g is the group index and L_i is the length of each section. In contrast to slotted lasers with periodic perturbations within the sections [202], the devices considered in this work have no perturbations within the sections to act as gratings. Instead, the section lengths are different so as to produce distinct sets of frequency combs with

different mode spacings; hence, by injecting currents into each section the local gain and refractive index can be altered to control the overall gain and phase resonances thus providing tuneability. The basic structure of a three-sectioned slotted Fabry-Pérot (3s-SFP) laser used in this work is illustrated in Fig. 4.15. Here, two single 1μm-wide slots are etched into the ridge to separate the laser cavity into three independently injected active sections.

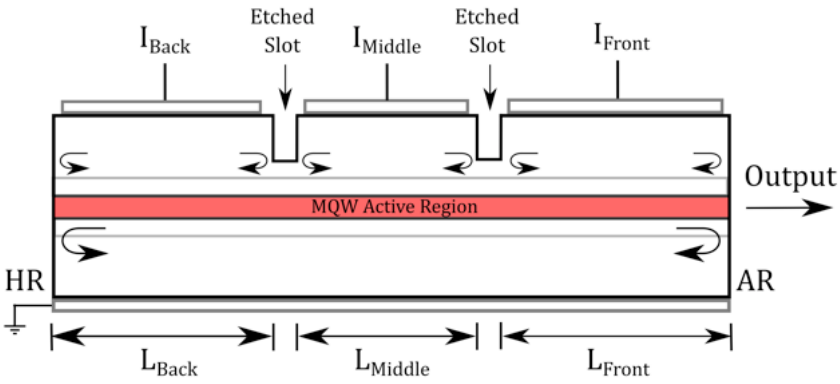


Figure 4.15: Cross-section of a three-sectioned slotted Fabry-Pérot laser.

Tuning Mechanism:

With careful device design, an overlap of the resonance peaks at the same wavelength implies that the other resonances do not overlap within the tuning range, hence, single-mode lasing is achieved at this wavelength. Fine tuning of the selected resonance can then be achieved by varying the bias applied to one or all sections simultaneously. Alternatively, by coarsely tuning the active sections, the previously overlapping resonances will misalign and a different combination of resonances overlap resulting in a mode-hop. In this way, even a small index variation can produce a relatively large wavelength change; this is known as the *Vernier effect*. It should be noted that this is a simplified explanation of the tuning process for these SFP lasers and that the actual tuning mechanism is more complex as the resonance conditions are also influenced by gain changes within each section as a function of the applied bias. As the intricacies and predictability of this process are beyond the scope of this thesis, the reader is directed to [203] for further information.

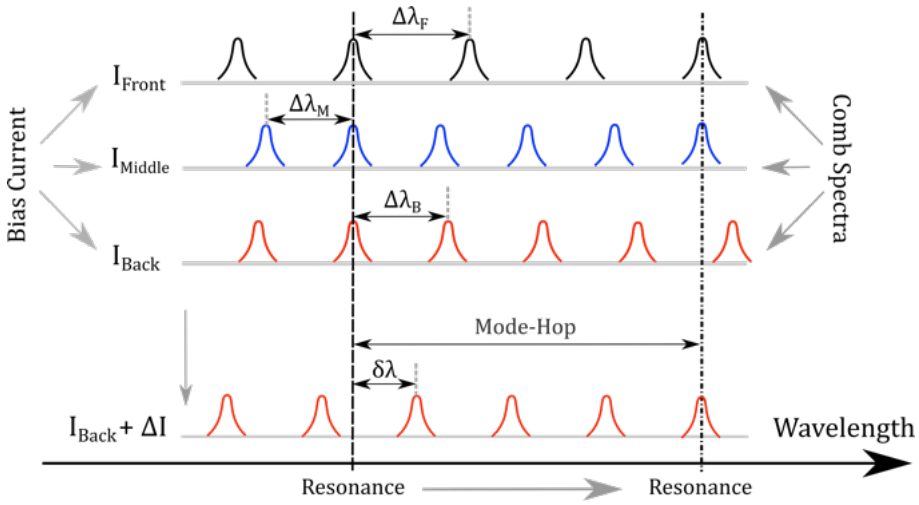


Figure 4.16: Illustration of the Vernier tuning effect for a three-sectioned slotted Fabry-Pérot laser where each section has a different mode spacing in accordance with its length (i.e. $\Delta\lambda_F \neq \Delta\lambda_M \neq \Delta\lambda_B$).

The primary advantage of these SFP lasers over alternative structures is that they require only a single epitaxial growth process and standard photolithography techniques. This approach significantly reduces the fabrication complexity thereby increasing reliability while also reducing cost. Moreover, as these lasers do not explicitly need cleaved facets to form the laser cavity they can be employed to integrate monolithically with other electro-optic devices such as modulators or semiconductor optical amplifiers (SOAs) through the implementation of deeply etched facets.

In this work, we present the first iteration of a 10G-capable optical transmitter consisting of a discretely tuneable 3s-SFP laser that has been monolithically integrated with an absorptive modulator and an SOA using foundry-compatible fabrication methods that offer the potential for low-cost mass production. The following section briefly outlines the transmitter design and fabrication processes undertaken by the III-V Materials and Devices Group within the Tyndall National Institute, while section 4.6.1 - 4.6.5 presents the primary characterisation results alongside the impact of inter-section crosstalk and the continuous-mode (CM) transmission performance at 10Gb/s using NRZ-OOK. Finally, in section 4.6.6, an innovative time-resolved chirp measurement technique is used to determine the wavelength stability of the transmitter under modulation as well as various SOA gating conditions in order to examine the implications for the set carrier frequency during the generation of optical bursts.

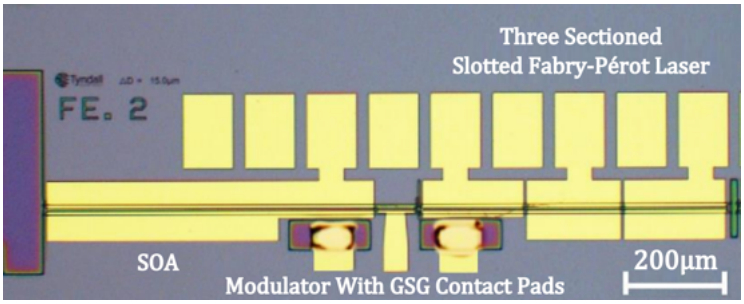


Figure 4.17: Optical microscope image of the monolithically integrated transmitter with a total length of approximately 1.4mm incorporating a three-sectioned discretely tuneable slotted Fabry-Pérot ridge waveguide laser (614μm), modulator (80μm) and an SOA (675μm).

Device Design and Fabrication

The integrated transmitter chip was fabricated using a single epitaxial growth process and standard lithography techniques with a standard off-the-shelf AlInGaAs/InP structure from a global wafer supplier comprised of multiple quantum wells on an n-doped substrate. As shown in Fig. 4.17, the length of the laser was defined using deeply (5μm) etched facets. The light produced by the laser is guided using a surface ridge with three separately contacted sections of slightly different lengths, 210μm, 192μm and 212μm, each divided by a shallow etched slot as shown in Fig. 4.18 (c) and (d). These partially reflective 1μm-wide slots with a depth of 1.85μm are defined in the same step as the ridge waveguide. Therefore, they present no additional complexity in the fabrication process. During operation, reflections from these slots cause interference and by varying the drive current to each section, the gain and index of each section of the laser can be controlled such that single-mode lasing is achieved. The integrated modulator is an in-line absorbing section with a length of 80μm that is accessed through a ground-signal-ground (GSG) contact pad for which no effort was made to reduce the pad capacitance in this initial implementation. The input facet of the modulator section was separated from the laser output by 15μm using a deep etch (5μm) with an angle of 7° with respect to the ridge in order to mitigate back reflections while the output facet was separated from the 675μm long SOA section with a shallow, 1μm-wide angled slot. As shown in Fig. 4.18 (a) and (b), the output facet of the integrated SOA was lithographically

etched with an angle of 7° with respect to the ridge to reduce undesirable optical feedback. It is important to note that the use of lithographic etching in the fabrication process eliminates cleave errors and ensures that the dimensions of all the elements on the wafer are well controlled. Since all the integrated components operate at the same band gap, the fabrication process is completely regrowth-free and foundry-compatible which is expected to greatly reduce the cost of the devices.

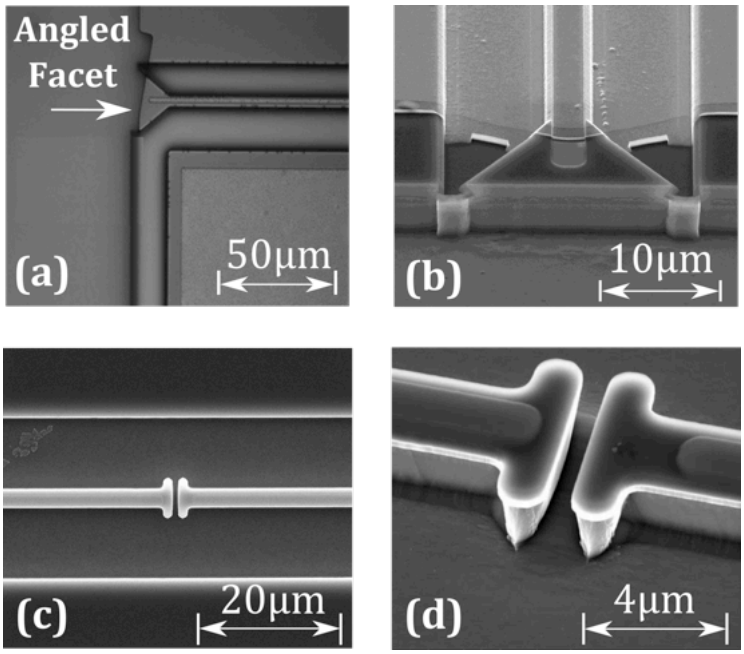


Figure 4.18: (a) Scanning electron Microscope (SEM) image of a deeply etched facet which is angled with respect to the ridge for reduced optical feedback in the SOA section (b) facet view of the ridge, (c) a shallow slot etched into the ridge waveguide of the laser section and (d) tilted view of an etched slot.

As shown in Fig. 4.19, this first generation monolithically integrated transmitter chip was characterised in an unpackaged state using a probe station which consisted of a temperature controlled sub-mount, a 40GHz GSG RF probe, a multi-contact DC wedge probe and a lensed single-mode fibre (SMF) into which the light was coupled via free-space alignment using an XYZ translational stage.

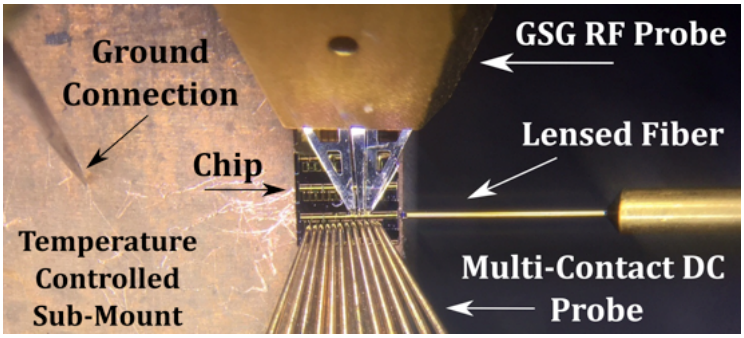


Figure 4.19: Microscope view of the probe station setup showing the integrated transmitter chip, RF GSG probe, multi=contact DC probe and the lensed fibre.

4.6.1 Laser Section

To examine the relation between the tuning currents and the peak transmission wavelength, a coarse calibration of the transmitter was performed by varying the bias currents supplied to each section of the SFP laser in steps of 5mA and examining the resultant spectra using an optical spectrum analyser (OSA). The results of this calibration, shown in figures 4.20 and 4.21 indicate a discrete tuning range of approximately 12nm between 1551 and 1563nm which has been defined using a side-mode suppression ratio (SMSR) threshold of 30dB as required by the NG-PON2 standard (G.989.2) [172]. Moreover, as outlined in [204], the primary mode spacing within these lasers is determined by the overall length of the laser cavity ($\sim 614\mu$m) with every third mode being preferentially selected due to the sectioning of the cavity. This corresponds to a mode spacing of roughly 200GHz; however, a smaller spacing can be achieved by increasing the length of each section and vice versa. Nonetheless, due to the Vernier effect, only a single mode from the sets of cavity modes can be aligned; therefore, any unintended variations in the actual length of the sections will result in a shift in the tuning map with respect to the applied current. It is also important to note that the resonance conditions are dependent on the refractive indices of the individual sections which in turn are temperature dependent, therefore, the achievable modes are not strongly predictable at present. As a result, the information presented in Fig. 4.20 is included purely for indicative purposes. However, for further information on the tuning mechanisms of these lasers the reader is directed to [203].

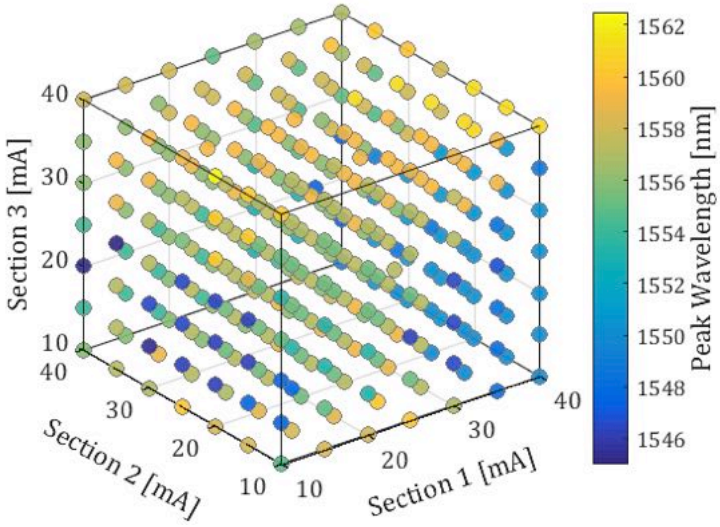


Figure 4.20: Coarse tuning map recorded using 5mA steps [Modulator bias = -1.0V, SOA bias = 30mA and T = 20°C].

As the applied tuning currents also manipulate the gain within each section of the laser, there will be an appreciable peak-power variation across the tuning range. For instance, in the device reported in this work, the power variation across the specified tuning range was measured to be approximately 7.5dB, hence, it is expected that the integrated SOA could be used to equalise the power between the different selected lasing wavelengths. Lastly, in order to fill in the spectral gaps evident in Fig. 4.21, fine-tuning can be accomplished by adjusting the granularity of the tuning currents and by varying the chip temperature as demonstrated in [205]. However, it should be noted that this mechanism is limited since a significant variation in the refractive index can alter the resonance conditions causing the present lasing mode to hop to a different mode. Nonetheless, to demonstrate the single-mode operation of the transmitter, the spectral profile of 10 arbitrarily chosen tuning settings are presented in Fig. 4.22, which exhibit a positive detuning from the material gain peak (~ 1542nm), where the modulator and SOA sections are biased at -1.0V and 30mA respectively while the sub-mount temperature is set at 20°C.

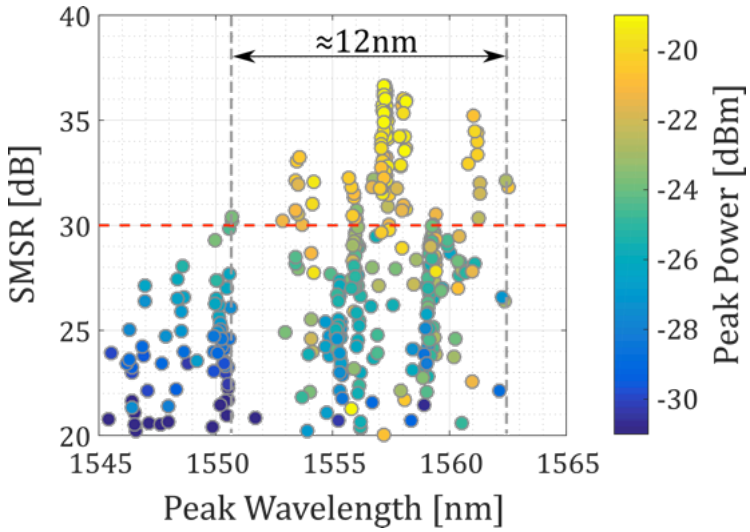


Figure 4.21: Coarse Calibration: SMSR of the achieved lasing modes plotted against the peak wavelength [Modulator bias = -1.0V, SOA bias = 30mA and T = 20°C].

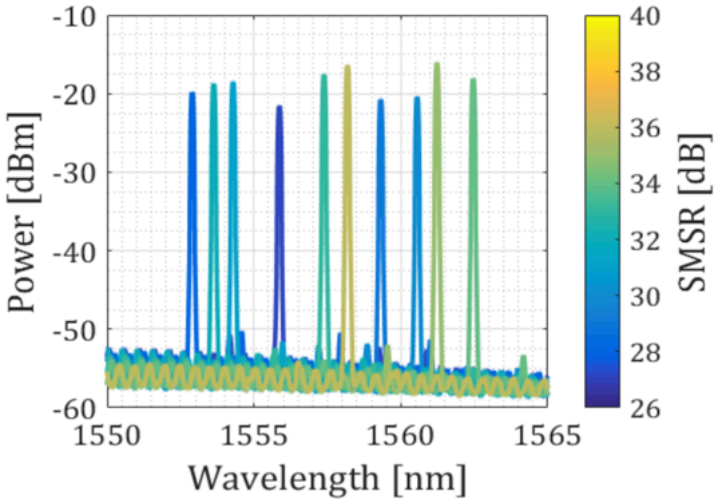


Figure 4.22: Coarse calibration: Optical spectra of 10 discrete lasing modes with SMSR > 30dB [Modulator bias = -1.0V, SOA bias = 30mA and T = 20°C].

4.6.2 Modulator Section

As outlined in section 4.6, the modulator section fabricated within this test device was simply an 80μm-long absorbing section accessible through a GSG contact pad. This approach was taken in order to examine the feasibility of integrating the 3s-SFP

laser with other electro-optic components and to investigate the potential high-speed capabilities of the envisaged transmitter. However, in the absence of quantum well intermixing (QWI) [206], the trial modulator structure exhibited an undesirably high level of loss (~ 20dB, as detailed in Section 4.6.3). Moreover, when this feature was combined with the fibre coupling loss, an external optical amplifier was required during the characterisation process in order to achieve powers comparable with commercial devices (+5dBm). Nonetheless, to determine the modulation capability of this section, the small-signal frequency response was recorded for various laser tuning settings using a vector network analyser (VNA) and a calibrated high-speed photoreceiver whose response was removed from the total system response through calibration. It should also be noted that the response of the cabling between port 1 of the VNA and the tip of the GSG probe was also removed through calibration in order to isolate the frequency response of the transmitter chip. An illustration of the experimental setup is provided in Fig. 4.23.

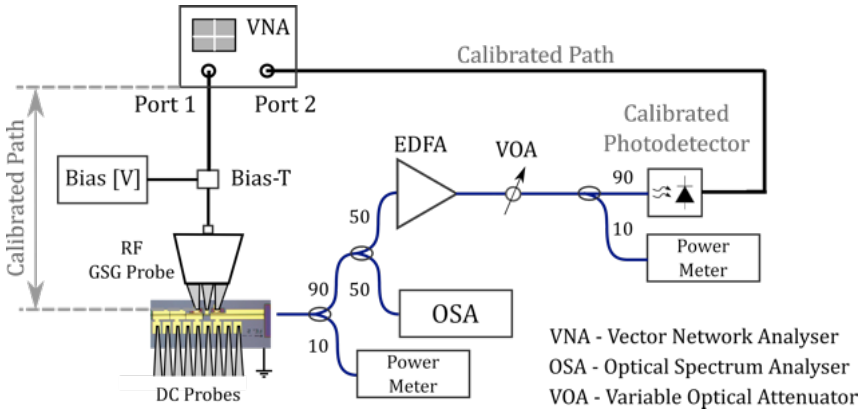


Figure 4.23: Illustration of the measurement setup used for the frequency response measurement.

A VNA enables the electrical performance of high-frequency electrical systems to be determined through examination of the network scattering parameters (S-parameters) which describe the behaviour of linear electrical systems when undergoing various steady-state stimuli by electrical signals that lie within the radio frequency (RF) band (3Hz - 3THz). For example, the S-parameter conventions which describe the relationship between the incident, transmitted and reflected waves for a 2-port system are shown in Fig. 4.24 while the corresponding matrix is given in Eqn. 4.6.2.

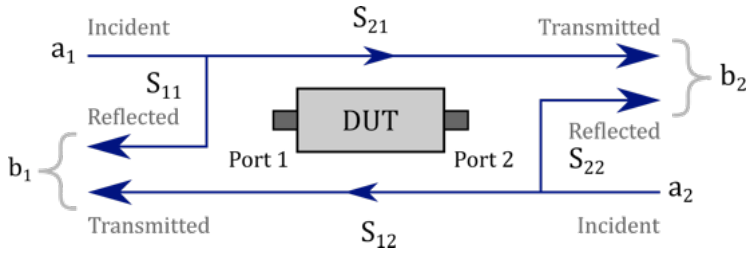


Figure 4.24: The S-Parameter conventions for a two-port device-under test.

$$\begin{bmatrix} b_1 \\ b_2 \end{bmatrix} = \begin{bmatrix} S_{11} & S_{12} \\ S_{21} & S_{22} \end{bmatrix} \begin{bmatrix} a_1 \\ a_2 \end{bmatrix} \tag{4.6.2}$$

From Eqn. 4.6.2, the equations which describe the relationship between the amplitude of the signal and the S-parameters at both of the network ports can be determined as

$$b_1 = S_{11}a_1 + S_{12}a_2 \tag{4.6.3}$$

$$b_2 = S_{21}a_1 + S_{22}a_2 \tag{4.6.4}$$

In the case of a source located at port 1, the forward S-parameters, S_{11} and S_{21} are determined when port 2 is terminated by an ideal load which is equal to the characteristic impedance (Z) of the test system; by convention, this value is typically 50Ω. Moreover, in accordance with the maximum power transfer theorem (also known as Jacobi's law), b_2 will be completely absorbed, hence, there will be no reflection (i.e. $a_2 = 0$). Consequently, S_{11} is known as the forward reflection coefficient or the impedance and S_{21} gives the forward transmission coefficient, both of which are typically complex valued. Alternatively, by placing the source at port 2 and terminating port 1 with an ideal load (i.e. $a_1 = 0$), the reverse S-parameters, S_{22} and S_{12} can be measured which represent the output reflection coefficient (reverse impedance) and the reverse transmission coefficient respectively.

In this work, the primary parameter of interest in relation to the integrated modulator section is that of the forward transmission coefficient (S_{21}) from which the scalar logarithmic gain (g_{dB}) can be determined and plotted as a function of the applied frequency to demonstrate the small-signal frequency response. From this

data, the 3dB bandwidth can be determined easily.

$$g_{dB} = 20log_{10}|S_{21}| \quad [dB] \quad where, S_{21} = \frac{b_2}{a_1}\bigg|_{a_2=0} \tag{4.6.5}$$

The frequency response of the chip for four arbitrarily chosen laser tuning settings are presented in Fig. 4.23, where the modulator was biased at -1.0V and the SOA section was biased at 30mA. It should be noted that due to the low output power from the chip, the integrated SOA section was operating within the linear regime, hence it did not influence these measurements. With this in mind, it can be seen that the 3dB bandwidth of the modulator section lies between 5.5 and 6.5GHz depending on the laser tuning settings, which is sufficient for 10Gb/s modulation albeit with a power penalty. However, alongside the use of QWI, we believe that the performance of the modulator section can be significantly improved in future iterations through a reduction in the parasitic capacitance of the RF contact pads through the addition of a low-k dielectric polymer as demonstrated in [207].

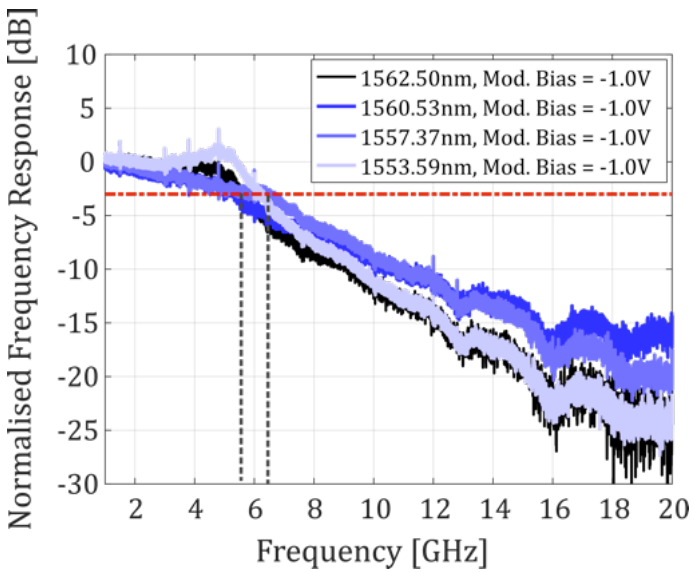


Figure 4.25: Normalised small-signal frequency response of the integrated transmitter for four arbitrary lasing modes [SOA bias = 30mA, T = 20°C].

4.6.3 SOA Section

The integration of an SOA section within the transmitter was originally targeted not only to compensate for the intrinsic loss of the modulator but also to provide a gating function necessary for burst-mode operation as demonstrated in [208]. As shown in Figure 4.18(a), the output facet of the 675μm-long SOA section was angled at 7° with respect to the ridge waveguide to reduce unwanted reflections. However, due to the absence of an anti-reflection (AR) coating, a residual facet reflectivity is responsible for producing FP modes in the amplified spontaneous emission (ASE) spectrum of the SOA section as shown in Fig. 4.26.

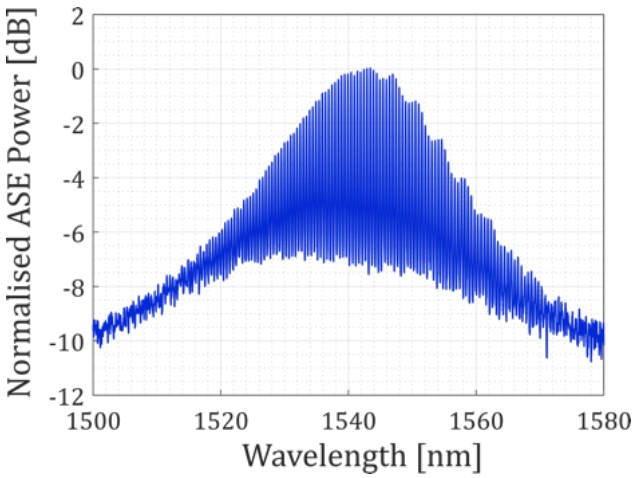


Figure 4.26: ASE spectrum of the integrated SOA section for an applied bias of 30mA indicating an appreciable level of optical feedback [Laser Bias = 0mA, 0mA, 0mA, Modulator bias = 0V, T = 20°C].

In accordance with the model presented in [209], which does not take into account the roughness of the inductively coupled plasma (ICP) etch, this residual facet reflectivity was estimated to be approximately 0.02 [210]. It should be noted that we have assumed the same reflectivity for both facets as they were formed during the same etch step and have the same physical properties (i.e. tilt angle, depth). In addition, the ripple observed to encompass the amplitude of the FP modes indicates that the 80μm-long modulator section (separated from the SOA using a shallow 1μm-wide etch) is contained within the ASE resonance cavity, resulting in a total length of 756μm. Nonetheless, as the presence of the FP modes served to degrade

the attainable SMSR, it ultimately placed a limit on the achievable output power from this test device. As a result, it is clear that further structural optimisation is required for this integrated SOA section in future iterations of this transmitter. For instance, in addition to the use of an AR coating, a modified facet employing tapers or mode expanders may further minimise any undesired optical feedback [211]. In order to achieve a better understanding of the performance of the integrated SOA section, the single-pass gain was determined using a modified Hakki-Paoli technique as proposed by L. D. Westbrook in [212].

Estimating the Single-Pass Gain of the Integrated SOA:

The Hakki-Paoli method outlined in [213], is one of the most widely recognised techniques used to estimate the gain of semiconductor laser diodes and optical amplifiers if the form of the emission spectrum (below threshold in the case of a laser diode) takes the form of cavity resonances whose transmission can be described by the product of the spontaneous emission and the transmission of the Fabry-Pérot resonator which is given by

$$T = \frac{(1-R_1)(1-R_2)e^{g_0 L}}{(1-\sqrt{R_1 R_2}e^{g_0 L})^2 + 4\sqrt{R_1 R_2}e^{g_0 L}\sin^2(\frac{2\pi n_{eff} L}{\lambda})} \tag{4.6.6}$$

where, $R1$ and R_2 are the facet reflectivities, L is the cavity length, n_{eff} is the effective refractive index of the guided mode, λ is the emission wavelength and g_0 is the net modal gain which can be expressed as a function of the confinement factor (Γ), the material gain (g_m) and the waveguide loss (α)

$$g_0 = \Gamma g_m - \alpha \tag{4.6.7}$$

Assuming that the edge facets have equal reflectivity (i.e. $R_1 = R_2$), the ratio (r) of a maximum transmission at $2\pi n_{eff} L/\lambda = m\pi$ to an adjacent minimum at $2\pi n_{eff} L/\lambda = (2m+1)\pi/2$ can be derived from Eqn. 4.6.6 as

$$r = \frac{T_{max}}{T_{min}} = \frac{(1+Re^{g_0 L})^2}{(1-Re^{g_0 L})^2} \tag{4.6.8}$$

Hence, the net modal gain (g_0) can be derived as

$$g_0 = \frac{1}{L}\left(log_e(\frac{\sqrt{r}-1}{\sqrt{r}+1}) + log_e(\frac{1}{R})\right) \tag{4.6.9}$$

At this point it is important to recognise that the Hakki-Paoli analysis assumes an infinitely narrow resolution bandwidth (RBW) for the spectrometer. Consequently, the effect of a finite passband serves to reduce the measured transmission ratio with a corresponding decrease in the net modal gain. While this effect could be reduced through the utilisation of a very small RBW it would also reduce the signal-to-noise ratio (SNR). To address this issue, a consequent modification was proposed by Westbrook in [212] which allows for the use of a larger RBW (wider passbands) thus improving the SNR with no loss of accuracy in determination of the modal gain. The difference between the idealised Hakki-Paoli measurement and the Westbrook technique can be seen schematically in Fig. 4.27.

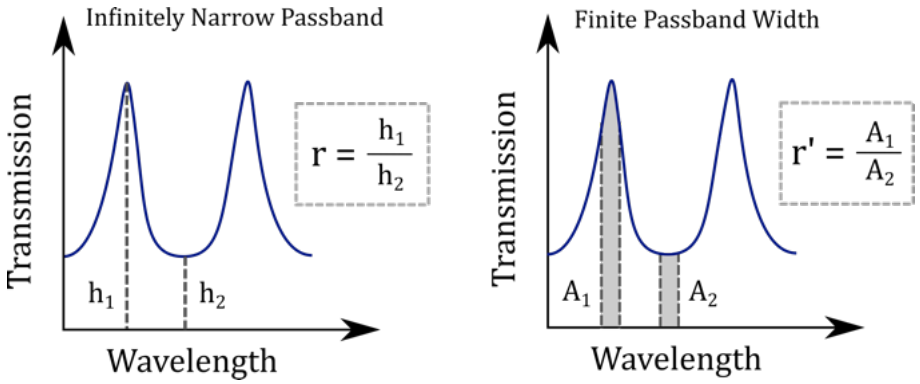


Figure 4.27: Illustration of the idealistic Hakki-Paoli approach compared with the Westbrook method which considers the impact of a finite resolution bandwidth.

In practice, the passband can be well-approximated by a rectangle, therefore, it allows for the calculation of r' which is defined as the ratio of the maximum to the minimum transmission as measured by a spectrometer with a specified passband B in accordance with Eqn. 4.6.10.

$$r' = \frac{\int_{\lambda_{max}-\frac{B}{2}}^{\lambda_{max}+\frac{B}{2}} T(\lambda)\, d\lambda}{\int_{\lambda_{min}-\frac{B}{2}}^{\lambda_{min}-\frac{B}{2}} T(\lambda)\, d\lambda} \tag{4.6.10}$$

where λ_{max} and λ_{min} represent the wavelengths at the maximum and minimum o the resonator transmission respectively. The result of this calculation is presented in Fig. 4.28, which plots r' as function of the normalised passband, $B/\delta\lambda$, where $\delta\lambda$ signifies the wavelength difference between two adjacent resonances. Notably, this data permits the direct conversion of a measured ratio for a given RBW to the modal gain in the form Re^{gL} where R is the facet reflectivity and L is the length of the device. Moreover, it should be noted that r' is in fact the parameter which is directly obtained from the measurements.

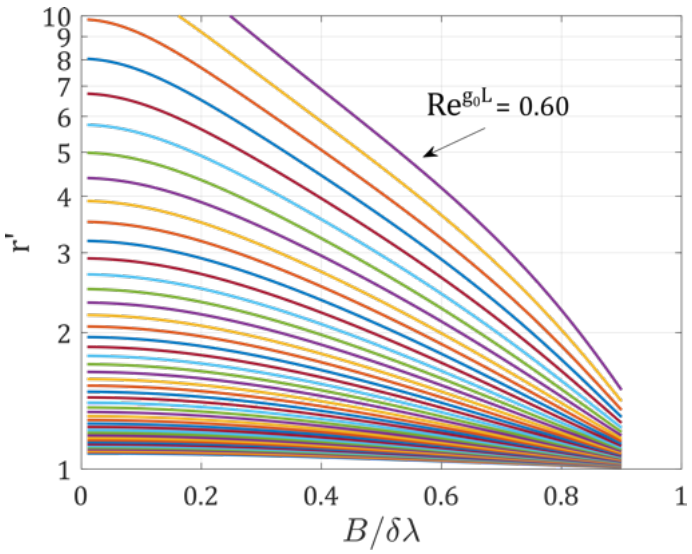


Figure 4.28: Calculation of the transmission ratio, r', as a function of the normalised passband, $B/\delta\lambda$, for values of the reflectivity-gain product, Re^{gL}, ranging from 0.02 to 0.6.

For the device-under-test, the SOA bias that provided the optimum trade-off between output power and SMSR was found to be around 30mA. The corresponding single-pass gain shown within Fig. 4.29 was then determined using Eqn.4.6.11 in accordance with the Westbrook technique shown in Fig. 4.28 through measurement

of the transmission ratio, r', from the respective ASE spectrum captured using an OSA with a RBW of 0.1nm. Notably, at this bias, the gain available to the lasing wavelengths within the specified tuning range (1551- 1562nm) was estimated to be between 10.2dB and 12.7dB.

$$G = e^{g_0 L} \quad \rightarrow \quad G_{dB} = 10log_{10}(e^{g_0 L}) \tag{4.6.11}$$

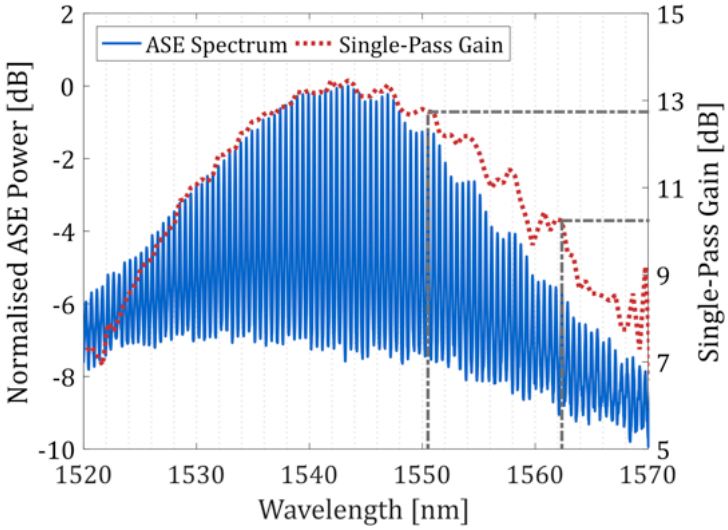


Figure 4.29: ASE spectrum and the corresponding single-pass gain generated by the integrated SOA section for an applied bias current of 30mA [SOA Length = 675μm, Facet Reflectivity = 0.02, OSA RBW = 0.1nm, T = 20°C].

Using a Gaussian field approximation and assuming an angular alignment accuracy $\leq 0.15^{\circ}$ with zero lateral offset, the coupling loss between the chip and the lensed fibre can be as much as 5dB [214]. Taking this value into account and using the estimated gain of the SOA at a test wavelength of 1557.37nm ($\approx$ 11.1dB), which exhibited a peak fibre-coupled power of -17.5dBm in Fig. 4.22, the power at the output of the modulator can be estimated as -23.6dBm. Additionally, the typical peak power achievable from a discrete 3s-SFP laser is in the range of +5dBm to -5dBm depending on the selected mode, hence by assuming a minimum peak output power of -5dBm, the loss of the modulator section within this test device can be estimated

to be 18.6dB. This value suggests that the loss of the modulator section in dB is three or four times the typical value reported for monolithically integrated electro-absorption modulators (EAMs) [195, 215]. Nonetheless, by considering a structural optimisation of the modulator section (e.g. through QWI) in order to achieve an insertion loss representative of a typical value (≈ 5dB), the same SOA section should provide a sufficient level amplification at 30mA to achieve a peak output power of roughly +1dBm. However, by accounting for modulation and including a typical fibre coupling loss for packaged devices of 2dB, the achievable output power from the chip would be further reduced by 5dB. Consequently, a larger gain provided by an increased SOA bias could allow higher output powers to be reached such as those required by current PON standards, provided that the residual facet reflectivity is improved with the inclusion of an AR coating. However, as demonstrated in [216], the presence of thermal crosstalk within monolithically integrated devices has the potential to compromise the integrity of the transmission wavelength, hence, it must be investigated.

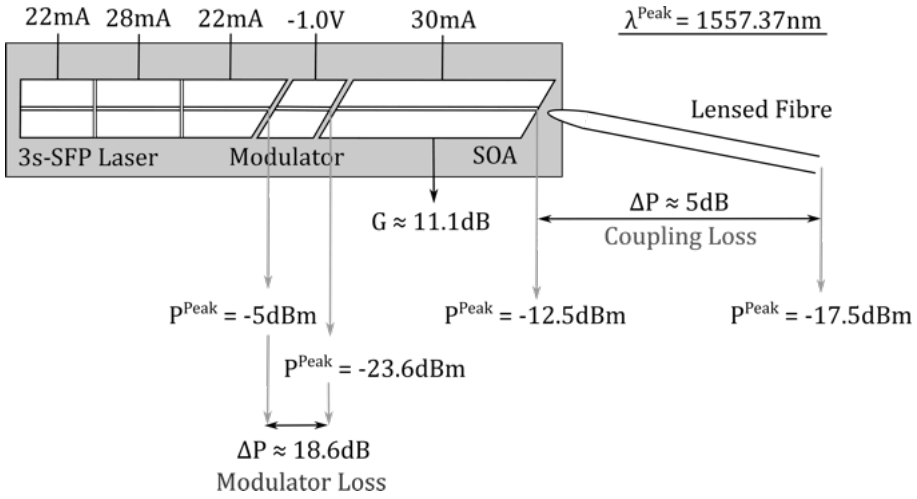


Figure 4.30: Estimating the insertion loss of the integrated modulator section.

4.6.4 Temperature Dependence and Inter-section Crosstalk

The discrete nature of the lasing modes obtained from the monolithically integrated transmitter demands a novel strategy for local wavelength identification coupled with a technique for fine tuning and stabilisation in order to reach and maintain the

wavelengths specified by the ITU-T DWDM spectral grid [217]. In particular, as the global temperature plays an important role in defining the resonance conditions of a 3s-SFP laser, the influence of a temperature variation on the set lasing wavelength was studied using two distinct tuning settings for which the peak was monitored as the sub-mount temperature was varied. The corresponding results are shown in Fig. 4.31. It is important to recognise that depending on the tuning settings, the temperature variation can cause either a linear variation of the wavelength with temperature or a mode-hop. Moreover, if the mode-hop regions are excluded, the temperature dependence of the lasing wavelength can be quantified as approximately 0.17nm/°C. This value is relatively high when compared with the corresponding value obtained for other test devices (~ 0.11nm/°C), which may be caused by a discrepancy in the material structure. Nevertheless, this dependence can be exploited to complement the tuning achieved by the applied bias currents in order to fine tune and stabilise the wavelength to a desired ITU-T channel through the use of a feedback control loop and an appropriate wavelength referencing strategy.

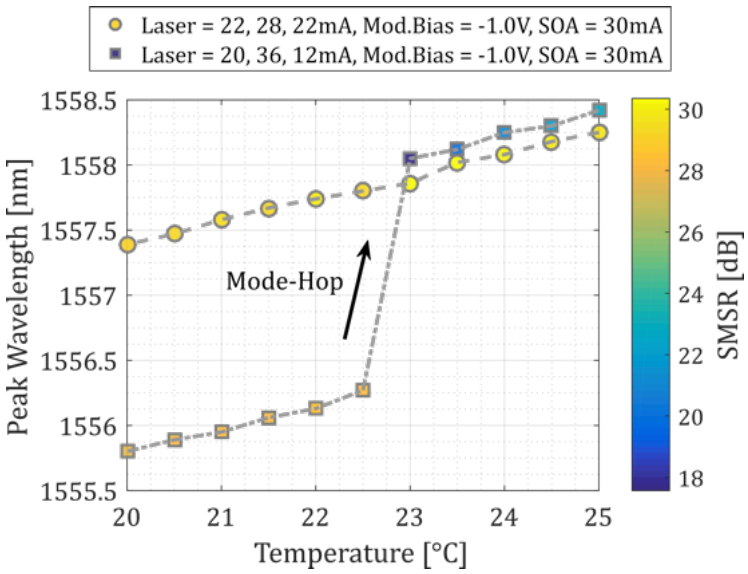


Figure 4.31: Temperature dependence of the lasing wavelength.

In order to examine the impact of inter-section crosstalk, the peak transmission wavelength of an arbitrary tuning setting was monitored using an OSA while the bias supplied to the integrated modulator and SOA sections were varied for a fixed sub-

mount temperature of 20°C. The results of this analysis are presented in Fig. 4.32. Notably, the peak wavelength was largely independent of the DC voltage applied to the modulator section; however, increasing the bias current supplied to the SOA section produced an undesirable shift in the peak that occasionally resulted in abrupt mode-hops. As the tuning efficiency observed here is very low, this information suggests that localised heating produced by the SOA section may be shifting the laser cavity closer to the SOA, hence, the resulting cavity misalignment may be the reason for the induced mode-hop; however, a residual optical reflection within the cavity may also be a contributing factor. Nonetheless, a thermal interaction between the SOA and laser sections is an undesirable effect that serves to complicate the calibration and tuning of the integrated transmitter in terms of wavelength and output power. However, it is important to recognise that thermal cross-talk is a common feature of all monolithically integrated tuneable transmitters [216] and, as outlined previously, bias currents can be found for this test device which provide an optimum trade-off between wavelength tuning SMSR and output power for continuous-mode operation. The effect of thermal cross-talk on the wavelength stability will be further analysed dynamically in section 4.6.6 which accounts for the pulsed SOA bias current used to emulate burst-mode operation.

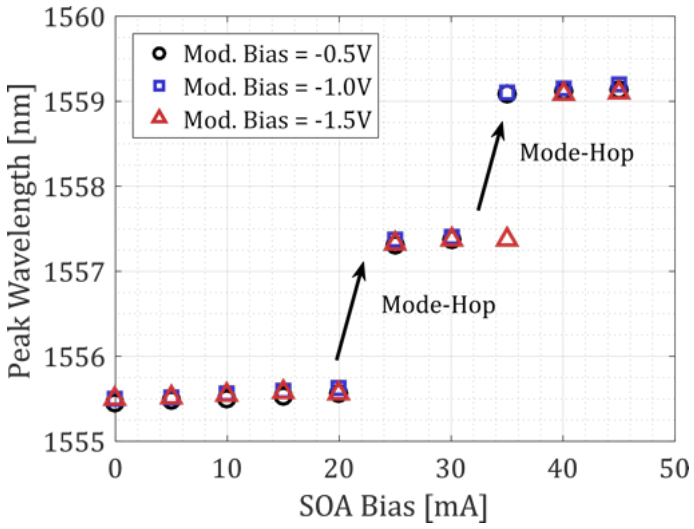


Figure 4.32: The impact of crosstalk between the transmitter components, captured by varying the applied modulator and SOA bias for a fixed laser tuning bias (22mA, 28mA, 22mA) and sub-mount temperature (20°C).

4.6.5 Transmission Performance Evaluation

To evaluate the transmission capability of the integrated transmitter, the BER performance was investigated for various tuning settings under intensity modulation at 10Gb/s. The corresponding experimental setup is illustrated below in Fig. 4.33.

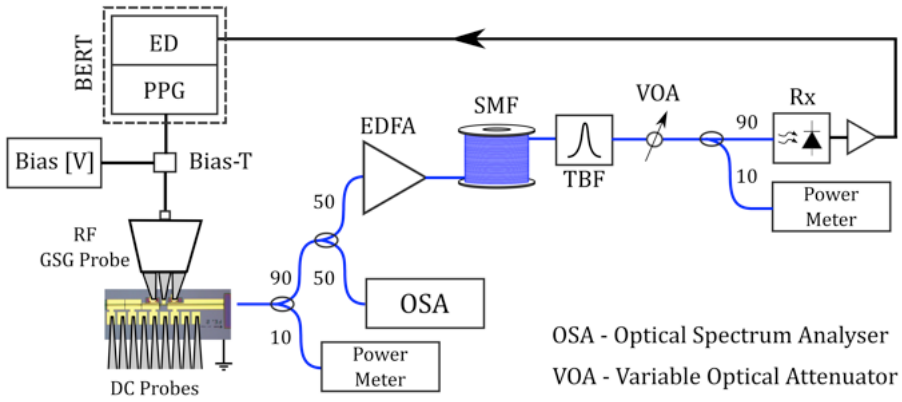


Figure 4.33: Experimental setup: 10G continuous-mode transmission tests.

At the transmit side, a pulse-pattern generator (PPG) was used to produce a pseudo-random binary sequence (PRBS-7) for NRZ-OOK modulation at 10.3125Gb/s with a peak-to-peak voltage swing of 1V (±500mV). This signal was supplied through a bias-tee to the RF GSG probe connected to the modulator section. The voltage swing supplied by the PPG to the modulator was then optimised in order to achieve the best compromise between the extinction ratio (ER) and eye crossing point; this process is shown in Fig. 4.34 for a lasing mode located at 1557.37nm. Notably, the observed reduction in the crossing point can be attributed to an appreciable level of non-linear absorption introduced by the modulator section in response to the increased level of reverse bias. Moreover, as the insertion loss of the trial modulator structure resulted in an appreciably low fibre coupled output power from the unpackaged chip, a gain-stabilised erbium-doped fibre amplifier (EDFA) was used to boost the power of the signal launched into the transmission fibre for all the test wavelengths to a value close to +5dBm which is comparable with devices specified for current PON standards [172]. At the receiver (Rx) side, a tuneable bandpass filter (TBF) with a 3dB passband of 0.5nm was used to remove the excess out-of-band amplified spontaneous emission (ASE) while a variable optical attenuator

(VOA) was used to control the average power of the signal entering the commercial 12.5GHz PIN-based photo-receiver (Rx). An electrical amplifier with an effective gain of 14dB was then used to optimise the electrical signal from the Rx for use with the error detector (ED) which has a minimum sensitivity of 50mV peak-to-peak.

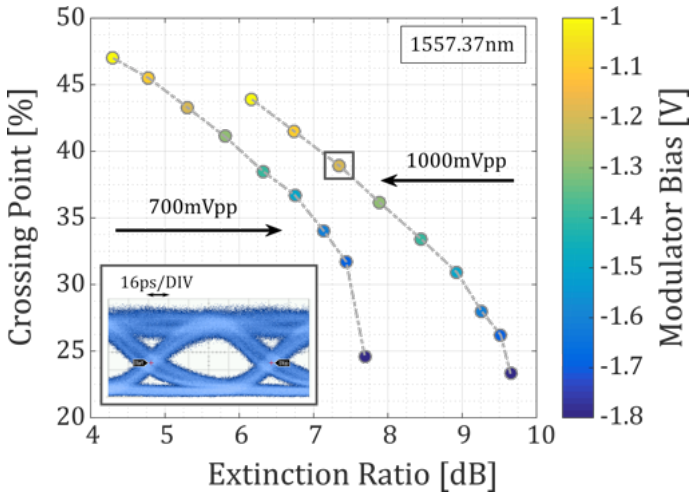


Figure 4.34: 10G NRZ-OOK eye crossing point and extinction ratio as a function of the applied modulator bias for a typical lasing mode.

Multiple lasing modes with an SMSR ≥ 30dB were tested in back-to-back at 10Gb/s, five of which are presented in Fig. 4.35(a). These results demonstrate successful error-free transmission with a residual sensitivity variation of ~ 0.5dB is present around the forward error correction (FEC) threshold of 1.1×10^{-3} [80]; this can be attributed to a slight difference in the ER achieved for each mode. In addition The performance of the transmitter was also examined using 20km and 50km of standard SMF; the results of this analysis are presented in Fig. 4.35(b) using a test wavelength at 1557.37nm (SMSR ≈ 34dB). It should be noted that as the bias applied to the integrated modulator section has been adjusted to optimise the signal quality for each transmission length, the penalty observed in Fig. 4.35(b) may appear exaggerated. For instance, the performance quoted for commercial devices typically involves optimising the applied bias for a certain transmission distance and comparing the resulting BER performance with the back-to-back measurement taken at the same bias. In this case, the penalty would appear smaller, but only because the back-to-back performance is not optimised. In addition, adjusting the

modulator bias for the exact distance in a real deployment scenario may not be feasible in large volume, low-cost transmitters, hence it is important to note that the results presented here simply serve to indicate the entire transmission performance capabilities of the transmitter. Nonetheless, based on these initial results, it is expected that future iterations of the integrated transmitter which incorporate an optimised modulator design to enable an improved output power will be capable of achieving error-free transmission in the absence of dispersion compensation for fibre lengths which encompass the typical physical reach targeted by current PON standards [172].

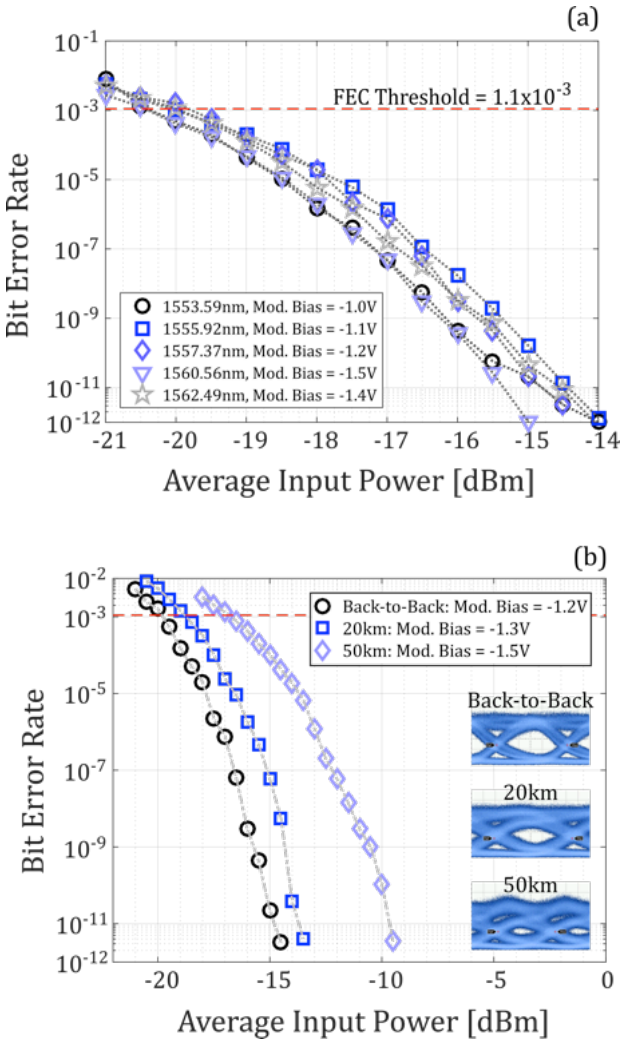


Figure 4.35: (a) Back-to-back transmission performance of 5 lasing modes using an optimised modulator bias, (b) transmission performance comparison at 1557.37nm optimised modulator bias [Back-to-Back, 20km, 50km].

4.6.6 Dynamic Wavelength Stability: Signal Modulation and Optical Burst Generation

To investigate the dynamic wavelength stability of the integrated transmitter, a time-resolved chirp measurement technique was employed using a programmable optical bandpass filter as a frequency discriminator as shown in the corresponding experimental setup which is presented in Fig. 4.37. The basic theoretical background for the measurement process is presented here; however, for a more detailed description the reader is referred to Appendix B which is expanded from [218].

Definition of Frequency Chirp:

The electric field of an intensity modulated optical signal can be denoted by

$$E_{in}(t) = \sqrt{P_{in}(t)}.e^{i\omega_c t}.e^{i\phi(t)} \tag{4.6.12}$$

where, P_{in} and ϕ represent slowly varying power and phase functions that can be associated with carrier-induced index changes and $\omega_c(t)$ represents the angular carrier frequency [rad/s]. The corresponding instantaneous frequency is given by the differential of the overall phase over time

$$\omega(t) = \frac{d}{dt}\left(\omega_c t + \phi\right) = \omega_c + \frac{d\phi}{dt} \tag{4.6.13}$$

The frequency chirp is then defined as the instantaneous frequency shift around ω_c in accordance with Eqn. 4.6.14

$$\Delta\omega = \frac{d\phi}{dt} \quad \Rightarrow \quad \Delta f = \frac{1}{2\pi}\frac{d\phi}{dt} \tag{4.6.14}$$

where, $\omega = 2\pi f$, with f representing the linear frequency [Hz].

Chirp Measurement Method:

In this experiment, a programmable optical filter based on high-resolution liquid-crystal-on-silicon (LCoS) technology was employed as a frequency discriminator with a transfer function, $H(\omega)$, designed to be linear in magnitude to the frequency, ω_p,

around the carrier frequency, ω_c, with a transmission amplitude T_0 and differential coefficient c_1:

$$H(\omega_p) = T_0[1 \pm c_1(\omega_p - \omega_c)] \tag{4.6.15}$$

As outlined in [218], c_1 is typically complex and dependent on frequency where the imaginary part gives the chromatic dispersion of the filter. However, in this work, the use of a programmable filter enables c_1 to be set as a real value that is defined by the frequency discriminator bandwidth ($f_{BW} = \omega_{BW}/2\pi$) which specifies the frequency range bounded by transmission values of 0.1 and 0.9 where the centre carrier frequency has a transmission of 0.5.

$$c_1 = \frac{0.9 - 0.1}{(0.5)2\pi f_{BW}} \tag{4.6.16}$$

This approach enables the sensitivity of the measurement to be adjusted in order to capture chirp traces with amplitudes ranging from a few GHz to approximately 100GHz. Consequently, by adjusting the filter profile, as shown in Fig. 4.36, two optical power waveforms P_+ and P_- can be obtained when the filter slope is positive and negative respectively. The derivation of these relations is presented within Appendix B.

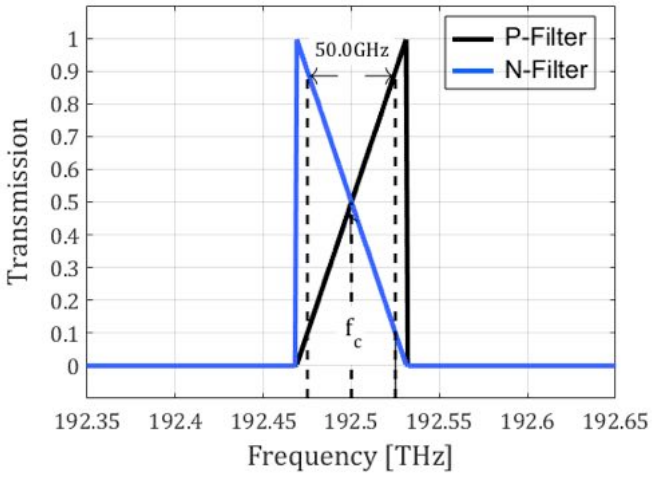


Figure 4.36: Optical filter profiles used for frequency discrimination [P-Filter: Filter with positive slope, N-Filter: Filter with negative slope].

$$P_+ \cong T_0^2 P_{in}\left(1 + 2c_1\frac{d\phi}{dt}\right) \tag{4.6.17}$$

$$P_- \cong T_0^2 P_{in}\left(1 - 2c_1\frac{d\phi}{dt}\right) \tag{4.6.18}$$

From Eqn. 4.6.17 and 4.6.17, two additional values can be obtained

$$P_{AM} = \frac{P_+ + P_-}{2} = T_0^2 P_{in} \tag{4.6.19}$$

$$P_{FM} = \frac{P_+ - P_-}{2} = 2T_0^2 P_{in} c_1 \frac{d\phi}{dt} \tag{4.6.20}$$

where, P_{AM} is the amplitude modulation, P_{FM} gives the power profile produced by carrier-induced frequency variations and P_{in} represents the optical power incident on the filter. The frequency chirp as specified in Eqn. 4.6.14 can then be derived as

$$\Delta\nu = \frac{1}{2\pi}\frac{d\phi}{dt} = \frac{1}{4\pi c_1}\frac{P_{FM}}{P_{AM}} \tag{4.6.21}$$

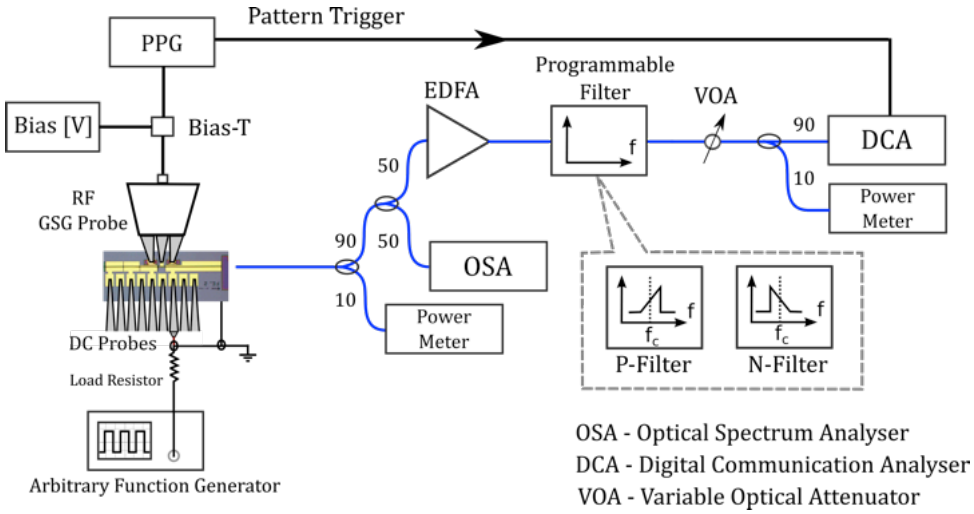


Figure 4.37: Experimental setup: Time-resolved chirp measurement using a programmable optical filter.

Chirp Contribution from the Modulator Section:

The chirp contribution from the modulator section was examined at 10Gb/s with NRZ-OOK modulation using two distinct data patterns. The first consisted of alternating 1's and 0's in order to examine the impact of high frequency data transitions on the carrier frequency while the second pattern contained a lower frequency content consisting of an alternating sequence of 64 1's followed by 64 0's. For example, the peak-to-peak chirp ($\Delta\nu_{pp}$) obtained from four different laser tuning settings using the high frequency test pattern are presented in Table 4.2. In each case, the reverse bias applied to the modulator has been set with the optimum value for back-to-back CM transmission while the voltage swing was set at ±500mV as this was found to provide the optimum ER as demonstrated in Fig. 4.34. The corresponding P_{AM} and chirp traces at a set centre frequency of 192.5THz (1557.36nm) are presented in Fig. 4.38 for an applied modulator bias of -1.2V. Notably, the chirp dynamics demonstrate positive frequency deviation at the leading edge of the pulse followed by a negative deviation on the trailing edge indicating that the chirp is positive for this value of reverse bias.

Peak Wavelength [nm]	Modulator Bias [V]	$\Delta\nu_{pp}$ [GHz]
1551.59	-1.0	3.45
1555.92	-1.1	2.99
1557.37	**-1.2**	**1.96**
1562.49	-1.4	3.69

Table 4.2: Chirp contribution from the modulator section using the high frequency NRZ-OOK test pattern.

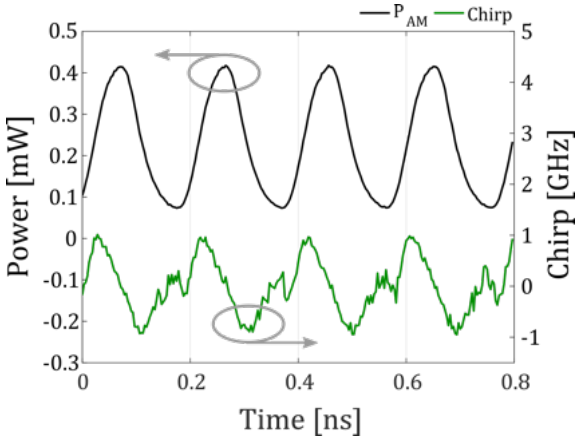


Figure 4.38: P_{AM} and chirp traces for 10G NRZ-OOK modulation using the high frequency test pattern for an applied modulator bias of -1.2V. [$\lambda_{peak} \approx$ 1557.37nm, SOA Bias = 30mA, ER ≈ 7.5dB]

The subsequent results obtained using the low frequency test pattern are presented in Fig. 4.39. Here, $\Delta\nu_{pp}$ is presented as a function of the applied modulator bias where the laser and SOA sections have been maintained at fixed values. In particular, there is an appreciable increase in $\Delta\nu_{pp}$ as the value of reverse bias applied to the modulator section is increased beyond -1.3V.

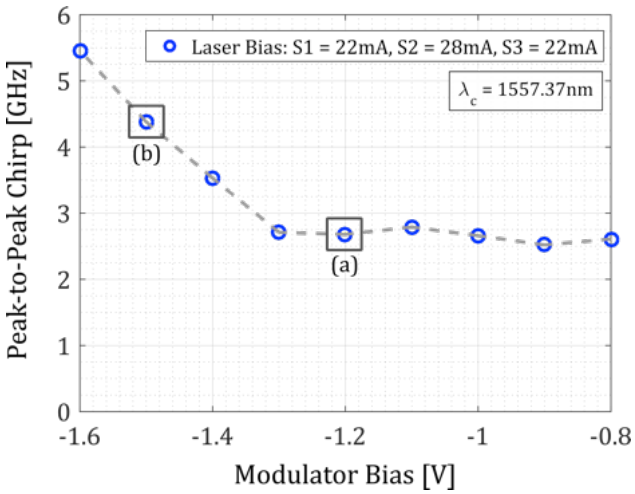


Figure 4.39: Peak-to-peak chirp contribution from the modulator section using the low frequency test pattern [61x1 + 64x0] for a fixed laser (22mA, 28mA, 22mA) and SOA Bias (30mA).

For comparison with the results presented in Fig. 4.38, the chirp trace obtained using the low frequency pattern for an applied modulator bias of -1.2V is presented in Fig. 4.40(a). From these results, it is evident that the chirp dynamics are more complex for the low frequency test pattern due to the presence of an adiabatic contribution which may be the result of optical feedback as discussed in Section 4.6.3. Nonetheless, the chirp dynamics clearly exhibit a negative frequency excursion at the trailing edge of each pulse which suggests a positive chirp as observed for the high frequency pattern at the same modulator bias. Alternately, for a larger modulator bias of -1.5V, as shown in Fig. 4.40(b), the chirp demonstrates a substantial negative frequency excursion at the leading edge of the pulse alongside a subtle positive deviation the trailing edge. Notably, this feature increases as the reverse bias is increased further, resulting in the trend observed in Fig. 4.39. This response also suggests that the sign of the chirp has flipped from positive to negative; however,

as a detailed analysis of the chirp dynamics falls beyond the scope of this work, this investigation is left for further study.

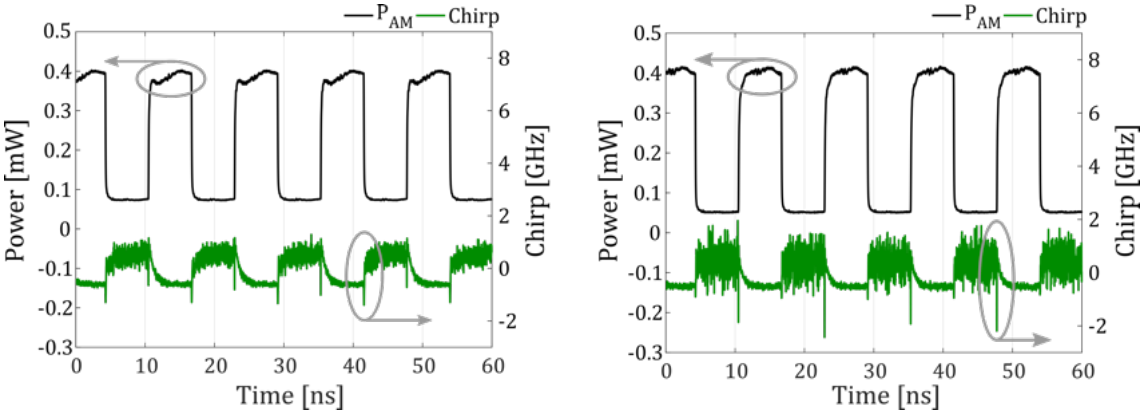


Figure 4.40: P_{AM}, P_{FM} and chirp traces for 10G NRZ-OOK modulation using the low frequency test pattern for an applied modulator bias of (a) -1.2V (ER = 7.5dB) and (b) -1.5V (ER = 9.1dB) [Laser Bias: S1 = 22mA, S2 = 28mA and S3 = 22mA ($\lambda_{peak} \approx$ 1557.37nm), SOA Bias = 30mA].

This behavior can be an advantageous as negatively chirped pulses undergo compression due to chromatic dispersion within standard SMF [219, 220]. In other words, pulses exhibiting the type of chirp demonstrated in Fig. 4.40(b) are desirable for networks requiring transmission over a longer physical reach. It is also important to note that this value of bias (-1.5V) corresponds to the setting required to optimise the signal performance for transmission over 50km of fibre in Fig. 4.35(b). Moreover, the observed peak-to-peak frequency deviation ($\leq$ 6GHz) is well within the maximum spectral excursion of ±12.5GHz targeted by current PON standards for systems employing a 50GHz channel spacing [172].

Carrier Frequency Deviation Induced By Dynamic Operation of the Integrated SOA:

For upstream transmission within a dynamic TDM-DWDM PON, each ONU is required to transmit data within an allocated timeslot in order to avoid data collisions over the shared network infrastructure. These packets of data can be successfully generated using an SOA to carve the required optical envelopes [19]. Compared

to other methods used to generate optical bursts, the use of a gating SOA has the advantage that the laser can be left in the on-state, which simplifies the problem of maintaining the wavelength stability. For instance, the main approach used to generate optical bursts within single-channel PONs involves gating the bias of directly modulated lasers (DMLs), however, this process introduces an appreciable frequency drift that is currently a significant performance limiting issue for the current multi-channel PON standards [140, 221].

The wavelength stability of the integrated transmitter for burst-mode operation was investigated using the time-resolved chirp measurement technique also used to examine variations in the unmodulated carrier frequency induced by the dynamic performance of the integrated SOA. As shown in Fig. 4.37, a programmable function generator (FG) was connected to the SOA section of the transmitter to facilitate the generation of the burst envelopes. In addition, a load resistance was connected in series with the SOA section in order to match the output impedance (50Ω) of the FG and maximise the power transfer to the device. The voltage-current (V-I) profile obtained from the SOA section under different operating conditions is presented in Fig. 4.41.

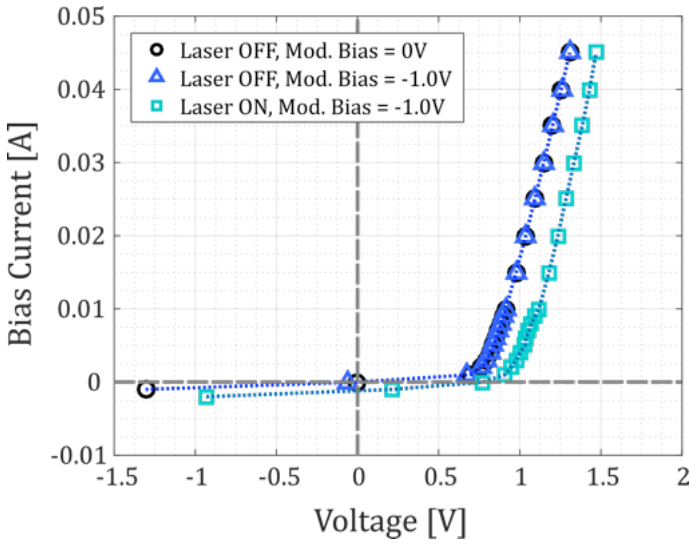


Figure 4.41: V-I Profile of the integrated SOA section demonstrating a thermally induced threshold shift with injected light at 1556.51nm [Laser Bias = 25mA,30mA, 40mA].

These results show that with injected light, the threshold voltage of the SOA section is increased from roughly 650mV to approximately 800mV due to depletion of the

excited carrier density by stimulated emission and an appreciable thermal influence that can be attributed to the laser section. It is also important to note that the reverse bias applied to the modulator section did not have an observable impact on the V-I profile of the neighboring SOA section and hence we can assume that there is negligible electrical crosstalk between these components. The voltages applied to the SOA in order to generate the burst envelopes were 1.33V (V_{High}) and -0.9V (V_{Low}). The value of V_{High} was chosen as it corresponds to a bias current of 30mA which provided the best trade-off between SMSR and output power during the DC characterisation while the value of V_{Low} was chosen in an attempt to maximise the on/off power ratio of the SOA section through the application of a reverse bias. For DC operation, the extinction provided by the SOA section under these bias conditions was measured to be approximately 27dB. For the purpose of this analysis, a square wave signal with a rise/fall time of 5ns and a duty cycle of 50% was applied to the SOA section and its frequency was varied coarsely from 100Hz to 100kHz. While it should be recognised that these gating conditions are unlikely to occur in a real deployment scenario, they represent extreme cases that can help in analysing the internal behavior of the transmitter. The corresponding deviation of the carrier frequency was measured using optical filters similar to that presented in Fig. 4.36. However, for these measurements the passband (f_{BW}) was increased to 100GHz.

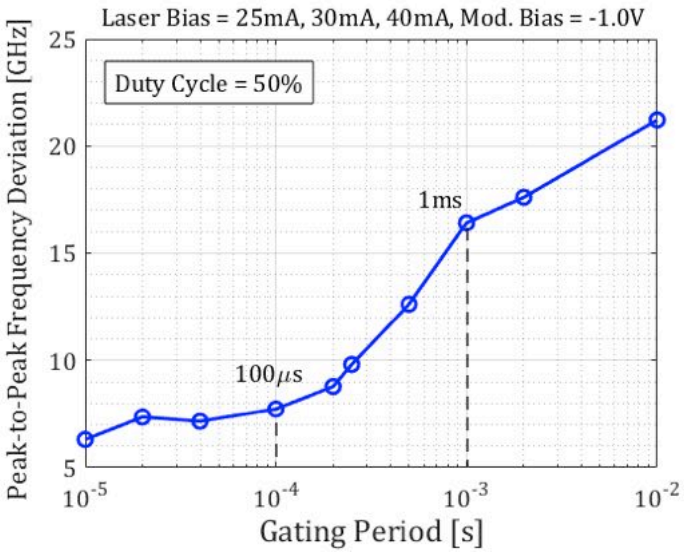


Figure 4.42: Peak-to-peak carrier frequency deviation induced by a square-wave gating signal with a 50% duty cycle applied to the SOA Section. ($\lambda_c \approx 1556.51$nm)

The measured peak-to-peak frequency deviation is presented in Fig. 4.42 as a function of the applied SOA gating frequency. This data indicates that the deviation is fairly constant (< 8GHz) for gating frequencies above 10kHz which is comparable with typical burst durations of 125μs as required by current PON standards [140]. However, as the gating frequency is decreased the carrier frequency deviation begins to increase rapidly reaching a value of approximately 22GHz for a gating frequency of 100Hz. This trend is in line with the assumption that thermal crosstalk associated with the bias applied to the SOA section can be significant enough to perturb the set carrier frequency as initially presented in Fig. 4.32, which examined the wavelength stability of the transmitter for a constant SOA bias. However, the timescales of the heat transfer between the SOA and the laser sections are extremely important in order to understand the dynamic operation of this monolithically integrated transmitter. For instance, as shown in Fig. 4.43, the frequency deviation presents fast transients at the leading and trailing edges of the gating signal with timescales below 1μs for burst durations up to around 50μs. We believe that this fast wavelength deviation might not be related to heat transfer, which is usually a slower effect, and might be due to the residual cavity interaction between the SOA and the laser. For bursts durations above 100μs the heat transfer becomes the dominant factor causing the large wavelength deviations measured dynamically in Fig. 4.42 and statically in Fig. 4.32.

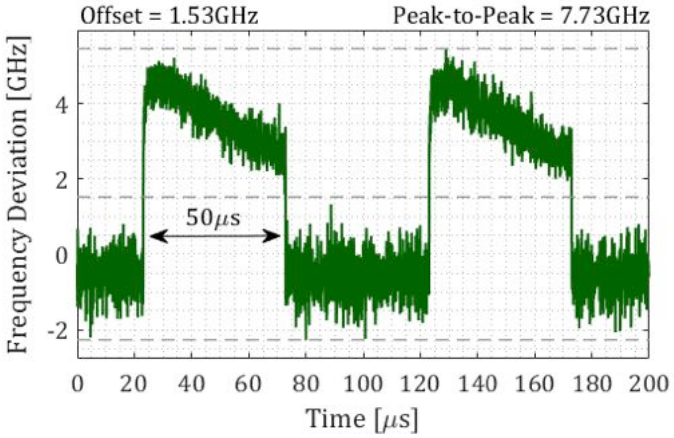


Figure 4.43: Frequency deviation induced by a 10kHz square-wave signal with a 50% duty cycle applied to the SOA section. [Centre filter frequency = 192.605THz (1556.51nm), f_{BW} = 100GHz]

These results suggest that for typical PON burst durations of up to 125μs, the heat generated by the SOA section in the ON state does not have the time to transfer substantially into the laser section, maintaining a relatively small wavelength drift of around 8GHz. This is an interesting result as it represents a highly desirable feature for low-cost tuneable transmitters for use in wavelength agile PONs and shows the advantages of an integrated transmitter employing a separate SOA section to perform the burst gating function. Moreover, directly modulated lasers (DMLs) which are presently of high interest for deployment in ONU transmitters of next-generation PONs have been shown to exhibit an appreciable burst-mode induced frequency drift of up to 62GHz for burst durations of 128μs [221]. Nonetheless, further investigations are essential in order to better understand the heat transfer in the proposed integrated structure in order to improve the overall performance of this device in future iterations.

4.6.7 Overview of the Monolithically Integrated Transmitter

This section has outlined the initial progress towards developing a potentially low-cost monolithically integrated tuneable 10G transmitter consisting of a slotted Fabry-Pérot laser, an absorptive modulator and an SOA targeted for deployment within the ONUs of wavelength-agile PONs. The transmitter structure is primarily driven by the substantial cost savings that can be achieved through the use of efficient re-growth free fabrication techniques that facilitate monolithic integration, by defining lithographically the various components.

This tuneable transmitter was developed by the III-V Materials and Devices Group of the Tyndall National Institute using an 'off-the-shelf' AlInGaAs/InP MQW structure on an n-doped substrate and following a coarse calibration it demonstrated a discrete single-mode tuning range of approximately 12nm between 1551 and 1563nm with an SMSR $\geq$ 30dB. Using an external amplifier to counteract the excess insertion loss introduced by the trial modulator structure and the fibre coupling loss attributed to the experimental setup, error-free (BER $\leq$ 1E-12) transmission was achieved using NRZ-OOK modulation at 10Gb/s with a PRBS-7 pattern for fibre lengths up to 50km which encompasses the physical reach targeted by the latest PON standards. Furthermore, in order to determine the inherent wavelength stability of

the transmitter, a time-resolved chirp measurement technique was used to examine deviations in the set carrier frequency induced by modulation and the dynamic operation of the integrated SOA section. Notably, the modulator section demonstrated a chirp contribution of < 6GHz for NRZ-OOK modulation at 10Gb/s using test patterns with high and low frequency content. Furthermore, the application of a gating function to the SOA section to emulate the generation of optical bursts was found to shift the unmodulated carrier frequency of a typical lasing mode by ≤ 8GHz when the gating period was comparable with typical PON bursts durations of 125μs which is faster than the thermal response time of the transmitter material. These recorded values are significantly better than those currently achievable from ONU transmitters utilising DMLs in the absence of active chirp compensation [124]; however, despite the challenges facing future iterations of this device, the experimental results presented in this work ultimately serve to highlight the advantages offered by monolithic integration coupled with low-cost, re-growth-free fabrication processes.

4.7 Summary and Conclusions

The work presented in this chapter has motivated and addressed the main challenges facing the realisation of low-cost tuneable lasers for use within the optical network units of wavelength-agile PONs. In particular, driven by the potential for appreciable cost savings through an increased yield, a lower power consumption and simplified fabrication processes, two innovative tuneable laser technologies including a MEMS-VCSEL and a monolithically integrated 3s-SFP laser were examined in detail.

Having been assigned the task of characterising and assessing the transmission performance of unpackaged, widely-tuneable MEMS-VCSELs developed and fabricated by our project partners in the EU project SUBTUNE [179], the primary contribution of this work was the recognition and evaluation of the wavelength instability attributed to the flexible surface DBR membrane. This undesirable behaviour which may have multiple sources including the release of material stress was shown to severely compromise the integrity of the set transmission wavelength; hence, a LabVIEW-based feedback loop using an optical spectrum analyser was developed to actively control the output wavelength. Subsequently, having successfully stablised

the set wavelength to ≤ ±0.25nm (≤ ± 31.25GHz), the transmission performance of the MEMS-VCSEL was examined through external intensity modulation at 10Gb/s using an R-EAM-SOA. Notably, the wavelength-stabilised unpackaged VCSEL compared favourably with that of a commercial ECL for fibre lengths up to 50km which encompass the physical reach targeted by the latest PON standards [140].

Alternatively, a detailed investigation was carried out on an unpackaged prototype transmitter developed by the III-V Materials and Devices Group of the Tyndall National Institute as part of the DISCUS project. The potentially low-cost transmitter was comprised of a single-growth monolithically integrated discretely tuneable 3s-SFP laser, a 10G-capable absorption modulator and an SOA. Notably, the device demonstrated a discrete tuning range of roughly 12nm (1551- 1563nm) with an SMSR ≥ 30dB alongside an achievable extinction ratio in excess of 8dB under intensity modulation at 10Gb/s using NRZ-OOK. However, the key contribution from this work involved the evaluation of the inherent wavelength stability of the transmitter under dynamic operation (e.g. modulation and optical burst generation). This analysis was accomplished using an innovative time-resolved chirp measurement technique (outlined in Appendix B) which used a programmable optical filter as a frequency discriminator in order to allow for adjustment of the measurement sensitivity.

Notably, the chirp measurements demonstrated that the integrated transmitter exhibited an appreciable level of inherent wavelength stability under NRZ-OOK modulation at 10Gb/s (≤6GHz) and optical burst generation (≤8GHz) for packet lengths comparable to that required by the latest PON standards [222]. For instance, the results obtained for the former case which are presented in section 4.6.6 serve to validate the use of external modulation in order to facilitate 10Gb/s transmission over distances targeted by LR-PONs (i.e. ~ 100km). In addition, the measured level of wavelength deviation induced for optical burst generation achieved by applying a gating function to the integrated SOA is particularly noteworthy. For example, the results presented in section 4.6.6 highlight the advantage of monolithic integration over alternative technologies such as DMLs where the process of self-heating can result in substantial shifts in the carrier frequency [221].

5

Physical Layer Design and Subsystem Analysis

This chapter presents the physical layer design strategy and subsystem analysis for the optical access architectures proposed under the European Framework 7 (FP7) Integrated Project (IP) DISCUS. The main objectives of this work are to address the principal design guidelines of the physical layer which targets the development of novel end-to-end optical access architecture based on dynamic TDM-DWDM LR-PON in order to deliver ubiquitous broadband irrespective of geographic location.

In section 5.1, the chapter begins with an overview of the physical layer design proposed by the DISCUS project whose respective feasibility is examined using a linear power and OSNR model which is described in Appendix C. This model is used to estimate the achievable physical reach and split for the respective architectures using optical amplifier gain as the main processing variable. Subsequently, section 5.2 examines the amplification strategy required to support the nominated architectures. In particular, commercial erbium-doped fibre amplifiers (EDFAs) with active gain stabilisation are examined in section 5.3 to assess their ability to support dynamic traffic from optical distribution networks supporting at least 40 (bidirectional) dense wavelength division multiplexed (DWDM) channels. Finally, section 5.4 presents the key enabling burst-mode subsystems realised for the DISCUS experimental test-bed which include a 10G-capable linear burst-mode receiver (LBMRx) and forward error correction (FEC) that has been implemented using field programmable gate arrays (FPGAs). In particular, the performance of the FPGA-based FEC algorithm is tested in section 5.4.4 by measuring the pre- and post-FEC BER as a function of the relative delay and amplitude of emulated residual EDFA transients with respect to incident optical bursts.

5.1 Physical Layer Design Strategy

The fundamental design strategy adopted by the DISCUS project was to exploit the two fundamental advantages of optical technology: (i) the potential to offer a large bandwidth and (ii) the ability to supply this over long distances to all parts of the network. When this approach is applied to the access network, the outcome specifies an architecture that is long enough to directly reach the core nodes. With this in mind, the following sections present the LR-PON configurations considered by DISCUS with the objective of economically bridging the ever growing digital divide between densely populated urban areas and sparse rural communities.

5.1.1 Urban Access: The 'Tree-Structured' LR-PON

The architecture proposed for deployment in urban areas is shown schematically in Fig. 5.1. This tree-structured (or "lollipop") configuration is similar to the systems previously demonstrated by researchers at British Telecom (BT) [223], the Photonic Systems Group in University College Cork [17] and the EU project PIEMAN [13]. In particular, the architecture is based on a single amplifier node (AN) which targets a total physical reach $\geq$ 100km and a split $>$ 500 within the optical distribution network (ODN). Moreover, the proposed configuration utilises two-fibre-working in the backhaul section where separate fibre links are used for downstream (DS) and upstream (US) transmission. In addition, a distance of $\geq$ 80km between the metro/core (M/C) node and the AN located at a strategically selected local exchange (LE) site allows for dual parenting of the local exchange as a protection scheme by accounting for distances representative of a realistic geographical distribution [224].

On the other hand, single-fibre-working is deployed within the ODN ($\leq$ 20km) to minimise infrastructure deployment by facilitating bi-directional transmission. Notably, this approach has become the conventional practice for FTTP networks as optimal sharing of minimal infrastructure presents an obvious economic advantage. For instance, the size and location of the splitter closest to the customer premises has a direct impact on utilisation and the ODN costs. As a result, the LR-PON concept illustrated in Fig. 5.1 for dense urban areas would typically target 32-way splitters at the drop point (DP) location with 4-way splitters employed at the primary-cross-connect point (PCP) while at the addition of a 4x4 star coupler at LE site gives the total split of 512. Moreover, by locating the first splitting stage of the ODN within

the AN, a resiliency connection for the backhaul section can be established with a back-up M/C node to facilitate a loop-back path to the primary node in the event of a failure such as a fibre break.

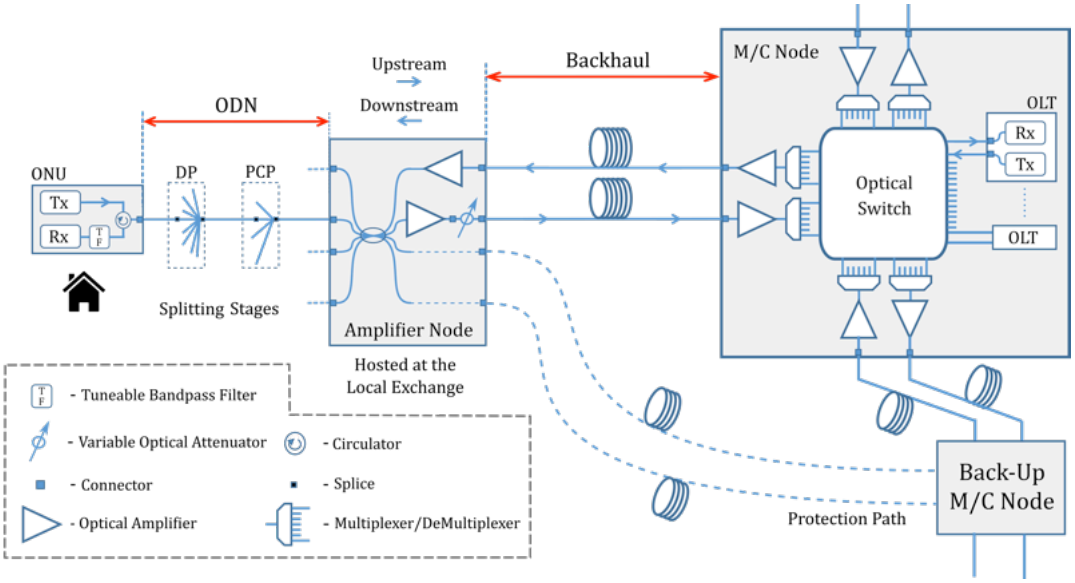


Figure 5.1: Tree-structured LR-PON physical layer proposed for urban areas.

The LR-PON configuration presented in Fig. 5.1 has been used as an example to calculate the US and DS power and OSNR budget presented in Fig. 5.2, the details of which can be found in Appendix C. In particular, the model has been used to examine the feasibility of a LR-PON with a physical reach of 100km which is comprised of an 80km backhaul section, a 20km ODN and a total split of 512. To support these physical layer targets, multi-channel erbium-doped fibre amplifiers (EDFAs) are an obvious candidate due to their high gain capabilities (30-40dB), inherently low noise figure (typically 5-6 dB for commercial modules), moderate cost and off-the-shelf availability. EDFAs also have the advantage of being mature components in optical networks which makes them attractive for deployment in an access scenario [225]; however, it should be noted that the useable spectrum is limited to the C and L bands (i.e. 1520nm - 1620nm).

Another crucial aspect of the amplifiers used in the US links is that they need to operate with high dynamic range burst signals. Today's EDFAs are typically designed to operate with continuous traffic in conventional metro and core networks. However, for access applications, the power ratio of US bursts arriving from an ODN with a large differential loss has the potential to generate significant am-

plitude distortions due to saturation-induced gain transients. These transients can compromise the transmission performance in single-channel or multichannel systems unless suitable mitigation strategies are employed [226, 227]. With this in mind, the requirement to support dynamic channel reconfiguration in WDM networks containing reconfigurable optical add and drop multiplexers (ROADMs), has driven recent developments in EDFA transient control circuitry [228] that may also provide a solution for supporting burst-mode traffic in the proposed DISCUS architectures.

The power and OSNR budgets presented in this work are calculated under the assumption that the linear burst-mode receiver (LBMRx) technology developed by the Photonics Systems Group of the Tyndall National Institute will be employed within the optical line terminal (OLT) [146]. The LBMRx requires 15dB OSNR at a dynamic range of 20dB to achieve BER $\approx 10^{-3}$ at 10Gb/s which enables restoration of the signal quality to a BER $\leq 10^{-12}$ when applying forward error correction (FEC) [145]. Burst-mode electronic dispersion compensation (EDC) is also assumed [144] to compensate for chromatic dispersion on the fibre lengths considered here. Therefore, in this initial study we have used 15dB as the minimum (end-of-life) OSNR target for US transmission. Moreover, in this case and in all following cases (unless otherwise stated), all distribution arms are investigated in terms of losses, optical amplifier input powers and OSNR figures.

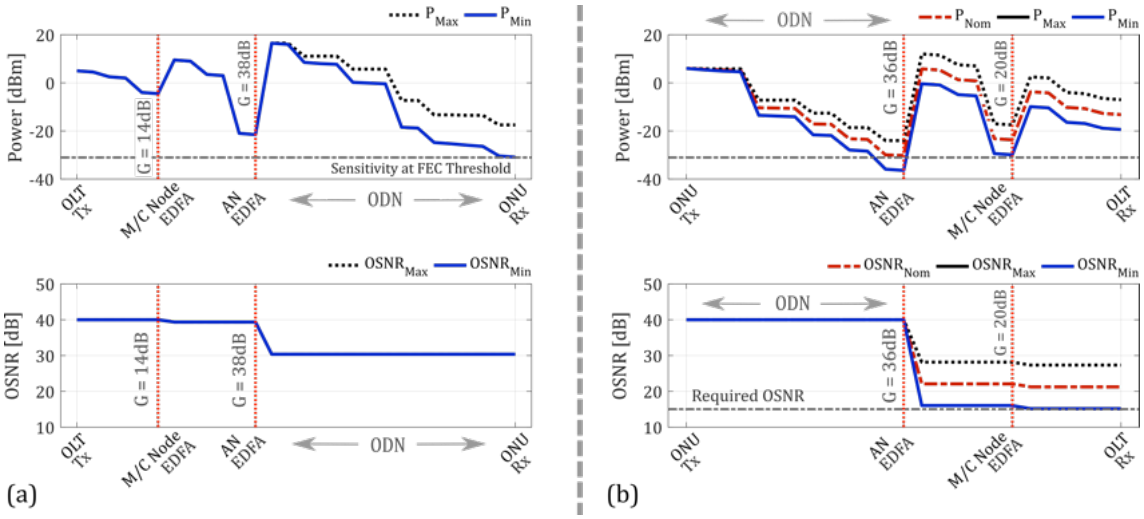


Figure 5.2: (a) Downstream and (b) upstream optical power and OSNR budget for the proposed urban 'tree-structured' architecture (Physical Reach = 100km, Split = 512).

The results presented in Fig. 5.2(a) indicate that the system performance in the DS direction is expected to be mainly limited by the low power arriving at the ONU receiver, rather than OSNR degradation. For instance, in order to overcome the high loss of the ODN (20km, 512-split), the DS amplifier requires a gain of 38dB launching approximately +16.5dBm of power per-channel (representative of the typical achievable values if SBS mitigation techniques are employed [13]) to achieve a worst-case incident power at the ONU-Rx of approximately -31dBm. Although this required launch power is quite high, the first splitting stage of the ODN which is located within the AN (x4,IL ≈7dB) serves to reduce the non-linearity concerns such that the minimum per-channel power launched into the distribution fibre is roughly +8dBm. In addition, it is expected that a band filter (IL ≈1.5dB) may also be required at the output of the EDFA in order to remove the out-of-band ASE which may interfere with the US signals through back-reflections. While this inclusion would lower the achievable power margin at the ONU-Rx, it would also serve to further reduce any signal degradation attributed to nonlinear impairments. It is also important to note that the required launch power from the DS amplifier is continuous, hence, there are no statistical averaging effects. As a result, the total aggregate launch power needed to support a system with 40 channels is approximately +32.5dBm. This value is larger than most widely-deployed amplifiers today, however, considering that it does not require fast gain stabilisation, it is achievable. Moreover, the cost of such an EDFA would be shared by all users of the network. Furthermore, while it is evident that the worst-case received power at the ONU is quite low (≈ -31dBm), it may be possible to support such a link through the use of an APD-based ONU-Rx whose sensitivity can support a BER below the targeted FEC threshold of 1.1×10^{-3} [80].

Conversely, the results presented in Fig. 5.2(b) suggest that the US link is primarily OSNR limited. This limitation can come from both the ODN, where there is a large loss due to the high split from the backhaul section where fibre lengths of 80km can also introduce considerable loss before the amplifier in the M/C node. In addition, based on the modelling parameters used, the non-uniform loss in the ODN presents a burst-to-burst dynamic range (DR) that could be up to 12.5dB for a 512-split. This means that, while the majority of the channels present instantaneously an average nominal power (P_{Nom}) which lies in the middle of the DR, there is the possibility that some channels present the highest power in the dynamic range.

However, due to statistical multiplexing, it is very unlikely that all channels will present the maximum burst power, so it may be possible to use EDFAs with a lower aggregate output power. Nonetheless, careful design of the gain and consideration of the NF of both amplifiers is necessary in order to maintain the OSNR above the minimum required value of 15dB. For instance, in this US case study, optical amplifiers with a 5.5dB noise figure and a gain of approximately 36dB and 20dB are required for the AN and the M/C node amplifiers respectively. It should be noted that although the per-channel launch power from the AN amplifier is relatively high ($\approx$ +12dBm), a variable optical attenuator (VOA) has been included to mitigate the actuation of non-linear impairments in the 80km backhaul link.

Overall, the results of the power and OSNR model indicate that the proposed physical layer for densely populated urban areas can support a split of 512 with a total physical reach of 100km in both transmission directions. However, in the worst-case scenario which sees the maximum path loss there is negligible margin.

5.1.2 Rural Access: The 'Open-Ring' Architecture

A major area where DISCUS goes beyond the state-of-the-art of previous projects is to tackle up front the issue of the digital divide, where current broadband roll out and performance favours citizens living in dense urban areas and neglects those living in sparse rural regions. For instance, while the tree-structured model (similar to that shown in Fig. 5.1) has been shown to work well for urban areas it is not optimal for rural communities where the splitting portion of the network needs to be distributed over larger geographical areas. In fact, the primary difficulty for fibre deployment in rural zones is that the communities to be served can be much smaller than the total achievable split which would mean that conventional LR-PON designs can be considerably underutilised which leads directly to an increased cost per customer. Moreover, the longer distances required between splitter nodes and customers requiring extended cable lengths with a higher fibre count increases the costs even further. Consequently, a central focus in DISCUS was therefore to develop alternative physical layer designs and fibre splitter layouts that improve the utilisation, reduce costs and are more suitable for deployment these regions.

To account for these physical layer challenges, the architecture proposed within DISCUS for rural fibre deployment is based on a ring configuration that has been

inspired by the topology of today's metro networks. This 'open-ring' LR-PON configuration which is dual-parented on two geographically separated M/C nodes of a flat optical core employs two fibre paths with counter-propagating traffic to connect a chain of ANs. Each AN is located at a strategically selected LE site with access to electrical power which maintain full wavelength availability while supporting a single fibre-working ODN carrying both US and DS wavelength bands in all distribution fibres. The main advantage of this configuration is that it distributes the overall customers between multiple nodes in order to efficiently achieve a lower density of customers ports. Moreover, this architecture has the added benefit of directly reusing deployed fibre while in the event of a fibre cut or of a failure in the primary M/C node (or in an AN), the traffic can be routed to the protection M/C node, hence providing the same intrinsic resilience as metro ring networks.

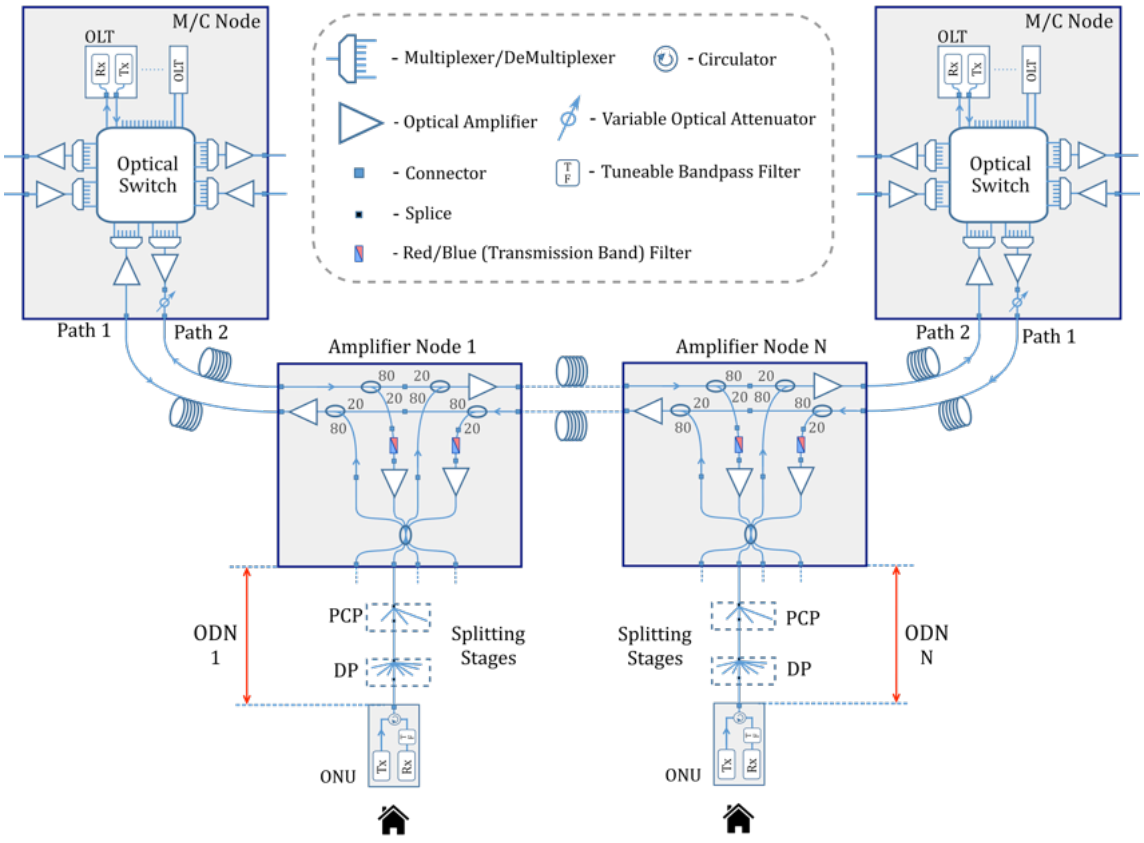


Figure 5.3: Alternative LR-PON 'open-ring' architecture proposed for rural areas.

As shown in Fig. 5.3, in order to provide access to the primary and protection paths, part of the total ODN split (4x4) is employed within each AN connecting two DS drop ports and two US add ports. As a result, each AN requires four optical amplifiers; two are located after the US add points to compensate for the ODN loss and to boost the signals prior to transmission towards the next AN while the other two amplifiers are located after the DS drop ports in order to boost the power of the DS channels before entering the high-loss ODNs.

The entry points for the US channels consist of 1x2 couplers with an asymmetric 80/20 coupling ratio in order to help the power budget by reducing the add loss (80% port introduces ~1dB) in the US direction. Similarly, the exit ports from the open-ring fibres for the DS channels also utilise 1x2 asymmetric 80/20 splitters where the 20% port is used to drop the DS channels towards the ODN while the lower loss 80% port is used to minimise the loss of the path forwarded to the next node. Moreover, in the path of the DS channels dropped towards the ODNs, a band filter is required to remove the US channels added by previous nodes, as their presence would waste the achievable output power of the DS amplifier while they may also interfere with local US traffic due to Rayleigh backscattering and reflections in the ODNs. It should be recognised that although there is wavelength mixing between US wavelengths from the local ODN and the ODN of the preceding ANs, there will be no US wavelength collisions as they are avoided through deployment of an appropriate TDMA protocol. For instance, in the open-ring configuration, all the ANs in the chain form a single LR-PON controlled by a single instance of the protocol where only 1 ONU is transmitting an US burst at any instant of time. Finally, although they are not explicitly shown in the figure, power and management units would also be required in this design and the management unit could communicate with the M/C node using an ONU. Notably, this is also true for the urban LR-PON architecture.

To examine the initial feasibility of the 'open-ring' configuration, the power and OSNR budget was calculated for an architecture similar to that presented in Fig. 5.3; however, the system under investigation was designed with four chained ANs, each separated by 30km of fibre supporting an ODN with a physical reach of 20km consisting of 128 users (4x2x16) giving a total of 512 users (128x4). In addition, the modelled AN chain is supported by a 10km feeder fibre which connects to the primary M/C node resulting in a total physical reach of 120km. For the purpose of

this analysis the US and DS performances have been calculated for an ONU located in the ODN of the fourth AN which is the furthest from the primary M/C node and hence the respective signal propagates through the largest number of amplifiers. Moreover, the gain of the in-line amplifiers are set to compensate for the loss in the fibre and components of each link between the ANs, which in this case for a 30km fibre link is approximately 20dB.

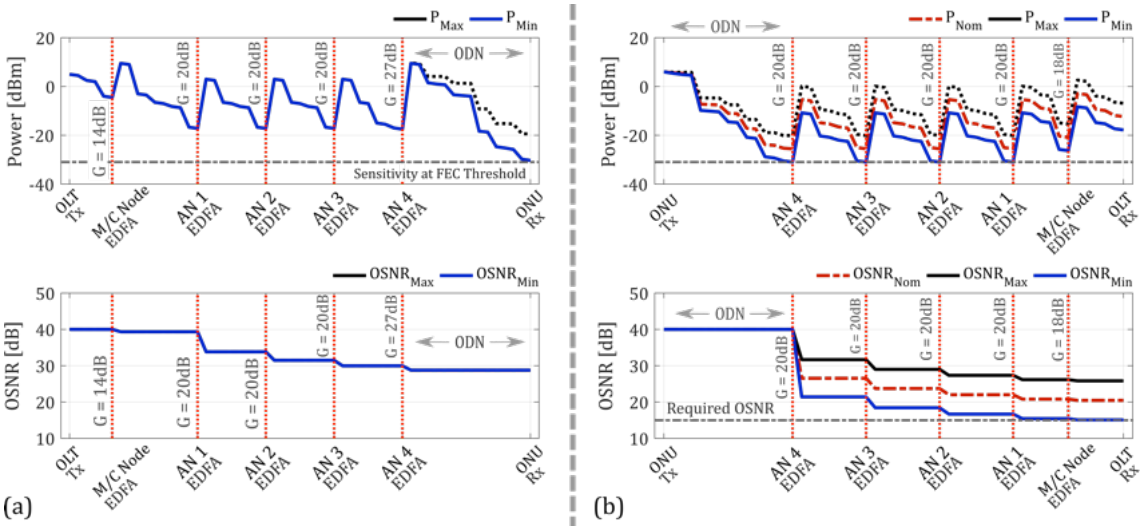


Figure 5.4: (a) Downstream and (b) upstream optical power and OSNR budget for the proposed rural 'open-ring' architecture for a physical reach of 120km and a total split of 512 supported by 4 chained amplifier nodes spaced by 30km.

As shown in Fig. 5.4(a), the maximum per-channel launch power from each in-line amplifier in the DS link is calculated as +3dBm which corresponds to an aggregate power of +19dBm for a system comprised of 40 channels which is well within the power range available for commercial EDFAs. Nonetheless, the primary limiting factor in the DS link is the relatively low optical power available at the ONU-Rx which is attributed to the high loss of the ODN. Consequently, the booster EDFA at the drop point of AN 4 must be capable of supplying a gain of at least 27dB and a total average power of approximately +25.5dBm in order to launch a per-channel power of +9.5dBm. This will ensure a minimum power of roughly -30dBm at the ONU-Rx in the worst-case scenario which can be supported using an APD-based ONU-Rx and FEC.

Alternately, in the US direction, Fig. 5.4(b), the maximum per-channel output power is approximately 0dBm, which translates to a total output power of +16dBm for a 40 channel system. While this is an achievable aggregate power, statistical considerations can be used to account for the nature of the burst-mode traffic such that the total output power of the chained EDFAs can be designed around the nominal channel power, which in this case is around -5.4dBm. As a result, the total (mean) output power required for each in-line amplifier would then be roughly +10.6dBm, which is well within the power range available for commercial fast gain-stabilised EDFAs. Nonetheless, as these amplifiers carry both US and DS traffic, they must be dimensioned for both up- and downstream channels. For instance, within the specific case analysed here, the mean DS channel output power is ~8.4dB higher than the nominal US channel power, hence, the total aggregate output power for 40 channels up- and down-stream is around +19.6dBm, which is also within the power range available for commercial fast gain-stabilised EDFAs. Another key consideration is that the in-line amplifiers carrying the live DS could suffer from residual gain transients induced by the dynamic nature of the US channels, however, it is expected that the continuous behaviour of the DS channels will clamp the available optical gain thus mitigating this effect.

Finally, it is evident that the primary cost-penalty of the open-ring architecture compared to the tree-structured model proposed for urban access is due to the higher number of amplifiers per customer due to the smaller split of each ODN. As a result, the number of chained ANs should be kept as low as necessary in order to serve the targeted rural area. Nonetheless, the feeder fibre and inter-node fibres remain highly shared as with the urban model, therefore, they should not add significantly to the cost per customer. Furthermore, due to the distributed amplification scheme, a lower output power is required from the amplifiers which could be highly advantageous if cheaper, lower power, optical amplifiers can be employed. However, while the ODN split and physical reach can be traded off where each factor of two reduction in split can provide ~10km increase in the physical reach. Moreover, the longest path length from an M/C node through the chain to the furthest ONU is kept less than 125km as increasing the round trip delay time while meeting XG-PON delay targets may add significantly to PON overheads and reduce payload efficiency. Similarly, the total split across all aggregated ODNs in the chain is limited to ≤ 1024, hence, it is expected that there will be no more than three or four amplifier nodes per chain.

5.2 Optical Amplification Scheme

Following the power and OSNR budget analysis, it is clear that the optical amplifiers are key enabling technologies for the LE and M/C nodes which must be carefully designed in order to support the long reach and the high number of users targeted by the DISCUS architecture [8]. In particular, a key parameter of the amplifiers is the NF which must be as low as possible in order to maintain the OSNR of the US link within acceptable levels. Moreover, the amplifier technology must also provide a high gain and high output power in order to overcome the high splitting loss of the distribution network and the link loss in the backhaul section of the long reach passive optical network (LR-PON). As in conventional metro DWDM network design, the preferred option to minimise cost and operational complexity would be to use a single multi-channel amplifier for each direction in the AN if feasible. For this reason, the remainder of this chapter is focussed on investigating the suitability of modern EDFA technology for deployment in dynamically reconfigurable LR-PONs.

Amplifier Node Specifications:

Table 5.1 summarises the specifications of the amplifiers required for the ANs of both proposed LR-PON architectures. The exact specifications are relative to the configurations analysed in the previous section using the power and OSNR model presented in Appendix C.

	Gain [dB]	**NF [dB]**	**Total Output Power [dBm]**
Urban Configuration			
Downstream	38	5.5	+32.5
Upstream	36	5.5	+28
Rural Configuration			
Inline Amplifiers	20	5.5	+19.6
Downstream Drop Amplifier (AN 4)	27	5.5	+25.5

Table 5.1: Specifications for the amplifier nodes required for the proposed urban and rural LR-PON configurations based on the results of the power and OSNR model.

5.2.1 Erbium-doped Fibre Amplifiers

Since their realisation in 1987, EDFAs have revolutionised optical communications [229]. Their ability to provide large optical gain (> 20dB) which is independent of the data rate alongside a relatively low noise figure (< 6 dB) and a high polarisation insensitivity across the C-band (1530-1565nm) has been studied extensively and used alongside wavelength-division multiplexing (WDM) technology to establish high-capacity, long-reach optical networks.

In its simplest form, an EDFA consists of a silica glass host in the form of a single-mode fibre core which has been doped (~ 1%) with active Er^{3+} ions that can be optically pumped using semiconductor lasers at 980nm or 1480nm [230, 231] to establish a gain medium which is typically shorter than 50m. Notably, the pump light can be combined in the same direction as the signal (co-propagating) or opposite to the signal direction (counter-propagating) using a wavelength selective coupler (often referred to as a wavelength division multiplexer or WDM). The reason to use a WDM combiner instead of a simple optical coupler is to reduce the combination loss. Finally, in order to prevent oscillations and excess noise due to unwanted reflections in the assembly, optical isolators are included at either side of the gain medium as shown in Fig. 5.5.

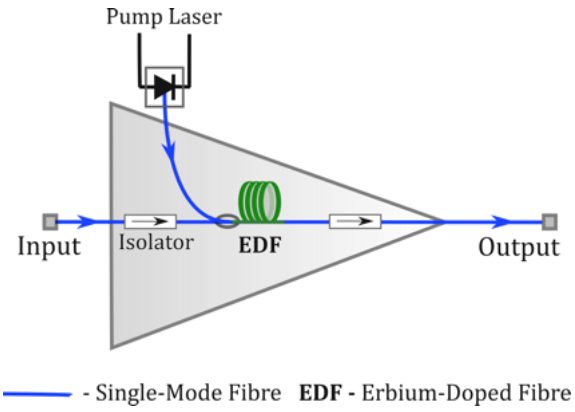


Figure 5.5: Illustration of a single-stage (forward pumped) erbium-doped fibre amplifier.

Principle of Operation:

The energy levels and associated spontaneous lifetime of an Er^{3+}-doped fibre are illustrated in Fig. 5.6. Notably, the surrounding crystalline field causes a Stark

splitting of the Er^{3+} orbitals while site-to-site variations of the field due to the amorphous nature of the glass results in an inhomogeneous broadening of the transition bands. This property allows for pumping at a wavelength near 1480nm in order to excite the erbium ions directly to the metastable $I^4_{13/2}$ state which enables amplification in the spectral range from 1525nm to 1570nm. Alternately, the $I^4_{13/2}$ state can also be populated by erbium ions having undergone a non-radiative transition (e.g. heat generation) from the $I^4_{11/2}$ state following excitation by photons of light around 980nm. Subsequently, amplification occurs when the excited state ions decay from the metastable state back to a lower energy level via stimulated emission of photons at the signal wavelength. However, the excited state ions also decay spontaneously with the generation of photons that subsequently undergo amplification via stimulated emission to generate amplified spontaneous emission (ASE). As outlined in Chapter 2, ASE serves to degrade the optical signal-to-noise ratio (OSNR) which can impair the signal performance at the receiver; hence, a low noise figure (NF) is desirable. Nonetheless, the excited erbium ions can also decay to a lower energy level through non-radiative mechanisms which involve interactions with phonons of the glass, thus, reducing the efficiency of the amplification process.

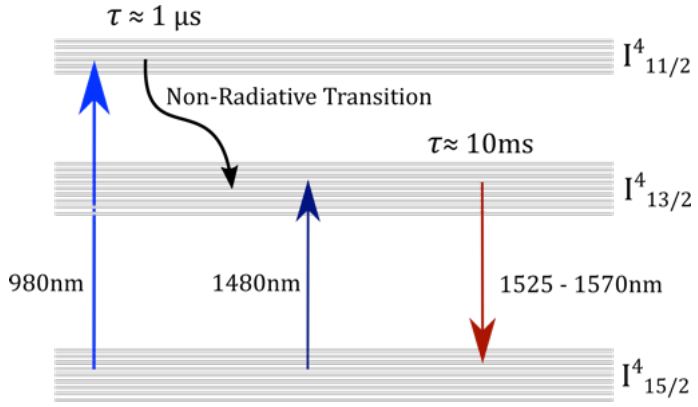


Figure 5.6: Illustration of the energy level structure of Er^{3+} ions in a glass host.

The success of EDFAs can be attributed to the commercial availability of reliable pump lasers whose output power is enough to stimulate gain from the medium. In fact, the wavelength of the pump ultimately determines the performance of the EDFA. For instance, as the carrier lifetime in the metastable state, $I^4_{13/2}$, is on the

order of 10ms (which is four orders of magnitude longer than the carrier lifetime in the $I^4_{11/2}$ state), almost all of the carriers will be accumulated in the metastable state with constant optical pumping at 980nm, hence, the three-level system can be simplified into two levels for most of the practical applications. Alternatively, for pumping at 1480nm, pump photons directly excite carriers from the ground state to the top of the metastable state, therefore it is a more efficient process; however, stimulated emission at the pump wavelength leads to a degradation of the noise figure while the achievable inversion level is usually lower. Furthermore, if the pump is injected in the backwards direction (counter-propagation), it will be absorbed along the length of the fibre resulting in a relatively low level of inversion at the input side. As a result, the NF will be degraded due to the low signal gain available at the input with respect to the backwards propagating ASE. Alternately, injecting the pump in the forwards direction (co-propagation) will provide a high signal gain at the input with respect to the ASE, resulting in a lower NF.

5.2.2 EDFA Gain Dynamics

In practice, the gain dynamics of EDFAs are considered to be relatively slow as a result of the comparatively long lifetime of the metastable state. Consequently, for transmission of high-speed data, the EDFA gain remains undisturbed by the signal modulation, hence, if the average input power remains constant the induced crosstalk will be negligible in multichannel systems [232]. This property is a critical advantage of EDFAs and is the reason why steady-state models have been extensively used to predict network performance and guide the design of EDFAs [233]. Nonetheless, one of the key issues facing the realisation of reconfigurable LR-PONs is the dynamic characteristics of EDFAs whose gain can fluctuate significantly for variations in input power associated with channel add/drop events, the burst-mode nature of the US traffic, fibre cuts or components failures [234].

To illustrate the nature of these power excursions, Fig. 5.7 presents a trace captured using an oscilloscope showing optical transients with an appreciable overshoot of approximately 11.3dB at the output of a commercial EDFA in the absence of active gain control for a dynamic optical signal at 1550.12nm whose input varies by approximately 15dB with a repetition frequency of 500Hz (T = 2ms).

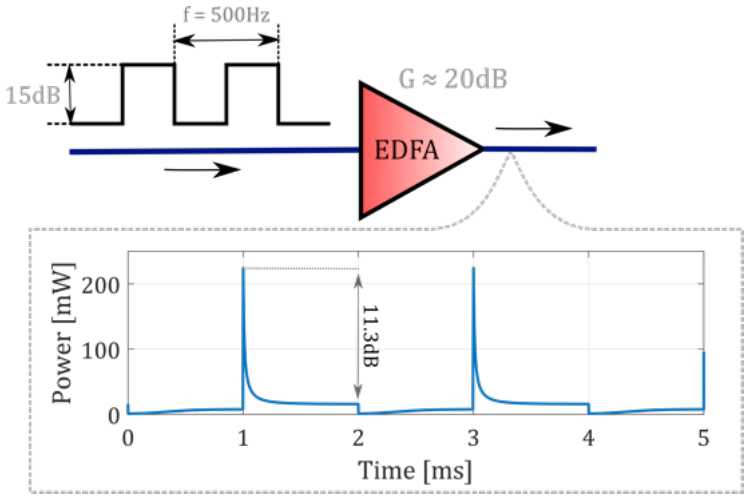


Figure 5.7: Data captured from an oscilloscope showing transients from a commercial EDFA in the absence of active gain control for a dynamic optical signal at 1550.12nm.

Consequently, a time-dependent model of EDFA gain dynamics is required to understand the transient behaviour resulting from the change in saturation levels that can produce significant inter-channel crosstalk in DWDM systems. As outlined in the previous section, for pump wavelengths at 980nm or 1480nm, EDFAs can be modelled as a two-level system despite the fact that pumping at 980nm results in a fast non-radiative interaction ($\tau \approx 1\mu s$) before populating the metastable $I^4_{13/2}$ state with excited carriers. Notably, the two-level model serves as a good approximation for pump powers less than 1W at 980nm, which is generally true in practice [235]. With this in mind, an overview of the two-level time-dependent gain model developed by Sun et. al [227] is presented in Appendix D alongside the resulting analytical formula which describes the inherent transient response of these amplifiers [236].

It is clear from the results demonstrated in Fig. 5.7 that the gain dynamics of EDFAs must be controlled in order to suppress these undesirable power excursions. In practice, such behaviour has the potential to compromise the performance of receiver subsystems resulting in corrupted data while in extreme cases these transients may result in physical damage to components such as photodiodes. As a result, various EDFA gain control techniques have been established for dynamic network applications over the last twenty years. A brief overview of these techniques is presented in the following section.

5.2.3 Gain Control Techniques

In the literature, many gain control strategies have been proposed to suppress EDFA transients; these can generally be classified into three categories from the viewpoint of the operating principle: active pump control [237], active input power monitoring [228] and all-optical gain control schemes [238]. Nonetheless, within all of these strategies, the fundamental idea is to maintain the relative balance between the pump power and the total input power in order to maintain a constant amplifier gain. For instance, gain-controlled amplification of burst-mode signals has been investigated by introducing dummy power signals during intervals between bursts to maintain a constant input power to the EDFA [239] however K. Okamura et al. revealed substantial results in 2005 based on a fast feedback pump control scheme [240]. Here, the optical powers at the input and output of the EDFA were continuously monitored using photodiodes in order to generate an error signal based on the required and actual gain values ($e(t) = G_{Req}.P_{In} - P_{Out}$). The error signal was then used by a linear control circuit ($\tau_{eff} < 1\mu s$) to adjust the pump power and correct the gain as necessary. This scheme produced negligible packet envelope distortions and a negligible power penalty (back-to-back) for $25\mu s$ bursts carrying data at 2.5Gb/s when compared with operation under a fixed pump bias (power penalty = 2.9dB). In the same year, similar results were published by Otani et. al [241] using an AGC-EDFA with fast feedback control for 10Gb/s signals with optical burst lengths of 333μs (f = 3kHz). As the response time of the control loop was significantly faster than the excited state lifetime of the Er^{3+} ions (≈10ms) the experiment was successful in mitigating the gain transients and the saturation-induced crosstalk respectively, thus highlighting the benefits of gain-controlled EDFAs for multichannel signal amplification.

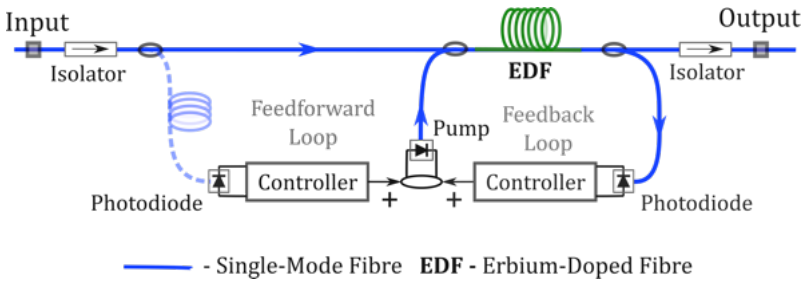


Figure 5.8: Schematic of a single-stage, forward-pumped EDFA configuration with active gain stabilisation via dynamic pump control.

To address the impact of significant channel variations within reconfigurable networks, Y. Horiuchi et al. of Fujikura Ltd. presented an 'ultra-fast' AGC-EDFA comprised of a hybrid feed-forward/feedback pump control circuit, a gain equalising filter (GEQ) and a high-speed variable optical attenuator (VOA) [242]. The feedback loop was introduced to compensate for any inaccuracies in the feed-forward control while the VOA (whose response time was less than $1\mu s$) was added to compensate for differences between the required and the actual gain values at the EDFAs output. A 39-channel add/drop analysis was carried out at various test wavelengths across the C-band to characterise the control scheme and the results demonstrate a maximum gain excursion of 1.2dB (settling time $\approx 20\mu s$) following a 'drop' event while an 'add' event produced a gain excursion of 0.7dB (settling time $< 3\mu s$). Notably, the response of the feed-forward control loop in the hybrid configuration presented in [242] can be improved even further through the addition of an optical delay line (ODL) using standard single-mode fibre (SSMF) as demonstrated in [228]. This approach effectively compensates for delays within the control circuit as well as the slow response of the Er^{3+} ions to a change in pump current.

From these investigations, it is evident that by using a combination of well-designed feedback and feed-forward control loops it is possible to build broadband WDM EDFAs with excellent transient suppression which provide flat gain over a large dynamic gain range with low noise contributions and a high saturation output power. These EDFAs have been shown to provide stable gain performance under a variety of conditions allowing them to address most applications and functions in modern optical networks.

5.3 Analysis of Residual Transients from Gain-Controlled EDFAs

The EDFAs identified as candidates for deployment within the proposed DISCUS architectures are commercial modules that have been developed for application in reconfigurable optical add/drop multiplexers (ROADMs) in flexible metro networks. Due to the nature of this application, the gain control circuitry has been designed to reduce the transients introduced by a fluctuation in the channel loads. Notably, the timescale of the add-and-drop events in these types of networks are typically on the order of milliseconds which is much longer than the timescale of the TDMA

traffic fluctuations in a PON. Nonetheless, despite not being designed specifically for burst-mode applications, these amplifiers provide a simple and effective solution for transient reduction. In particular, the devices examined in this analysis are *Oclaro PureGain^{TM} 2800* EDFAs. These modules operate across a wavelength range of approximately 35nm (1529nm - 1564nm) with an input power threshold of -29dBm, a maximum output power of +19dBm, a typical noise figure < 5.5dB and a variable gain between 16dB and 30dB which has been optimised for optimal flatness (~0.5dB) at a set-point of 20dB. These performance parameters were selected in accordance with the specifications required for the in-line amplifiers of the proposed 'open-ring' LR-PON configuration which have been derived from the associated optical power budget as indicated in Table 5.1. The typical gain and noise figure performance of these EDFAs is presented in Fig. 5.9 as a function of the average input power under automatic gain-control (AGC) for a maximal set-point gain of 30dB using a continuous-wave source at 1550.12nm.

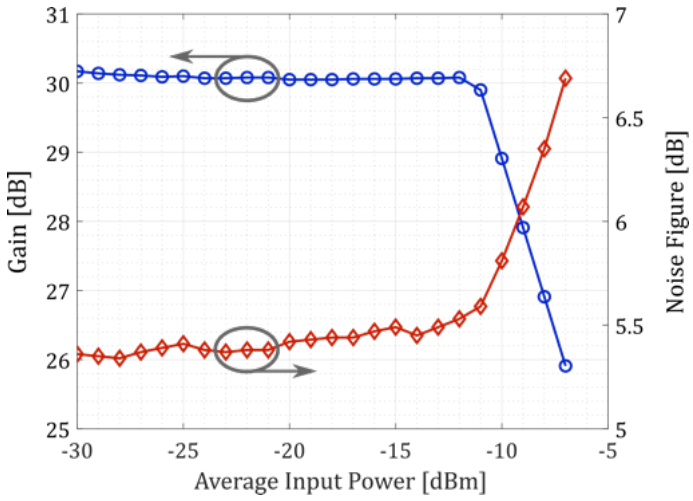


Figure 5.9: Gain and noise figure of a commercial dual-stage EDFA operated in automatic gain control (AGC) with a setpoint value of 30dB for a signal at 1550.12nm

In accordance with the theory presented in [236], the output power is a key factor with respect to the gain transients, since higher powers can place a greater stress on the pump laser(s) while also creating higher gain saturation in the erbium-doped fibre. As a result, the following measurements are performed at the maximum output power (~ +19dBm), sub-dividing the total power equally between the channels.

Furthermore, while this work presents experimental results obtained from the Oclaro PureGain^{TM} amplifiers, it is reasonable to expect that the findings and conclusions presented in the following sections can be extended to similar devices that have been developed by other manufacturers.

Experimental Setup Description:

The experimental setup used to analyse the residual transient contribution from the gain-controlled (GC) EDFAs is illustrated within Figure 5.10. In order to emulate the dynamic traffic from a fully loaded system, a wavelength selective switch (WSS) was used to spectrally slice the amplified spontaneous emission (ASE) generated by an EDFA which was subsequently amplified by two semiconductor optical amplifiers (SOAs). Besides providing gain to boost the power of the ASE, the SOAs are deployed in order to dynamically adjust the power of the ASE channels through adjustment of their respective bias currents using an arbitrary function generator (AFG) in order to emulate dynamic network traffic. Moreover, the wavelength groups allocated to each SOA are interleaved using the functionality of the WSS to assign alternating channels to specific ports. Subsequently, the optical power of each channel is then equalised through the controlled application of attenuation on a channel-by-channel basis using a remote, custom-designed instrumentation algorithm in order to flatten the optical spectrum.

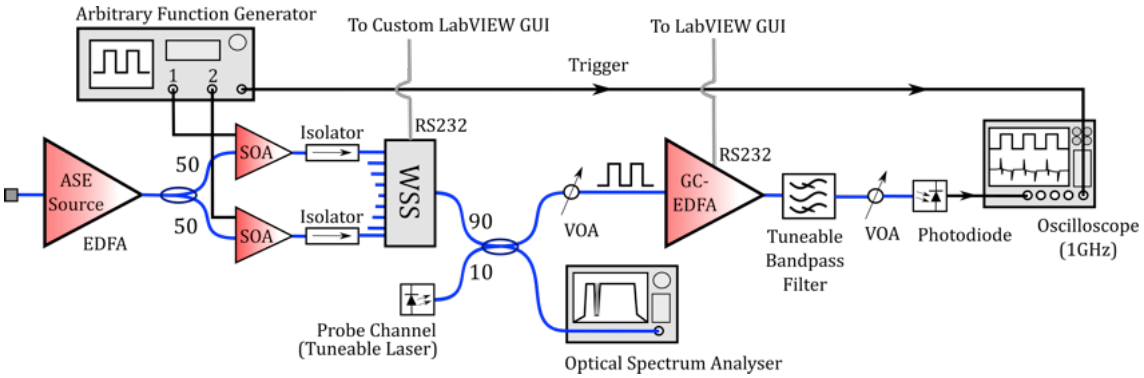


Figure 5.10: Experimental setup used to characterise the residual EDFA gain transients.

An example of an optical spectrum at the input of the GC-EDFA under test is shown in Fig. 5.11. Here, a spectral gap has been carved into the ASE spectrum (red trace) using the WSS in order to load the probe channel (blue trace) at 1530.33nm. This probe channel is generated by a tuneable laser and combined with the spectrally sliced and flattened ASE using a 90/10 coupler. The second output port of that coupler is then used to monitor the spectrum at the input of the EDFA using an optical spectrum analyser (OSA). The setup can hence emulate an arbitrary set of dynamic DWDM wavelengths and allow analysis of the residual gain transient on any probe wavelength in the C-band. The timing of the dynamic (ASE) channels is controlled using the AFG and the two SOAs, which together with the WSS allows the power of two groups of channels to be controlled independently.

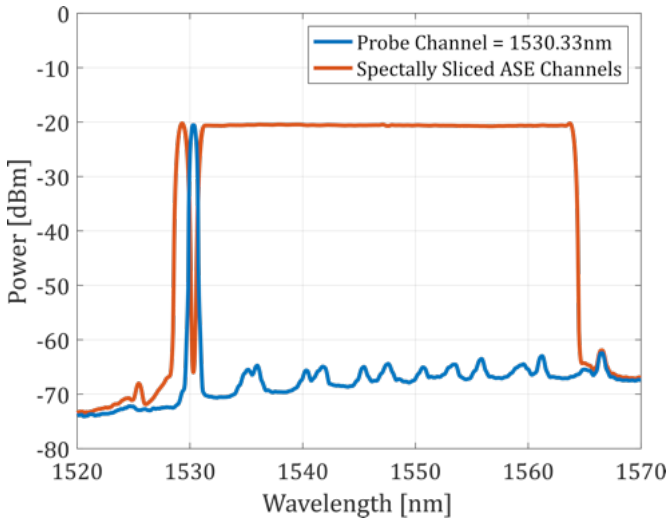


Figure 5.11: Data captured from an optical spectrum analyser demonstrating the emulation of a system with 80 DWDM channels between 1529.16nm and 1563.86nm.

At the output of the EDFA under test, a tuneable bandpass filter filter (TBF) is used to separate the probe wavelength from the dynamic ASE channels and the power of the probe wavelength is adjusted using a variable optical attenuator (VOA). The probe wavelength is then detected by a photodiode (PD) and a real-time oscilloscope is used to acquire the trace. For instance, Fig. 5.12 shows the residual power excursion induced on a probe channel located at 1530.33nm when the background ASE channels (1529.16 - 1563.86nm) are modulated with a square wave signal with a repetition rate of 100Hz (T = 10ms) producing an add/drop ratio of roughly 19dB.

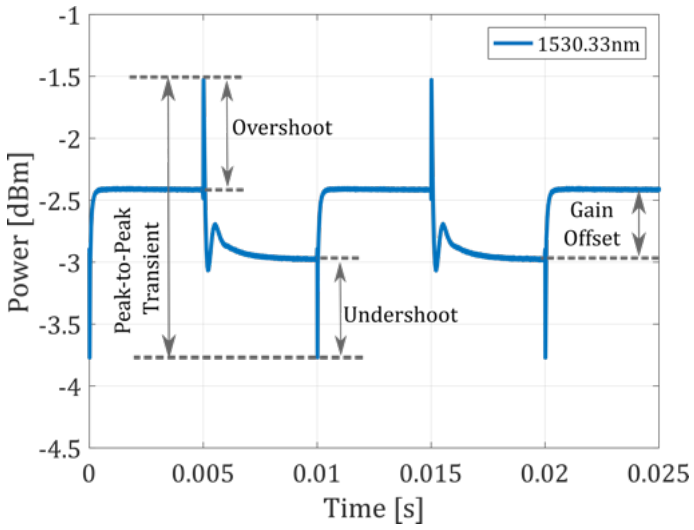


Figure 5.12: Data captured from an oscilloscope demonstrating a residual gain transient imparted on the output power of a probe channel located at 1530.33nm.

When a number of channels are dropped, the EDFA gain control circuitry detects the input power change and adjusts (reduces) the current of the EDFA pump to retain the required gain. However, there is a delay of several microseconds between the detection of the input power change and the reduction in the population inversion of the amplifier due to the subsequent pump current reduction. During this time the surviving channel experiences a sudden power surge called an overshoot. Once the gain of the EDFA is adjusted, the power of the probe channel drops. The opposite situation happens when a number of channels are added within the network. In this case the surviving channel power drops due to insufficient gain available from the EDFA and an undershoot is observed. Notably, even in the case of an ideal control system, there is always some residual gain error that cannot be resolved by the EDFA photodiodes. In general, even a very slow change in the total input power causes a permanent gain change at the probe frequency (due to spectral hole burning and redistribution of the spectral gain). This localised gain error is referred to as a gain offset and needs to be treated separately from the fast transients (over- and undershoot). This offset can be managed by using more accurate gain flattening filters however, reducing the fast transient requires more sophisticated strategies such as that presented in [228].

To compliment the trace presented in Fig. 5.12, the results presented in Fig. 5.13 outline the peak-to-peak transient and the corresponding offset measured us-

ing various probe wavelengths ranging from 1530.33nm to 1563.86nm with a dynamic background (ASE) spectrum extending over the entire C-band to emulate 80 (50GHz-spaced) wavelength channels. In particular, the power of each channel was equalised such that the total input power to the EDFA under test is near the nominal input power ($\approx -1dBm$). However, as outlined previously, the power of the ASE channels is actively controlled using the SOAs such that the ratio between high power and low power at the input to the EDFA represents an add/drop event of all the ASE channels which achieves a value of approximately 19dB. In addition, the periodic time of the dynamic events which switches between the high and low input power was set at 10ms (100Hz) in order to allow sufficient time for the gain to recover so that the transient dynamics can be examined in full.

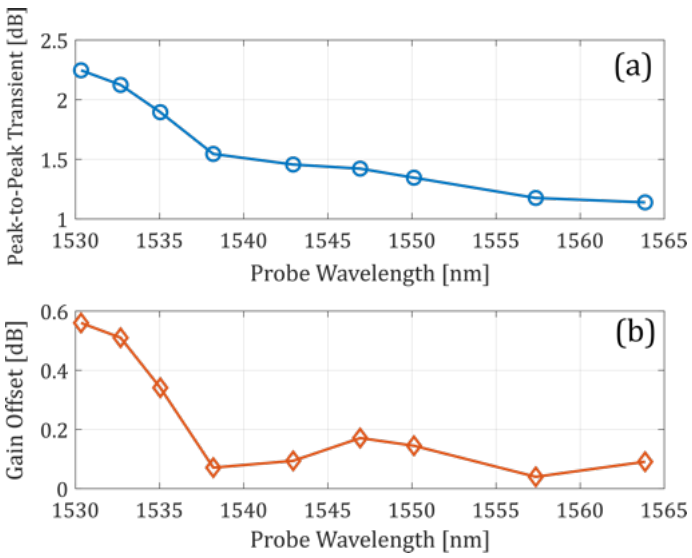


Figure 5.13: Analysis of (a) the peak-to-peak transient and (b) the gain offset, measured as a function of the probe channel wavelength with the dynamic ASE channels extending from 1529.16nm to 1563.86nm (c).

It is important to note that the procedure used here represents the extreme worst case in terms of the gain transient induction; however, the results can be used to effectively provide an upper bound to the maximum power excursions to be expected from these devices. Moreover, in a real deployment scenario, events where such a variation in input power could occur would be extremely unlikely and typically not

allowed by the protocol; nonetheless, it may facilitate an examination of the link resiliency in the event of a fibre cut or equipment failure.

Nonetheless, the results presented in Fig. 5.13 clearly show that the shorter probe wavelengths are more strongly impacted by the residual gain transients with the probe wavelength at 1530.33nm demonstrating a peak-to-peak power excursion of approximately 2.3dB and a gain offset of up to 0.6dB. This feature can be attributed to the fact the primary gain peak of the EDFA is located around 1532nm. Nonetheless, the large variation of the saturation-induced power excursion with wavelength suggests the longer wavelength portion of the C-band (1546.92nm - 1564.86nm) is more suitable to host the US channels which operate in burst-mode. Using this approach, the peak-to-peak transients and gain offset were measured for dynamic ASE channels extending from 1546.92nm to 1563.86nm which encompasses roughly half of the C-band which is capable of supporting 40 (50GHz-spaced) wavelength channels; the associated results are presented within Fig. 5.14. As in the previous case, the GC-EDFA was operated at the set-point of 20dB in order to achieve optimal flat gain across the wavelength range of interest, however, due to the reduction in the number of emulated active channels the EDFA (i.e. 80 → 40) the amplifier is not at the maximum output power. As a consequence, the amplitude of the residual transients should be less than those presented in Fig. 5.13 using equivalent probe channel wavelengths.

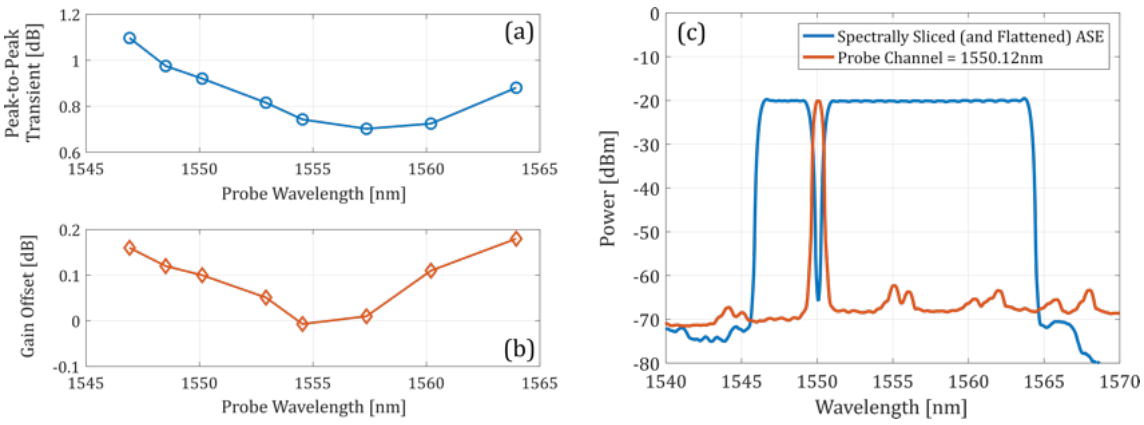


Figure 5.14: Analysis of (a) the peak-to-peak power excursion and (b) the gain offset measured as a function of the probe channel wavelength with the dynamic ASE channels extending from 1546.92nm to 1563.86nm as shown in (c).

In the results presented in Fig. 5.14, the controlled input power variation of the ASE channels corresponds to approximately 16dB; however, the worst case peak-to-peak power excursion is now reduced to 1.1dB at a probe wavelength at 1546.92nm, while the gain offset is maintained below 0.2dB. Notably, the same test was performed on the short wavelength side of the C-band (1529.16-1546.12nm) showing as expected maximum transients almost twice as large in dB scale.

5.3.1 Evolution of Residual Transients in Chained EDFA Links

While the preceding analysis focuses on a single EDFA, the proposed DISCUS LR-PON architecture actually employs multiple, concatenated EDFAs. Even in the simplest configuration with one amplifier node (i.e. the urban 'tree-structured' configuration) there are two EDFAs in the US path, one in the AN and one at the input of the M/C node. Both these EDFAs can introduce transients caused by the active US channels. As a result, the concatenation of optical transients is a noteworthy characteristic to be examined. Similar measurements to those presented in the previous sub-section have been performed for a chain of EDFAs. The link is constituted by 1 to 5 GC-EDFAs working at the nominal gain of 20dB with 20dB loss between each device in order to simulate a fully gain compensated link similar to that required in the 'open-ring' configuration proposed for rural access in 5.1.2.

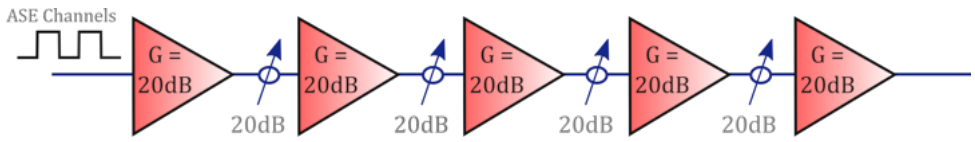


Figure 5.15: Illustration of the chained EDFA configuration used to investigate the evolution of residual transients in systems with concatenated amplifiers.

The peak-to-peak transients measured as a function of the number of chained EDFAs and for an input power variation of 16dB with a repetition period of 10ms (100Hz) are shown Fig. 5.16. The measurements presented here have been performed for dynamically switched ASE channels on the long wavelength side of the C-band be-

tween 1546.92nm and 1563.86nm using a probe wavelength at 1550.12nm as shown in Fig. 5.14(a). The results indicate that the transients accumulate linearly (with respect to the logarithmic scale) when travelling through multiple amplifiers with a maximum peak-to-peak transient of approximately 4.4dB measured after transmission through 5 chained EDFAs. This is an important result as it is not obvious that the cascaded EDFAs are essentially independent and more importantly the transient suppression controls of the EDFAs are not affected by transients introduced by the previous amplifiers.

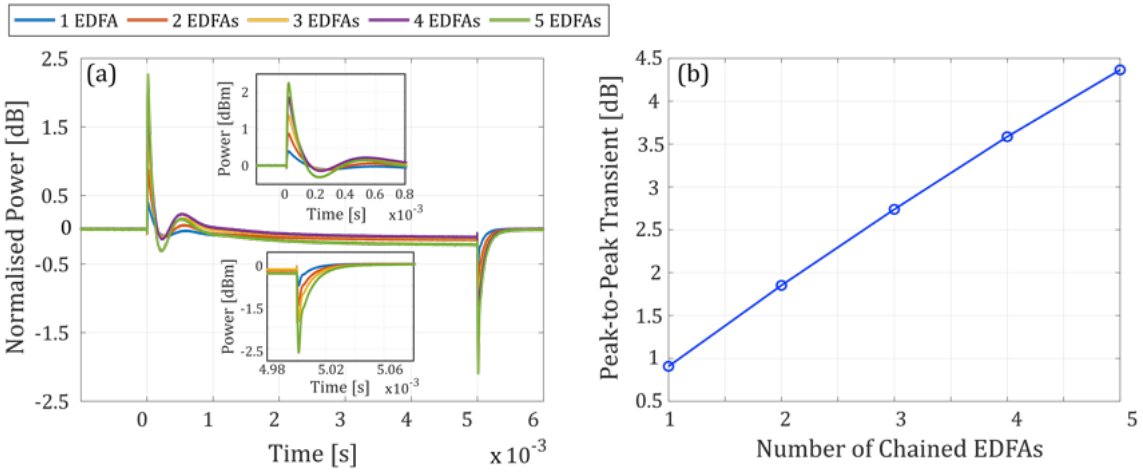


Figure 5.16: (a) Residual transient profiles and (b) the evolution of the peak-to-peak power excursion measured as a function of the number of chained EDFAs for a probe channel located at 1550.12nm in response to dynamically switching the ASE channels (1546.92nm - 1563.86nm) with a repetition rate of 100Hz.

In the preceding analysis, a relatively low repetition frequency of 100Hz (T = 10ms) was used to vary the input power of the ASE channels in order to establish the performance boundaries of the EDFAs under test by allowing adequate time for the EDFA gain to return to the steady-state between switching events. Nonetheless, in a real deployment scenario, the bursty nature of US traffic in accordance with the applied TDMA protocol will produce input power variations on a timescale of microseconds. With this in mind, the evolution of the residual transient produced by a chain of up to five GC-EDFAs has been examined for a probe wavelength at 1550.12nm when switching frequencies of 10kHz (T = 100μs) and 100kHz (T = 10μs) are applied to control the input power of the ASE channels ($\Delta P \approx 16dB$)

which encompass the targeted US wavelength band (1546.92nm to 1563.86nm). The corresponding results are presented in Fig. 5.17. As outlined previously, this procedure represents the worst case in terms of the gain transient induction. Moreover, in practice, events where such a variation in input power could occur would be typically not be allowed by the protocol. Nonetheless, from these measurements it is evident that there is a marked reduction in the peak-to-peak power excursion as the repetition period is reduced below 100μs, which roughly corresponds to the time scale of the fast part of the captured gain transient shown in Fig. 5.12. Moreover, as the repetition rate increases the EDFA gain does not have time to fully recover between switching events and hence the amplitude of the transients is reduced.

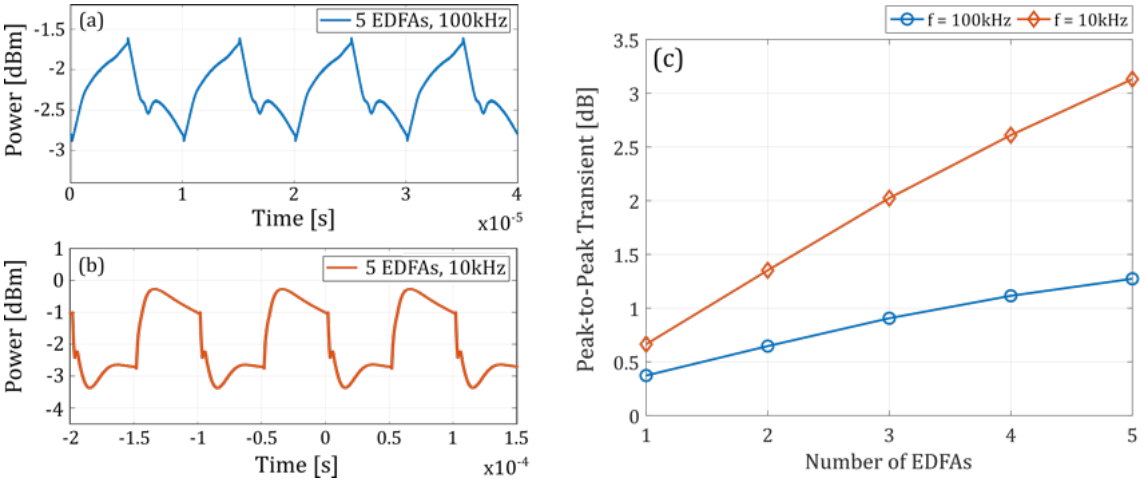


Figure 5.17: Residual transient profiles induced on a probe channel located at 1550.12nm by dynamically switching the upstream wavelength band (1546.92nm - 1563.86nm) with a repetition rate of (a) 100kHz and (b) 10kHz with (c) the corresponding peak-to-peak power excursion measured as a function of number of chained EDFAs.

The results presented in this section clearly indicate the importance of emulating a realistic burst traffic pattern for the characterisation of the EDFA performance. In addition, it should be noted that designing a burst-mode link and the optical amplifiers based on the worst case traffic pattern might not be the optimal solution as it will lead to an over-specification of the EDFAs performance; moreover, such events are likely to be extremely rare (i.e. fibre cut, equipment failure) or possibly not allowed by the protocol (i.e. burst scheduling).

In practice, the performance impact of residual EDFA transients will likely depend on the architecture of the burst-mode receiver (BMRx) that is deployed in the OLT. For instance, the outcome will depend on whether it is a limiting or linear BMRx, how the power of the burst is measured and if the gain is continuously adjusted or fixed after an initial measurement within the burst preamble. Moreover, any mechanism that contains memory of a preceding burst (e.g. charge and discharge on a capacitor) can spoil the initial conditions at the start of a new packet resulting in unacceptable requirements on the length of the guard time and the preamble. In particular, due to the high number of ONUs connected to an OLT, high traffic efficiency is required; therefore, the OLT-based BMRx must remove all memory of a preceding packet within a short guard time ($\leq 25.6ns$) while adjusting its gain and DC offsets within a preamble on the order of a few tens of nanoseconds. To demonstrate such a receiver, the following section presents an overview of the innovative 10G-capable linear burst-mode receiver (LBMRx) technology developed within the Tyndall National Institute, Cork. Subsequently in section 5.4.4, the impact of residual optical transients is examined with respect to the performance of the 10G LBMRx in conjunction with burst-mode forward error correction (BM-FEC) which has been implemented on field programmable gate arrays (FPGAs) in order to optimise the available power budget within the DISCUS testbed [147].

5.4 10G Burst-Mode Subsystems

The low-cost requirements of the ONU (outlined in Chapter 4) suggest that the chosen tuneable transmitter technology which generates C-band wavelengths might not have a chirp characteristic optimised for the long physical reach and high bit rates targeted by LR-PONs; therefore, dispersion compensation is required [144]. While dispersion compensating fibre (DCF) can be used, DCF is bulky, costly and has a large insertion loss. Furthermore, the incident bursts may have undergone differing levels of impairments to due to the appreciable differential reach of the ODN; therefore, electronic dispersion compensation (EDC) can provide a superior solution as it has no insertion loss, negligible physical volume (a small chip), minimal additional power consumption as well as a reduced CAPEX and inventory cost.

Notably, the implementation of BM-EDC requires a linear burst-mode receiver (LBMRx), which is used to preserve the signal shape by linearly amplifying its input

such that the average or peak amplitude equals a reference in order to keep the burst-to-burst amplitude variation at the output of the LBMRx as small as possible to simplify the interface with clock and data recovery chips or analogue-to-digital (A/D) converters. This amplification mechanism requires the ability to adjust the LBMRx gain over a continuous range of values across the input dynamic range according to the strength of the incoming burst, unlike switching between a few discrete gain settings as undertaken in [243] and [244]. Furthermore, it is essential that the LBMRx can handle incoming bursts without requiring overly large guard times (the minimum allowable time between bursts, mainly required to reset the LBMRx after the end of a burst and prepare it for the next burst) and preambles (the data pattern at the start of the burst required for adjusting the gain and dc-offsets of the LBMRx).

5.4.1 Linear Burst-Mode Receiver

Within the DISCUS project, a 10G-capable AC-coupled linear burst-mode receiver (LBMRx) with fast gain adaptation based on 0.25μm Silicon-Germanium (SiGe) Bipolar and Complementary Metal–Oxide–Semiconductor (BiCMOS) technology developed by researchers within Photonic Systems Group of the Tyndall National Institute is proposed for deployment within the OLT-Rx. This advanced receiver configuration has been successfully shown to support a burst-to-burst dynamic range of $\geq$ 22.7dB with guard times as short as 25.6ns with a worst-case OSNR of 15dB at a BER of 1.1×10^{-3}. This value represents the pre-FEC threshold required to achieve error-free transmission assuming Reed-Solomon RS(216,248) encoding as widely used in 10G-PON standards today [80]. As the realisation of the LBMRx is beyond the scope of this work, the reader is referred to [146] for detailed information on the internal architecture including the circuit design and initial performance evaluation. Moreover, a brief overview of the packaging assembly of the LBMRx is presented in Appendix E.

Packaged LBMRx Characterisation:

The experimental setup illustrated in Fig. 5.18 was used to characterise the performance of the LBMRx. In particular, a pulse pattern generator (PPG) loaded

with a custom data pattern was used to produce two 10μs-long data packets at 10.3125Gb/s. Using this repeating data pattern, the output from a commercial ECL was modulated with NRZ-OOK using an electro-absorption modulator (EAM) which provided an extinction ratio (ER) of approximately 8dB. Furthermore, using a trigger signal generated at the start of the pattern, a drive signal produced by an AFG connected to a booster SOA was used to carve an alternating series of 'loud' and 'soft' packets (LP, SP), each with a total length of 103168 bits separated by a guard time of 25.6ns (264 0's) where the power of the packets was set by adjusting V_{Loud} and V_{Soft} to manipulate the dynamic range. An optical bandpass filter with a 3dB bandwidth of 0.5nm was used to remove the out-of-band ASE noise generated by the optical amplifiers. Each packet included a preamble with a total length of $\approx$ 150ns to enable the LBMRx to adjust its gain for the incoming packet and to account for the settling of a transient across the coupling capacitors. The remainder of the packet consisted of a 101392-bit payload containing pseudo-random binary sequence (PRBS-7) data and a 32-bit end of burst (1010...) sequence. Moreover, prior to the arrival of each burst, a 10ns-wide pulse was sent to the LBMRx using a second AFG in order to trigger the receivers gain settings to return their nominal values.

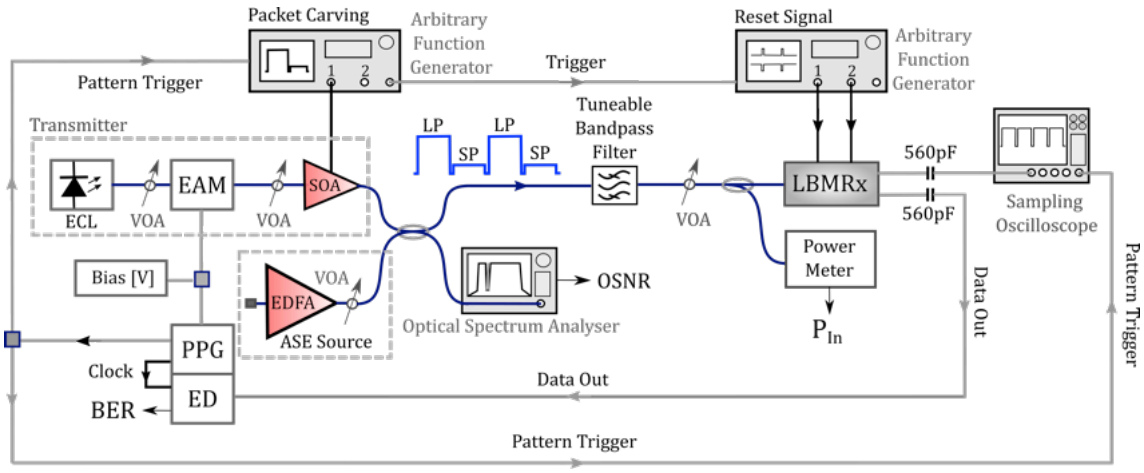


Figure 5.18: Illustration of the experimental set-up used to characterise the LBMRx.

For this analysis, the BER was selectively measured on the SP payloads using a

synchronised error detector (ED) as this represents the most stressful condition for the LBMRx. An example of the generated optical signal with a dynamic range of 15dB is presented in Fig. 5.19(a) while Fig. 5.19(b) presents the corresponding equalised output from the LBMRx.

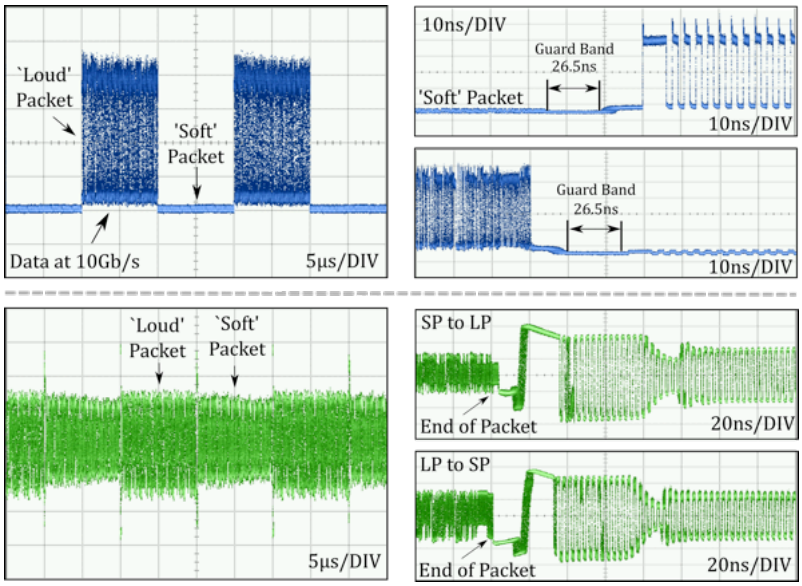


Figure 5.19: Traces captured from a sampling oscilloscope of optical bursts with a 15dB dynamic range carrying NRZ-OOK data at 10Gb/s Arriving at the OLT-Based LBMRx (blue trace) and the corresponding output of the LBMRx showing the equalised packets (green trace).

Prior to these measurements, it was found that the photodiode in the LBMRx subassembly was not high enough in comparison to the heat-sink level which in turn blocked the lensed fibre and preventing it from being lowered further, hence, the fibre was welded at a non-optimum distance from the photodiode resulting in a coupling loss of roughly 2dB. This loss was determined by comparing the post-packaging characterisation results with the initial measurements recorded using a probe station setup. Nonetheless, a sensitivity of approximately -20dBm is measured at a BER of 1.1×10^{-3} when the LBMRx is operated in burst-mode with the BER for powers below -14dBm measured on the SP while maintaining the LP power at -2dBm (Fig.5.20(a)). The burst-mode curve measured at low powers presents less than 0.5dB power penalty (at FEC threshold) in comparison to the continuous-

mode case (not shown in Fig. 5.20(a) for clarity); this penalty is attributed to the transient from the AC-coupling capacitors as indicated in [146].

With respect to Fig. 5.20(b), the power of the LP and SP were maintained at -2dBm and -17dBm respectively to achieve a dynamic range of 15dB while the OSNR, measured using the OSA, was degraded through the controlled addition of ASE noise from an EDFA using a variable optical attenuator (VOA). From these results, it can be seen that to achieve a BER of at least 1.1×10^{-3} for the SP requires an OSNR of approximately 15dB which is in line with the assumptions made during the power and OSNR budget analysis. However, the error floor seen at high OSNR values is attributed due to the thermal noise of the LBMRx at the SP power as shown in Fig. 5.20(a).

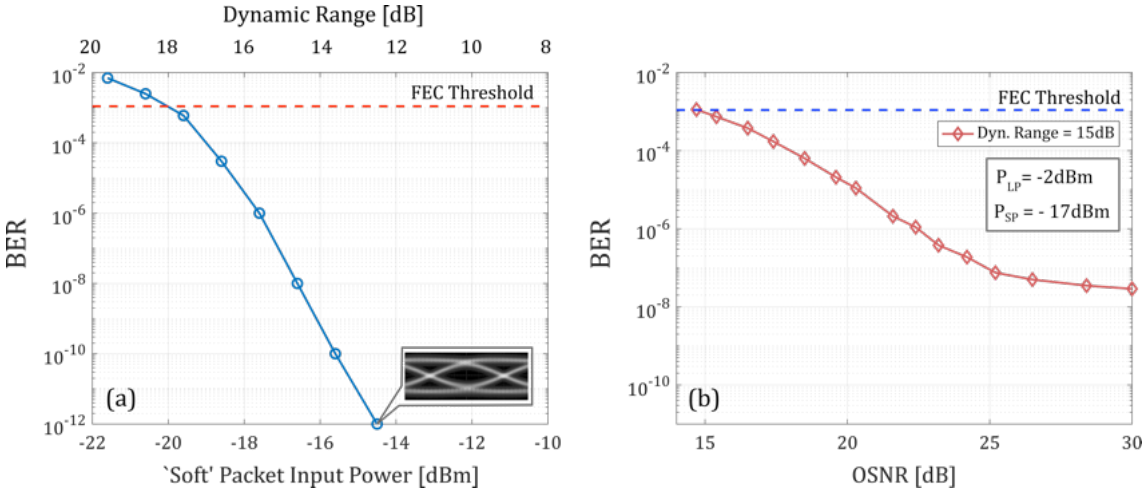


Figure 5.20: Performance of the packaged LBMRx assembly: (a) BER as a function of the power of the SP when the LP power is maintained at -2dBm.(b) BER of the SP as a function of OSNR for an incident dynamic range of 15dB (LP = -2dBm, SP = -17dBm).

5.4.2 Forward Error Correction

In addition to the realisation of a high-speed LBMRx which is capable of handling high-dynamic range (≥ 15dB) burst-mode traffic, the LR-PONs configurations proposed in 5.1 will require innovative digital signal processing (DSP) functions such as electronic dispersion compensation (EDC) and forward error correction (FEC) on

a burst-by-burst basis in order to mitigate the varying channel impairments while improving the overall transmission quality within a link impaired by noise [245].

As outlined in section 5.1, the implementation of burst-mode forward error correction (BM-FEC) plays a crucial role for the proposed architectures as it allows optimisation of the available power and OSNR budget afforded by the operating range of the OLT-based LBMRx. The implementation of FEC typically involves the addition of redundant information which is encoded with the data stream prior to transmission using a suitable error correcting algorithm. At the receiver end, a decoder processes the data stream and uses the redundant bits to detect and correct transmission errors. Consequently, in order to achieve the desired transmission performance, each network component must be carefully designed as burst-mode FEC can be affected by strongly correlated an localised errors within the burst which can be introduced by the transient behaviour of network components such as EDFAs [246]. For instance, as outlined previously, the occurrence of residual EDFA transients can lead to a burst of bit errors which violates the assumption of a Gaussian noise distribution that governs the theoretical performance of Reed-Solomon FEC [247] which is actively deployed within the current generation of PON standards [81, 140].

Reed-Solomon Forward Error Correction:

Reed-Solomon (RS) codes are linear block (non-binary) codes that are typically specified as RS(n, k) where an encoder at the transmit side takes k data symbols of s-bits each and adds parity (also known as redundancy) symbols to make an FEC block with a total of n symbols where $n \leq 2^s - 1$. Notably, within each FEC block, there are $n - k = 2t$ parity words, where t signifies the maximum number of symbol errors that can be corrected within a block.

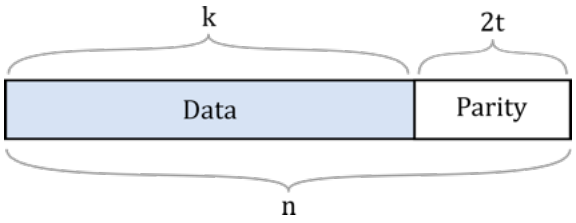


Figure 5.21: Illustration of a Reed-Solomon FEC Block (also known as a Codeword) Consisting of k Data Symbols and $2t$ Parity Symbols.

Notably, when an RS decoder corrects a symbol, it replaces a compromised symbol with the correct one regardless if the error was caused by one bit or by all of the bits within that symbol; this property offers a significant resilience against burst errors which makes RS codes preferential for use in communication systems. Nonetheless, the number of correctable errors is ultimately dependent on the dimensions of the code used, RS(n,k), and by adding more parity words to the signal more errors can be corrected. However, this process is limited as the encoded bit rate (B_e) must increase relative to the uncoded bit rate (B_u) in order to account for the associated FEC overhead (α_{FEC}) which is given by

$$\alpha_{_{FEC}} = \frac{n}{k} - 1 \equiv \frac{B_e}{B_u} - 1 \tag{5.4.1}$$

where, the proportion of the data-stream that is useful (non-redundant) is traditionally known as the FEC code rate, R_c,

$$R_c = \frac{k}{n} = \frac{B_u}{B_e} \tag{5.4.2}$$

In general, a lower value of R_c indicates a higher potential for successful error correction; however, it also impacts the overall implementation and cost severely. As a result, the analysis within this work considers the RS(248,216) code which was targeted for use within the DISCUS project in accordance with current PON standards [81]. This algorithm encodes a block of 216 data symbols into a block of 248 symbols by adding 32 parity symbols, where each symbol is a group of 8 bits. When a block of 248 symbols is received, the RS(248,216) algorithm uses the 32 parity symbols for correcting up to 16 corrupted symbols within the received block. Notably, the RS(248,216) code is the truncated version of the RS(255,239) code which in turn allows for a more convenient block length where the shortened block of 248 FEC words is padded at the encoder with 7 leading zero symbols which are not transmitted but are instead reinserted at the receiver prior to decoding. While the ITU-T G.987.3 XG-PON standard (2014) specifies the use of RS(248,216) for DS transmission (10Gb/s) and RS(248,232) for US transmission (2.5Gb/s), in this work, the RS(248,216) code is utilised for both transmission directions with a symmetric B_u of 10Gb/s in order to maintain a consistent FEC threshold of approximately $1.1{\times}10^{-3}$ with $\alpha_{_{FEC}} \approx 14.8\%$ and $R_c \approx 0.87$ in accordance with Eqn. 5.4.1 and 5.4.2.

Nonetheless, as shown in Fig. 5.22, a key criterion for the evaluation of the intrinsic error correcting performance of RS codes is the theoretical relationship between the decoded (post-FEC) BER and the coded (pre-FEC) BER which can be mathematically computed with the assumptions that the errors occur independently from each other and that the probability of incorrect decoding equals zero (i.e. the decoder never fails) [80]. For instance, if the $BER_{pre-FEC}$ represents the probability that a certain bit will be received with error, the expression $1 - BER_{pre-FEC}$ will signify the probability of receiving a correct bit. Subsequently, within an 8-bit symbol, the probability of receiving concurrently correct bits can be determined as $(1 - BER_{pre-FEC})^8$; hence, the probability of receiving a symbol error (P_{sym}) can be written as

$$P_{sym} = 1 - (1 - BER_{pre-FEC})^8 \tag{5.4.3}$$

By re-arranging the terms in 5.4.3, the pre-FEC BER can be written as a function of P_{sym}

$$BER_{pre-FEC} = 1 - (1 - P_{sym})^{1/8} \tag{5.4.4}$$

The probability of generating an uncorrected symbol given the probability of receiving a corrupted symbol and assuming uniformly distributed errors along the FEC block is given by Eqn. 5.4.5, which accounts for all possible outcomes of picking i unordered outcomes from a total of n possibilities [80].

$$P_u = \sum_{i=1+t}^{n} \frac{i}{n}\binom{n}{i} \underbrace{P_{sym}^{i}}_{\substack{\text{Symbol}\\ \text{Errors}}} \underbrace{(1 - P_{sym})^{n-i}}_{\substack{\text{Correct}\\ \text{Symbols}}} \tag{5.4.5}$$

where, i signifies the word index, n represents the total number of FEC words within one FEC block, $2t$ is the number parity symbols within one FEC block and $\binom{n}{i}$ is a binomial co-efficient. Finally, using Eqn. 5.4.5, the post-FEC BER can be written as a function of P_u using an analogous approach to that used to derive Eqn. 5.4.4.

$$BER_{post-FEC} = 1 - (1 - P_u)^{1/8} \tag{5.4.6}$$

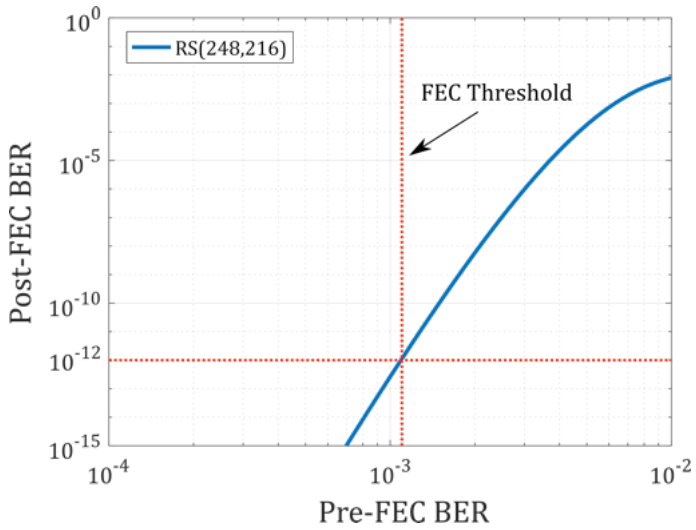


Figure 5.22: Theoretical performance of the RS(248,216) FEC algorithm.

The BER improvement realised through FEC is typically quantified in terms of the coding gain, G_C. For instance, in power limited systems, G_C is used to signify the increase in receiver sensitivity afforded by the application of FEC; while, in OSNR limited systems the G_C represents the effective improvement in OSNR sensitivity. As BER is related to the Q-factor, the G_C is often expressed as the ratio of the Q-factors for the post-FEC and pre-FEC data as shown in Eqn. 5.4.7.

$$G_C\,[dB] = 20log_{10}(\frac{Q_{post-FEC}}{Q_{pre-FEC}}) \tag{5.4.7}$$

where, $Q\,[dB] = 10log_{10}(Q^2) = 20log_{10}(Q)$. Notably, for systems impaired by Gaussian noise statistics, this relation can then be re-written as a function of the post-FEC and pre-FEC BER as follows:

$$G_C\ [dB] = 20log_{10}\left(\frac{\text{erfc}^{-1}(2BER_{post-FEC})}{\text{erfc}^{-1}(2BER_{pre-FEC})}\right) \tag{5.4.8}$$

where,

$$BER_{post-FEC} = \frac{1}{2}\text{erfc}(\frac{Q_{post-FEC}}{\sqrt{2}}), \qquad BER_{post-FEC} = \frac{1}{2}\text{erfc}(\frac{Q_{post-FEC}}{\sqrt{2}})$$

Using the data presented in Fig. 5.22, the theoretical performance threshold for the RS(248,216) code which provides a post-FEC BER of 1×10^{12} is determined to be approximately 1.1×10^{-3}. As a result, using 5.4.8, the corresponding value of G_C can be estimated to be 7.2dB.

5.4.3 FPGA Implementation of Burst-Mode FEC

Forward error correction is usually implemented on application specific integrated circuits (ASICs); however, as flexibility and development costs are crucial for PON deployment field-programmable gate arrays (FPGAs) have emerged as a potentially cost-effective technology to address certain DSP challenges. For instance, the ONUs and OLTs designed for use in the experimental testbed were realised by researchers within the Optical Access Team of the Tyndall National Institute using commercially available VC709 development boards which are equipped with Xilinx Virtex-7 XC7VX690T FPGAs [248]. Although the development of these units was not part of the work undertaken for this thesis, an brief overview of their structure is presented here for context as they were deployed within the physical layer testbed which is demonstrated in Chapter 6.

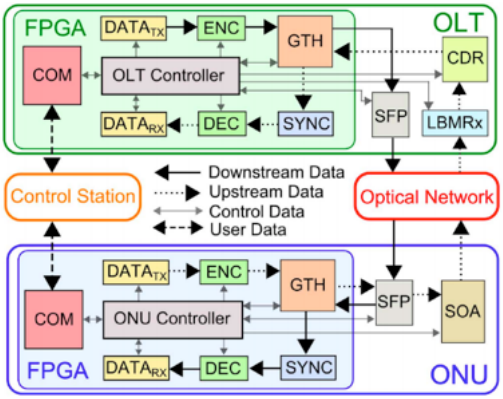


Figure 5.23: FPGA architecture of the implemented ONU and OLT. Arrows indicate the data flows in upstream and downstream directions (Image Reproduced from [248])

As shown in Fig. 5.23 the ONU and OLT were comprised of the following building blocks: a pseudo-random data generator (DATA_{Tx}), a data receiver (DATA_{Rx}) for analysis of network performance, an RS encoder (ENC) and decoder (DEC) for error correction using the RS(248,216) coding technique, a gigabit transceiver

(GTH) to serialise and de-serialise the transmitted and received data respectively, a frame synchroniser (SYNC) used to determine the boundary of deserialised data, a communication unit (COM) to mange the exchange of information between the ONUs/OLTs and the control station and the FPGAs and a central controller which is used to configure the functions of all the blocks through a custom graphical user interface (GUI).

Although the ONUs and OLT contain the same FPGA architecture, their respective building blocks are used differently in accordance with the nature of the transmission direction (i.e. burst-mode upstream, continuous-mode downstream) which in turn leads to differing frame structures. However, as the design of the FPGA architectures goes beyond the scope of this work, it is not discussed further, hence, for additional details on the development of the FPGA-based DSP blocks including the implementation of the burst-mode frame synchroniser and the time-multiplexed RS decoder, the reader is referred directly to [248].

Notably, the ONU requires two additional components which are external to the FPGA; the first is a standard small form-factor pluggable (SFP+) transceiver supporting 10Gb/s on-off-keying transmission using an externally modulated laser which can be tuned to ITU-T DWDM grid wavelengths across the C-band. The second additional component is a discrete SOA which is actively controlled by the FPGA in order to carve the optical envelopes which emulate multiple ONUs allocated to the same US wavelength through the TDMA protocol. The OLT also has an SFP+ transceiver, identical to the unit found in the ONU; however, only the transmitter section is used here as the LBMRx has been connected with the development board through a commercial clock and data recovery (CDR) unit. The recovered and re-timed signal at the output of the CDR module was then sent to the frame synchroniser which was the first processing block implemented in the FPGAs. Subsequently, a group of 8 interleaved RS decoders was used to process 8 symbols simultaneously at the FGPA clock rate of 161.133MHz to achieve a bit rate of 10.3125Gb/s.

The performance of the BM-FEC was characterised in back-to-back using optical bursts with equal amplitude (dynamic range of 0dB), the corresponding results are presented in Fig. 5.24. Notably, the measured FEC threshold compared favorably with the theoretically expected value of 1.1×10^{-3}; therefore, in accordance with the theory it can be assumed the error distribution is uniform within the burst.

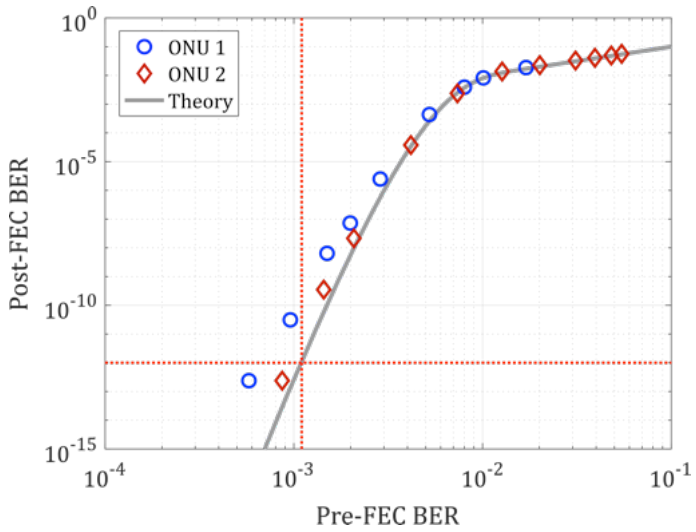


Figure 5.24: Comparison between measured and theoretical upstream FEC performance with burst dynamic range of 0dB and CDR preamble duration of 1μs.

5.4.4 FEC Performance of Upstream Channels Impaired by Optical Transients

Through a collaborative research effort, the performance impact of optical transients on US burst-mode traffic was evaluated using the FPGA-based ONUs and OLTs developed for use within the DISCUS experimental testbed. As shown in the experimental setup presented in Fig. 5.25, the optical power transients within the optical bursts are emulated by driving a discrete SOA with a waveform representative of the residual optical power excursion generated by a chain of GC-EDFAs within a LR-PON US link. In comparison to generating the residual transients directly through a link of concatenated amplifiers as shown in section 5.3.1, this approach has the advantage of being able to vary the amplitude of the residual transients which corresponds to a change in the number of chained amplifiers by simply scaling the waveform that drives the SOA. Moreover, the generation of emulated residual optical transients can be synchronised with the transmitted bursts in order to examine the effect of these transients as a function of their position with respect to the bursts. To achieve this, the OLT FPGA was used to provide an electrical trigger to the AFG while also controlling the ONUs through the implemented DS protocol as outlined in [248].

The waveform used to reproduce the profile of the residual optical transient was measured at the output of a chain of 5 GC-EDFAs using a continuous-wave probe channel located at 1550.12nm using the technique demonstrated in section 5.3 when the background channels consisting of spectrally sliced ASE located between 1546.12nm and 1563.86nm have been gated with a repetition period of 20μs to produce dynamic events every 10μs. Furthermore, in order to equally effect the data packets from both ONUs, the duration of the optical bursts was set to 5μs which is equal to half of the time period between the switching events. This concept is illustrated in Fig. 5.26 which demonstrates the profile of the residual transient alongside the time-multiplexed bursts from both ONUs.

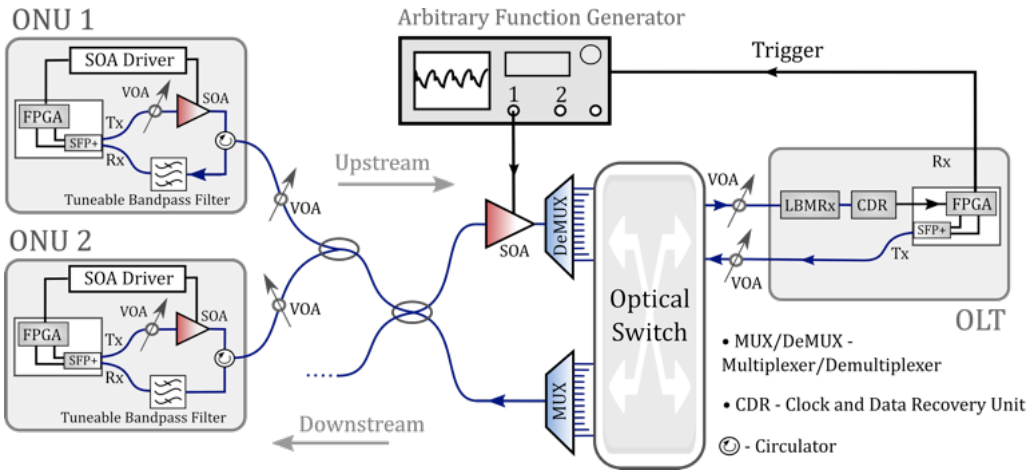


Figure 5.25: Experimental setup used for residual EDFA transient emulation and FEC performance evaluation.

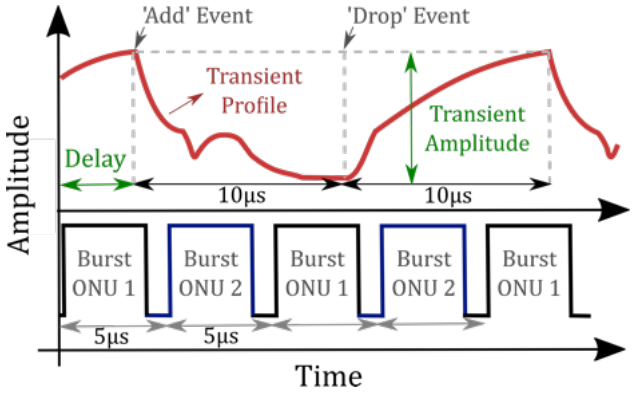


Figure 5.26: Illustration to demonstrate the duration of the emulated transient profile compared with the duration of optical bursts transmitted by two time-multiplexed ONUs

From the concept presented in Fig. 5.26, it is clear that the transient delay must be swept between 0 and 10 μs in order to test all possible alignments of the optical transients and the bursts. These considerations led us to the characterisation presented in Fig. 5.27, where the measured pre- and post-FEC BER for the two ONUs is plotted with varying transient delay and with a transient amplitude of 5.2dB. This particular value of amplitude has been experimentally determined in order to be close to the minimum transient amplitude before the FEC degradation. In particular, the measured pre-FEC BER of both ONUs always stays below the FEC threshold, hence the post-FEC BER of both ONUs is expected to be lower than 1×10^{-12}. However, for a transient delay close to 0 the post-FEC BER of ONU1 clearly raises above 1×10^{-12}, while for a transient delay close to 5μs the post-FEC BER of ONU2 increases. This degradation of the FEC performance occurs because the optical transients introduce correlated and localised errors within the bursts which are beyond the correcting capability of the FEC algorithm. Hence, Fig. 5.27 demonstrates that, in US PON links affected by optical transients, the verification of a pre-FEC BER lower than the FEC threshold is not sufficient for assuring the correct FEC performance. In these cases, the post-FEC BER must also be characterised in order to verify the correct FEC behaviour.

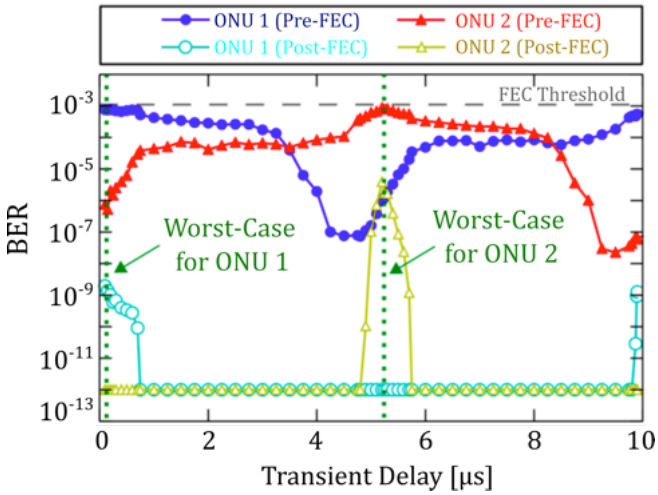


Figure 5.27: Measured burst-mode FEC performance with fixed transient amplitude of 5.2dB and with the delay varied with respect to the upstream bursts.

The measurements presented in Fig. 5.27 have been used to identify the following transient delays which represent the two worst cases for the FEC degradation: 0.1μs for ONU1 and 5.2μs for ONU2 (b). These two cases, which correspond to an 'Add Event' aligned with the start of the burst, have been analysed in Fig. 5.28 (a) and (b) respectively, where the measured pre- and post-FEC BER of both ONUs has been plotted as a function of the emulated transient amplitude.

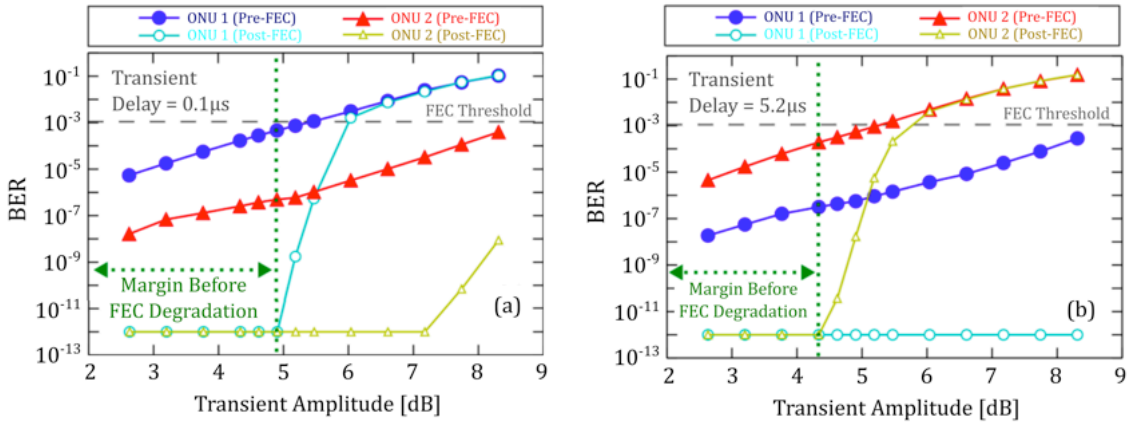


Figure 5.28: Measured burst-mode FEC performance for two ONUs when the amplitude of the emulated EDFA transients is varied with transient delays of (a) 0.1μs and (b) 5.2μs.

The pre-FEC BER of both ONUs can be seen to increases with the transient amplitude. This behaviour is expected considering that the increase of the transient amplitude leads to the increase of the number of errors within the burst. Moreover, a maximum performance margin of approximately 5dB can be estimated by considering solely a pre-FEC BER below the FEC threshold. However, for transient amplitudes larger than 4dB the post-FEC BER begins to increase above 1×10^{-12} even though the pre-FEC BER is lower than the theoretical threshold of 1.1×10^{-3}. This feature indicates an appreciable degradation of the FEC performance due to a significant amount of localised errors which compromises the correcting capability of the employed RS algorithm. Nonetheless, it should be noted that the minimal performance margin of 4dB presented in Fig. 5.28(b) is roughly 1dB higher than the worst-case power excursion demonstrated previously in Fig. 5.17. This observation suggests that the residual transients induced in a real deployment scenario whose channels are controlled by an appropriate PON protocol should not impact the transmission performance.

It is also important to recognise that the difference of approximately 0.3dB between the performance margins measured for ONU1 and ONU2 is expected to be within the fabrication tolerances of the different SFP+ transmitters employed in the ONUs. However, the difference of approximately 1dB between the pre- and post-FEC performance margins could be particularly relevant when designing PON architectures within the strict optical power budget of the current PON standards. As a result, this work also serves to highlight the relevance of characterising the post-FEC BER in US TDM channels as a function of the temporal distribution of the errors within the burst as demonstrated in [248].

5.5 Summary and Conclusions

Through the objectives of the DISCUS project, the work presented in this chapter has outlined the physical layer design strategy of two distinct wavelength-agile LR-PON architectures aimed at economically bridging the ever growing 'digital divide' between urban and rural communities with the aim of providing ubiquitous broadband services through advanced FTTP architectures. Moreover, it should be noted that the physical layer of the 'tree-structured' (single AN) and 'open-ring' (chained AN) designs introduced here have since been assembled as part of a full-scale testbed demonstrator which is evaluated in detail within Chapter 6.

The feasibility of the proposed DISCUS architectures was initially examined using a linear optical power and OSNR model in order to establish the achievable reach and split by deriving the detailed specifications of the in-line optical amplifiers. Subsequently, based on the performance boundaries set by the transmitter and receiver specifications, EDFAs emerged as suitable candidates due to their ability to provide a high gain (>30dB) and a relatively low noise figure (~ 5.5dB) across a wide band of channels. However, as their relatively slow gain dynamics are known to produce gain transients, EDFAs with active gain controls were required to ensure the link performance of the architectures under consideration. With this in mind, commercial EDFAs with active transient suppression circuitry whose performance specifications (e.g. gain, noise figure and aggregate output power) were derived from the power and OSNR model were acquired for deployment within the physical layer experimental testbed.

In order to examine the extent of the residual EDFA transients attributed to the limited response time of the gain control circuitry, the performance of the amplifiers procured for the physical layer testbed was evaluated under different dynamic loading conditions. In particular, the induction and evolution of residual transients were studied using a continuous-wave probe channel for which the measurement system was used to emulate the effect of 39 DWDM channels operated dynamically within a link comprised of up to five chained amplifiers as would be the case in the proposed 'open-ring' LR-PON architecture. Notably, the results presented in section 5.3.1 demonstrate that the amplitude of the residual transients induced by these switching events were observed to accumulate linearly (with respect to the dB scale) as a function of the number of chained amplifiers. For instance, in response to a worst-case add/drop power ratio of ~ 16dB using repetition rates of 10kHz (T = 100μs) and 100kHz (T = 10μs) which are representative of typical burst timescales, the amplitude of the compounded residual optical transients attained values of approximately 3dB and 1.4dB respectively within the wavelength band assigned to the US channels (1546.92nm to 1563.86nm).

As the performance impact of these residual EDFA transients will ultimately depend on the architecture of the OLT-based BMRx, a more comprehensive analysis was required with respect to the proposed DISCUS architectures. Subsequently, the primary contribution of the work in this chapter was the result of a collaborative research effort that involved examining the resilience of an FPGA-based BM-FEC algorithm used in conjunction with an innovative 10G-capable LBMRx [146]. Here, the pre-FEC and post-FEC BER were monitored as a function of the relative delay and amplitude of emulated optical transients imparted on incident bursts transmitted from two time-multiplexed ONUs.

The results from this analysis demonstrated an appreciable performance margin of 4dB with respect to the optical transient amplitude prior to FEC degradation. Notably, this margin is roughly 1dB larger than the amplitude of the worst-case residual transient induced by emulating the effect of dynamically switching 39 DWDM channels simultaneously within the allocated US wavelength band for a link with up to five chained gain-controlled EDFAs. Moreover, this outcome indicates that when the burst traffic is regulated by an appropriate PON protocol, the residual power excursions produced by these commercial GC-EDFAs should not compromise the transmission performance of the US 10G-TDMA traffic in either of the LR-PON

configurations proposed by the DISCUS project. Subsequently, this work was presented at the International Conference on Optical Network Design and Modeling (ONDM) which was held in Dublin in 2018 [147].

6

Demonstration of Dynamically Reconfigurable TDM-DWDM Long-Reach PONs

This chapter presents the results obtained from the physical layer testbed aimed at demonstrating the functionality of the network architectures and subsystems developed during the EU FP7 project DISCUS.

In the previous chapter, two distinct TDM-DWDM LR-PON topologies were identified for the demonstration; a tree-like topology with a single amplifier node which is suitable for deployment in densely populated urban areas and a novel chained amplifier node ('open-ring') architecture for deployment in rural, sparsely populated regions. Both baseline configurations use EDFAs as optical amplifiers, however, an alternative tree-structured configuration using SOAs was also investigated as an alternative technology with the potential to increase the flexibility of the system by extending the usable spectral range beyond the C-band. This work substantially extends previous demonstrations of evolutionary access networks [167], [249] and [250] in relation to the size of the network demonstrated, the level of reconfigurability and integration with the higher control and service layers.

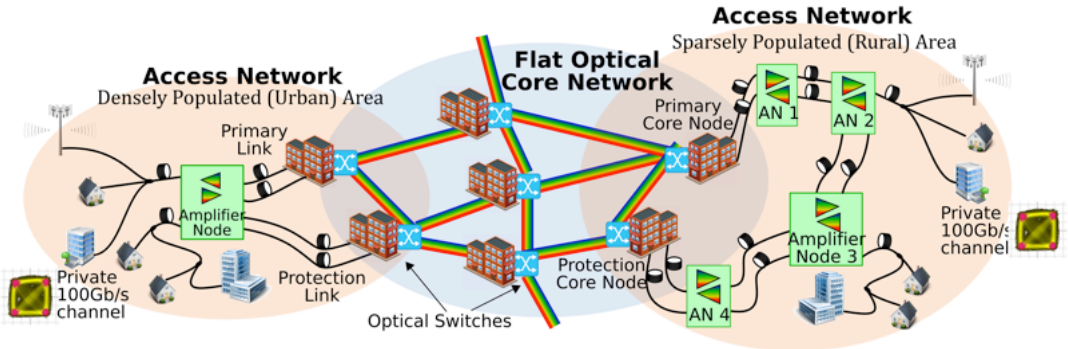


Figure 6.1: High-level network view of the proposed DISCUS architecture.

The experimental results demonstrate that with an emulated load of 40 DWDM channels in both transmission directions, the EDFA-based urban ('tree-structured') architecture shown in Fig. 6.1 (a), supports a physical reach of up to 100km with 1024 users [19], while the rural ('open-ring') architecture presented in Fig. 6.1 (b), supports up to 1024 users with a physical reach of 120km [20]. Both network configurations are dual parented on separate core nodes for link protection and support high dynamic range (>15dB) burst-mode transmission in the upstream direction facilitated by a 10Gb/s linear burst-mode receivers (LBMRx) [251] and forward error correction (FEC) [252] [145]. The amplifier nodes (ANs) significantly extend the physical reach (≥100km) while supporting the transmission of heterogeneous services and modulation formats. By exploiting the dynamic allocation of DWDM channels, the proposed infrastructure can support the convergence of different user types and service demands, from residential users, which share a 10G PON channel, to business users, with options to rent dedicated 10G PON channels or high capacity 100G point-to-point links.



Figure 6.2: EU FP7 Project DISCUS testbed, December 2015.
(Photonic Systems Lab, Tyndall National Institute, University College Cork, Ireland).

The first section of this Chapter (section:6.1) outlines the physical layer details of both architectural variants assembled for the laboratory testbed demonstration. The feasibility of both network designs is then examined in detail through a performance evaluation of the 10G TDM-PON channels alongside a 100G point-to-point overlay to examine the viability of service convergence; the corresponding results are presented in section 6.2. Finally, a brief overview of the software defined networking (SDN) and control plane services integrated with the tree-structured LR-PON architecture is presented in section 6.3; however, as this work is primarily focussed on the design and feasibility of the physical layer, this section is only provided for context.

6.1 Experimental Testbed Configuration

For experimental convenience, both architectural variants utilised the same core nodes (CNs), optical network units (ONUs) and ballast channels; this was achieved using a Polatis™ optical switch (I-VST-32x32-FAI-GSENS-200) to reliably interchange between the network designs. This configuration, shown in Fig. 6.3, proved very useful by allowing for a quick reconfiguration of the testbed without having to manually break connections. The typical insertion loss measured for the optical matrix switches was ~ 1dB.

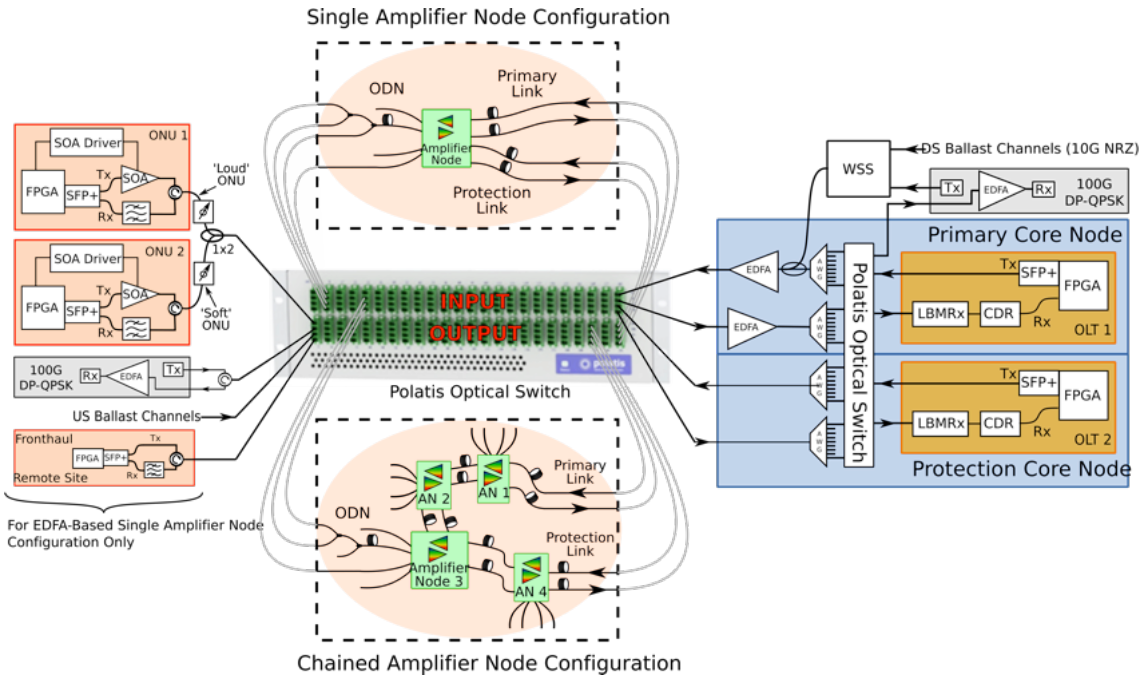


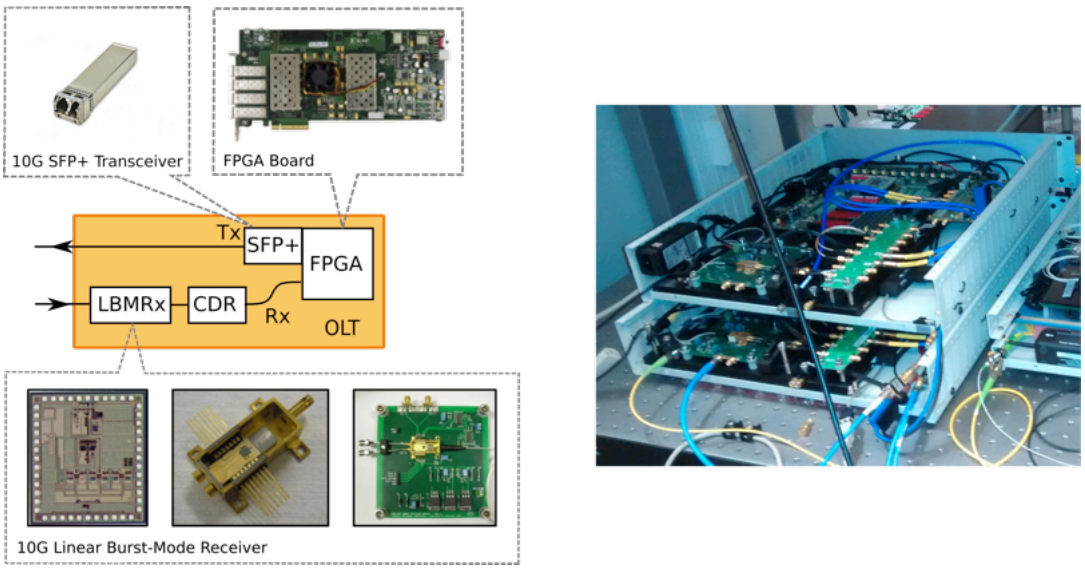
Figure 6.3: Experimental testbed configuration.

Core Nodes and Optical Line Terminals:

As shown in Fig. 6.3, reconfiguration and tuneability was achieved at the head end of the testbed by routing the ports of a wavelength multiplexer/demultiplexer (MUX/DeMUX) to two optical line terminals (OLTs) using a second Polatis™optical switch (N-VST-24x24-LUI-MMHNS-300). It should be noted that this additional switch was logically partitioned to facilitate the emulation of two separate CNs, namely the primary node and the backup/protection node. Although the associ-

ated OLTs can serve as primary and backup modules respectively, they can also be connected to the same LR-PON to support operation at different wavelengths.

Within the OLTs, whose structure is presented in Fig. 6.4, the downstream (DS) signal was generated using commercial 10G tuneable enhanced small form factor pluggable (SFP+) transceivers controlled by commercial field programmable gate arrays (FPGAs) using a simplified LR-PON protocol, which controls the ONU burst timings. In particular, the SFP+ transmitter employs a chirp optimised externally modulated tuneable laser, with a typical 1dB dispersion penalty at 80km of standard single mode fibre (SMF). Since the downstream is operated in continuous-mode no extra components are required in the transmitter. The upstream (US) signal was received at the OLT using a 10G-capable linear burst-mode receiver (LBMRx) [146]. As outlined in the previous chapter, this device is still in the development stage, but for this work it was packaged with high speed outputs and fibre coupled. The signal from the LBMRx was fed to a commercial continuous-mode electronic dispersion compensation (EDC) - clock and data recovery (CDR) module (Vitesse VSC8240).



(a) (b)

Figure 6.4: (a) Structure of the optical line terminals and (b) the housing units for the LBMRx and EDC-CDR Modules.

In contrast to a conventional limiting BMRx, the LBMRx (discussed in section 5.4.1) enables preservation of the signal's pulse shape which can then be processed by the

EDC [253]. Within the testbed, static EDC was deployed in the OLTs; this was sufficient as the ONUs were located at the same physical distance from the OLTs hence they experienced the same amount of chromatic dispersion; however, in a real system, an adaptive EDC capable of operation on a burst-by-burst basis would be necessary to compensate for bursts experiencing different amounts of chromatic dispersion and having different pulse distortions. Here, the EDC taps were trained with a continuous-mode sequence and then frozen during burst-mode operation. The output of the EDC-CDR module was then sent to the frame synchroniser; the first processing block of the PON protocol implemented on the OLT-FPGA.

As outlined in the previous chapter, the FPGAs were also used to encode and decode the DS and US signals using the RS(248,216) forward error correction (FEC) algorithm, which has a theoretical performance threshold of 1.1×10^{-3}, [80]. The encoded data was received by each FPGA in blocks of 248 symbols and each symbol of 8 bits was processed by one Reed-Solomon (RS) decoder. A group of 8 interleaved decoders was used to process 8 FEC symbols (64 bits) simultaneously at a clock rate of ~161MHz for a bit rate of 10Gb/s. In particular, the BER was measured at the OLT-Rx in burst-mode operation for 2μs bursts whose basic structure is shown in Fig. 6.5. A 50ns preamble with a specific binary sequence was required for the LBMRx to facilitate the receivers gain adjustment on a burst-by-burst basis. A supplementary preamble of 150ns using PRBS 2^7-1 data was required for the static EDC-CDR module. In addition, a synchronisation word of known sequence with a temporal length corresponding to one FPGA clock cycle (~6ns) was required for the error correcting algorithm while the payload contained groups of 8 FEC blocks interleaved at the symbol level, where 1 symbol corresponds to 8 bits.

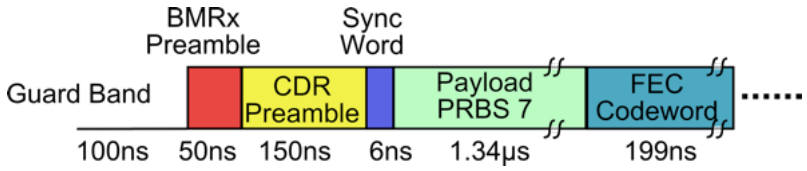
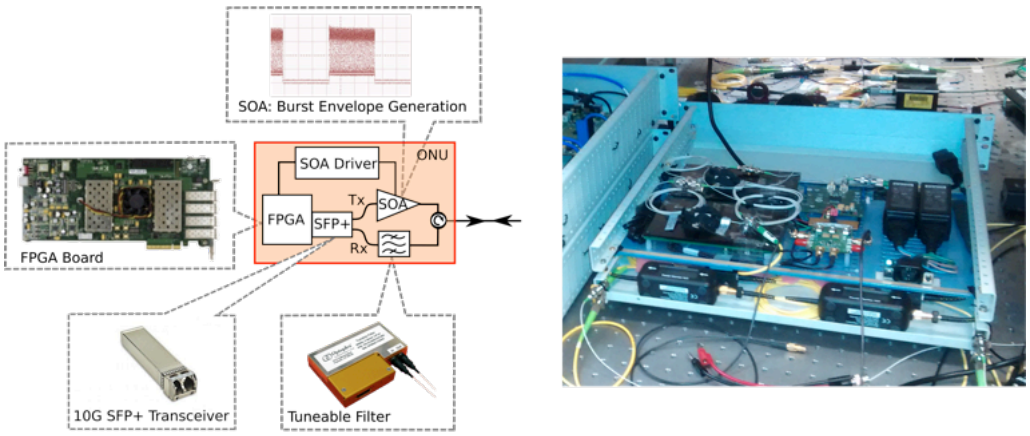


Figure 6.5: Basic structure of the upstream bursts.

Optical Network Units:

At the access edge, two ONUs were comprised of an FPGA test board (Xilinx Virtex7 XC7VX690T) as shown in Fig. 6.6, which implemented the custom LR-

PON protocol and also could mount a commercial SFP+ tuneable transceiver used as the ONU transmitter and receiver. The physical layer FPGA code implements the full burst structure (i.e. guard bands, preamble, synchronisation and burst envelope generation) while it also enabled a more accurate BER measurement (since the payload was a selectable PRBS) and also allows for synchronisation of the bursts with test and measurement and diagnostic equipment such as oscilloscopes. The SFP + receiver employs an APD with a worst case sensitivity of –24dBm at a BER of 1×10^{-12}, while the transmitter employs a chirp optimised externally modulated tuneable laser, with a typical 1dB dispersion penalty at 80km of standard SMF. The SFP+ receiver is preceded by a commercial tuneable filter with 35GHz 3dB bandwidth (~23GHz at 1dB), which could be controlled by serial communication via USB. An external SOA was also used after the SFP+ transmitter to create the burst envelopes and blank the ONU output during the periods of time where it was not transmitting data. This was necessary since the high speed modulator used in the transmitter has to be operated in continuous mode in order to obtain good performance since it is AC coupled. Idle data is hence transmitted from the FPGA in between bursts to maintain the DC balance of the sequence. The idle data signal is blocked by the SOA whose bias current is driven by a burst envelope signal generated by the FPGA. Up- and downstream signals were combined in the ONU using a circulator. The assembled ONUs were then placed in an equipment rack along with the CN instruments; this setup is shown on the left of Fig. 6.7.



(a) (b)

Figure 6.6: (a) Structure of the optical network units and (b) the housing units for the external gating SOAs used to generate the burst envelopes.

To emulate the effect of differential loss imparted on the US signals by the optical distribution network (ODN), the dynamic range (DR) between the bursts transmitted by both ONUs is generated by changing the value of a variable attenuator (VOA) in front of each ONU. For these measurements ONU 1 was chosen to be the 'loud' ONU transmitting the high power bursts and ONU 2 was chosen to be the 'soft' ONU, with low power bursts. The up- and downstream signals of the two ONUs were combined using a 1x2 (50/50) coupler. The combined output of the 1x2 coupler is connected to the ODN of the LR-PON architecture under test. In this way both the VOAs and the 1x2 coupler are effectively part of the ODN loss. This was been taken into account when measuring the ODN loss during the experiments. It should be noted that the use of an SFP+ transmitter with an external gating SOA is only an emulation which is sufficient for the purpose of this system demonstration; the transmitter used in a real ONU would have to be optimised for the specific application in terms of cost and performance. In fact, this requirement prompted the investigation presented in section 4.6, for which an SOA was monolithically integrated with a tuneable laser and absorptive modulator using low-cost, foundry compatible techniques [254]. Notably, the ONU receiver and tuneable filter assembly would also need to be optimised in terms of cost, while the FPGA would probably be replaced by an application specific integrated circuit (ASIC).

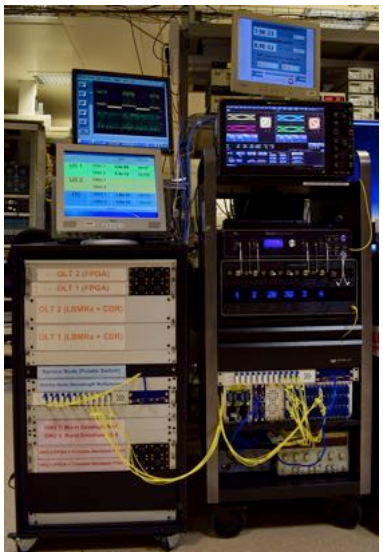


Figure 6.7: Testbed equipment: (L) rack containing the OLTs and ONUs and (R) 50GHz real-time oscilloscope and coherent receiver.

100G Point-to-Point Overlay

An important target of the DISCUS network architecture was to implement the "principle of equality" where all optical terminations in the network have equivalent connection capability independent of their geographical location. This can be achieved through flexible use of the wavelength domain, with channels capable of carrying a wide range of services and capacities. For example, the same access infrastructure could deliver in parallel 10Gb/s TDM-DWDM PON services for residential customers as well as point-to-point core services at 100Gb/s (or higher) for business customers located at any point within the network. Hence, this requires that the LR-PON must have the capability to offer such capacities to a few selected customers without disrupting the on-going TDMA traffic to and from the conventional customers attached to that network and that the high capacity link is also resilient against the impairments created by the TDMA traffic, such as, for example, linear and non-linear cross-talk.

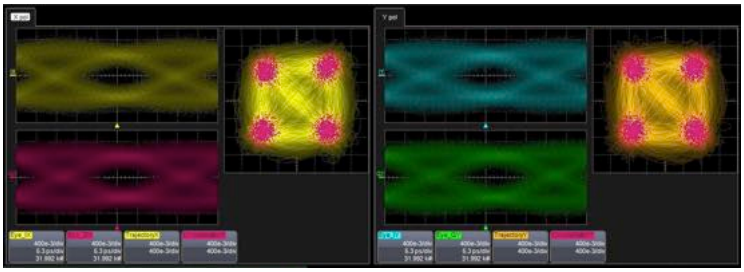


Figure 6.8: Constellation and eye diagrams for both polarisations of a 100G point-to-point DP-QPSK channel captured post-reception on a real-time oscilloscope.

As discussed in Chapter 3, the 100G point-to-point (P2P) channel deployed in the DISCUS testbed used dual-polarisation quadrature phase-shift keying (DP-QPSK) as it is the most commonly adopted solution for 100G in long haul and metro optical channels. Moreover, within the experimental testbed, the signal was generated using a prototype transponder that was on loan from a commercial vendor. The constellation and eye diagrams for both polarisations of the 100G channel captured post-reception by the real-time oscilloscope (shown on the right of Fig. 6.7) is presented in Fig. 6.8. The 100G channel was added to the network at similar entry points as the US and DS ballast channels which can be seen in Fig. 6.14 and Fig.6.17 for the urban and rural network designs respectively. The transponder included an

internal soft-decision forward error correction (SD-FEC) encoding technology that uses a low density parity check (LDPC) code and features an overhead of up to 20% resulting in an actual line rate of up to 128Gb/s. Typically, another layer of FEC is then applied by external components (i.e. standard Reed-Solomon); however, this was not implemented for this transponder, hence, only the pre-FEC BER is measured and an FEC threshold of 1.1×10^{-3} was assumed, as done for the 10G PON channels [19]. For the physical layer analysis, the optical carrier for the 100G DP-QPSK channel was set to 1533.47nm and 1551.32nm for the DS and US respectively. At this point, the author would like to gratefully acknowledge Oclaro™ for the loan of the 100G transponder.

LR-PON Wavelength Plan:

The wavelength plan for the LR-PON strongly depends on the technology of choice, especially with respect to the availability of suitable optical amplifier technologies within the desired wavelength region as discussed in the DISCUS deliverable D3.2 [255]. For instance, the C-band is typically used for the operation of long-haul networks because of the availability of mature components such as wavelength multiplexers and EDFAs which are a key enabling technology for operation in this wavelength region. Alternatively, other spectral regions of the fibre, such as the O-band (1260nm - 1360nm), continue to attract attention [256]. Here, SOAs are a promising technology as they offer spectral coverage over the entire wavelength region of the fibre (1250nm - 1600nm) at reasonable cost [257]. In particular, linear SOAs offer a constant modest gain (~ 15dB) and ASE output power with a moderate noise figure (~ 8dB) over a large range of input powers [258, 259]. However, the availability of mature transmitter and receiver components in these wavelength bands must be improved to increase the attractiveness of such an approach.

As outlined in the previous chapter, EDFAs are the primary amplifier technology of choice in this work as they are capable of supplying a large gain (> 30dB) to a high number of channels between 1525nm and 1565nm with a relatively low noise figure. This enables long-reach architectures in which a few EDFAs are deployed only at the CN and AN sites whose cost is then shared equally among the end users making them an attractive option for deployment. Nonetheless, this work also examines the feasibility of an alternative SOA-based AN configuration albeit using

C-band wavelengths in order to utilise the same ONU and OLT equipment within the physical layer testbed.

With respect to the wavelength allocation between the US and DS channels, band splitting or interleaving could be considered as the wavelength routing is achieved via the optical switch located in the CN. However, there is a significant advantage in using the band splitting approach as it could relax the specifications of the tuneable components (e.g. lasers, filters) which in turn would reduce the cost of such components. As shown in Fig. 6.9, in this work, the DS channels are located between 1530.33 and 1542.14nm while the US channels are located between 1548.51 and 1560.61nm, leaving a spectral guard band of approximately 6nm. The allocation of these wavelength bands is in response to the results presented in the previous chapter which demonstrates that the amplitude of residual transients induced by dynamic network events is less in the longer wavelength portion of the C-band (i.e. 1545nm - 1565nm), hence, it is more suitable for burst-mode traffic. Notably, this strategy also serves to demonstrate a fully loaded system that can be used to stress the amplifier technology and non-linearities in the fibre. However, it should be noted that even though the system (in particular the EDFAs) are designed to support 40 channels in both transmission directions, the wavelength plan adopted in this demonstration can only support 32 channels in order to use available band splitting filters.

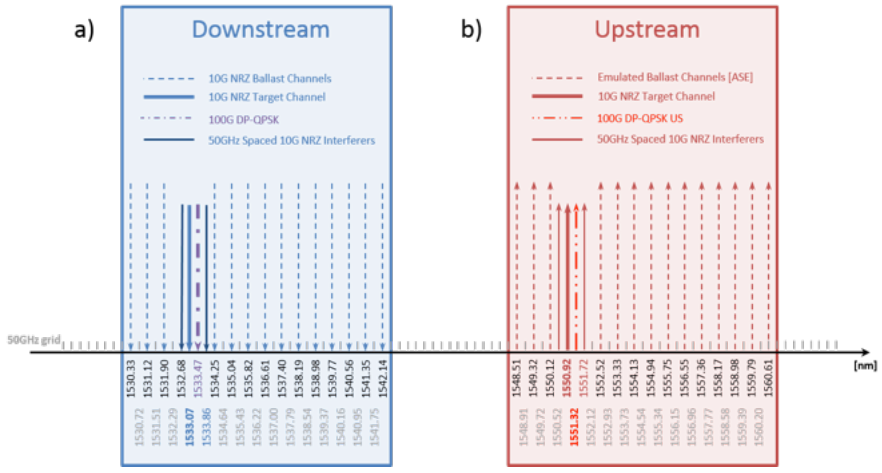


Figure 6.9: Wavelength transmission bands: (a) downstream, (b) upstream.

The DS ballast channels were generated by a bank of 100GHz spaced distributed feedback (DFB) lasers which were multiplexed using a thermally stabilised arrayed

waveguide grating (AWG) before being modulated at 10Gb/s with a non-return to zero on-off keying (NRZ-OOK) pseudorandom binary sequence using a lithium niobate ($LiNbO_3$) Mach-Zehnder modulator (MZM). All DS ballast channels were linewidth broadened using a 3% amplitude, 2kHz frequency, sinusoidal current modulation to prevent impairments due to Stimulated Brillouin Scattering (SBS). A wavelength selective switch (WSS) was used to level the power and to selectively remove channels in order to inject the live 10G PON channel generated by the OLT (1533.07nm), a 100G DP-QPSK channel (1533.47nm) and a continuous-mode 10G NRZ-OOK interfering channel (1533.86nm) spaced at 50GHz from the 100G P2P channel. The power of four 10G channels neighbouring the 100G P2P channel (two at lower wavelengths, two at higher wavelengths) were set to the nominal DS channel power while the power of the remaining 13 channels was adjusted in order to obtain an overall DS power equivalent to 40 DWDM channels at nominal power. The optical spectrum of the DS channels is shown in Fig. 6.10. For experimental convenience, the ballast channels coupled into the testbed at the primary CN, after the Polatis™switch and before the booster amplifier were always present to allow the use of simpler EDFA controls in the DS link.

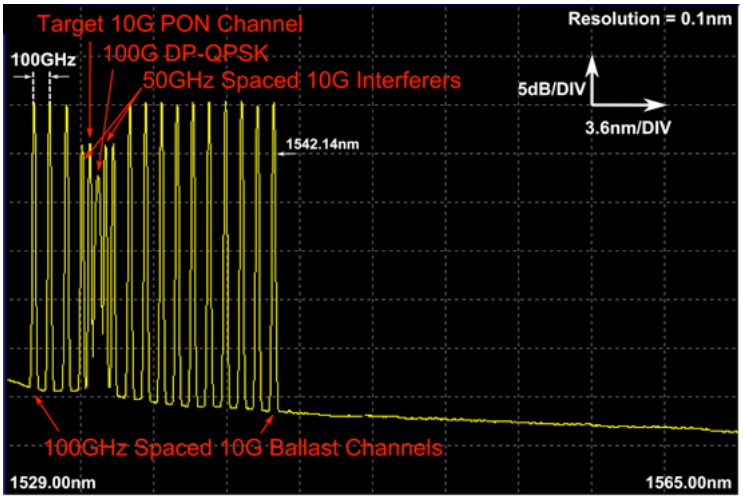


Figure 6.10: Downstream spectrum: channels launched from the core node.

The US ballast channels were generated using amplified spontaneous emission (ASE) generated from a cascade of an EDFA and SOAs. The spectral profile of the emulated US channels is carved using a wavelength selective switch (WSS), which is also

used to flatten the ASE by applying attenuation on a channel-by-channel basis. The SOAs used to amplify the ASE were driven by a function generator which enabled the application of an amplitude modulation in order to emulate the power variation from traffic patterns due to burst-mode operation. The ASE spectrally emulates 31 US DWDM channels (from 1548.51nm to 1560.61nm) with a gap carved to allow the insertion of a continuous-mode 10G NRZ-OOK fronthaul channel (1550.52nm), the target 10G PON channel generated by the two ONUs (1550.92nm), a 100G DP-QPSK channel (1551.32nm) and a second continuous-mode 10G NRZ-OOK channel (1551.72nm) used as a second interferer to the 100G P2P channel. The target 10G PON channel generated by the ONUs is typically recognisable because of the high average power due to the large DR, which means that one of the ONUs is transmitting power larger than the nominal channel power used for the ballast channels, the 100G channel and the NRZ interferers.

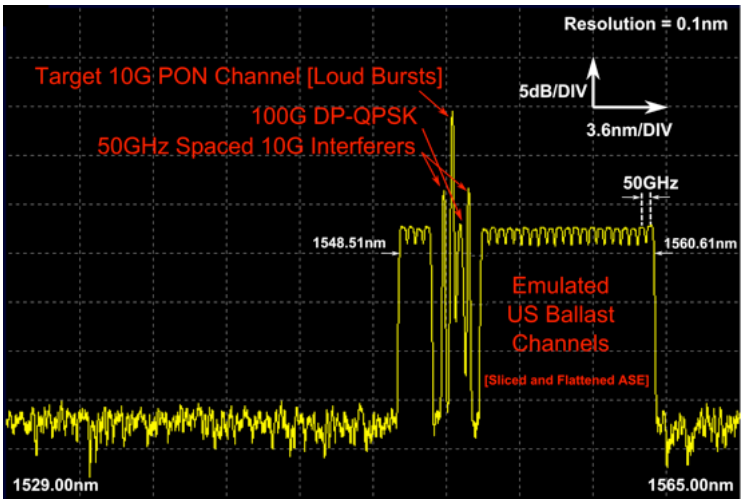


Figure 6.11: Upstream spectrum with 'loud' target channel bursts.

In the spectrum provided in Fig. 6.11, both ONUs are set to transmit 'loud' bursts, hence they have a significantly larger average power. In addition, the per-channel power of the US ballast channels carved using the WSS which has a flat-top filter profile with a 50GHz channel bandwidth is more accurately captured using a larger resolution bandwidth (i.e. 0.5nm, ~62.5GHz) on the OSA. Consequently, using a resolution bandwidth of 0.1nm, the observed power appears lower than the nominal channel power. The emulated US ballast channels were inserted into the ODN using

a spare splitter arm and the power was adjusted to emulate the power equivalent of 36 DWDM channels at the nominal channel power.

6.1.1 Single Amplifier Node ('Tree-Like') Architecture

Densely populated areas can be efficiently connected by deploying a simple optical access architecture where each LR-PON served by the backhaul fibre cable is supported by a single amplifier node. Each AN connects to a totally passive ODN, supporting 512 or 1024 users and reaches of up to 20km, forming a tree-like topology [17]. In this work, a dynamically reconfigurable TDM-DWDM LR-PON supported by a single AN which utilises EDFAs or SOAs is demonstrated as an efficient solution to enable the convergence of multiple services and user types on a single architecture for urban deployment. Fig. 6.12 illustrates the high-level network concept while the details of the physical layer testbed are presented in Fig. 6.14.

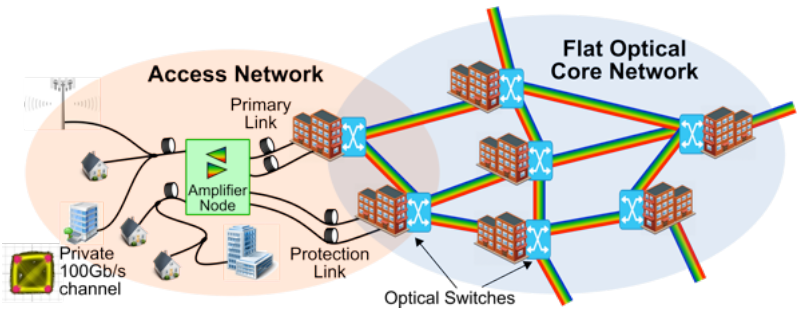


Figure 6.12: Proposed network concept for urban access deployment.

As indicated in Fig. 6.12, part of the total ODN split was located in the AN; a 4x4 split was used in the EDFA-based AN while a 2x4 for was used in SOA-based ANs. This is used to combine up- and down-stream traffic and also provides access to a redundancy path in the backhaul link for resilience and protection. The protection link was only implemented for the EDFA design and consisted of just a few metres of fibre to achieve the maximum differential reach with the primary path. Optical attenuators were used to emulate the end-of-life standard SMF attenuation (0.3dB/km) and realistic splitter losses in the ODN including excess loss [260].

EDFA-Based Amplifier Node:

In the EDFA-based AN (Fig. 6.13 and Fig. 6.14(a)), the DS signals coming from the primary backhaul link were amplified using a two stage EDFA configuration providing an overall gain of 38dB. A module of dispersion compensating fibre (DCF), equivalent to -40km (~ -680ps/nm at 1550nm) of standard single mode fibre (SMF) was used mid-stage to partially compensate the primary DS link as the SFP+ has a dispersion tolerance of ~ 80km. The high power second stage EDFA, with a maximum output of +30dBm was shared between the primary and secondary DS link in order to reduce the number of EDFAs in the laboratory testbed; however, in a real deployment scenario the secondary path should employ a separate device to increase resilience. A 3dB coupler was used mid-stage to provide access to the second stage EDFA from the secondary path. Due to the high power launched into the ODN from the amplifier node, the backscattered power was comparable with the power of the US signals and hence it was subtracting gain and power from the US EDFAs. To remove the Rayleigh backscatter, band blocking (red/blue) filters were used in front of the US amplifiers. The US primary and secondary path EDFAs were each connected to to a port of the 4x4 splitter through a red/blue C-band filter in order to remove potential back-reflection from the high power DS signals. All the EDFAs used in the US were commercial devices with fast gain stabilisation in order to reduce the impact of gain transients induced by burst traffic [228]. In contrast to the DS link, it was not necessary to use optical dispersion compensating modules (i.e. DCF) since electronic dispersion compensation was used in the OLTs.

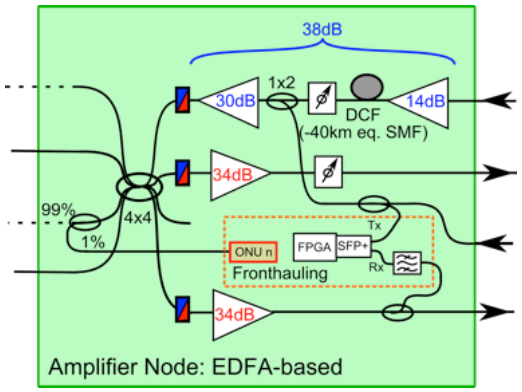


Figure 6.13: Illustration of the EDFA-based amplifier node configuration used in the 'tree-structured' (urban) LR-PON configuration.

As the long-reach of the proposed architecture can introduce round-trip transmission times of ~1ms; this is generally not compatible with the ultra-low latency required by some wireless architectures and some future services discussed for 5G [261]. This latency issue could be addressed by placing small active nodes containing an ONU and the necessary processing equipment in the AN where a dedicated wavelength could be used to carry a common public radio interface (CPRI) channel from the AN to the remote site over the distribution network. To investigate the feasibility of this approach, a fronthaul channel was also emulated for the EDFA-based single AN physical layer; this was achieved by adding an SFP+ transceiver driven by an FPGA located in the AN at one ODN arm as shown in Fig. 6.13. Architecturally, the backhauling part of the wireless signal can be carried over one of the 10G PON channels and terminated in the AN using an ONU connected to a 1% power tap on one of the ODN 4x4 ports.

SOA-Based Amplifier Node:

The SOA-based AN presented Fig. 6.14(b) was developed by researchers from Nokia Bell Labs in Stuttgart. It was comprised of a chain of SOAs for individual amplification of DS and US wavelength bands. The chained SOA configuration was implemented in order to bridge a large loss budget by offering the signals twice the gain over a large range of input powers. Red/blue C-band filters are used to separate the US and DS bands at each instance. The amplifier chain is established by equipping each branch of a 2×4 splitter with an SOA for the down- and up-stream direction, respectively. In the experiments, the DS direction is equipped with an SOA at the primary backhaul connection as well as one of the 2×4 splitter branches. In the US direction, each of the ×4 branches include an SOA to consider the effect of noise funneling. The effective small-signal gain of the entire amplifier node is 18dB at 1550nm in US and 19dB at 1530nm for the DS direction. The effective noise figure of the amplifier node is around 13dB in the US direction including the noise funneling contributions and about 9dB in the DS direction. The 3dB saturation input power of the AN is +1dBm in the US direction and −2dBm in the DS direction, while the 1dB saturation input power is −5dBm and −6dBm respectively. To optimise the physical layer with respect to the available gain from the SOA-based AN, the outside plant comprised a 62km long feeder fibre while 12km of SMF was used in the ODN alongside splitters and VOAs in order to adapt the loss budget.

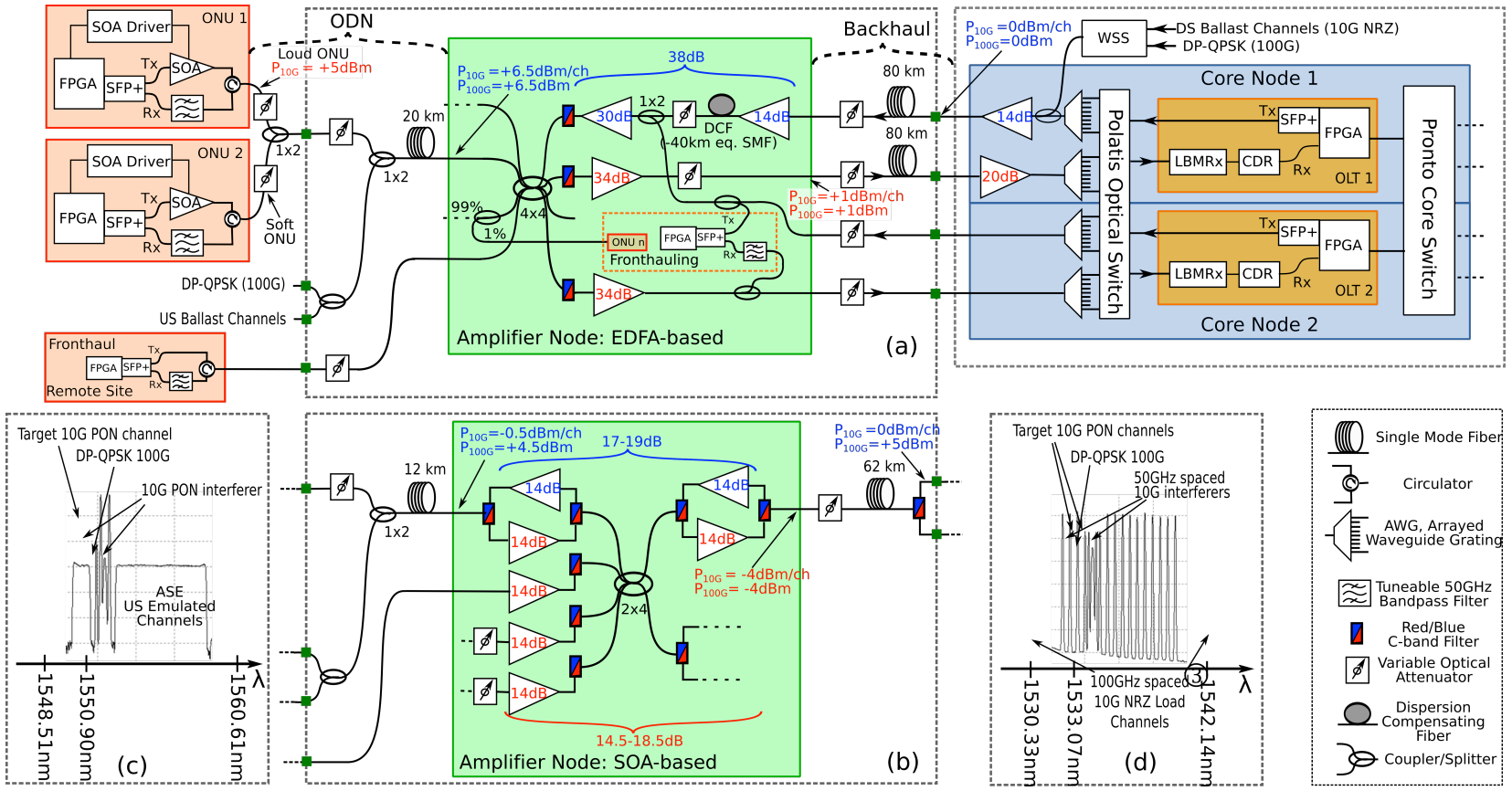


Figure 6.14: The LR-PON physical layer proposed for urban areas With (a) EDFA-based and (b) SOA-based amplifier nodes alongside (c) upstream and (d) downstream spectra. (Reproduced from [19])

6.1.2 Chained Amplifier Node ('Open-Ring') Architecture

As discussed in 5.1.2, the communities to be served in rural areas can be much smaller than the total achievable LR-PON split, therefore the conventional tree-structured design would be considerably underutilised, directly increasing the cost per customer. The utilisation and efficiency of rural access deployment can be improved using an alternative TDM-DWDM PON structure that uses a chain of ANs. The architecture is based on the structure of metro rings, where two fibres with counter-propagating traffic connect a chain of nodes. In the proposed design, the ring is open and the two head-ends are the CNs, while the intermediate nodes are the ANs where the ODNs are optically aggregated into the system. The 'open-ring' network concept for rural deployment is presented in Fig. 6.15 while details of the physical layer testbed are presented in Fig. 6.17.

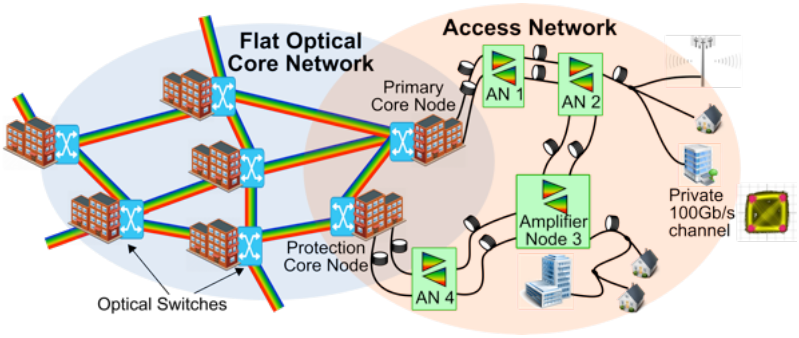


Figure 6.15: Proposed network concept for rural access deployment.

In the experimental testbed, a chain of 4 ANs, connected by fibres links between 0km (representing co-located ANs used to facilitate the provision of a higher split in a specific area) and 40km, is demonstrated; this is easily adequate to cover the typical distances between today's local exchanges or central offices. The total physical reach of the chained AN configuration is 120km, which includes an ODN length of 20km. Commercially available wideband gain-stabilised EDFAs are employed as in-line amplifiers in the ANs to reduce the impact of gain transients caused by the bursty nature of the US traffic [20]. Within the ANs, an additional 4x4 splitter was used to connect the DS 'drop' ports (x2) and the US 'add' ports (x2) of the ODN to the 'open-ring' feeder fibres so that in the event of a fibres cut or of a failure in the primary CN or within an AN, the traffic can be routed to the protection CN, hence providing the same intrinsic resilience as metro rings. Four asymmetric 1x2

80/20 couplers are used in each AN to add and drop the traffic from the links in both directions. At both entry points for US traffic, the 80% port of the asymmetric couplers minimises the addition loss (~1dB). In contrast, the exit points utilise the 20% port of the asymmetric couplers (loss ~ $7dB$) thus allowing the lower loss 80% port to be used for traffic forwarded to the next AN. A band filter is required to isolate the DS channels dropped to each ODN as the presence of US channels would deplete the gain available from the 'drop' amplifier while Rayleigh backscattering and reflections in the ODNs could interfere with US traffic. For practical reasons, within the testbed, ANs 1 and 4 were fully implemented (Fig. 6.1.2(a)) while ANs 2 and 3 were only partially realised using optical attenuators to emulate the loss of the 80/20 couplers (Fig. 6.1.2(b)). A module of dispersion compensating fibre (DCF), equivalent to -80km of SMF (~ -1370ps/nm at 1550nm) was used in AN 2 to partially compensate the primary DS link while an identical module was installed in AN 3 to compensate the US link in addition to the static EDC-CDR module located in the OLT of the primary CN.

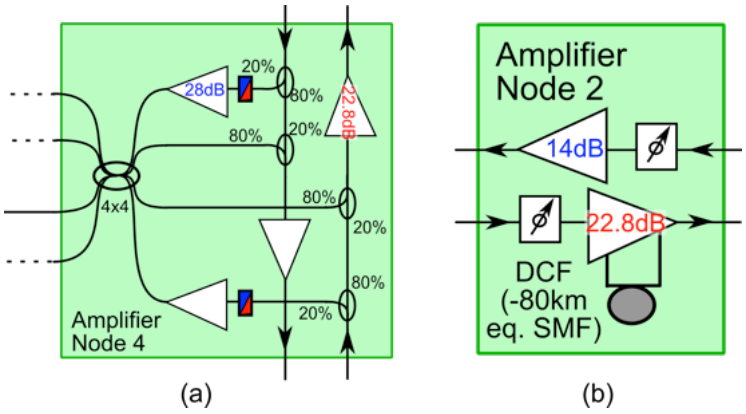


Figure 6.16: EDFA-based amplifier nodes for the 'open-ring' configuration: (a) fully and (b) partially implemented.

To study the feasibility of the 'open-ring' physical layer, the ODN from AN 4, which is the furthest from the primary CN at a fibre equivalent physical reach of 100km was connected to both ONUs, the 100G (DP-QPSK) channel and the US ballast channels. It should be noted that even though some of the nodes were not fully realised, the power budget and number of optical amplifiers in the system (with the required gain and saturated output power) as seen by traffic to/from the ODN of AN 4 are the same as that for a fully implemented system. In addition, only the primary path was considered for the 'open-ring' demonstration.

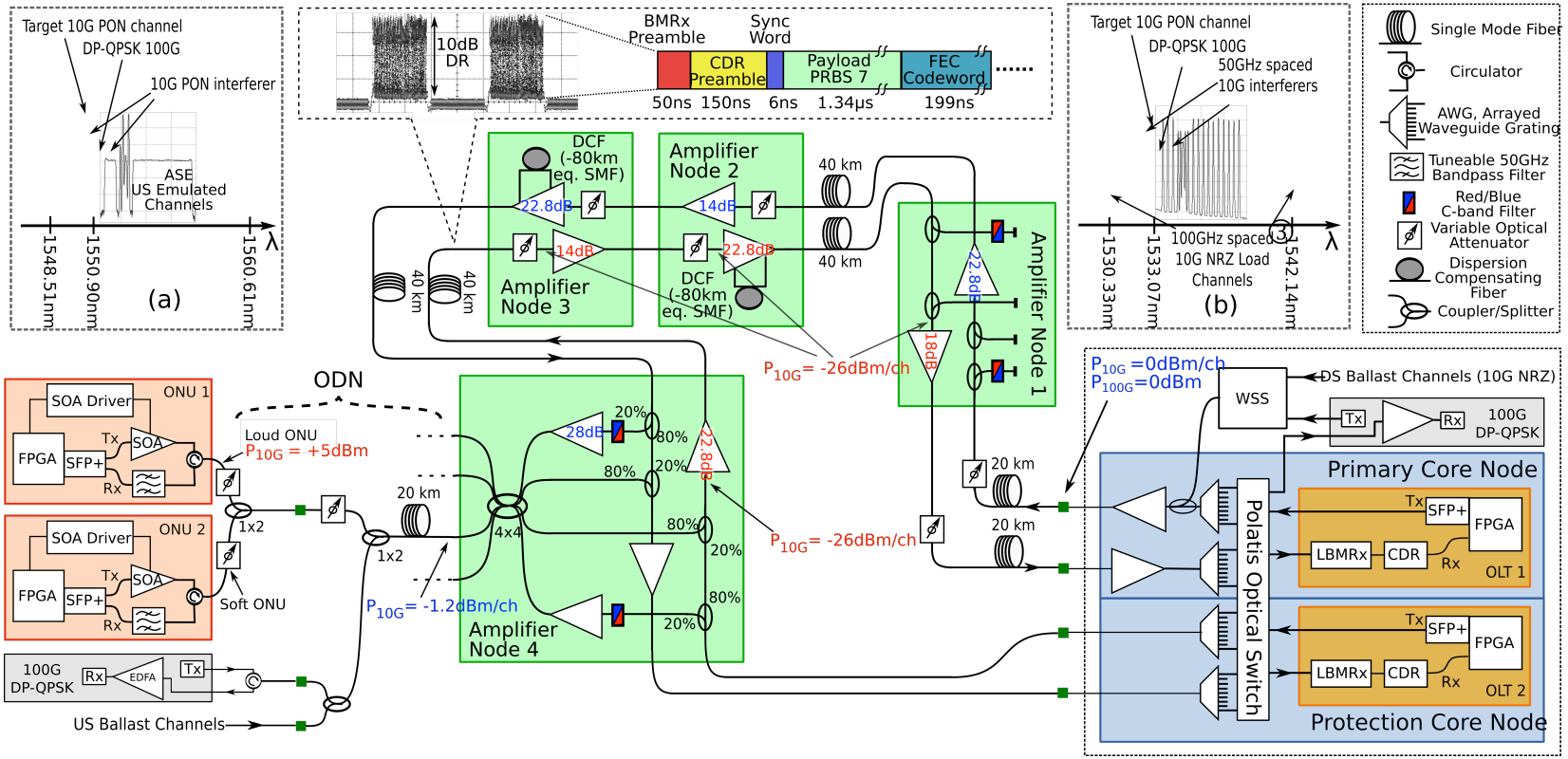


Figure 6.17: The novel LR-PON physical layer for rural areas using chained amplifier nodes alongside the (a) upstream and (b) downstream spectra. (Reproduced from [20])

6.2 Experimental Results

This section presents the results from the physical layer characterisation of the experimental testbed. Unless otherwise stated, the ballast channels were active in order to provide an emulated load of 40 DWDM channels in both transmission directions. It is also important to note that attenuators were used in the ODNs to emulate the end-of-life standard SMF attenuation (0.3dB/km) and realistic splitter losses including excess loss [260]. For instance, a worst-case loss of 3.5dB is assumed for each x2 split.

6.2.1 10G TDM-PON and Fronthaul Channels

Downstream Characterisation:

To evaluate the performance in the DS direction, the BER (pre- and post-FEC) of the 10G PON target channels were measured internally using the ONU FPGAs as a function of the ODN loss for both architectural designs; the corresponding results are presented in Fig. 6.18. While the results of the 'tree-structured' and 'open-ring' LR-PON designs are provided here side-by-side, a direct numerical comparison should be avoided as the topologies are too dissimilar, having been designed for different deployment scenarios; each having a unique power and OSNR budget as demonstrated in the previous chapter.

In this analysis, the main points of comparison focus on the physical reach and total number of users that can be supported by each infrastructure. With this in mind and by considering an FEC threshold of 1.1×10^{-3}, the DS physical layer characterisation results presented in Fig. 6.18 demonstrate that the urban (single AN) architecture can support an ODN loss of at least 36dB. This value corresponds to a 256-split with 20km of standard SMF with a system margin of ~2dB. Considering the additional x4 split within the AN, an overall split ratio of 1024 (256x4) can be achieved with a total physical reach of 100km. Alternatively, the 'open-ring' (chained AN) architecture was shown to support an ODN loss of at least 27dB; this corresponds to a 64-split plus 20km of fibre with no system margin and an overall split ratio of 256 (64x4) per AN. Assuming a fully realised system with 4 ANs, a total split ratio of 1024 can be achieved for the open-ring configuration with a total

physical reach of 120km. In addition, the proposed fronthaul channel configuration demonstrates error-free transmission (BER $< 1 \times 10^{-12}$) without FEC for an ODN loss of up to 28dB; this value corresponds to a 64-split ODN with 20km of fibre which is effectively the same as that for the 10G TDM-PON target channel.

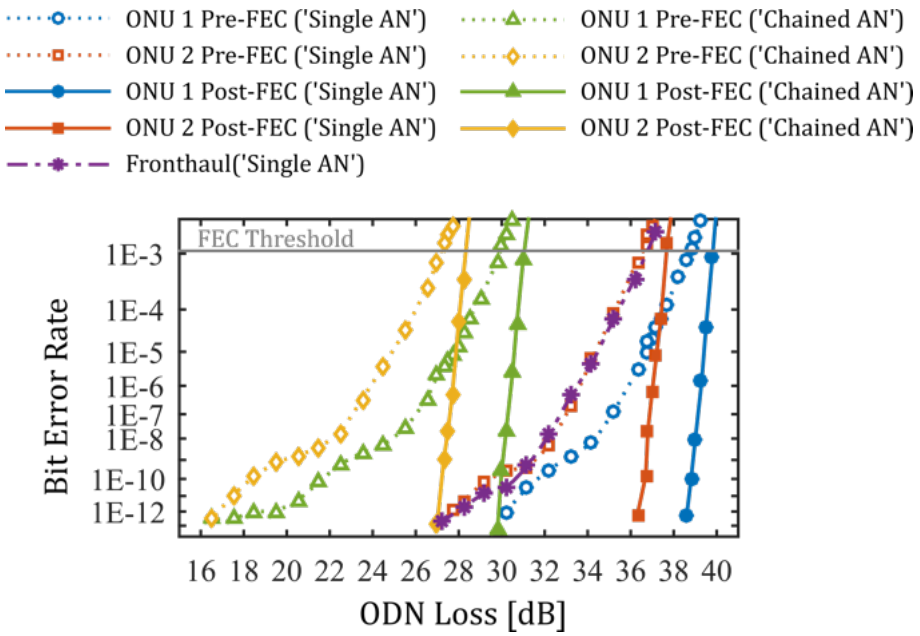


Figure 6.18: Downstream performance of the 10G PON channels as a function of the ODN loss.

In both LR-PON architectures, a performance discrepancy of < 3dB is present between ONU 1 and ONU 2 due to a variation in receiver sensitivity; this difference is within the tolerance of commercial SFP+ transceivers. The post-FEC results confirm that a BER of $< 1 \times 10^{-12}$ is obtained with a confidence interval of 95% for a pre-FEC BER below the theoretical threshold of 1.1×10^{-3}. Notably, due to the insertion loss of the optical coupler preceding the CN EDFA, the maximum OSNR of the 10G target channel at the output of the CN was ~26dB. In fact, the ballast channels and the private 100G channel enter the CN EDFA with relatively low power due to the high accumulated insertion loss of the WSS, the optical coupler and the various passive elements in between; this results in an additional OSNR degradation. While this is highly unlikely to occur in a real network where the transmitted OSNR should be substantially higher (i.e. >30dB), it represents a worst case scenario study.

In practice, through the use of commercial C-band gain-flattened EDFAs, pas-

sive optical components (filters, AWGs, etc.) and dispersion compensation, the performance of each DWDM channel should not vary significantly within the DS transmission band outlined earlier in Fig. 6.9. As a result, in order to demonstrate the physical layer feasibility it is sufficient to emulate a spectral load of 40 DWDM channels and select a typical target channel for analysis.

In the case of the tree-structured LR-PON using the SOA-based AN, the performance of the DS link was characterised by monitoring the pre-FEC BER as a function of the ODN loss. As in the case of the EDFA-based AN design, a performance discrepancy of < 3dB is present between both ONUs near the theoretical FEC threshold of 1.1×10^{-3}, due to a variation in receiver sensitivity; this difference is attributed to a sensitivity variation between the SFP+ receivers and is within the manufacturers performance tolerance. The results, presented in Fig. 6.19(a), indicate that the SOA-based AN supports an ODN loss of at least 28.2dB. This value corresponds to a 128-split plus 12km of fibre; if the additional x4 split within the AN is considered the system can support up to 512 users, however, it should be noted that there is no system margin.

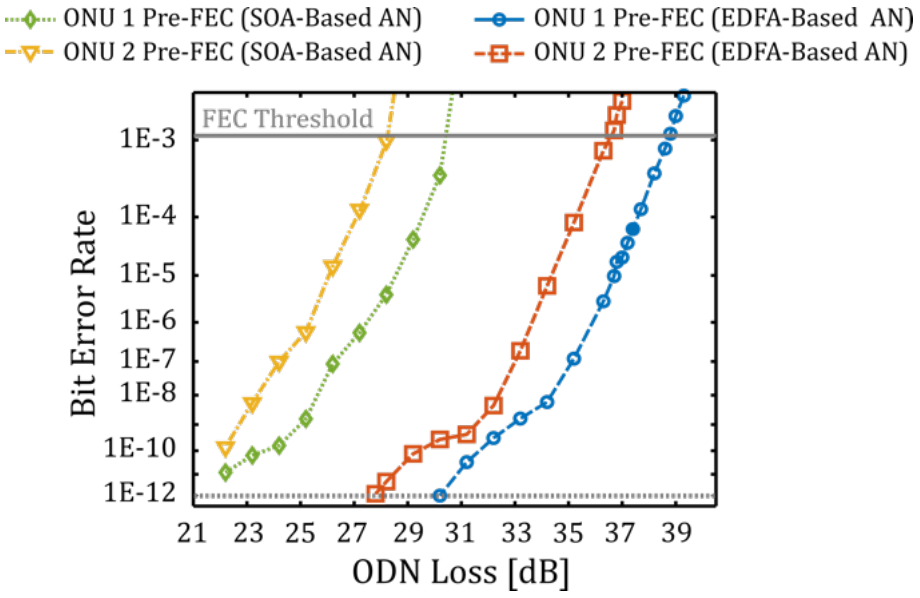


Figure 6.19: Comparing the downstream pre-FEC BER of the 10G NRZ target channel as a function of the ODN loss in the 'tree-structured' (single AN) LR-PON architecture using EDFA and SOA-based amplifier nodes.

Compared to the system with the EDFA-based AN; the SOA-based AN design is a performance difference of ~8dB which roughly corresponds to the difference in power launched into the ODNs. The launch power is limited in the SOA case by the saturation power of the available devices. In particular, the total output power measured from the SOA-based AN was ~+16dBm which is beyond the 3dB saturation power of the SOAs used in the system (+14dBm). For single channel operation; these conditions should produce severe patterning which would impair the performance of the 10G PON channels; however, as the channels are decorrelated and the per-channel power is below the 3dB saturation power the performance impact of patterning is reduced.

Upstream Characterisation:

To evaluate the performance of the burst-mode link, the power of the 'loud' bursts transmitted from ONU 1 was maintained at a value close to the overload of the LBMRx with an ODN loss of 16dB and 15dB for the single AN (urban) and chained AN (rural) systems respectively. The ODN loss was then varied from 15dB to 35dB for ONU 2 only in order to adjust the dynamic range (DR) of the burst powers reaching the LBMRx in the OLT as demonstrated in Fig. 6.20. In this way, the 'loud' bursts from ONU 1 act as a worst-case interferer for the 'soft' bursts from ONU 2, with respect to the LBMRx operation.

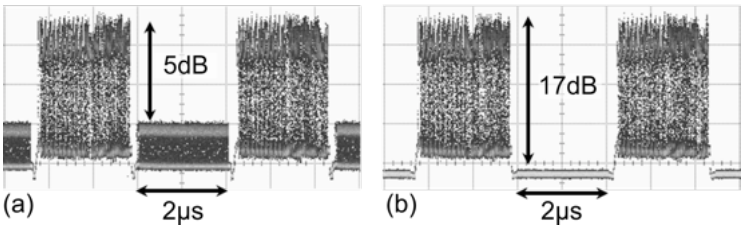


Figure 6.20: Consecutive bursts from ONU 1 ('loud') and ONU 2 ('soft') launched into the ODN with (a) 5dB DR and (b) 17dB DR.

The comparison of the pre- and post-FEC BER for ONU 2 in Fig. 6.21 confirms that the FEC threshold of 1.1×10^{-3} is applicable also in burst-mode operation in the US link. The results demonstrate that the single AN (urban) network design is capable of supporting an ODN loss of up to 34dB which corresponds to a DR of 18dB and

a 256-split ODN with 20km of fibre; however, there is no system margin. If the additional split within the AN is considered, an overall split ratio of 1024 (256x4) can be achieved. Alternatively, for an ODN loss of 30.5dB, the urban design can support a 128-split ratio over 20km of fibre with a system margin of ~3dB; this gives an overall split of 512 (128x4). In addition, the emulated fronthaul channel configuration demonstrates error-free transmission (BER <1E-12) without FEC for an ODN loss of up to 28dB; this value corresponds to a 64-split ODN with 20km of fibre. Notably, this channel shows a slightly better BER performance than the 10G TDM-PON channels as it is not transmitted through the link towards the primary CN; hence, it maintains a higher OSNR. Moreover, this channel constitutes a continuous-mode link, therefore it does not require the use of a burst-mode receiver.

For the open-ring system, the results demonstrate that ONU 2 operates with a post-FEC BER $< 1 \times 10^{-12}$ for an ODN loss of up to 30dB. This is equivalent to a 64-split ODN with 20km of fibre with a performance margin of ~3dB and a DR of 15dB at the LBMRx. An overall split ratio of 256 (64x4) can be achieved when the additional AN split is accounted for while a fully implemented system of 4 ANs can provide an overall split of up to 1024 (256x4). In both system designs, the post-FEC BER of ONU 1 was $< 1 \times 10^{-12}$; therefore, the performance ONU 1 is not reported in Fig. 6.21.

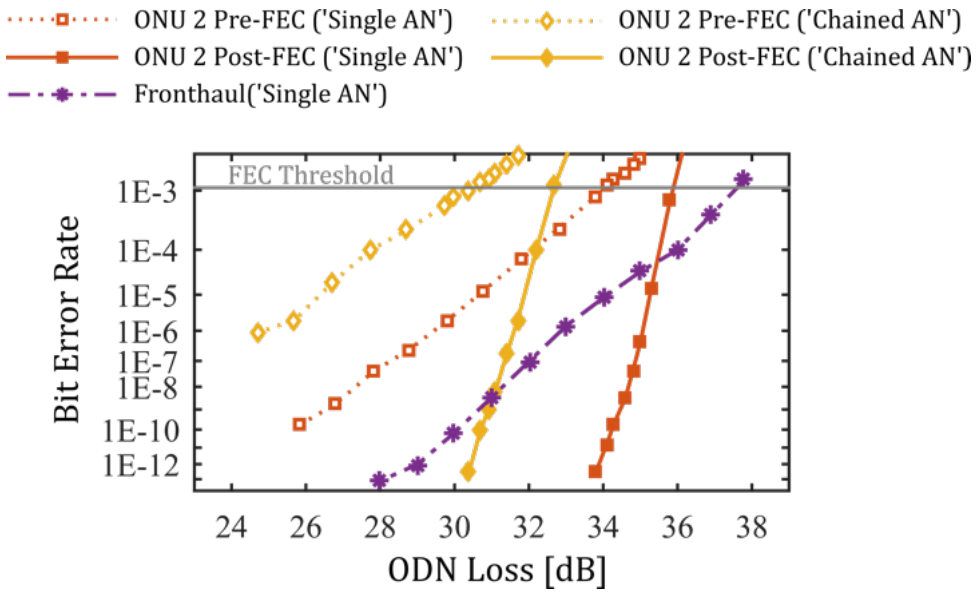


Figure 6.21: Upstream performance of 10G channels as a function of the ODN loss.

With respect to the tree-structured LR-PON architecture supported by the SOA-based AN, the US link was characterised using the same technique as that used for the EDFA-based configuration. In this case, the ODN loss for ONU 1 was maintained at 16dB while the ODN loss for ONU 2 was varied from 16dB to 35dB in order to adjust the DR of the burst powers reaching the LBMRx in the OLT. As before, the 'loud' bursts from ONU 1 act as a worst-case interferer for the 'soft' bursts from ONU 2, with respect to the LBMRx operation. The corresponding results, presented in Fig. 6.22, show that the pre-FEC BER of ONU 1 was below the FEC threshold for all values of DR; more precisely between 1×10^{-7} and 1×10^{-8} for the case of the SOA-based AN and $\sim 1 \times 10^{-12}$ for the EDFA-based AN. On the other hand, the results obtained for ONU 2 demonstrate that this SOA-based AN can support a DR of up to 15.5dB with a corresponding ODN loss of 31.5dB. This value corresponds to a 128-split with 12km of fibre with a 3.4dB margin; giving a total split ratio of 512 when the additional AN split is considered. As in the case of the EDFA-based AN; the results demonstrate that the SOA-based AN is capable of supporting a higher DR than that introduced by the non-uniform loss of the ODN splitters, which can be up to 12dB for a 512-split ratio using realistic splitter losses [260]. As the US performance of the tree-structured architecture is OSNR limited, the EDFA-based AN exhibits a slightly better performance compared to the SOA-based AN due to the lower noise figure values.

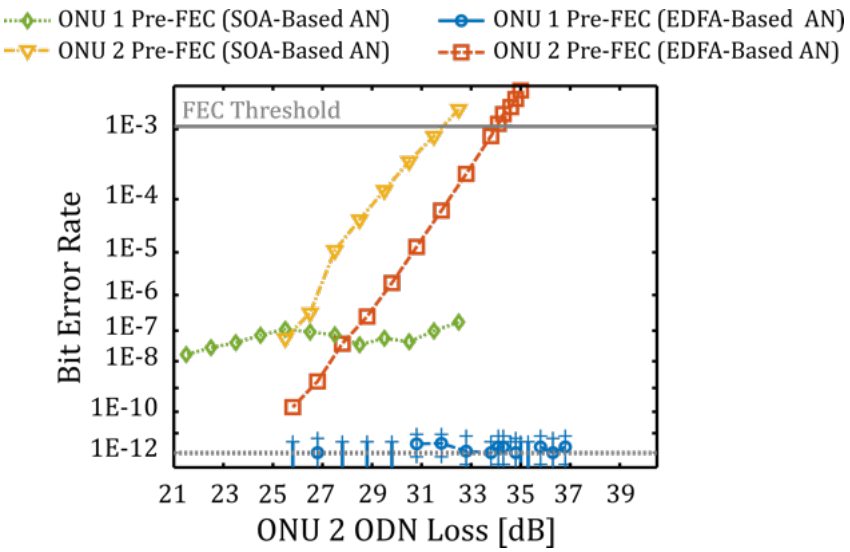


Figure 6.22: Pre-FEC BER performance of the 10G NRZ target channel for upstream transmission in the 'tree-like' architecture for SOA- and EDFA-based amplifier nodes.

6.2.2 Evaluating the FEC Performance in the 'Open-Ring'

To evaluate the FPGA-based FEC implementation, the BER (pre- and post-FEC) performance of the 10G PON target channel in the 'open-ring' (chained AN) network design was compared with the expected theoretical FEC behaviour which is outlined in the previous chapter. For instance, it can be seen from the results presented in Fig. 6.23 that the BER measurements taken from the open-ring testbed closely follow the theoretical curves for both DS (a) and US (burst-mode) transmission (b) while demonstrating that the measured FEC threshold is close to the expected theoretical value of 1.1×10^{-3} for the RS(248,216) code. These results indicate that the system performance converges towards the theoretical behaviour for both down- and upstream (burst-mode) transmission and that the BER above and below the FEC threshold is predicted correctly. Notably, this result is a further validation the FPGA-based FEC implementation presented in Chapter 5.

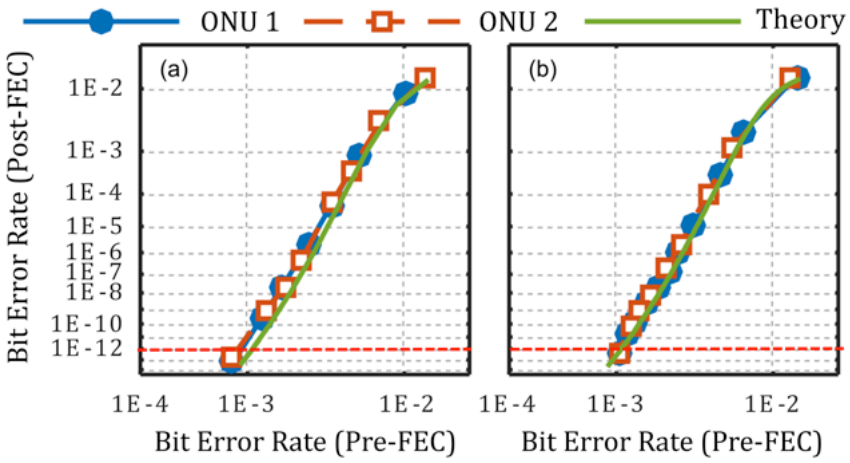


Figure 6.23: FEC performance evaluation: (a) downstream and (b) upstream.

Performance Impact of Residual EDFA Gain Transients:

As outlined in the previous chapter, the wide-band (DWDM) gain-flattened EDFAs deployed within the testbed used a dynamic gain control system to suppress transients induced by sudden change in input power such as that caused by the addition or reduction in the number of active channels. These commercial amplifiers were not specifically designed for burst-mode operation; however, as demonstrated

previously, the level of transient suppression they provide should be sufficient for such applications. With this in mind, the impact of accumulated residual EDFA transients within the open-ring (chained AN) testbed which has up to five chained EDFAs on the primary link was studied by dynamically varying the amplitude of the ASE used to emulate the US channels was modulated asynchronously with respect to the bursts from both ONUs in order to imitate the bursty nature of US traffic. Of the 40 emulated DWDM channels, 36 were added and dropped for various repetition frequencies using a 50% duty cycle giving a power ratio of ~10dB. The peak-to-peak amplitude of the resulting transient is presented in Table 6.1 while the profile of the induced power excursion for a repetition frequency of 10kHz (measured using a continuous-wave probe channel) is shown in Fig. 6.24.

$T_{Add/Drop}$ [μs]	Peak-to-Peak [dB]
300	1.2
100	1.2
50	1.1
20	1
10	0.6

Table 6.1: Analysis of accumulated residual EDFA transients.

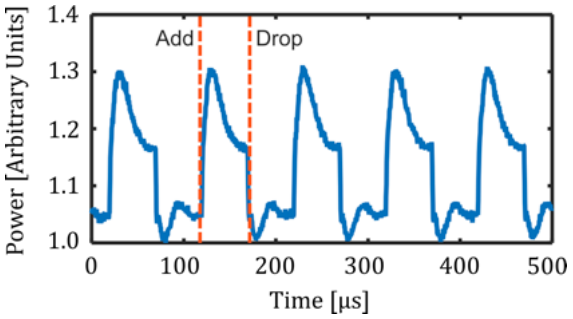


Figure 6.24: Temporal profile of an accumulated residual EDFA transient on a CW probe channel at 1551.72nm for $T^{ASE}{}_{Add/Drop} = 100\mu$s.

The peak-to-peak power variation at the OLT observed on a continuous wave probe channel at 1551.72nm (~100GHz from the 10G PON target channel) is presented in Table 6.1 while the profile of the transient induced by a 100μs add/drop period is shown in Fig. 6.24. These results indicate that peak-to-peak amplitude of the transient is dependent on the modulation frequency; however, no significant increase in amplitude was observed beyond an add/drop period of 100μs. The latter observation may be attributed to the performance of the EDFA gain control system which has been designed for ROADM (reconfigurable optical add-drop multiplexer) applications where power variations from dynamic add/drop events occur on a timescale

on the order of milliseconds (~kHz).

The US performance impact of the accumulated residual EDFA transient induced by an add/drop period of 100μs was examined by repeating the US characterisation of the 10G PON target channel. Using the experimental method outlined previously in section 6.2.1, the BER of ONU 2 was measured at the OLT in burst-mode operation for 2μs bursts where the power of the 'loud' bursts from ONU 1 was maintained at a value close to the overload of the LBMRx with an ODN loss of 15dB. The ODN loss was then varied from 15dB to 35dB for ONU 2 only in order to adjust the DR of the burst powers reaching the LBMRx in the OLT.

The results presented in Fig. 6.25 indicate that a marginal performance impact of ~0.5dB is present for a post-FEC BER ~ 1×10^{-12}. This penalty is not present for a pre-FEC BER ~ 1×10^{-3}; therefore, this observation suggests that the transient (peak-to-peak ~ 1.2dB) may have slightly altered the error distribution which in turn compromised the performance of the FEC algorithm. Nonetheless, the accumulated transient caused by add/drop of almost the entire traffic load for the worst-case repetition rate for a link with 5 chained EDFAs produces a barely noticeable power penalty of 0.5dB. These results further validate those presented in the previous chapter, highlighting the suitability of these commercial gain-controlled EDFAs for burst-mode applications.

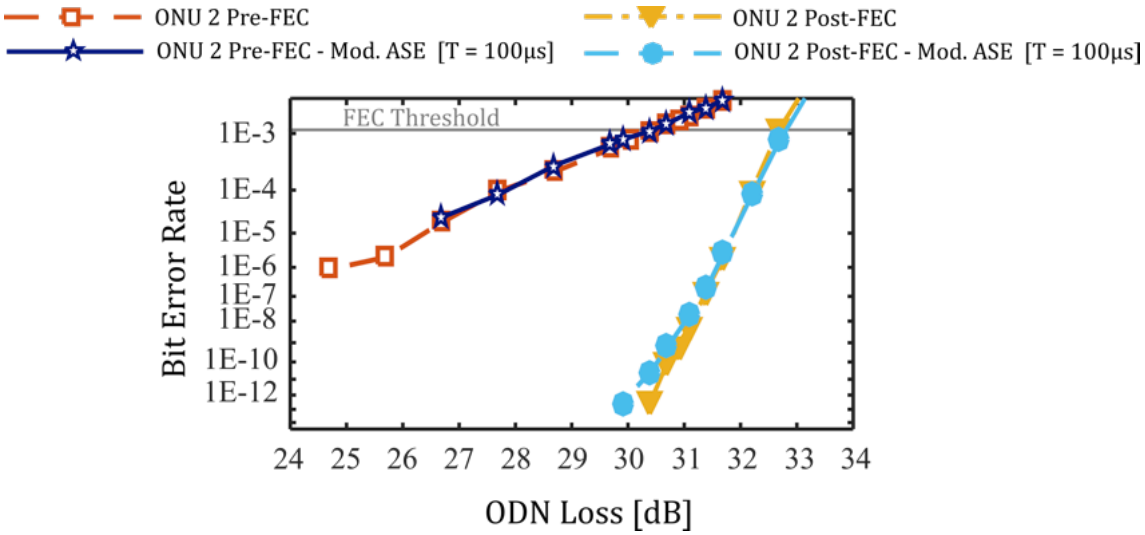


Figure 6.25: Upstream performance impact from accumulated residual EDFA transients in the 'open-ring' architecture where $T^{ASE}{}_{Add/Drop} = 100\mu$s.

6.2.3 100G DP-QPSK Point-to-Point Overlay

In this section, the performance of a private 100G point-to-point DP-QPSK channel is examined in the presence of co-propagating 10Gb/s NRZ neighbouring channels for both proposed LR-PON topologies. The results from this collaborative research effort were included in the peer-reviewed journal Optics Express (see 'List of Publications' [J4]) [151].

Downstream Characterisation:

Similar to the 10G PON channel analysis, the BER of the 100G link was characterised as a function of the ODN loss in the DS direction with the results presented in Fig. 6.26. Assuming an FEC threshold of 1.1×10^{-3}, the experimental curves show that the conventional tree-structured architecture can support a 100G link with ODN loss up to ~38.5dB, which corresponds to 128 split plus 20km of distribution fibre and ~8dB system margin. Considering the additional split in the AN, the overall split ratio supported by the urban configuration is 128×4 = 512, that could be further increased at the expense of the ~8dB system margin. Similarly, the 'open-ring' architecture can support the 100G channel with ODN loss up to ~30dB, which corresponds to 64 split plus 20km of distribution fibres and ~3dB system margin. That is at least 64×4 = 256 splits when the additional split in AN 4 is taken into account, and 256×4 = 1024 users when all intermediate ANs are aggregated.

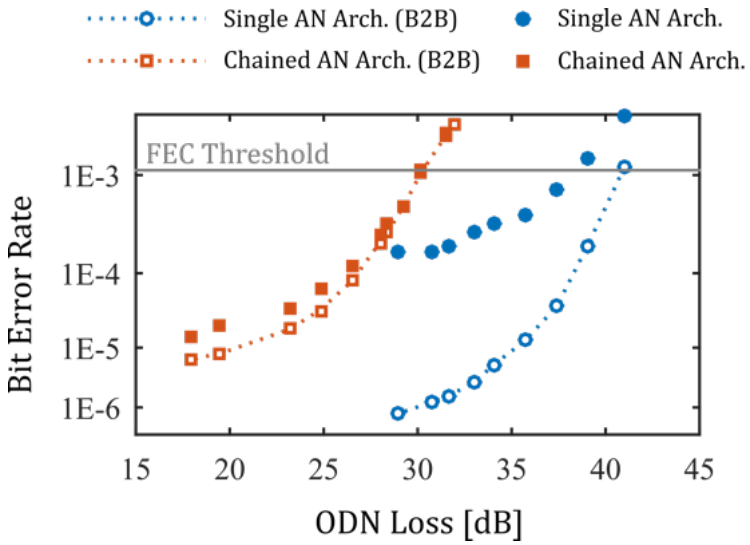


Figure 6.26: Downstream BER performance of the 100G DP-QPSK channel.

As indicated in Fig. 6.26, the DS performance of the 100G DP-QPSK channel is impaired by OSNR degradation as well as by nonlinear fibre effects. The difference of approximately 8dB at the FEC threshold between the experimental curves relative to the both network designs is due to the fact that in the urban architecture, a higher 100G signal power is launched into the ODN (i.e. +6.5dBm against -1.2dBm). In fact, the tree-structured architecture is designed to potentially support a higher split-ratio (up to 4 times) from one AN in comparison to the 'open-ring' architecture.On the other hand, for a low ODN loss, the maximum achievable OSNR is limited by the AN and CN amplifiers and it is equal to ~23dB and ~21dB for the 'tree-structured' and the 'open-ring' designs respectively. It should be noted that, due to limitations introduced by the experimental set-up, the maximum OSNR of the DP-QPSK signal at the output of the CN was about 26dB; which can be taken to represent a worst case scenario study. For high ODN loss the OSNR of the 100G channel is limited by the ASE introduced by the pre-amplifier EDFA. From the experimental curves in Fig. 6.26 it is possible to see that for low ODN loss, despite the higher OSNR, the urban architecture has a worse performance than the 'open-ring' due to the higher impact of the nonlinear crosstalk with the 10Gb/s NRZ channels in the fibre. This results in a BER floor approximately one order of magnitude higher than the open-ring design (i.e. $\sim 1 \times 10^{-4}$ versus $\sim 1 \times 10^{-5}$).

In order to evaluate the effect of nonlinearities for both network schemes in more detail, Fig. 6.26 also shows the BER measured as a function of the ODN loss in back-to-back (B2B), where the output of the CN is connected directly to the pre-amplifier EDFA with all the 10Gb/s NRZ channels off and without going through the LR-PON physical layer. In this case, the ODN loss is emulated by a variable optical attenuator (VOA) which changes the OSNR at the input of the coherent receiver. The value of the ODN loss is estimated by comparing the B2B OSNR (measured after the EDFA pre-amplifier) with the corresponding value measured from the PON testbeds. Assuming a negligible impact from other sources of impairments, such as chromatic dispersion, the effect of the nonlinearities can be clearly seen by comparing the B2B curves for both network designs with the values obtained from the respective LR-PON. Notably, in the urban architecture, the effect of nonlinearities is highly visible, as the BER floor increases by approximately two orders of magnitude in comparison to the B2B case. It should be noted that this analysis represents a worst case study in terms of XPM crosstalk from neighbor-

ing channels due to the additional residual penalty from all the NRZ channels at ≥200GHz spacing with ~3.7dB higher-than-nominal power (necessary to emulate a full system load of 40 channels). Nevertheless, the impact from those NRZ channels is reasonably smaller in comparison to the effect of cross-phase modulation (XPM) crosstalk from adjacent channels (at the same power of the 100G signal) and therefore the overall DS performance is not significantly affected. On the other hand, in the open-ring architecture the effect of nonlinearities is rather small as shown by the experimental curve in Fig. 6.26 which almost lies on the top of the B2B measurements. This is due to the fact that in the open-ring design the maximum power launched into the various fibre links (≤0dBm) is significantly smaller than in the urban design (≤6.5dBm). Therefore, despite the fact that in the open-ring case there is an accumulated effect of XPM from the multiple fibre links, this is still negligible in comparison to the effect of XPM from the backhaul link of the tree-structured urban architecture.

With respect to the LR-PON configuration supported by the SOA-based AN; the DS performance of the 100G DP-QPSK channel was also characterised as a function of the ODN loss using a pre-amplifier with a NF of ~5.5dB. As shown in Fig. 6.27, the 100G channel is impaired by the OSNR degradation alongside non-linear impairments introduced in the fibre propagation and in the SOAs.

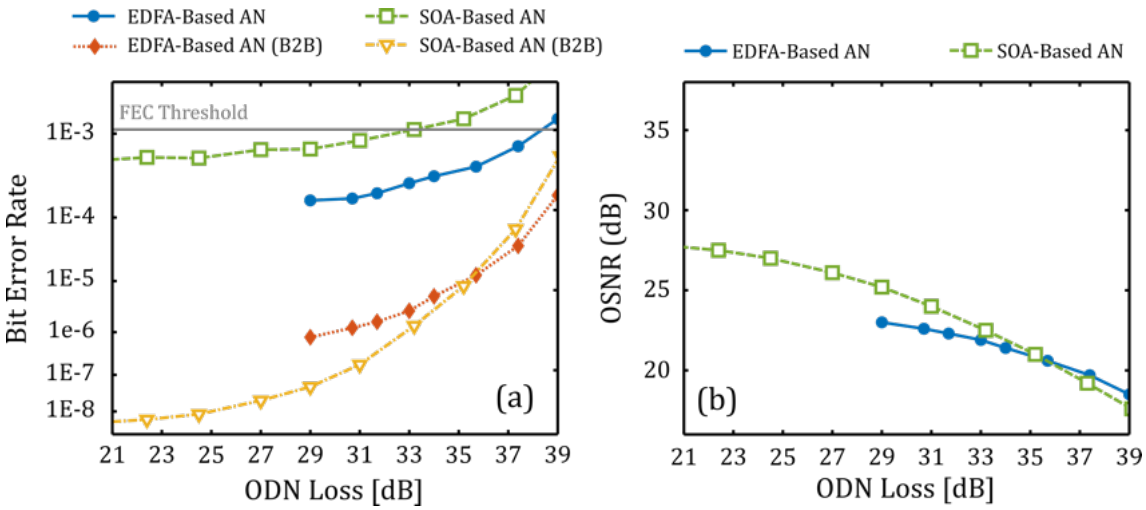


Figure 6.27: (a) Downstream BER performance and (b) OSNR of the 100G DP-QPSK channel as a function of the ODN loss.

For high ODN loss ($> 30dB$), the OSNR is limited by ASE introduced by the pre-amplifier at the receiver. Conversely, for low ODN loss ($< 30dB$), the OSNR limitation can be attributed to the AN and CN amplifiers. Moreover, it should be noted that the SOA design has a better OSNR with respect to the EDFA-based AN because the power of the 100G channel was set 5dB higher than the other nominal channels while it also has lower backhaul losses due to a shorter link of 50km. Notably, the results of the DS characterisation demonstrate that both EDFA- and SOA-based AN designs are capable of supporting an ODN loss greater than 28.1dB which corresponds to a 128-split with 12km of fibre. Overall, the SOA-based AN demonstrates a poorer performance despite having a higher OSNR. This can be attributed to non-linear crosstalk with the 10G DS PON channels resulting from cross-gain and coupled phase modulation within the saturated SOAs.

The technique used to evaluate the impact of non-linearities is identical to that outlined for the EDFA-based AN. The first step was to measure the back-to-back BER performance of the 100G channel as a function of the ODN loss where the 100G transmitter was connected directly to the EDFA preamplifier without going through the LR-PON physical layer. The ODN loss was emulated using a variable optical attenuator located at the input to the pre-amplifier. By adjusting the value of attenuation, the OSNR of the 100G signal at the input of the coherent receiver could be altered. The corresponding value of ODN loss was then determined by comparing each value of OSNR measured after the pre-amplifier with that measured from the LR-PON characterisation. By comparing the back-to-back curve with the corresponding measurements taken from the LR-PON physical layer, the performance impact of the non-linearities can be identified. This approach is based on the assumption of a negligible impact from other sources of impairments, such as chromatic dispersion. With this in mind, the impact of the cross-gain and coupled phase modulation within Fig. 6.27 is clearly evident.

Upstream Characterisation:

In the US direction, the 10G NRZ PON traffic which is interfering with the 100G channel, presents bursts with different power. In the urban architecture, the non-uniform ODN loss can cause up to 12dB of DR between burst powers, while in the open-ring design the resulting DR can be up to 9dB. These values have been

estimated considering a 512 and a 256 split ratio for both architectures respectively, and realistic splitter losses [260].

By system design, the 100G channel power should be set in the middle of the PON channels DR. This is also referred to as the nominal US power and in these experiments it is set to achieve an ODN loss of 28.6dB and 24dB respectively for the tree-design and the open ring designs. The experimental values of the nominal ODN loss are slightly higher than the ODN loss that would be obtain considering a worst case loss of 3.5dB for each ×2 split, which represent a worst case in terms of achieved OSNR for the DP-QPSK signal as well as for the 10Gb/s PON channels. The transmitted power from all ONUs (100G and NRZ) is fixed to +5dBm. The 100G channel was characterised in terms of penalty caused by the nonlinear crosstalk from the two neighboring 10Gb/s NRZ PON channels bursting with high power, as this represents a realistic worst case. The BER of the 100G US link was measured as a function of the power of two 50GHz-spaced interfering channels operated with 2µs bursts and 2µs gaps overlapped in time to provide also a worst case for the nonlinearity.

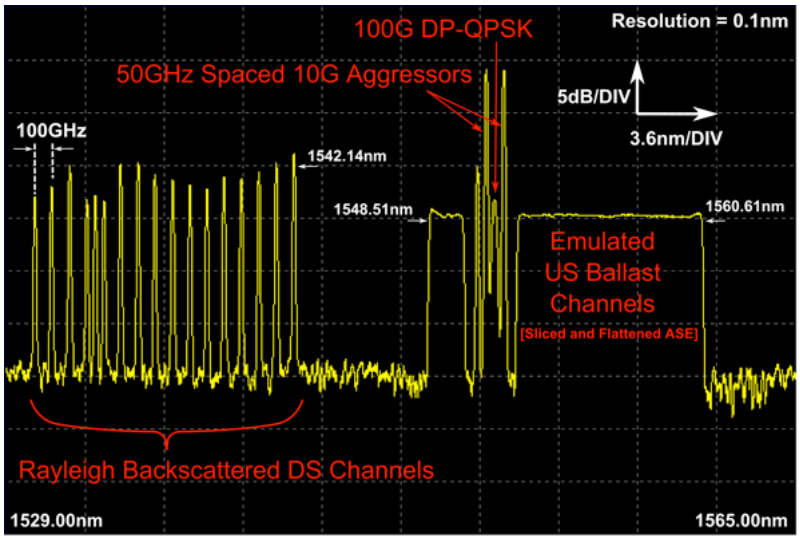


Figure 6.28: 100G DP-QPSK channel analysis: upstream spectrum at the monitor port of the AN in the 'tree-like' architecture showing the neighbouring 10G NRZ aggressor channels.

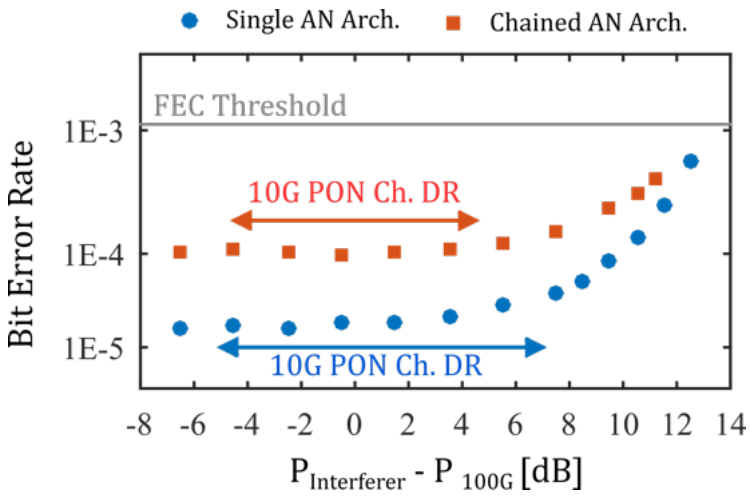


Figure 6.29: Upstream performance of the 100G channel as a function of the power of the neighbouring 10G NRZ PON channels for the EDFA-based ANs.

The experimental results in Fig. 6.29 show that for small NRZ channels powers the BER of the tree-structured architecture is almost an order of magnitude lower than the open-ring architecture, due to the fact that it is possible to achieve a ~2dB higher OSNR (~21.5dB versus ~19.5dB) respectively. In contrast to the DS case, the maximum launched power into the various fibre links is very similar for both network architectures. This corresponds to approximately -4dBm into the 80km backhaul fibre for the tree-structured design, as well as into the two 40km links for the open-ring design. As a consequence, the performance of both architectures degrades with a similar trend and the experimental curves tend to converge towards the FEC threshold for NRZ channel powers ~12dB higher than the DP-QPSK channel power. Fig. 6.29 also indicates the DR expected from a non-uniform ODN loss for tree-structured design (12dB) and for the open-ring design (9dB). The 100G channel can work below the FEC threshold even when the neighboring bursty channels present DR larger than expected from the non-uniform ODN loss. It should also be noted that, while in the open-ring case the DR is distributed symmetrically around the nominal value, in the tree-structured design the DR is asymmetric with -5dB and +7dB. This is caused in the experiment by misalignment of 1dB between the ODN loss range and the LBMRx DR.

The performance analysis of the 100G channel in the US direction for the SOA-based AN is identical to the technique outlined in section 6.2.3. By design, the power

of the 100G channel is set in the middle of the 10G PON channels DR. As the burst power of the 10G NRZ-OOK channels can vary in power by up to 12dB due to non-uniform ODN loss, the US performance of the 100G channel was characterised in terms of impairments caused by the non-linear cross-talk from two neighbouring 10G channels with high burst power which is representative of a worst-case scenario study. The BER of the 100G link was measured as a function of the power of the two 50GHz spaced interfering channels operated with 2μs bursts and 2μs gaps overlapped in time to provide a worst case for non-linearity.

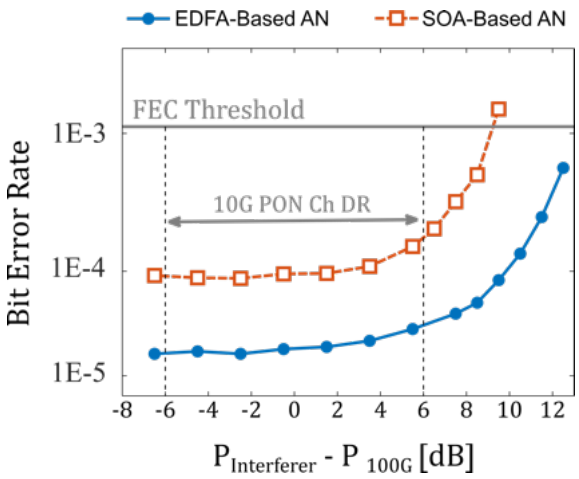


Figure 6.30: Upstream performance of the 100G DP-QPSK channel as a function of the power of the neighbouring 10Gb/s NRZ PON channels for the EDFA and SOA-based amplifier node designs.

The results, presented in Fig. 6.30 show that the 100G channel can operate below the FEC threshold when the DR of the bursts from the nearest-neighbour (50GHz-spaced) 10G NRZ-OOK channels is greater than the 12dB variation caused by non-uniform ODN loss for both AN designs. As presented in section 6.2.3, cross-phase modulation (XPM) in the backhaul fibre is a major source of impairment for the EDFA-based AN. In contrast, the performance of the SOA-based AN is mostly degraded by the cross-gain and coupled-phase modulation within the SOAs. The nominal power of the NRZ-OOK channels launched from the SOA, which was set in the middle of the DR, is ~3.5dB lower compared to the DS case, which reduces the impact of non-linearities. For the EDFA case, the effect of XPM induced by

channels beyond 100GHz channel spacing is negligible; however for the SOAs the effect would be roughly the same within the entire gain bandwidth. For this reason, the absolute worst-case performance impact for the SOA-based AN design would be if the 39 remaining channels were bursting with the highest power within the DR. due to the statistical nature of the ODN loss distribution and randomness in traffic patterns this scenario is highly unlikely to occur; therefore this case study can be considered a realistic worst-case scenario study.

6.3 Integrated SDN Control Plane Services

The static architecture of conventional networks is now ill-suited to the dynamic needs of modern carrier environments; therefore a cost-effective, agile and adaptive control plane is required to improve bandwidth efficiency and capacity flexibility.

Software-defined networking (SDN) is an emerging configuration which removes the control plane from the network hardware and implements it in software instead. This enables the programmatic initialisation, control, change, and management of dynamic network behavior via open interfaces which makes network administration much more flexible [262]. For instance, through the use of SDN, a network administrator can regulate the data transfer from a centralised location to assure a certain level of performance without having to manually configure individual switches.

Through a collaborative research effort as part of the DISCUS project, the ability to dynamically allocate resources within a high-capacity LR-PON was demonstrated using the physical layer of the EDFA-based urban architecture using a custom SDN control plane. In particular, two specific use cases were examined: (i) a fast protection mechanism with end-to-end service restoration in the event of a primary link failure and (ii) dynamic wavelength allocation (DWA) to enable flexible service provisioning in response to an increased bandwidth demand.

It is important to note that the SDN control plane whose basic structure is shown in Fig. 6.31 was developed and integrated with the LR-PON testbed by our DISCUS project collaborators from the CONNECT research centre in Trinity College Dublin (TCD). This experimental overview is included with permission in order to supplement the design, assembly and investigation of the physical layer presented in this work by demonstrating the resiliency and flexibility of the architecture. As

the development of the SDN control plane is beyond the scope of this work, it is not discussed further; however, for further information the reader is referred to [19] and [263].

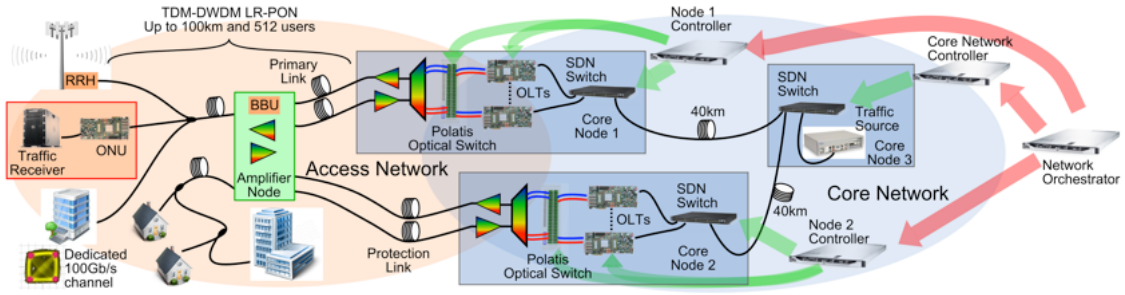


Figure 6.31: Network level view of the tree-structured LR-PON and the SDN control plane equipment.

The protocol used in the SDN experiments was a partial implementation of the 10G symmetric XG-PON standard [118]. While not all functions from the standard were implemented in the testbed, some modifications were required in order to support the longer physical reach (125km as opposed to 60km) and the higher split ratio (512 versus 64). This modified protocol was implemented over four Xilinx Virtex7 XC7VX690T FPGAs which acted as the primary and secondary OLTs and two ONUs. In addition, a Xilinx Microblaze soft processor, was instantiated on the FPGAs to provide a universal asynchronous receiver/transmitter (UART) management interface to the OLT and ONU hardware. This allowed control of PON functionalities such as resetting the hardware, viewing the hardware status, simulating a hardware failure, loading the bandwidth map and setting XG-PON encapsulation method (XGEM) mappings [263]

A simplified core network was also emulated in the testbed using a Pronto 3780 10G Ethernet (10GbE) SDN switch which was configured with three virtual *OpenFlow* (OF) bridges. The PON backplane connection between the OLTs and the core network was enabled by the Pronto switch 10GbE interfaces which were also used to interconnect the virtual bridges using SFP+ transceivers and two 40km fibre links.

6.3.1 Link Protection and Resiliency

As illustrated in Fig. 6.32, the link protection experiment was triggered by a failure event emulated using the optical switch to simulate a fibre cut in the backhaul fibre link between the primary OLT and the AN. The corresponding silence in the US path then activated a countdown timer within the primary OLT which generated a failure detection and an in-band alarm to the controller of the primary CN on expiry via the device-controller plane interface (D-CPI). Notably, the duration of this timer was designed to take into account all typical silences on the PON including the 1.25ms quiet windows and 1.25ms roundtrip transmission time for the maximum distance supported by the protocol (125km) giving a total of 2.5ms. The primary node controller (NC) was then used to alert the overarching network orchestrator (NetO) which then calculated a path to restore services to the ONUs according to its knowledge of the full end-to-end topology. Once an available path was established, the core network controller (CNC) and the relevant NC are then instructed by the NetO via the intermediate-controller plane interface (I-CPI) to provision the protection path through the optical switch and the secondary OLT.

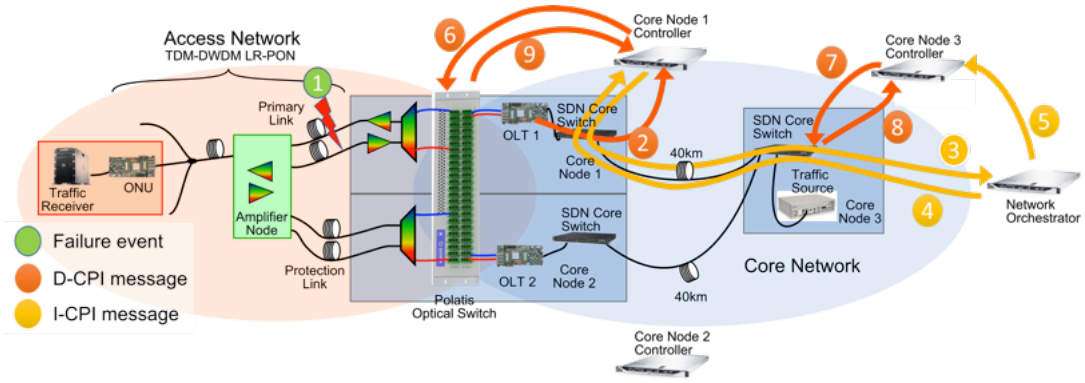


Figure 6.32: Overview of the control plane processes for the link protection experiment.

The event timings that comprise the protection scenario illustrated in Fig. 6.32 are presented in Fig. 6.33. For instance, as mentioned earlier, the hardware monitoring at the OLT can detect a failure in the network after approximately 2.5ms. An additional ~1ms is taken for the alarm packet to be created and sent to the CN SDN switch. The time needed by the protocol to re-establish DS synchronisation is typically between 2-3ms. Furthermore, from previous work [264], it is known that some

extra time may be needed to re-range the ONUs in addition to the synchronisation time (between 2 and 4ms); however, in this work it was assumed that ranging to the backup OLT can be done during normal operation of the PON. Intra-control plane communication is done through a dedicated network with typical latencies. The network latencies between both the OLT and NetO and the NetO and the NCs are emulated in the test-bed and set at 4ms each. The latency and the processing times for both the NCs is also emulated as 5ms each. It is important to note that the core network recovery happens in parallel to the access network recovery time. Accordingly, within 15ms of the failure, the optical and electronic switch components and the backup OLT have been instructed to reconfigure their protection paths. Within 33ms after the failure, the electronic switch components within the core and access are configured and by 38ms, the optical switch is ready.

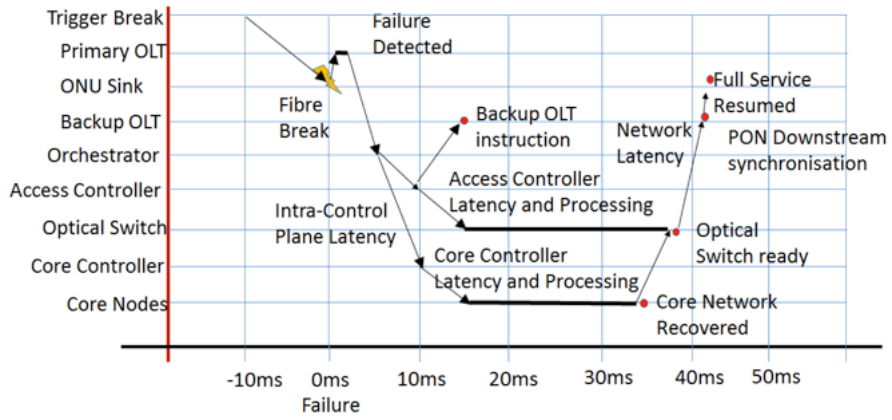


Figure 6.33: Overview of the control plane link protection experiment timings.

The average time required for service restoration following a primary link failure in the tree-like (urban) architecture using the custom SDN-based protection mechanism was found to be 41ms following 70 consecutive measurements. In addition, to understand the effect of centralising both the NetO and the NCs, the measurements were then repeated for the case where orchestrator and controllers are co-located within the CN. This was accomplished by setting the emulated intra-control plane latencies at zero with the results shown in Fig. 6.34 as the basic protection curve. On average, this basic protection can be accomplished within 27.8ms.

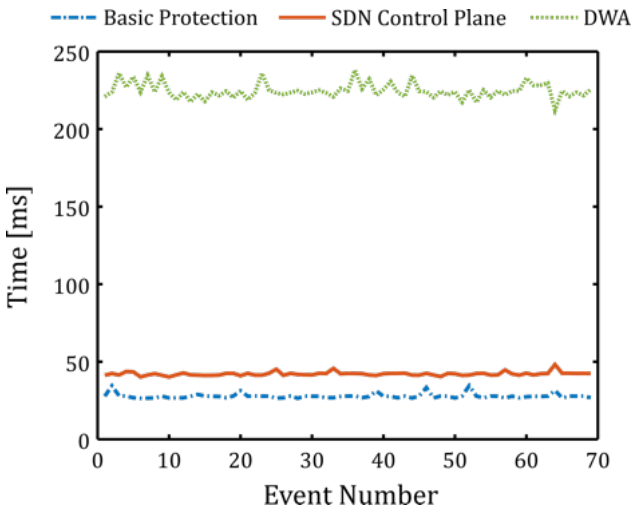


Figure 6.34: Service restoration time for the protection scenario and wavelength allocation time from the SDN control plane experiments.

6.3.2 Dynamic Wavelength Allocation

Through the use of dynamic wavelength allocation (DWA), capacity constraints in a PON may be overcome by actively re-allocating one or more ONUs to a different wavelength channel in order to improve bandwidth efficiency and assure quality of service. Moreover, this approach could also be used for the opportunistic provision of high bandwidth services (on-demand video and big data transfers) to specific PON users on a dynamic basis. With this in mind, the SDN control plane was used to examine the feasibility of supporting DWA within a TDM-DWDM LR-PON for the purpose of flexible capacity provisioning. It is important to note that in this scenario, wavelength assignment is not required on a burst-by-burst basis, hence reconfiguration times were targeted in the region of a few hundred milliseconds. The main processes involved in the DWA experiment are illustrated in Fig. 6.35.

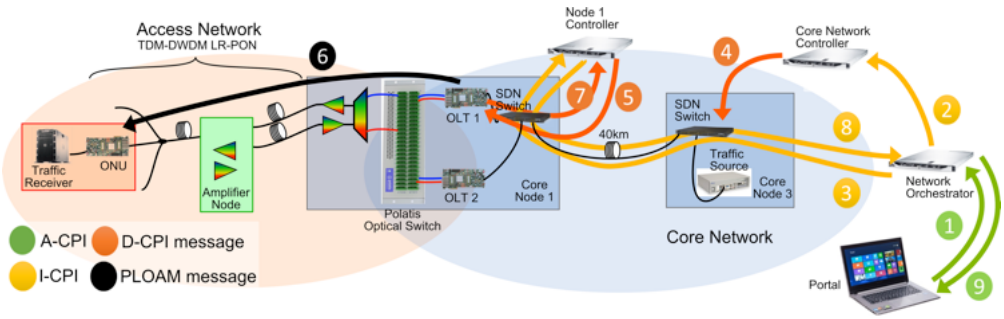


Figure 6.35: Overview of the control plane processes for the DWA experiment.

Following a resource request via the application-controller plane interface (A-CPI), the NetO orchestrated the provisioning of the new path according to its knowledge of the full end-to-end topology by directing the CNC and the relevant NC using the I-CPI. The NC was then used to instruct the Polatis optical switch and the secondary OLT using the D-CPI to provision a new wavelength for the ONU. Since the ONU was remote from the control plane, the request to tune to a different channel was performed through the OLT interface by the invocation of a custom LR-PON protocol message embedded in the DS signal. At the ONU, wavelength reconfiguration was achieved by controlling the tuneable laser within the SFP+ transceiver using an i^2c bus and the tuneable filter through a UART interface. Subsequently, the secondary OLT was used to acknowledge the ONU registration to the NC via the D-CPI which then reported to the NetO through the I-CPI confirming that it had successfully completed the provision of the new path.

The typical timing of the main events associated with this DWA experiment are presented in Fig. 6.36 while the results of 70 consecutive measurements which capture the service restoration time (i.e. event 4.a to 6.a) can be found in Fig. 6.34. Following analysis of these results, it is believed that by optimising the design of the communication interfaces between the ONU FPGA and the tuneable components it may be possible to further reduce the average provisioning time of ~ 225ms.

Event Number	Type	Source	Destination	Message	Time [s]
1	A-CPI	Portal	NetO	Resource_Request	0
2	I-CPI	NetO	CNC	Create_Path	0.207
3	I-CPI	NetO	NC	Create_Path	0.215
4	D-CPI	CNC	SDN Switch	Add-Flow	0.229
4.a	**MEAS**	**--**	**--**	**Traffic_Measurement_Break**	**0.264**
5	D-CPI	NC	OLT	Set_DS_Lambda	0.298
6	PLOAM	OLT	ONU	Set_Wavelength	0.366
6.a	**MEAS**	**--**	**--**	**Traffic Restored**	**0.485**
7	D-CPI	OLT	NC	Status_Report: ONU_Registration	0.666
8	I-CPI	NC	NetO	Create_Path_Confirmation	0.668
9	A-CPI	NetO	Portal	Resource_Confirmation	0.969

Figure 6.36: Control plane processes and timings for the DWA experiment.

Although the successful demonstration of DWA proves that this approach could work for the TDM-DWDM LR-PON architecture under consideration, it must be recognised that the lasers used in this investigation were commercially available C-band tuneable SFP+ modules with fast tuning and high-precision wavelength locking. Nonetheless, this implementation remains valid from a control plane timing perspective and in practice additional delays could be accounted for in estimating the overall provisioning time for lower-cost transceivers which are required for deployment within the ONUs as outlined in Chapter 4.

6.4 Summary and Conclusions

This chapter presents the experimental demonstration of two distinct dynamically reconfigurable TDM-DWDM LR-PON architectures that were assembled in accordance with the physical layer design strategy outlined in Chapter 5. The primary objective of this work was to experimentally verify the proposed DISCUS architectures whose physical layer targets (e.g. reach ≈100km, split ≥ 512) have the potential to bypass the majority of power-hungry, hierarchical switching and signal regeneration sites present in modern telecommunication networks. Consequently, as mentioned previously in Chapter 3, the effective integration of the access and metro networks using a long-reach optical access infrastructure, optimisation models undertaken by our industrial project partners have shown that the number of core nodes can be reduced by up to two orders of magnitude [8] thus simplifying the overall network infrastructure and the associated traffic management.

It is important to note that the work presented in this chapter represents the culmination of a remarkable amount of research undertaken by the various academic and industrial partners within the DISCUS project which ran from November 2012 to December 2015. For instance, each partner was focussed on developing different aspects of the network ranging from optimising the core to the simplification of traffic management through the integration of a custom SDN control-plane. In particular, the authors role within this large-scale EU-funded project was primarily focussed on the design, assembly and investigation of the LR-PON physical layer resulting in the detailed collection of data presented in this chapter which was achieved through extensive collaborative research.

For instance, in section 6.2, the 'tree-structured' LR-PON proposed for urban access deployment consisting of a single EDFA-based AN was demonstrated to support the convergence of multi-service traffic (e.g. 10G-TDM channels, coherent 100G point-to-point overlay and wireless fronthaul) with a total physical reach of up to 100km, 1024 end users and an emulated system load of 40 DWDM channels in both transmission directions. Moreover, through a collaboration with researchers from Nokia Bell Labs in Stuttgart, a 'tree-structured' LR-PON architecture employing linear SOAs within the AN was also investigated. The corresponding results demonstrated that the physical layer was capable of supporting up to 512 users over a physical reach of 74km. It should be noted that the experimental results obtained from the investigation of the urban LR-PON architecture using both EDFA- and SOA-based ANs were presented at the Optical Networking and Communication Conference (OFC) in 2016 [265] with an invited paper subsequently published in the IEEE Journal of Lightwave Technology in 2017 [19].

Alternatively, to address the critical challenge facing FTTP deployment in rural regions, a novel LR-PON architecture was developed using a chain of ANs from which the ODNs can be aggregated in order to reach wide areas with dispersed communities. This innovative 'open-ring' physical layer was assembled and demonstrated using up to four chained EDFA-based ANs with the ability to support the convergence of multi-service traffic for a total physical reach of up to 120km, 1024 end users and an emulated system load of 40 DWDM channels in both transmission directions. To the best of our knowledge, this was the first time that such an architecture was proposed and experimentally demonstrated as a potential solution for rural fixed-line access. Notably, this work represents one of the most significant contributions of this thesis with the corresponding results being presented at the European Conference on Optical Communications (ECOC) which was held in Düsseldorf in 2016 [20].

Finally, through a collaboration with researchers from Trinity College in Dublin, a custom SDN control plane was integrated with the physical layer testbed of the urban LR-PON architecture to examine the feasibility of programmatically managing the dynamic access and core network elements. In particular, two key service scenarios were investigated, these included: i) a fast protection switchover to a backup OLT due to a failure in the active backhaul link and ii) the dynamic reassignment of an ONU wavelength in response to increased traffic demand. Notably, as shown in

section 6.3, the results demonstrate that end-to-end service restoration in the event of a fibre break in the backhaul link can be accomplished within an average time of 41ms which indicates a minimal disruption to services while an average wavelength provisioning time of 225ms was achieved with potential for further improvement though the use of optimised components.

At the time of investigation, the physical layer testbed designed, assembled and investigated in this work was the most advanced LR-PON demonstrator in the world, combining multiple research topics from the design of systems level solutions and technologies to link, node and control plane architectures. In turn, this project enabled the limits of various LR-PON configurations to be explored in detail and even though some of the components used were not specifically designed for access applications (e.g. the ONU-Tx and Rx) they represent the performance that is expected for such systems. Moreover, in line with emerging trends for access networks, the proposed architectures successfully enabled the convergence of multiple service traffic on the same infrastructure which can be deployed across a wide range of geotypes. Furthermore, the successful integration of SDN with the LR-PON physical layer through a collaborative research effort has proven that it is indeed possible to remotely manage a dynamic network such as DISCUS with a single control plane in order to provide reliable link protection and dynamic service provisioning for efficient capacity utilisation.

Overall, these testbed results have successfully verified the concept proposed by the DISCUS project in that dynamically reconfigurable TDM-DWDM LR-PONs have been shown to be capable of providing ubiquitous bandwidth across a wide range of service scenarios with the simplification of traffic management enabled through the consolidation of core nodes and network interfaces thus offering the potential for remarkable cost and power savings for future access networks.

7

Conclusions and Future Work

Passive optical networks (PONs) remain the one of the most economically attractive infrastructures for deploying fibre-to-the-premises (FTTP) where standards such as G-PON [84] and XG-PON [10] support multiple users through a time-division multiplexed (TDM) channel. Recently, this capability has been significantly extended by the NG-PON2 standard which has introduced wavelength division multiplexing (WDM) to facilitate multiple TDM as well as dedicated point-to-point (PtP) channels on the same infrastructure [11].

In this thesis, this latest access solution is further enhanced by the design, assembly and demonstration of dynamically reconfigurable time-division multiplexed (TDM) dense wavelength division multiplexed (DWDM) long-reach passive optical networks (LR-PONs) capable of providing an economically scalable network design supporting the convergence of multiple service scenarios and user types. The main technical findings of this work are outlined below.

7.1 Overview of this Thesis Contribution

In Chapter 4, the potential for appreciable savings through an increased yield, lower power consumption and simplified fabrication processes prompted an investigation into two prototype tuneable diode laser technologies which have been proposed as candidates for deployment within customer premises equipment.

For instance, section 4.5 presents a detailed investigation of a novel MEMS-VCSEL developed within the SUBTUNE project (2008 - 2011) [179]. Although, the laser under test demonstrated a noteworthy continuous tuning range of over 45nm between 1540nm and 1585nm, the output wavelength was observed to exhibit a significant level of instability which is attributed to various sources including resonance oscillations from residual air currents and the release of material stress. Consequently, a custom LabVIEW-based feedback loop was developed to actively

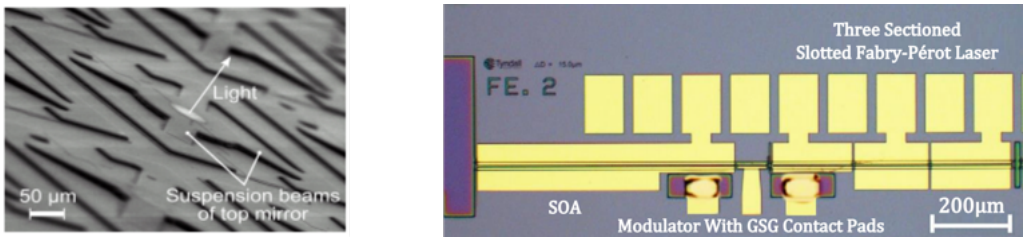
adjusted the applied tuning current in response to a continuous comparison between the target wavelength and the peak as measured by an OSA. Having successfully stabilised the output of the unpackaged VCSEL to ≤ ±0.25nm, the transmission performance was demonstrated to consistently achieve bit error rates less than 1×10^{-9} across a 30nm wavelength tuning range (i.e. 1540nm - 1570nm) using external intensity modulation at 10Gb/s. Notably, the device under test exhibited only a small average receiver penalty of approximately 0.2dB with respect to a commercial external cavity laser in both the back-to-back and 50km of single-mode fibre which encompasses the typical physical reach targeted by todays PON standards (see List of Publications: [J1]).

While the main advantages of this VCSEL technology include wafer-level testing, a lower power consumption and a remarkable continuous tuning range, the results presented in this work demonstrate that the main challenge facing these lasers involves optimising the stability of the surface DBR membrane which is essential to maintain the integrity of the set transmission channel. Nonetheless, recent work on these devices has instead focussed on improving the parasitic resistance and capacitance of the half-VCSEL structure in order to facilitate direct modulation at 10Gb/s [193]. Interestingly, to the best of our knowledge, the resulting chirp performance of these VCSELs is yet to be reported; moreover, based on the results published thus far, it is clear that the addition of an SOA will be required to reach the launch power specifications of current PON standards [140].

Alternatively, in section 4.6, a single-growth, monolithically integrated tuneable transmitter based on a slotted Fabry-Pérot (SFP) ridge-waveguide laser, a 10G-capable absorption modulator and a semiconductor optical amplifier (SOA) is investigated in detail. Developed and fabricated by the III-V Materials and Devices Group of the Tyndall National Institute as part of the DISCUS project, the main advantage of this transmitter structure is that it offers the potential for substantial cost savings when compared with alternative grating-based structures due to the use of a standard 'off-the-shelf' epitaxial MQW material and cost-efficient re-growth free fabrication techniques. In particular, within section 4.6.1 and 4.6.5 respectively, this unpackaged device was shown to attain a discrete tuning range of approximately 12nm between 1551nm and 1563nm with a side-mode suppression ratio ≥ 30dB and an extinction ratio in excess of 6dB for modulation at 10Gb/s using NRZ-OOK. While some challenges remain to improve the insertion loss and

bandwidth of the modulator section, the detailed time-resolved chirp measurements presented in section 4.6.6 indicate an noteworthy wavelength stability of less than 10GHz (~ 0.08nm) under intensity modulation at 10Gb/s and optical burst generation for packet lengths comparable with those of the latest PON standards (see List of Publications: [J6]).

The main contribution of this investigation demonstrates that this device shares key challenges faced by other well-established integrated transmitter technologies such as thermal crosstalk and residual optical feedback. While this behaviour was shown to compromise the resonance conditions of the slotted Fabry-Pérot laser in section 4.6.4, the time-resolved chirp measurements presented in section 4.6.6 have shown that when the gating function applied to the SOA section is faster than the thermal response time of the transmitter material, the amplitude of the induced frequency deviations can be ≤ 10GHz. Notably, the deviation in the carrier frequency induced by thermal crosstalk can be maintained below the strict maximum spectral excursion of ±12.5GHz specified for DWDM channels [140]. In fact, the work presented in section 4.6.6 demonstrates that the dynamic stability of the carrier frequency exhibited by the integrated transmitter under modulation or optical burst generation is significantly better than that of directly modulated lasers in the absence of active thermal chirp compensation [124].



(a) (b)

Figure 7.1: (a) Microscope image of a MEMS-VCSEL array (Reproduced from [187]) (b) Monolithically integrated transmitter based on a slotted Fabry-Pérot laser.

Focusing attention on the physical layer design strategy, the viability of two distinct LR-PON configurations are investigated in Chapter 5 in accordance with the targets of the DISCUS project [8] with the aim of bridging the ever growing 'digital divide' between urban and rural communities. In particular, the feasibility of a 'tree-structured' LR-PON for urban areas (5.1.1) and an innovative 'open-ring' LR-PON

proposed for rural regions (5.1.2) was investigated through a linear optical power and OSNR model (presented in Appendix C) to examine the achievable physical reach and split by deriving the detailed specifications of the amplifier nodes (ANs). Subsequently, based on the performance boundaries set by the transmitter (Tx) and receiver (Rx) specifications, erbium-doped fibre amplifiers (EDFAs) emerged as suitable candidates to support the proposed physical layer due to their ability to provide a high gain and a relatively low noise figure across a wide band of channels. However, as demonstrated in section 5.2.2 and Appendix D, their comparatively slow gain dynamics can produce saturation induced power excursions that can compromise the link performance; therefore, devices whose parameters (i.e. gain, noise figure and aggregate output power) were derived from the power and OSNR model were acquired with transient suppression circuitry.

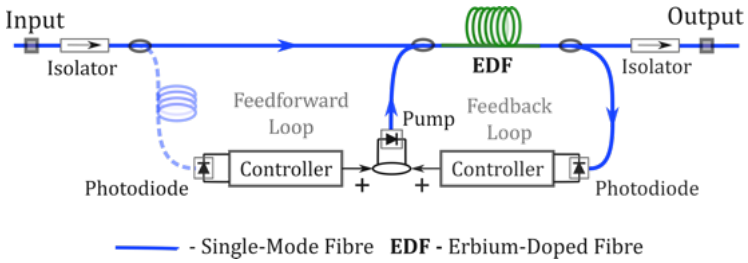


Figure 7.2: Schematic of a single-stage, forward-pumped EDFA configuration with active gain stabilisation via dynamic pump control.

As the upstream performance impact of residual EDFA transients will ultimately depend on the architecture of the OLT-based burst-mode receiver (BMRx), a collaborative investigation was undertaken to examine the resilience of an FPGA-based forward error correction (FEC) algorithm used in conjunction with an innovative 10G-capable linear BMRx when the incident bursts are impaired by optical transients. The results of this work demonstrated an appreciable performance margin of 4dB with respect to the transient amplitude prior to FEC degradation (see List of Publications: [C6]). By comparing these results with those presented in section 5.3, it is evident that if the burst-mode traffic is regulated by an appropriate PON protocol, the power excursions produced by these commercial gain-stabilised EDFAs should not compromise the US transmission performance of the 10G TDM-DWDM channels in either of the LR-PON configurations targeted for the DISCUS project testbed demonstration.

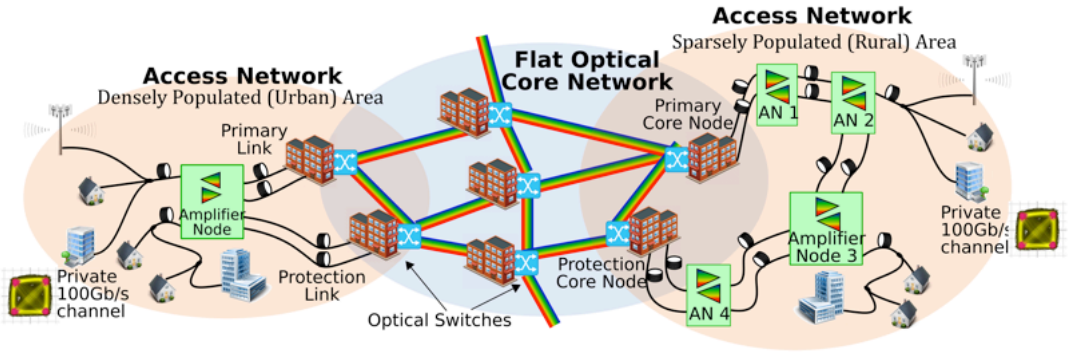


Figure 7.3: High-level network view of the proposed DISCUS architecture.

Following the initial physical layer feasibility analysis and the investigation of the main burst-mode subsystems in Chapter 5, the LR-PON experimental testbed was assembled and investigated in detail with the results presented in Chapter 6. At the time of investigation, this system was the most advanced LR-PON demonstrator in the world, combining multiple research contributions from multiple project partners including the design of systems level solutions and technologies to the development of a custom SDN control plane (see List of Publications: [C1 - C5, J3 - J5]). However, it is important to note that the main contribution from this work includes the design, assembly and investigation of the LR-PON physical layer testbed which resulted in the detailed collection of data through extensive collaborative research.

In particular, the results presented in section 6.2 demonstrate that the 'tree-structured' physical layer employing a single EDFA-based amplifier node is capable of supporting up to 1024 end users and a total physical reach of up to 100km with an emulated system load of 40 DWDM channels in both transmission directions. Moreover, through collaborative research efforts, a coherent 100G point-to-point overlay targeted for business users and a 10G wireless fronthaul channel were also successfully demonstrated to coexist with 10G-TDM PON channels over the same LR-PON infrastructure, thus verifying the feasibility of multi-service traffic convergence.

The innovative 'open-ring' LR-PON configuration, comprised of four chained EDFA-based ANs, was also shown to support the convergence of multi-service traffic (i.e. 10G TDM-PON channels, coherent 100G overlay) over a total physical reach of 120km with the ability to support up to 1024 end users with an emulated system load of 40 DWDM channels in both transmission directions [20]. In fact, to the best of our knowledge, this work represents the first experimental demonstration of such

an architecture which has been proposed for rural fixed-line access deployment which includes burst-mode operation of the 10Gb/s physical layer and the implementation of FEC in both down- and upstream transmission directions. Consequently, this work represents one of the most significant contributions of this thesis [20].

Finally, in section 6.3, through a collaboration with researchers in Trinity College Dublin, a custom software-defined networking (SDN) control plane was integrated with the physical layer of the 'tree-structured' LR-PON architecture in order to demonstrate the feasibility of remotely managing dynamic network elements using centrally located programmable algorithms. In particular, two crucial service cases were examined in section 6.3.1 and 6.3.2, these include: i) a fast protection mechanism with end-to-end service restoration in the case of a primary link failure and ii) dynamic wavelength allocation in response to an increased traffic demand.

While the results presented in this work have successfully verified the feasibility of the envisaged DISCUS architecture, it is important to note that as the infrastructure was designed around the physical reach of a LR-PON (~ 100km) it has the potential to facilitate a remarkable reduction of core nodes by up to a factor of 50 [8]. For instance, as outlined in section 3.3.2, ~100 DISCUS core nodes could cover the United Kingdom (UK) network instead of the 5600 nodes in service today. Similarly, in Ireland, approximately 20 DISCUS nodes would be capable of covering the national network, down from 1100 nodes. Crucially, this node consolidation simplifies the overall network infrastructure by enabling a flat optical core, which serves to remove the hierarchical structure between the nodes to significantly reduce optical-electrical-optical (OEO) signal regeneration and packet processing. As a result, the DISCUS architecture not only ensures compatibility with today's networks but also future technologies as they emerge.



Figure 7.4: EU FP7 Project DISCUS testbed.
(Photonic Systems Lab, Tyndall National Institute, University College Cork, Ireland).

7.2 Future Work

7.2.1 Wavelength Referencing and Control

The aging of semiconductor materials, fabrication tolerances, thermal sensitivity and current source inaccuracies are just a few causes of inadequate stability of tuneable lasers [266]. As a result, the introduction of an efficient wavelength referencing and control strategy for 'colourless' ONUs is of critical importance to maintain the integrity of the low-cost approach outlined in Chapter 4. In particular, such schemes are critical for networks targeting DWDM in order to avoid rogue wavelength behaviour and maintain the fine tuning capabilities of the chosen ONU laser technology within the assigned channel bandwidth with a prescribed spectral tolerance [267].

In practice, wavelength control strategies can be effectively grouped into two scenarios; local and centralised. The former case typically utilises an integrated etalon-based wavelength locker (WL) to provide a reliable reference in conjunction with a detailed device-by-device laser characterisation in order to establish the desired operating points [268, 269]. Notably, the WL must be small enough to fit inside the laser package. Moreover, through detailed fabrication, the optical path length of the etalon must be closely tuned to properly align the lock points on the etalon fringes with the desired ITU channels. Furthermore, depending on the etalon material, temperature may also need to be stabilised and/or monitored [270].

As the material and assembly costs of an integrated WL contribute significantly to the overall cost of the tuneable laser it makes sense to replace the individual WLs in each laser by a centralised implementation with only one locker located in the core node which is shared by all attached ONUs [271]. This approach can be complemented by the use of distinct low-frequency pilot tones generated by a low-amplitude envelope modulation of the upstream optical signals for the purpose of identification and analysis with active feedback to the ONUs through the network via the OLT by means of an adapted protocol [178].

With this in mind, the round trip latency within a LR-PON whose physical reach is in excess of 100km will ultimately place a limit on the speed of the control loop. Consequently, rogue wavelength behaviour may only be recognised when an upstream data collision has already occurred before being stabilised by means of the protocol. Nonetheless, embedded communication through the downstream channels should be fast enough to track a slow drift of the wavelength due to temperature

changes or ageing in the laser; however, it should be recognised that for this to work the wavelengths must already lie within the bandwidth of the assigned channels. As a result, coarse knowledge of the laser operating points is required to avoid rogue behaviour during start-up or wavelength switching events. Interestingly, this observation suggests that the optimal solution to maintain the low-cost approach may not be explicitly localised or centralised but in fact an efficient combination of both strategies.

7.2.2 Beyond 10G TDM-PONs

At present, peak and aggregate consumption of data over access networks are experiencing an average of ~ 50% year-over-year growth [272]. As outlined in Chapter 3, the main trends driving this demand for bandwidth include a rising number of subscribers, a growing number of connected devices per subscriber and increasing bandwidth requirements per device or application. In particular, beyond the provision of broadband access to residential and small businesses, the growing demand for advanced data-centric mobile multimedia services has accelerated the development and deployment of new wireless broadband access technologies such as the fifth-generation (5G) of cellular mobile communications [273]. Notably, 5G systems are aiming to deliver an unprecedented level of service capabilities to the end user which will inevitably require larger mobile broadband bandwidth with ubiquitous availability, a faster response time, higher reliability and security [274, 261].

The challenge now faced by both fixed network and mobile operators in order to deliver these advanced wireless services while continuing to reduce the cost per-bit will inevitably lead to a consolidation of the network infrastructure [275]. For instance, due to the difficulty and potentially prohibitive costs of supplying optical fibre to all end-user premises as well as the spectrum limitations of wireless access networks, hybrid optical-wireless access networks appear to be more attractive than relying on either technology as a standalone solution. Moreover, as mobile network operators start looking into the deployment of large numbers of small cells to offer a higher capacity per user, the idea of a shared, low-cost, fibre backhaul networks based on PONs becomes especially attractive. As a result, residential broadband, enterprise connectivity and wireless data traffic, which are today carried by separate networks, must converge onto a single network architecture able to provide flexibly

and economically the performances required by these different services [276]. Notably, this approach is exactly that of the DISCUS project whose innovative physical layer has been verified in this work, particularly in Chapter 6 which has also demonstrated the feasibility of deploying a 10G wireless fronthaul link within a LR-PON. In fact, the progression of PON standards completely validates the approach taken by DISCUS; one obvious example being the recent introduction of extended reach options for XG-PON [277] and another being the introduction of wavelength division multiplexing in NG-PON2 to support increased network capacity and heterogeneous service scenarios [11].

To support the envisaged bandwidth requirements of future access networks, investigating and developing options for increasing the serial bit rate beyond 10Gb/s is imperative to enable further cost-effective upgrades for PON. With this in mind, the IEEE 802.3ca task force was formed in 2015 and is currently working towards standardising a 25G TDM-PON by 2020 [278]. In particular, the focus is on a low-cost solution for 25G E-PON coexisting with 10G E-PON with a targeted extension of up to 100G (i.e. 25G → 50G → 100G) [279]. However, the main issues with increasing the serial NRZ bit rate beyond 10Gb/s include the reduction in optical power budget, due to a reduction in the SNR, a decreased chromatic dispersion tolerance and a consequently reduced fibre reach. Moreover, higher speed components will be required which correspond to an increased overall system cost. To address these challenges, advanced modulation formats must now be investigated which provide a high spectral efficiency and possess a higher CD tolerance with a minimum increase in implementation cost. Furthermore, since cost is the most important factor in access networks, increasing the serial rate for PON beyond 10G will only make economic sense if a lower cost per bit than 10G-PON is achieved [280].

Appendix A

Q-Factor Analysis in Power and OSNR-Limited Systems

The appendix is to supplement the analysis presented section 2.4.1 which describes the process of system characterisation and performance penalty analysis for power and OSNR-limited systems based on a various values of the transmitter extinction ratio (ER).

Power-Limited System:

To account for the '0'-bit statistics, the Q-factor of a power-limited system can be determined through the following relation

$$Q = \frac{R(P_{sig,1} - P_{sig,0})}{\sigma_1 + \sigma_0} \xrightarrow[\sigma_1 = \sigma_0 = \sigma_{th}]{} \frac{R(P_{sig,1} - P_{sig,0})}{2\sigma_{th}} \tag{A.0.1}$$

where σ_{th} can be obtained from Eqn. 2.3.13 and re-written as follows,

$$\sigma_{th} = \sqrt{\frac{4k_B T}{R_L} F_n . B_e} = R.(NEP).\sqrt{B_e} \tag{A.0.2}$$

where NEP signifies the noise equivalent power which specifies the minimum power per unit bandwidth when the SNR = 1. By specifying the NEP ($W/\sqrt{Hz}$), it allows for the calculation of the optical power required to achieve a specific value of SNR. For a system dominated by thermal noise, the NEP be derived from Eqn. 2.3.14 as

$$NEP = \frac{P_{sig,1}}{\sqrt{B_e}} = \sqrt{\frac{4k_B T F_n}{R^2 R_L}} \quad [W/\sqrt{Hz}] \tag{A.0.3}$$

Furthermore, by recognising that the average received optical power is given by,

$$P_{Rx} = \frac{P_{sig,1} + P_{sig,0}}{2} \tag{A.0.4}$$

the power corresponding to the '1'-bit and '0'-bit levels can be expressed with respect to the extinction ratio (ER):

$$P_{sig,1} = 2P_{Rx}\left(\frac{ER}{ER+1}\right), \quad P_{sig,0} = 2P_{Rx}\left(\frac{1}{ER+1}\right) \tag{A.0.5}$$

where,

$$P_{sig,1} - P_{sig,0} = 2P_{Rx}\left(\frac{ER-1}{ER+1}\right) \tag{A.0.6}$$

Hence, it is then possible to re-write Eqn A.0.1 as:

$$Q = \frac{P_{Rx}}{(NEP)\sqrt{B_e}}\left(\frac{ER-1}{ER+1}\right) \tag{A.0.7}$$

It is important to note that the BER curves presented in Fig. 2.16(a) were generated by using a B_{3dB} of 12.5GHz and a NEP of $24pW/\sqrt{Hz}$ obtained from the datasheet of a conventional 10Gb/s off-the-shelf receiver.

OSNR-Limited System:

In the case of an OSNR-limited system, the current noise variance on both bit levels must account for the signal-ASE and the ASE-ASE beat noise contributions as indicated in Eqn. A.0.8

$$\sigma_{1,0}^2 = \underbrace{4R^2 P_{sig,1,0} S_{ASE} B_e}_{\substack{\text{Signal-ASE} \\ \text{Beat Noise}}} + \underbrace{4R^2 S_{ASE}^2 B_{opt} B_e}_{\substack{\text{ASE-ASE} \\ \text{Beat Noise}}} \tag{A.0.8}$$

With respect to the '1'-bit level, Eqn. A.0.8 can be re-written with respect to the ASE power (P_{ASE}) using Eqn. 2.2.26:

$$\sigma_1^2 = 2R^2 P_{ASE} P_{sig,1} \frac{B_e}{B_{ref}} + R^2 P_{ASE}^2 \frac{B_e}{B_{ref}} \frac{B_{opt}}{B_{ref}} \tag{A.0.9}$$

By recognising that $P_{sig,1} = 2(OSNR.P_{ASE})(ER/ER+1)$ through Eqn. A.0.5 and 2.2.28, the current noise variance on the '1'-bit level can be re-written as

$$\sigma_1^2 = R^2 P_{ASE}^2 \left(\frac{B_e}{B_{ref}}\right)\left[4OSNR(\frac{ER}{ER+1}) + \frac{B_{opt}}{B_{ref}}\right] \tag{A.0.10}$$

Alternatively, following a similar procedure, the current noise variance on the '0'-bit level (σ_0^2) can be determined as

$$\sigma_0^2 = R^2 P_{ASE}^2 \left(\frac{B_e}{B_{ref}}\right)\left[4OSNR(\frac{1}{ER+1}) + \frac{B_{opt}}{B_{ref}}\right] \tag{A.0.11}$$

Finally, using Eqn. A.0.6, A.0.10 and A.0.11 the Q-factor for an OSNR-limited system is given by

$$\begin{aligned} Q = \frac{R(P_{sig,1} - P_{sig,0})}{\sigma_1 + \sigma_0} &= \frac{R(2.OSNR.P_{ASE}(\frac{ER-1}{ER+1}))}{\sigma_1 + \sigma_0} \\ &= \frac{2OSNR.(\frac{ER-1}{ER+1})\sqrt{\frac{B_{ref}}{B_e}}}{\sqrt{4OSNR(\frac{ER}{ER+1}) + \frac{B_{opt}}{B_{ref}}} + \sqrt{4OSNR(\frac{1}{ER+1}) + \frac{B_{opt}}{B_{ref}}}} \end{aligned} \tag{A.0.12}$$

It should be noted that the data presented in Fig. 2.16(b) was achieved using an optical filter bandwidth, B_{opt}, of 50GHz, a reference optical bandwidth, B_{ref} = 12.5Hz (~0.1nm) and a 3dB electrical bandwidth, $B_{3dB} = \frac{2}{\pi}.B_e$ = 12.5GHz.

Appendix B

Time-Resolved Chirp Measurement

This work is intended to supplement section 4.6.6 of Chapter 4 which outlines the background of the time-resolved chirp measurement technique which was used to examine the dynamic wavelength stability of the monolithically integrated transmitter.

Frequency Discrimination:

Using a programmable optical filter based on high-resolution liquid-crystal-on-silicon (LCoS) technology with a transfer function, $H(\omega)$, designed to be linear in magnitude to the frequency, ω_p, around the carrier frequency, ω_c, with a transmission amplitude T_0 and differential coefficient c_1:

$$H(\omega_p) = T_0[1 \pm c_1(\omega_p - \omega_c)] \tag{B.0.1}$$

where, c_1 can be set as a real value that is defined by the filter bandwidth ($f_{BW} = \omega_{BW}/2\pi$) which specifies the frequency range bounded by transmission values of 0.1 and 0.9 where the centre carrier frequency has a transmission of 0.5.

$$c_1 = \frac{0.9 - 0.1}{(0.5)2\pi f_{BW}} \tag{B.0.2}$$

For Eqn. B.0.1, the following notation is then applied, $\omega = \omega_p - \omega_c$; in order to determine the output field after propagation through the filter. For instance, considering the filter with positive slope (P-Filter), the output (E_+) can be determined as

$$E_+ = \frac{1}{2\pi}\int T_0(1+c_1\omega)\tilde{\mathrm{E}}_{in}(\omega)e^{i\omega t}d\omega \tag{B.0.3}$$

$$= \frac{1}{2\pi}\int \left(T_0\tilde{\mathrm{E}}_{in}(\omega)e^{i\omega t} + T_0c_1\omega\tilde{\mathrm{E}}_{in}(\omega)e^{i\omega t}\right)d\omega \tag{B.0.4}$$

$$= T_0\left[\frac{1}{2\pi}\int \tilde{\mathrm{E}}_{in}(\omega)e^{i\omega t}d\omega - ic_1\frac{d}{dt}\left(\frac{1}{2\pi}\int \tilde{\mathrm{E}}_{in}(\omega)e^{i\omega t}d\omega\right)\right] \tag{B.0.5}$$

$$= T_0\left[E_{in}(t) - ic_1\frac{dE_{in}(t)}{dt}\right] \tag{B.0.6}$$

where, $E_{in} = \sqrt{P_{in}}.E^{i\phi}$ and $\tilde{\mathrm{E}}_{in}(\omega)$ is the Fourier transform of the input field. The corresponding optical power waveform P_+ can then be determined as

$$P_+ \equiv |E_+|^2 = E_+.E_+^* \tag{B.0.7}$$

$$= T_0^2\left((E_{in} - ic_1\frac{dE_{in}}{dt}).(E_{in}^* + ic_1\frac{dE_{in}^*}{dt})\right) \tag{B.0.8}$$

$$= T_0^2\left(E_{in}.E_{in}^* + ic_1\frac{dE_{in}^*}{dt}.E_{in} - ic_1\frac{dE_{in}}{dt}.E_{in}^* + c_1^2\frac{dE_{in}}{dt}\frac{dE_{in}^*}{dt}\right) \tag{B.0.9}$$

$$\Rightarrow T_0^2\left(|E_{in}|^2 + 2c_1P_{in}\frac{d\phi}{dt} + c_1^2\left|\frac{dE_{in}}{dt}\right|^2\right) \tag{B.0.10}$$

$$= T_0^2P_{in}\left(1 + 2c_1\frac{d\phi}{dt} + \frac{c_1^2}{P_{in}}\left|\frac{dE_{in}}{dt}\right|^2\right) \tag{B.0.11}$$

As the third term within Eqn. B.0.11 is appreciably smaller than the second term, it can be neglected to give the final form of the P_+ waveform:

$$P_+ = \cong T_0^2P_{in}\left(1 + 2c_1\frac{d\phi}{dt}\right) \tag{B.0.12}$$

A similar analysis can be carried out to determine the P_- waveform,

$$P_- \cong T_0^2P_{in}\left(1 - 2c_1\frac{d\phi}{dt}\right) \tag{B.0.13}$$

Appendix C

Power Budget and OSNR Model

The optical power budget of a LR-PON is an initial feasibility test that theoretically examines the achievable physical reach, split and dynamic range for a particular modulation scheme by ensuring that the link design is within the transceivers operating specifications. Moreover, with the introduction of optical amplification, the optical signal-to-noise ratio (OSNR) rather than just received optical power level becomes one of the prominent system limitations. As the power budget and OSNR are closely interlinked both parameters must be considered together in the overall system design. As a result, the model presented here represents a high-level study of the OSNR and power budget limitations within LR-PONs. The model assumes linearity and is based on the principle of superposition where the signal power and the noise power are assumed to propagate through the system in parallel. The system is comprised of components that are categorised as either passive or active through assigned values of gain and noise figure; this concept is illustrated in Fig. C.1. For instance, a passive component will possess a negative value of gain (G) to represent an insertion loss (IL) while its corresponding noise figure (NF) will be 0 as it does not contribute noise to the system.

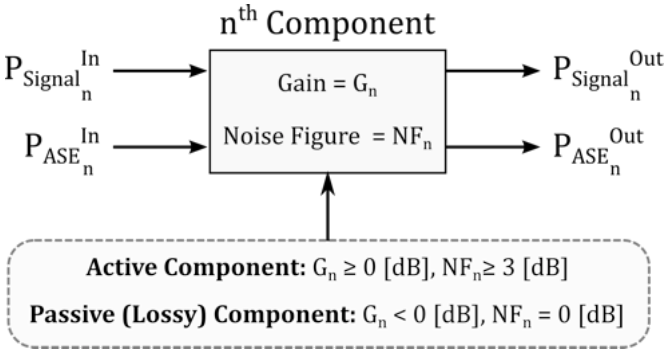


Figure C.1: Basic concept of the power and OSNR model.

Active Components:

The active components within the model are the optical amplifiers which contribute gain and optical noise (ASE) to each channel as they propagate through the system. In particular, the relations describing the amplified signal power and the corresponding ASE power at the output of an active component within the proposed system are presented in C.0.1 and C.0.2, where the amount of ASE produced is dependent on the associated noise figure (NF).

$$P^{sig}_{Out,n}\,[dBm] = P^{sig}_{In,n}\,[dBm] + G_n\,[dB] \tag{C.0.1}$$

$$P^{ASE}_{Out,n}\,[dBm] = 10.log_{10}(G_n.P^{ASE}_{In,n}\,[W] + P^{ASE}_{n}\,[W]) + 30 \tag{C.0.2}$$

where,

$$P^{ASE}_{In,n}\;[W] = \left(10^{\frac{P^{ASE}_{In,n}[dBm]}{10}}\right)\Big/1000, \qquad P^{ASE}_{n}\;[W] = 2h\nu B_{ref}G_n\left(NF_n - \frac{1}{G_n}\right)$$

$$[h \approx 6.626 \times 10^{-34}\;Js, \nu \approx 1.9341 \times 10^{14}\;Hz,\; B_{ref} = 12.5 \times 10^{9}\;GHz]$$

Passive Components:

Conversely, the passive components (optical switches, bandpass filters, optical splitters, fibre, etc.) contribute attenuation which can be interpreted as a negative gain. Moreover, as they do not contribute ASE to the system, their associated NF can be set as zero. The relations describing the attenuated signal power and the corresponding ASE power at the output of an passive component in the system are presented in C.0.3 and C.0.4 where G_n represents a *negative* value indicating an IL.

$$P^{sig}_{Out_n}\,[dBm] = P^{sig}_{In_n}\,[dBm] + G_n\,[dB] \tag{C.0.3}$$

$$P^{ASE}_{Out_n}\,[dBm] = P^{ASE}_{In_n}\,[dBm] + G_n\,[dB] \tag{C.0.4}$$

The optical signal-to-noise ratio (OSNR) at the output of the n^{th} component within the network can then be determined using the following relation:

$$OSNR_n\,[dB] = P_{out_n}^{Sig}\,[dBm] - P_{out_n}^{ASE}\,[dBm] \tag{C.0.5}$$

A list of the typical component parameters is presented in Table C.1 which outlines the maximum and minimum gain and the corresponding value of noise figure. The distinction between G_{Max} and G_{Min} values is only considered for components within the ODN in order to estimate the maximal dynamic range resulting from the varying path loss experienced by traffic from the ONUs. The splitter losses outlined in Table C.1 are derived from the ITU-T standard (G.671) [260] which accounts for the statistical variations in these components while datasheets of commercial components were used to obtain the values required for the ANs and backhaul links.

Component	**Gain (Max) [dB]**	**Gain (Min) [dB]**	**Noise Figure [dB]**
Circulator	-0.2	-0.6	0
Fibre (per km)	-0.2	-0.3	0
Splice	-0.0	-0.3	0
1:2 Splitter	-2.8	-4.1	0
1:4 Splitter	-5.4	-7.5	0
1:8 Splitter	-7.9	-11.05	0
1:16 Splitter	-10.5	-14.4	0
1:32 Splitter	-13	-18.1	0
Mux/DeMux	-4	-6.0	0
Optical Switch	-1.8	-2.0	0
Tuneable Filter	-4	-4	0
Optical Amplifier	$\mathbf{G}_{Max}$	$\mathbf{G}_{Min}$	**NF**

Table C.1: Component parameters for the power and OSNR model.

It is important to recognise that this power and OSNR model does not directly account for optical transients (e.g. from the amplifiers), dispersion or non-linear interactions between the optical signals and the fibre. In practice, these phenomena can produce interference, distortion and excess attenuation on the optical signals, hence, the limitations they impose must be considered within the network design. To address these issues in this analysis, we assume the utilisation of gain-stabilised EDFAs with adequate transient suppression circuitry, dispersion compensating fibre (DCF) or electronic dispersion compensation (EDC) while the output power levels

of transmitter and amplifiers are chosen in order to assure linear fibre propagation and linear amplifier operation.

Polarisation Dependent Loss

Within the component parameters presented in Table C.1, the polarisation dependent loss (PDL) of the commercial passive components (i.e. circulators, filters) has been included using the values specified within the associated datasheets while the PDL of the passive optical splitters has been accounted for using the following table which can be found in the ITU-T G.671 standard [260]. Notably, the separation of PDL from the analysis of polarisation-mode dispersion (PMD) is justified when the system limitations caused by PDL are related primarily to its role as a random attenuator [281]. In practice, the PDL must be considered in the power budget in order to accurately estimate the dynamic range of the upstream signal.

Component	**Maximum PDL [dB]**
1:2 Splitter	0.2
1:4 Splitter	0.2
1:8 Splitter	0.25
1:16 Splitter	0.3
1:32 Splitter	0.4

Table C.2: Polarisation dependent loss specifications for passive optical splitters.

In practice, PDL accumulation over a large number of components is statistical; therefore, the calculation of the worst-case PDL can lead to overestimation. Using the theory presented in [281], the probability distribution of the accumulated PDL for a series of components within an optical network ($P_z(\rho)$) can be estimated through the following relations:

$$P_z(\rho) = \frac{4\rho^2}{\sqrt{\pi}[2\sigma^2(z)]^{3/2}}.exp[-\frac{\rho^2}{2\sigma^2(z)}] \tag{C.0.6}$$

$$\langle\rho^2\rangle = 3\sigma(z)^2 = \frac{9\gamma^2}{2}(e^{2z/9} - 1) \tag{C.0.7}$$

where, ρ indicates the magnitude of the PDL [dB], σ gives the variance of the distribution, $\langle \rho^2 \rangle$ is the mean-square PDL and $\gamma = \frac{20}{log_e(10)} \approx 8.7$ is a constant.

Using the data within Table C.2, the probability distribution of the accumulated PDL within the open-ring architecture proposed for rural access in Chapter 5 is presented in Fig. C.2. It should be noted that as the PDL of some components was not defined within ITU-T G.671, corresponding values were taken from specifications of equivalent commercial components. In practice, the overall accumulated PDL will vary with time, hence the impact of this phenomenon will average to some extent. Nonetheless, the system under investigation consists of four chained amplifier nodes (ANs), each separated by 30km supporting a 20km distribution network with 128 users to give a total of 512 over a total physical reach of 120km. The PDL analysis is undertaken for an ONU connected to the ODN of AN 4 whose signal traverses the longest path with respect to the OLT which is located in primary metro/core node. In particular, this configuration presents 41 PDL contributions which produces a mean-square value of approximately 2dB and peak at 1.2dB. In practice, these values should be taken into account when considering the performance margin of the proposed open-ring configuration.

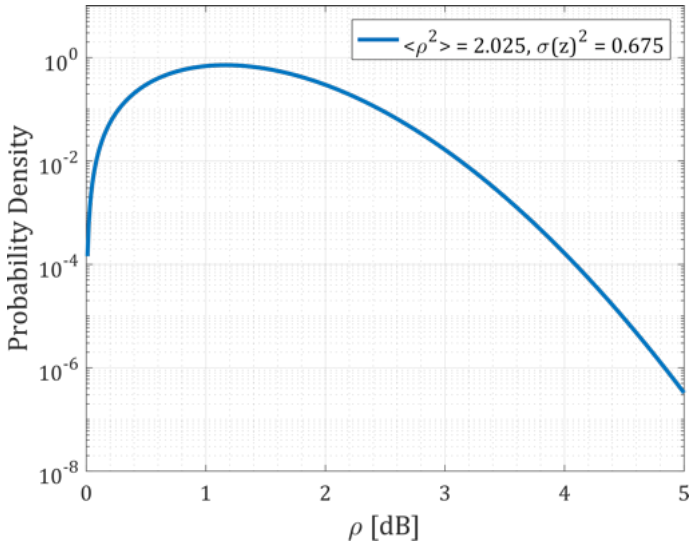


Figure C.2: Probability distribution of the accumulated PDL within the proposed open-ring configuration which employs 4 chained amplifier nodes, each supporting a 20km distribution network with 128 users.

Appendix D

Time-Dependent Gain Model for Erbium-Doped Fibre Amplifiers

Consider a length of Erbium-doped fibre (EDF) supporting N optical channels as shown in Fig. D.1. The n^{th} channel of wavelength, λ_n, has an optical power of $P_n^{In}(t)$ and $P_n^{Out}(t)$ at the input and output respectively at a time t.



Figure D.1: Model of an erbium-doped fibre supporting N channels [227].

The corresponding rate equation for the fraction of atoms in the excited state, $N_2(z,t)$, and the photon propagation equation for the n^{th} channel are given by

$$\frac{\partial N_2(t)}{\partial t} = -\frac{N_2(z,t)}{\tau_0} - \frac{1}{\rho S}\sum_{i=1}^{N} u_i \frac{\partial P_i(z,t)}{\partial z} \tag{D.0.1}$$

$$\frac{\partial P_n(z,t)}{\partial z} = u_n[(\gamma_n + \alpha_n)N_2(z,t) - \alpha_n]P_n(z,t) \tag{D.0.2}$$

where, τ_0 is the spontaneous lifetime of the upper level, ρ is the number density of the active erbium atoms, S is the fibre core cross-section, γ_n is the emission constant (i.e. the gain constant for complete inversion), α_n is the absorption constant and u_n is a unit vector with a value of +1 for forward propagation and -1 for counter propagation [227]. In this model, the signal and pump channels are treated equally

and the optical power is expressed as photons per unit time (i.e. normalised to their photon energy) while ASE can be modelled by adding effective input signals with appropriate power and bandwidth. Furthermore, it is important to note that the fractional populations of the upper and lower energy levels satisfy the following relation

$$N_1(z,t) + N_2(z,t) = 1 \tag{D.0.3}$$

By integrating Eqn. D.0.1 from 0 to L, the following expression can be obtained

$$\frac{d}{\partial t}\int_0^L N_2(z,t)dz + \frac{1}{\tau_0}\int_0^L N_2(z,t)dz = -\frac{1}{\rho S}\sum_{i=1}^{N}\left[P_i^{Out}(t) - P_i^{In}(t)\right] \tag{D.0.4}$$

At this point the key parameters of this two-level model are introduced; these include the average inversion level, $\bar{N}_2$, which represents the population of the upper level normalised to the total population density and the average amplifier gain coefficient of the i^{th} channel.

$$\bar{N}_2(t) = \frac{1}{L}\int_0^L N_2(z,t)dz \tag{D.0.5}$$

$$\bar{g}_i(t) = \frac{1}{L} log_e\left(\frac{P_i^{Out}(t)}{P_i^{In}(t)}\right) \tag{D.0.6}$$

Substituting Eqn. D.0.5 into Eqn. D.0.4 yields the characteristic relation for this analysis which is known as the time-dependent *average inversion model*.

$$\frac{d}{dt}[\rho SL\bar{N}_2(t)] + \frac{\rho SL}{\tau_0}\bar{N}_2(t) = -\sum_{i=1}^{N}\left[P_j^{Out}(t) - P_j^{In}(t)\right] \tag{D.0.7}$$

With respect to Eqn D.0.2, re-arranging the equation and integrating over the entire length of the fibre provides an expression for the overall amplifier gain for the i^{th} channel, $G_i(t)$, which highlights the relation to the average inversion level, $N_2(t)$.

$$\int_{P_i^{In}(t)}^{P_i^{In}(t)} \frac{\partial P_i(z,t)}{P_i(z,t)} = \int_0^L u_i[(\gamma_i + \alpha_i).N_2(z,t) - \alpha_i]\partial z \tag{D.0.8}$$

$$\Rightarrow log_e\left(\frac{P_i^{Out}(t)}{P_i^{In}(t)}\right) = [u_i(\gamma_i + \alpha_i)\bar{N}_2(t) - u_i\alpha_i]L \tag{D.0.9}$$

By recognising that the expression on the right hand side of Eqn. D.0.9 is related to the average gain coefficient defined in Eqn. D.0.6, an expression for the overall amplifier gain coefficient, $G_i(t)$, for forward propagating beams (u_i = +1) can be derived as

$$G_i(t) = \bar{g}_i(t)L = [(\gamma_i + \alpha_i)\bar{N}_2(t) - \alpha_i]L \tag{D.0.10}$$

Hence, the output power of the i^{th} channel can be written as

$$P_i^{Out}(t) = P_i^{In}(t)e^{G_i(t)} \tag{D.0.11}$$

By using Eqn. D.0.11, the expression on the right hand side of Eqn. D.0.7 can be re-written with respect to $G_i(t)$

$$-\sum_{i=1}^{N}[P_j^{Out}(t) - P_j^{In}(t)] = -\sum_{i=1}^{N}[P_i^{In}(t)e^{G_i(t)} - P_j^{In}(t)] \tag{D.0.12}$$

$$= -\sum_{i=1}^{N}[P_i^{In}(t).(e^{G_i(t)} - 1)] \tag{D.0.13}$$

In addition, by rearranging the terms in Eqn.D.0.10, an expression of the average inversion can be obtained with respect to $\bar{g}_i(t)$, γ_i and α_i.

$$\bar{g}_i(t) = [(\gamma_i + \alpha_i)\bar{N}_2(t) - \alpha_i] \quad \Rightarrow \quad \bar{N}_2(t) = \frac{\bar{g}_i(t) + \alpha_i}{\gamma_i + \alpha_i} \tag{D.0.14}$$

Substituting Eqn. D.0.14 and D.0.12 into Eqn. D.0.7, the following time-dependent relation with respect to $\bar{g}_i(t)$ can be obtained

$$\tau_0 \frac{d\bar{g}_i(t)}{dt} + \bar{g}_i(t) + \alpha_i = -\frac{\tau_0(\gamma_i + \alpha_i)}{\rho SL} \sum_{i=1}^{N} [P_i^{In}(t).(e^{G_i(t)} - 1)] \tag{D.0.15}$$

At this point, the intrinsic saturation power, P_i^{IS}, of the i^{th} channel as defined in [233] can be introduced

$$P_i^{IS} = \frac{\rho S}{\tau_0(\gamma_i + \alpha_i)} \tag{D.0.16}$$

By introducing P_i^{IS} into Eqn. D.0.15, the time-dependent gain model can be re-written as

$$\tau_0 \frac{d\bar{g}_i(t)}{dt} + \bar{g}_i(t) + \alpha_i = -\frac{1}{P_i^{IS} L} \sum_{i=1}^{N} [P_i^{In}(t).(e^{G_i(t)} - 1)] \tag{D.0.17}$$

Finally, by recognising that $G_i(t) = \bar{g}_i(t).L$ in accordance with Eqn. D.0.10; the final expression for the time-dependent EDFA gain model which represents the coupled relation between all wavelengths passing through the EDFA is given as

$$\tau_0 \frac{dG_i(t)}{dt} + G_i(t) + \alpha_i L = -\frac{1}{P_i^{IS}} \sum_{i=1}^{N} [P_i^{In}(t).(e^{G_i(t)} - 1)] \tag{D.0.18}$$

Notably, for dynamic processes such as an add/drop event, power variations due to the nature of burst-mode traffic or a partial link failure the expression on the right hand side of Eqn. D.0.18 will vary and result in gain variations over time in all the optical channels. This cross-gain modulation effect is a major concern for the use of EDFAs in the access domain.

The Transient Response of EDFAs

For small perturbations in the gain, the response of the EDFA can be assumed to have a single effective time constant, τ_{eff} where the Eqn. D.0.18 has been linearised for t close to the steady state value, $G_i(\infty)$, using a Taylor Series:

$$G_i(t) = G_i(\infty) - \tau_{eff} \frac{dG_i(t)}{dt} \tag{D.0.19}$$

where, τ_{eff} can be determined using Eqn.D.0.18:

$$\frac{1}{\tau_{eff}} = -\frac{\partial}{\partial G_i}\left(\frac{dG_i(t)}{dt}\right)\Bigg|_{t=\infty} \tag{D.0.20}$$

$$= -\frac{\partial}{\partial G_i}\left(\frac{1}{\tau_0}\left[-\frac{1}{P_i^{IS}}\sum_{j=1}^{N}[P_i^{In}(t).(e^{G_j(t)}-1)] - G_i(t) - \alpha_i L\right]\right)\Bigg|_{t=\infty} \tag{D.0.21}$$

$$= -\frac{1}{\tau_0}\left(-\frac{1}{P_i^{IS}}\sum_{j=1}^{N}[P_j^{In}(t).\frac{\partial G_j}{\partial G_i}(e^{G_j(t)})] - 1\right)\Bigg|_{t=\infty} \tag{D.0.22}$$

At this point, Eqn. D.0.16 and D.0.10 can be used to determine the differential gain between the channels ($\partial G_j/\partial G_i$) as

$$\frac{\partial G_j}{\partial G_i} \equiv \frac{\partial G_j/\partial \bar{N}_2}{\partial G_i/\partial \bar{N}_2} = \frac{(\gamma_j+\alpha_j)}{(\gamma_i+\alpha_i)} = \frac{P_i^{IS}}{P_j^{IS}} \tag{D.0.23}$$

Notably, Eqn. D.0.23 is independent of the degree of inversion and is only a consequence of the fibre parameters. Nonetheless, through substitution, τ_{eff} can be expressed as

$$\Rightarrow \quad \frac{1}{\tau_{eff}} = \frac{1}{\tau_0}\left(\frac{1}{P_i^{IS}}\sum_{j=1}^{N}[P_j^{In}(t).\frac{P_i^{IS}}{P_j^{IS}}.(e^{G_j(t)})] + 1\right)\Bigg|_{t=\infty} \tag{D.0.24}$$

$$= \frac{1}{\tau_0}\left(\frac{1}{P_i^{IS}}\sum_{j=1}^{N}[\frac{P_i^{IS}}{P_j^{IS}}.P_i^{Out}(\infty)] + 1\right) \tag{D.0.25}$$

$$= \frac{1}{\tau_0}\left(\sum_{j=1}^{N}\frac{P_i^{Out}(\infty)}{P_j^{IS}} + 1\right) \tag{D.0.26}$$

where, $P_i^{Out}(t) = P_i^{In}(t)e^{G_i(t)}$ used in accordance with Eqn. D.0.11 and $P_i^{Out}(\infty)$ is the steady state value. The effective time constant now takes the form

$$\tau_{eff} = \frac{\tau_0}{1+\eta} \tag{D.0.27}$$

where the saturation parameter, η, has been introduced to represent the summation of the output powers which are normalised to their corresponding saturation powers.

It is important to note that η only depends on the output power and not the power averaged over the fibre.

$$\eta = \sum_{j=1}^{N} \frac{P_i^{Out}(\infty)}{P_j^{IS}} \tag{D.0.28}$$

When a dynamic process such as a step change in input power of one or more channels or channel add/drop is assumed to occur at $t = 0$ and the EDFA once again reaches the steady-state condition at $t = \infty$; the overall gain coefficient of the EDFA as a function of time can be written using τ_{eff} [236]:

$$G_i(t) = G_i(\infty) + (G_i(0) - G_i(\infty)).e^{-\frac{t}{\tau_{eff}}}, \quad for \quad t > 0 \tag{D.0.29}$$

where the EDFA is assumed to be in the steady state when $t \leq 0$. The output power is then obtained through Eqn. D.0.11:

$$P_i^{Out}(t) = P_i^{Out}(\infty)\left[\frac{P_i^{Out}(0)}{P_i^{Out}(\infty)}\right]^{e^{-\frac{t}{\tau_{eff}}}} \tag{D.0.30}$$

where, $P_i^{In}(0) = P_i^{In}(\infty)$.

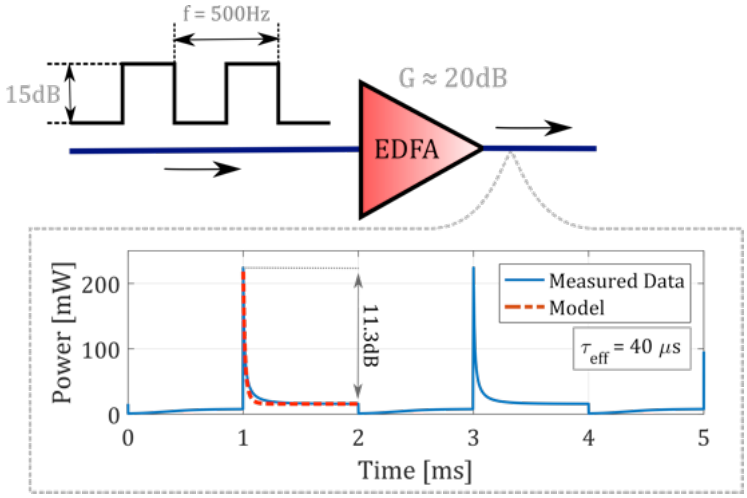


Figure D.2: Captured data from an oscilloscope showing transients from a commercial EDFA in the absence of active gain control for an optical signal at 1550.12nm. (The fitting curve was applied using Eqn. D.0.30 with $\tau_{eff} = 40\mu s$).

Appendix E

Overview of the Linear Burst-Mode Receiver Assembly

The 10G-capable linear burst-mode receiver (LBMRx) die measures 2.4 x 2.1 mm^2 and uses 650mW with 2.5V/3.3V supplies. It was flip-chipped onto an Aluminium Nitrate (AlN) substrate with tracks and coplanar waveguides (CPWs) for DC and RF electrical connections respectively before being wire-bonded to a 10G InGaAs/InP PIN photodiode along with four 1nF capacitors (one for each supply line) are attached to the substrate using silver epoxy as illustrated in Fig. E.1.

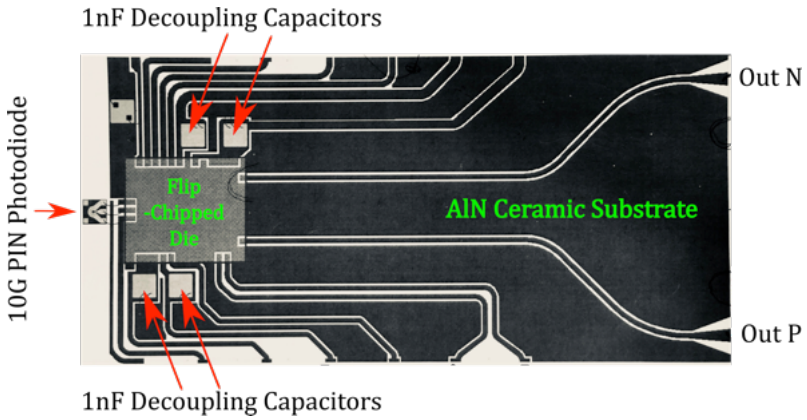


Figure E.1: Illustration of the unpackaged LBMRx subassembly chip showing the die flip-chipped onto the ceramic substrate and wire-bonded to the 10G PIN photodiode.

The LBMRx sub-assembly was then packaged into a customised 14-pin butterfly module with GPPO connections. To achieve this, the ceramic was placed flush with the package wall and aligned with the GPPO connector feedthroughs. Each track line was then wire bonded to the pins of the butterfly package. Notably, due to the absence of a TEC (thermoelectric cooler) underneath the assembly, the CPW

RF-outputs did not align with the GPPO outputs of the butterfly package. Consequently, to overcome this issue, a connection made of silver epoxy is built up to the GPPO level. A metalised lensed fibre with a bevel angle of 45°was employed to couple the light into the high-speed photodiode where an active optical alignment was performed using micro-positioning units to maximise the average photocurrent for a given optical power. To complete the packaging process, the fibre pigtail along with a strain relief boot was secured to the cylindrical window of the packaging unit using epoxy adhesive. The packaged LBMRx was then mounted and soldered on a custom printed circuit board (PCB) shown in Fig. E.2 which was designed to simplify the interface with the rest of the setup and to avoid non-optimal connections and its RF outputs are connected using semi-rigid cable assemblies (GPPO to 2.4mm).

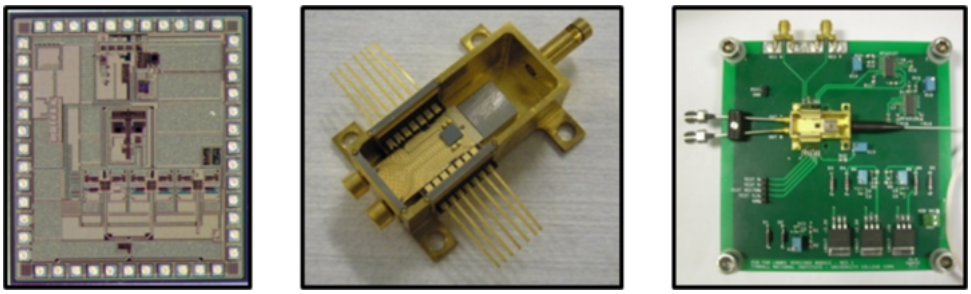


Figure E.2: LBMRx Assembly: (a) Image of the 10G LBMRx Die (b) packaged LBMRx chip (c) LBMRx with accompanying PCB.

Finally, the LBMRx and the LV 24-33 microcontroller board used to communicate with it were then mounted together on an aluminium optical breadboard. An additional PCB with a series of different ac-coupling capacitor values is also added to the configuration to compensate for the residual dc-offset between consecutive packets which arises from mismatch between transistors and resistors. In this work, the two RF outputs of the LBMRx are AC-coupled using 560pF capacitors.

Appendix F

DISCUS Demonstration: ECOC Exhibition, 2015

In order to increase the impact of the DISCUS project, a demonstration of the key enabling technologies and architecture was presented at the European Conference on Optical Communications (ECOC), which was held in Valencia, Spain in September 2015. The demonstration was hosted at the ECOC exhibition by our industrial project partners Polatis™ who manufacture the optical beam steering switches used within the experimental testbed to provide network reconfigurability.



Figure F.1: Logo for the European Conference on Optical Communications, 2015.

For the physical layer demonstration, it was decided to implement a simplified version of the single amplifier node (tree-structured) topology which could still demonstrate the novel features of the DISCUS architecture. In addition, through a collaboration with researchers from Trinity College in Dublin, control plane services integrated with the physical layer targeted streaming a 4K video downstream from the OLT to the ONU and a protection scenario which simulated a fibre break using the optical switch in order to interrupt active services and induce network reconfiguration.

The Physical Layer Configuration:

The details of the physical layer are illustrated in Fig. F.2. At the access edge, the ONUs consisted of commercially available tuneable small form factor pluggable (SFP+) 10G transceivers controlled using Xilinx™Virtex 7 FPGAs with external SOAs employed to carve the upstream burst envelopes; while, at the receiver side, a remotely tuneable bandpass filter was used to isolate the downstream wavelength. The optical distribution network was comprised of 20km of standard single-mode fibre (SMF) and a combination of passive splitters while a variable optical attenuator (VOA) was used to emulate end-of-life fibre attenuation and excess splitter loss [260]. The total emulated split factor for the portable DISCUS demonstration was 128 (4x4x8). In particular, part of the total ODN split (4x4) was located in the amplifier node alongside the commercial gain-stabilised erbium-doped fibre amplifiers (EDFAs) in order to combine upstream and downstream traffic while also providing access to a protection path in the event of a backhaul fibre break or service node (SN) failure. On the primary path, the amplifier node was connected to the SN using 50km of SMF, providing a total physical reach of 70km for the demonstration. At the head end of the system, the SN included a Polatis™optical switch, an *OpenFlow* SDN 10GbE switch, one access controller, in addition to two OLTs. As in the case of the ONUs, each OLT contained an FPGA controlled SFP+ transceiver, a packaged 10G linear burst mode receiver (LBMRx) and a commercial continuous-mode electronic dispersion compensation (EDC) chip which also performed the clock and data recovery (CDR). Notably, the optical switch was partitioned logically to emulate two geographically separated core nodes. Moreover, in order to provide the worst-case differential reach for the system, the protection path was created by connecting the amplifier node directly to the SN.

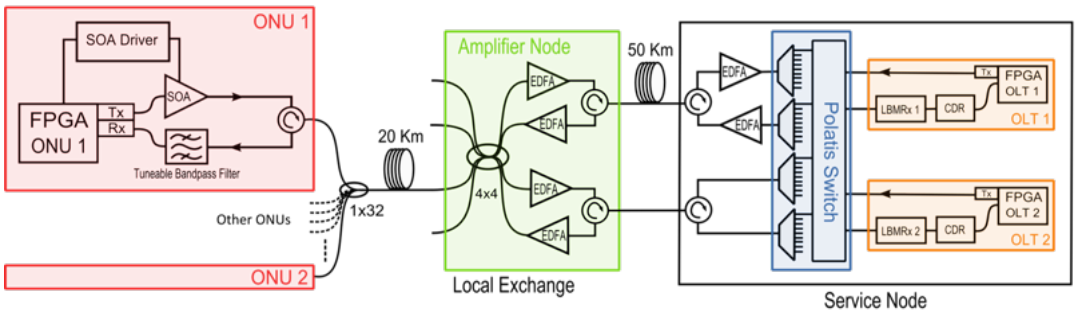


Figure F.2: Physical layer architecture of the portable DISCUS demonstrator.

Link Power and OSNR Model:

The feasibility of the physical layer for the ECOC demonstration was initially investigated using the power and OSNR model which is presented in Appendix C; the corresponding results are shown in Fig. F.3. Assuming the used of an APD-based photoreceiver and the implementation of FEC in both transmission directions, the performance of the portable physical layer demonstration designed for the ECOC exhibition can achieve *error-free* operation (post-FEC BER $\leq 1\times10^{-12}$). In particular, this performance requires the use of gain-stabilised EDFAs capable of supplying inline gain of 18dB and 14dB within the AN and SN receptively for both transmission directions. For instance, in the downstream direction, which is typically power-limited due to the high loss of the ODN, the required per-channel output power launched by both SN and AN EDFAs is approximately +9.5dBm which corresponds to a total aggregate power of +25.5dBm for a fully loaded system of 40 channels. While this value is relatively high, it is achievable for commercially-available amplifiers; moreover, as the downstream transmission is broadcast in continuous-mode, the requirements of the transient suppression circuitry can be relaxed. Alternately, in the OSNR-limited upstream link, the maximum per-channel output power is estimated to be approximately -2dBm at the AN and -6dBm at the SN corresponding to a total aggregate power of +14dBm and +10dBm respectively for a 40-channel system; these values are also well within the capabilities of commercial devices.

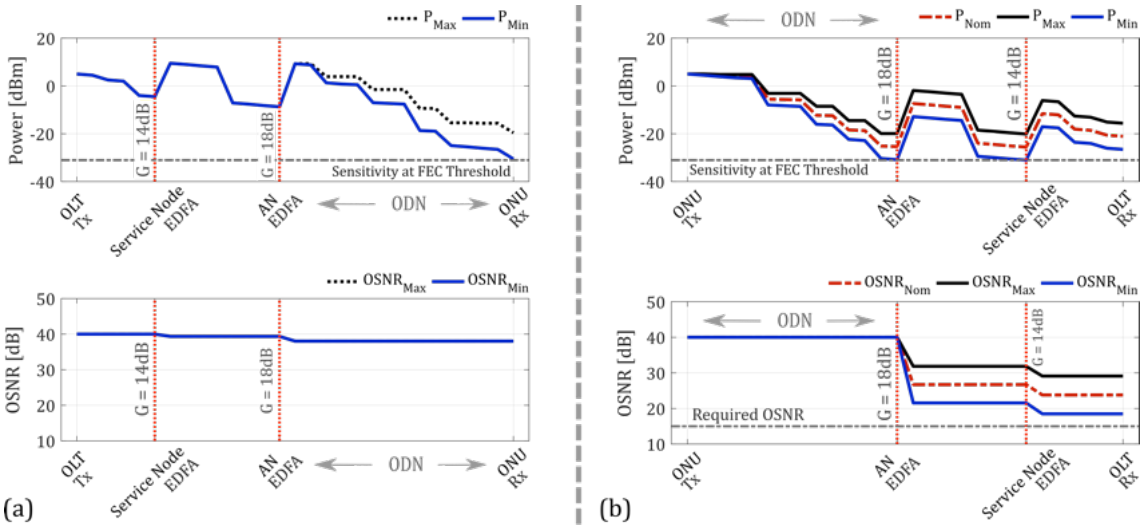
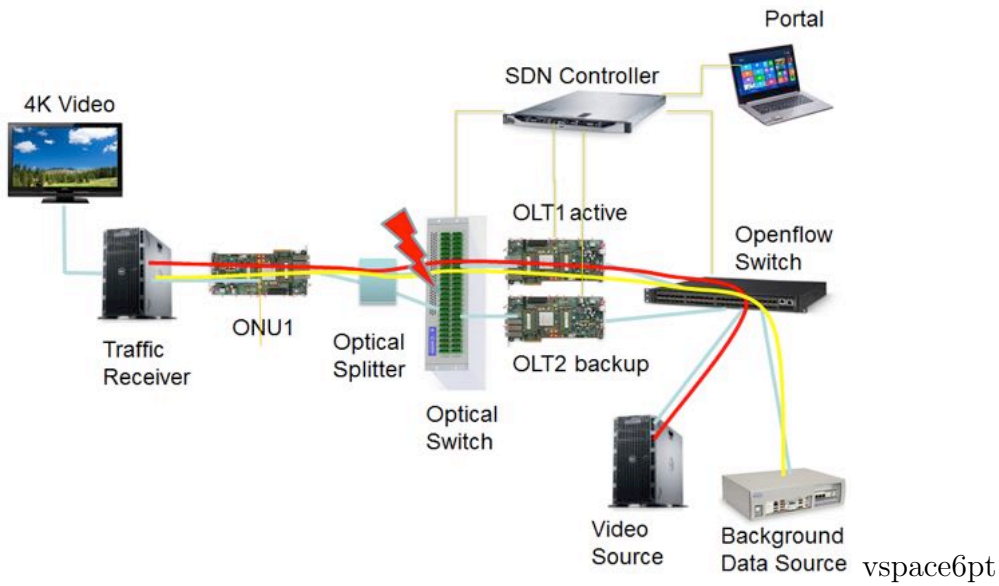


Figure F.3: The power and OSNR model for the (a) downstream and (b) upstream transmission directions of the ECOC physical layer demonstration.

The Integrated SDN Control Plane Services:

A high level overview of the control plane developed by researchers from Trinity College Dublin is presented in F.4. For the protection scenario, fibre breaks (identified by loss of light in the upstream path, considering round-trip-time, connected ONUs, and estimated quiet windows) trigger a failure alarm, which is directly notified from the PON controller to the OpenFlow controller through in-band signalling. This showcased the operation of OpenFlow switch, optical switch, OLT, ONU and control plane.



vspace6pt

Figure F.4: Control plane overview of the portable DISCUS demonstrator.

Unfortunately, unexpected issues with the mains power supply at the venue resulted in the failure of one of the OLT FPGAs and as a result the protection scenario could not be presented at the exhibition. Hence, only the 4K video streaming service over the LR-PON was presented. Nonetheless, The portable DISCUS testbed demonstrated the fundamental operation of a core node while showcasing a symmetric 10G-capable PON architecture comprised of physical layer transmission (with 10Gb/s burst mode components, wavelength reconfigurability, extended reach and switching technology) and Layer-2 protocols at the ONUs and OLTs, controlled by an SDN control plane capable of satisfying on-demand user requests, such as 4K definition video-on-demand applications.

Overall, despite some unforeseen technical difficulties, the demonstration was very successful and of high impact attracting more than 50 visitors from more than 40 companies (excluding DISCUS partners) that showed great interest in the project and the key enabling technologies.



Figure F.5: DISCUS demonstration hosted by Polatis™at the ECOC Exhibition, 2015.



Figure F.6: Portable DISCUS demonstration: ECOC 2015, Valencia, Spain.
(F. Slyne, C. Blümm, S. Porto, N. Brandonisio, G. Talli, D. Carey and P. Townsend)

Acronyms and Abbreviations

ADSL	Asymmetric Digital Subscriber Line
AFG	Arbitrary Function Generator
AM	Amplitude Modulation
AN	Amplifier Node
APD	Avalanche Photodiode
ASE	Amplified Spontaneous Emission
ASIC	Application Specific Integrated Circuit
AWG	Arrayed Waveguide Grating
BER	Bit Error Rate
BERT	Bit Error Rate Tester
BM	Burst-Mode
BMRx	Burst-Mode Receiver
BPF	Bandpass Filter
BT	British Telecom
CAPEX	Capital Expenditure
CATV	Community Access Television
CD	Chromatic Dispersion
CDR	Clock and Data Recovery
CID	Consecutive Identical Digits
CIP	Centre for Integrated Photonics (now Huawei), Ipswich, UK.
CN	Core Node
CPRI	Common Public Radio Interface
CW	Continuous Wave
DBA	Dynamic Bandwidth Assignment
DCF	Dispersion Compensating Fibre
DFB	Distributed Feedback
De-MUX	De-Multiplexer
DCF	Dispersion Compensating Fibre
DISCUS	DIStributed Core for ubiquitous bandwidth supply for all Users and Services

DML	Directly Modulated Laser
DP-QPSK	Dual-Polarisation Quadrature Phase Shift Keying
DR	Dynamic Range
DS	Downstream
DSL	Digital Subscriber Line
DWA	Dynamic Wavelength Allocation
EAM	Electro-absorption Modulator
EDC	Electronic Dispersion Compensation
EDFA	Erbium-Doped Fibre Amplifier
EMI	Electromagnetic Interference
E-PON	Ethernet Passive Optical Network
ER	Extinction Ratio
FP	Fabry-Pérot
FEC	Forward Error Correction
FTTC	Fibre-to-the-Cabinet
FTTH	Fibre-to-the-Home
FTTP	Fibre-to-the-Premises
FSAN	Full Service Access Network
FWM	Four Wave Mixing
G-PON	Gigabit Passive Optical Network
GVD	Group Velocity Dispersion
HD	High-Definition
IC	Integrated Circuit
IEEE	Institute of Electrical and Electronic Engineers
IP	Internet Protocol
IR	Infrared Radiation
ISI	Inter-symbol Interference
ITU	International Telecommunication Union
LE	Local Exchange
LP	'Loud' Packet
LPF	Low-Pass Filter
LTE	Long Term Evolution
M/C	Metro/Core
MEMS	Micro-Electro-Mechanical System

MUX	Multiplexer
NC	Node Controller
NetO	Network Orchestrator
NEP	Noise Equivalent Power
NG-PON	Next Generation Passive Optical Network
NRZ	Non-Return-to-Zero
OEO	Optical-Electrical-Optical
ODN	Optical Distribution Network
OLT	Optical Line Terminal
ONU	Optical Network Unit
OOK	On-Off Keying
OSNR	Optical Signal-to-Noise Ratio
OSA	Optical Spectrum Analyser
PCB	Printed Circuit Board
PD	Photodiode
PDG	Polarisation Dependent Gain
PDL	Polarisation Dependent Loss
PIN	Positive-Intrinsic-Negative
PMD	Polarisation Mode Dispersion
PON	Passive Optical Network
PPG	Pulse Pattern Generator
PRBS	Pseudorandom Binary Sequence
QWI	Quantum Well Intermixing
RE	Reach Extender
R-EAM	Reflective Electro-absorption Modulator
RF	Radio Frequency
SBS	Stimulated Brillouin Scattering
SDN	Software Defined Networking
SSMF	Standard Single-Mode Fibre
SN	Service Node
SNR	Signal-to-Noise Ratio
SOA	Semiconductor Optical Amplifier
SEM	Scanning Electron Microscope
SP	'Soft' Packet

SPM	Self-Phase Modulation
SRS	Stimulated Raman Scattering
TBPF	Tuneable Bandpass Filter
TDM	Time-Division Multiplexing
TDMA	Time Division Multiple Access
TIR	Total Internal Reflection
TWDM	Time and Wavelength Division Multiplexing
US	Upstream
VCSEL	Vertical Cavity Surface Emitting Laser
VDSL	Very High Bit Rate Digital Subscriber Line
VOA	Variable Optical Attenuator
WDM	Wavelength Division Multiplexing
WiMAX	Worldwide Interoperability For Microwave Access
WL	Wavelength Locker
XG-PON	Next-Generation 10G-PON
XPM	Cross Phase Modulation

List of Figures

1.1 Global submarine fibre-optic cable map 1
1.2 Compound annual growth rate forecast for internet protocol traffic . . 2
1.3 OECD: Annual growth of fibre subscriptions, December 2016-2017 . . 3
1.4 Conventional structure of a PON. 4
1.5 High-level network concept proposed for urban and rural deployment. 6

2.1 Single-mode fibre patch cord with magnified ferrule. 12
2.2 Illustrated cross section of a step-index single-mode fibre. 14
2.3 Diagram of a basic optical communication system using IM/DD. . . . 15
2.4 Illustration of an NRZ-OOK modulation signal. 16
2.5 Spectral envelope of a monochromatic carrier modulated at 10Gb/s. . 16
2.6 Attenuation spectrum of the first low-loss SMF (1979). 20
2.7 Propagation Loss in Optical Fibre for an Attenuation of 0.2dB/km. . 22
2.8 Dispersion parameter as a function of wavelength for SMF. 24
2.9 Illustration of the utilisation strategy for optical amplifiers. 27
2.10 Optical amplifier gain as a function of the output power. 29
2.11 SOA: Gain and noise figure as a function of the input power. 31
2.12 Walk-off length as a function of the channel spacing at 10Gb/s. 35
2.13 Illustration of the direct detection process with indicated noise sources. 39
2.14 Bit error rate as a function of the Q-factor. 48
2.15 Illustration of the main fibre-optic system characterisation processes . 50
2.16 BER simulation for a power-limited and OSNR-limited link. 51
2.17 Performance penalty in power- and OSNR-limited systems. 52

3.1 Illustration of a modern telecommunication network hierarchy. 56
3.2 Percentage of fibre connections in total broadband subscriptions (2017). 58
3.3 Theoretical performance of DSL technologies. 59
3.4 Baseline configuration of G-PON and E-PON. 61
3.5 Illustration of TDM and TDMA operation. 62
3.6 Node consolidation using a long-reach PON. 63
3.7 Wavelength map of 10G-EPON and legacy E-PON systems. 66
3.8 FSAN roadmap for the standardisation of optical access networks . . 67
3.9 NG-PON2 wavelength map. 71
3.10 Rural High-Speed Broadband Coverage, Europe, 2017 74
3.11 Status of High-Speed Broadband in the Republic of Ireland, 2017 . . . 75
3.12 Comparison of (a) National and (b) Rural Fibre-to-the-Premises Coverage Within the EU as of Mid-2017 76

3.13 DISCUS: High-level physical layer concept. 78
3.14 DISCUS: Predicted node reduction: Republic of Ireland. 79
3.15 DISCUS: Wavelength plan. 81
3.16 Illustration of gain transients from an EDFA-based amplifier node. . . 82
3.17 Burst-mode receiver and subsytems concept. 83

4.1 Electronic transitions between the conduction and valence bands. . . . 88
4.2 Basic laser configuration based on a Fabry-Pérot cavity. 89
4.3 InGaAsP Bandgap Energy as a function of the lattice constant. 90
4.4 Schematic of a generic tuneable laser. 91
4.5 Illustration of the backscattering and reflection mechanisms in a carrier distributed PON. 93
4.6 Illustration of a typical tuneable laser 'butterfly' package. 96
4.7 SEM image and schematic of the MEMS tuneable VCSELs. 99
4.8 L-I-V Curves measured for various MEMS tuning currents. 100
4.9 Demonstration of the MEMS-VCSEL tuneability. 101
4.10 Sample optical spectra produced by the MEMS-VCSEL. 102
4.11 Analysis of the VCSEL wavelength stability with time. 103
4.12 Illustration of the LabVIEW-based wavelength control loop. 104
4.13 Experimental setup used to determine the transmission performance of the MEMS-tuneable VCSEL. 105
4.14 BER analysis for the externally modulated MEMS-VCSEL. 106
4.15 Cross-section of a three-sectioned slotted Fabry-Pérot laser. 109
4.16 Illustration of the Vernier tuning effect For a three-sectioned slotted Fabry-Pérot laser. 110
4.17 Optical microscope image of the monolithically integrated transmitter. 111
4.18 SEM images of the monolithically integrated transmitter. 112
4.19 Microscope view of the probe station setup. 113
4.20 Coarse tuning map recorded using 5mA steps. 114
4.21 SMSR of the achieved lasing modes plotted against the peak wavelength 115
4.22 Optical spectra of 10 discrete lasing modes with SMSR > 30dB. 115
4.23 Illustration of the measurement setup used for the frequency response measurement. 116
4.24 The s-parameter conventions for a two-port device-under test. 117
4.25 Normalised small-signal frequency response of the integrated transmitter 118
4.26 ASE spectrum of the integrated SOA section for an applied bias of 30mA 119
4.27 Illustration of the idealistic Hakki-Paoli approach compared with the Westbrook method. 121
4.28 Calculation of the transmission ratio, r', as a function of the normalised passband. 122
4.29 Single-pass gain generated by the integrated SOA section for an applied bias current of 30mA. 123
4.30 Estimating the insertion loss of the integrated modulator section. . . . 124

4.31 Temperature dependence of the lasing wavelength. 125
4.32 The impact of crosstalk between the integrated transmitter components 126
4.33 Experimental setup: 10G continuous-mode transmission tests. 127
4.34 Eye crossing point and extinction ratio as a function of the applied modulator bias. 128
4.35 10G transmission performance of the integrated transmitter. 129
4.36 Optical filter profiles used for frequency discrimination. 131
4.37 Experimental setup: Time-resolved chirp measurement. 132
4.38 P_{AM} and chirp traces for 10G NRZ-OOK modulation using the high frequency test pattern 133
4.39 Peak-to-peak chirp contribution from the modulator section using the low frequency test pattern. 134
4.40 P_{AM}, P_{FM} and chirp traces for 10G NRZ-OOK modulation using the low frequency test pattern. 135
4.41 V-I Profile of the integrated SOA section demonstrating a thermally induced threshold shift with injected light. 136
4.42 Peak-to-peak carrier frequency deviation induced by a square-wave gating signal with a 50% duty cycle applied to the SOA Section. 137
4.43 Frequency deviation induced by a 10kHz square-wave signal with a 50% duty cycle applied to the SOA section. 138

5.1 Tree-structured LR-PON physical layer proposed for urban areas. . . 145
5.2 Optical power and OSNR budget for the proposed urban architecture. 146
5.3 Alternative LR-PON 'open-ring' architecture for rural areas. 149
5.4 Optical power and OSNR budget for the proposed rural architecture. 151
5.5 Illustration of a single-stage (forward pumped) EDFA. 154
5.6 Illustration of the energy level structure of Er^{3+} ions in a glass host. . 155
5.7 Data captured from an oscilloscope showing transients from a commercial EDFA in the absence of active gain control. 157
5.8 Schematic of a single-stage EDFA configuration with active gain stabilisation via dynamic pump control. 158
5.9 Gain and noise figure of a commercial dual-stage EDFA operated in automatic gain control. 160
5.10 Experimental setup used to characterise the residual EDFA transients. 161
5.11 Data captured from an optical spectrum analyser demonstrating the emulation of a system with 80 DWDM channels. 162
5.12 Data captured from an oscilloscope demonstrating a residual gain transient imparted on the output power of a probe channel. 163
5.16 Residual transient profiles and evolution of the peak-to-peak power excursion measured as a function of the number of chained EDFAs. 167
5.18 The experimental set-up Used to characterise the LBMRx. 171
5.19 Traces captured from a sampling oscilloscope of optical bursts with a 15dB dynamic range carrying NRZ-OOK data at 10Gb/s. 172

5.20 Performance of the packaged LBMRx assembly. 173
5.21 Illustration of a Reed-Solomon FEC block. 174
5.22 Theoretical performance of the RS(248,216) FEC algorithm. 177
5.23 FPGA architecture of the implemented ONU and OLT. 178
5.24 Comparison between measured and theoretical US FEC performance. 180
5.25 Experimental setup used for residual EDFA transient emulation and FEC performance evaluation. 181

6.1 High-level network view of the proposed DISCUS architecture. 187
6.2 EU FP7 Project DISCUS Experimental Testbed, December 2015. . . 188
6.3 Experimental testbed configuration. 189
6.4 Structure of the optical line terminals. 190
6.5 Basic structure of the upstream bursts. 191
6.6 Structure of the optical network units. 192
6.7 Laboratory Testbed Equipment. 193
6.8 Constellation and eye diagrams of the 100G DP-QPSK channel. . . . 194
6.9 LR-PON wavelength transmission bands. 196
6.10 Downstream spectrum: channels launched from the core node. 197
6.11 Upstream spectrum with 'loud' target channel bursts. 198
6.12 Proposed network concept for urban access deployment. 199
6.13 Illustration of the EDFA-based ANs used in for the urban LR-PON. . 200
6.14 The LR-PON physical layer proposed for urban areas. 202
6.15 Proposed network concept for rural access deployment. 203
6.16 EDFA-based amplifier nodes for the 'open-ring' configuration 204
6.17 The LR-PON physical layer proposed for rural areas. 205
6.18 Downstream performance of the 10G PON channels. 207
6.19 BER performance of the 10G target channel as a function of the ODN loss in the 'tree-structured' (single AN) LR-PON architecture using EDFA or SOA-based amplifier nodes. 208
6.20 Image of consecutive bursts launched into the ODN. 209
6.21 Upstream performance of the 10G PON channels. 210
6.22 BER performance of the 10G target channel for (a) DS and (b) US transmission. 211
6.23 FEC performance evaluation for the rural (chained AN) configuration. 212
6.24 Temporal profile of an accumulated residual EDFA transient. 213
6.25 US performance impact from accumulated residual EDFA transients. 214
6.26 Downstream BER performance of 100G DP-QPSK channel. 215
6.27 DS BER performance and OSNR of the 100G DP-QPSK channel as a function of the ODN loss. 217
6.28 100G DP-QPSK channel analysis: US spectrum in the 'tree-like' (urban) LR-PON architecture. 219
6.29 EDFA-based ANs: US performance of the 100G DP-QPSK channel as a function of the power of the neighbouring PON channels. 220

6.30 SOA-based AN: US performance of the 100G DP-QPSK channel as a function of the power of the neighbouring channels. 221
6.31 Network level view of the tree-structured LR-PON and the SDN control plane equipment. 223
6.32 Overview of the control plane processes for the link protection experiment. 224
6.33 Overview of the control plane link protection experiment timings. . . 225
6.34 Service restoration time for the protection scenario and wavelength allocation experiments. 226
6.35 Overview of the control plane processes for the DWA experiment. . . 226
6.36 Control plane processes and timings for the DWA experiment. 227

7.3 High-level network view of the proposed DISCUS architecture. 235

C.1 Basic concept of the power and OSNR model. 247
C.2 Probability distribution of the accumulated PDL within the proposed open-ring configuration. 251

D.1 Model of an erbium-doped fibre supporting N channels. 253
D.2 Data captured from an oscilloscope showing transients from a commercial EDFA. 258

E.1 Illustration of the unpackaged LBMRx subassembly chip. 259
E.2 Packaged LBMRx with accompanying PCB. 260

F.1 ECOC 2015 logo. 261
F.2 Physical layer architecture of the portable DISCUS demonstrator. . . 262
F.3 Power and OSNR model for the the portable DISCUS demonstrator. 263
F.4 Control plane overview of the portable DISCUS demonstrator. 264
F.5 DISCUS demonstration hosted by Polatis™at ECOC, 2015. 265
F.6 Portable DISCUS demonstration: ECOC 2015, Valencia, Spain. 265

List of Tables

2.1 Wavelength transmission bands for fibre-optic communications. 21

3.1 Estimated bandwidth requirements of typical broadband services. . . 57
3.2 Comparison of various access technologies. 60
3.3 Comparison of current-gneration PON standards. 61
3.4 Comparison of next-generation PON standards. 68
3.5 Overview of the NG-PON2 specifications. 70

4.2 Chirp contribution from the modulator section using the high frequency test pattern. 133

5.1 Specifications for the amplifier nodes required for the proposed urban and rural LR-PON configurations. 153

C.1 Component parameters for the power and OSNR model. 249
C.2 PDL specifiactions for passive optical splitters. 250

List of Publications

Journal Publications:

[J1] A. Daly, C. Gierl, T. Grundl, C. Grasse, K. Zogal, **D. Carey**, P. Townsend, M.C. Amann, P. Meissner, and B. Corbett. **"10 Gbit/s Transmission over 50km of SMF Using a MEMs Tunable VCSEL,"** *Electronics Letters*, 48(7):394-396, 2012.

[J2] S. Porto, C. Antony, A. Jain, D. Kelly, **D. Carey**, G. Talli, P. Ossieur, and P. D. Townsend,**"Demonstration of 10Gb/s burst-mode transmission using a linear burst-mode receiver and burst-mode electronic equalization [Invited],"** *IEEE/OSA Journal of Optical Communications and Networking* 7(1): A118-A125, 2015.

[J3] G. Talli, F. Slyne, S. Porto, **D. Carey**, N. Brandonisio, A. Naughton, P. Ossieur, S. McGettrick, C. Blumm, M. Ruffini, D. Payne, R. Bonk, T. Pfeiffer, N. Parsons and P. D. Townsend. **"SDN Enabled Dynamically Reconfigurable High Capacity Optical Access Architecture for Converged Services."** *Journal of Lightwave Technology, vol. 35, no. 3, pp. 550-560, 1 Feb. 1, 2017.*

[J4] S. Porto, **D. Carey**, N. Brandonisio, A. Naughton, C. Antony, P. Ossieur, N. Parsons, G. Talli and P. D. Townsend, **"Point-to-point Overlay of a 100Gb/s DP-QPSK Channel in LR-PONs for Urban and Rural Areas,"** *Opt. Express, 26, 3303-3319 (2018).*

[J5] N. Brandonisio, S. Porto, **D. Carey**, P. Ossieur, G. Talli, N. Parsons and P. D. Townsend, **"Burst-Mode FPGA Implementation and Error Location Analysis of Forward Error Correction for Passive Optical Networks"** *IEEE/OSA J. Opt. Commun. Netw. 10, 298-308 (2018).*

[J6] **D. Carey**, P. Ramaswamy, C. Antony, G. Talli, B. Roycroft, B. Corbett and P. D. Townsend, **"Characterization of a Low-Cost, Monolithically Integrated, Tuneable 10G Transmitter for Wavelength Agile PONs"**, *IEEE Journal of Quantum Electronics (JQE), vol. 54, no. 6, pp. 1-12, Dec. 2018, Art no. 6300612.*

Conference Publications:

[C1] **D. Carey**, N. Brandonisio, S. Porto, A. Naughton, P. Ossieur, N. Parsons, G. Talli and P. D. Townsend, **"Dynamically Reconfigurable TDM-DWDM PON Ring Architecture for Efficient Rural Deployment."** In *ECOC 2016; 42th European Conference on Optical Communication.*

[C2] G. Talli, S. Porto, **D. Carey**, N. Brandonisio, A. Naughton, P. Ossieur, F. Slyne, S. McGettrick, C. Blumm, M. Ruffini, D. Payne, R. Bonk, T. Pfeiffer, N. Parsons and P. Townsend. **"Demonstration of SDN Enabled Dynamically Reconfigurable High Capacity Optical Access for Converged Services."** In *2016 Optical Fibre Communications Conference and Exhibition (OFC), 37th.*

[C3] N. Brandonisio, S. Porto, **D. Carey**, P. Ossieur, G. Talli, N. Parsons and P. Townsend. **"Forward Error Correction Analysis for 10Gb/s Burst-Mode Transmission in TDM-DWDM PONs."** In *2017 Optical Fibre Communications Conference and Exhibition (OFC), 38th.*

[C4] G. Talli, S. Porto, **D. Carey**, N. Brandonisio, A. Naughton, P. Ossieur, F. Slyne, S. McGettrick, C. Blumm, M. Ruffini, D. Payne, R. Bonk, T. Pfeiffer, N. Parsons and P. Townsend. **"Multi-Service SDN controlled Reconfigurable Long-Reach Optical Access Network"** In *2017 European Conference on Networks and Communications (EuCNC), 26th pages 1-5.*

[C5] G. Talli, S. Porto, **D. Carey**, N. Brandonisio, A. Naughton, P. Ossieur, F. Slyne, S. McGettrick, C. Blumm, M. Ruffini, A. Hill, D. Payne, R. Bonk, T. Pfeiffer, N. Parsons and P. Townsend. **"Technologies and Architectures to Enable SDN in Converged 5G/Optical Access Networks"** In *Optical Network Design and Modeling Conference (ONDM), Budapest, 2017.*

[C6] N. Brandonisio, **D. Carey**, S. Porto, G. Talli and P. Townsend. **"Burst-Mode FEC Performance for PON Upstream channels with EDFA Optical Transients"** In *Optical Network Design and Modeling Conference (ONDM), Dublin, 2018.*

References

[1] C. E. Shannon. **A Mathematical Theory of Communication**. *The Bell System Technical Journal*, 27(3):379–423, July 1948.

[2] R. N. Hall, G. E. Fenner, J. D. Kingsley, T. J. Soltys, and R. O. Carlson. **Coherent Light Emission From GaAs Junctions**. *Phys. Rev. Lett.*, 9:366–368, Nov 1962.

[3] K. C. Kao and G. A. Hockham. **Dielectric-fibre Surface Waveguides for Optical Frequencies**. *Electrical Engineers, Proceedings of the Institution of*, 113(7):1151–1158, July 1966.

[4] TeleGeography: A Division of PriMetrica Inc. **Submarinecable Map**. `https://www.submarinecablemap.com`, 2017.

[5] Cisco Systems Inc. **The Zettabyte Era: Trends and Analysis**. `http://www.cisco.com/c/en/us/solutions/collateral/service-provider/visual-networking-index-vni/vni-hyperconnectivity-wp.html`, June 2017.

[6] S. Gillett W. Lehr and A. Sirbu. **Measuring Broadband's Economic Impact**. *Broadband Properties*, 2005.

[7] Michael Minges. **Exploring the Relationship Between Broadband and Economic Growth**. *World Development Report Background Papers, World Bank Group, Washington, D.C.*, 2016.

[8] M. Ruffini, L. Wosinska, M. Achouche, J. Chen, N. Doran, F. Farjady, J. Montalvo, P. Ossieur, B. O'Sullivan, N. Parsons, T. Pfeiffer, X. Z. Qiu, C. Raack, H. Rohde, M. Schiano, P. Townsend, R. Wessaly, X. Yin, and D. B. Payne. **DISCUS: An End-to-End Solution for Ubiquitous Broadband Optical Access**. *IEEE Communications Magazine*, 52(2):S24–S32, February 2014.

[9] Institute for Electrical and Electronic Engineers. **IEEE Standard for Information Technology - Local and Metropolitan Area Networks–Specific Requirements - Part 3: CSMA/CD Access Method and Physical Layer Specifications Amendment 1: Physical Layer Specifications and Management Parameters for 10 Gb/s Passive Optical Networks**. *IEEE Standards Association, 802.3av*, 2009.

[10] ITU Telecommunication Standardization Sector. **10-Gigabit-Capable Passive Optical Network (XGPON): General Requirements**. *ITU-T Recommendations, G Series*, 2010.

[11] ITU Telecommunication Standardization Sector. **40-Gigabit-Capable Passive Optical Networks (NG-PON2): General Requirements**. *ITU-T Recommendations, G Series*, 2015.

[12] P. D. Townsend, G. Talli, C. W. Chow, E. M. MacHale, C. Antony, R. Davey, T. De Ridder, X. Z. Qiu, P. Ossieur, H. G. Krimmel, D. W. Smith, I. Lealman, A. Poustie, S. Randel, and H. Rohde. **Long Reach Passive Optical Networks**. In *LEOS 2007 - IEEE Lasers and Electro-Optics Society Annual Meeting Conference Proceedings*, pages 868–869, Oct 2007.

[13] P. Ossieur, C. Antony, A. Naughton, A. M. Clarke, H. G. Krimmel, X. Yin, X. Z. Qiu, C. Ford, A. Borghesani, D. Moodie, A. Poustie, R. Wyatt, B. Harmon, I. Lealman, G. Maxwell, D. Rogers, D. W. Smith, S. Smolorz, H. Rohde, D. Nesset, R. P. Davey, and P. D. Townsend. **Demonstration of a 32×512 Split, 100km Reach, 2×32×10 Gb/s Hybrid DWDM-TDMA PON Using Tunable External Cavity Lasers in the ONUs**. *Journal of Lightwave Technology*, 29(24):3705–3718, Dec 2011.

[14] Organisation for Economic Co-Operation and Development. **Penetration and Data Usage: Percentage of Fibre Connections in Total Broadband Subscriptions**.

[15] White Paper: **'Broadband Access Technologies'**. `www.ftthcouncil.eu`, 2012.

[16] R. P. Davey, D. B. Payne, D. Nesset, P. Tomlinson, T. Gilfedder, P. Chidgey, and A. Rafel. **Long-Reach Access and Future Broadband Network Economics**. In *33rd European Conference and Exhibition of Optical Communication*, pages 1–4, Sept 2007.

[17] G. Talli and P. D. Townsend. **Hybrid DWDM-TDM Long-Reach PON For Next Generation Optical Acess**. *IEEE Journal of Lightwave Technology*, 24:2827–2834, 2006.

[18] S. Smolorz, H. Rohde, P. Ossieur, C. Antony, P. D. Townsend, T. De Ridder, B. Baekelandt, X. Z. Qiu, S. Appathurai, H. G. Krimmel, D. Smith, and A. Poustie. **Next Generation Access Networks: PIEMAN and Beyond**. In *2009 International Conference on Photonics in Switching*, pages 1–4, Sept 2009.

[19] G. Talli, F. Slyne, S. Porto, D. Carey, N. Brandonisio, A. Naughton, P. Ossieur, S. McGettrick, C. Blümm, M. Ruffini, D. Payne, R. Bonk, T. Pfeiffer, N. Parsons, and P. Townsend. **SDN Enabled Dynamically Reconfigurable High Capacity Optical Access Architecture for Converged Services**. *Journal of Lightwave Technology*, 35(3):550–560, Feb 2017.

[20] D. Carey, N. Brandonisio, S. Porto, A. Naughton, P. Ossieur, N. Parsons, G. Talli, and P. Townsend. **Dynamically Reconfigurable TDM-DWDM PON Ring Architecture for Efficient Rural Deployment**. In *ECOC 2016, 42nd European Conference on Optical Communication*, pages 1–3, 2016.

[21] K. Grobe, M. H. Eiselt, S. Pachnicke, and J. P. Elbers. **Access Networks Based on Tunable Lasers**. *Journal of Lightwave Technology*, 32(16):2815–2823, Aug 2014.

[22] D. Menashe, A. Shlifer, and U. Ghera. **Optical Amplifiers for Modern Networks**. In *2006 International Conference on Transparent Optical Networks*, volume 1, June 2006.

[23] Vivek Alwayn. ***Optical Network Design and Implementation***. Networking Technology. Cisco Press, 2004.

[24] H. H. Hopkins and N. S. Kapany. **A Flexible Fibrescope, Using Static Scanning**. *Nature*, 173, June 1954.

[25] F. P. Kapron, D. B. Keck, and R. D. Maurer. **Radiation Losses in Glass Optical Waveguides**. *Applied Physics Letters*, 17(10):423–425, 1970.

[26] Govind P. Agrawal. ***Fiber-Optic Communication Systems***. John Wiley and Sons Inc., 2011.

[27] D. Gloge. **Weakly Guiding Fibers**. *Appl. Opt.*, 10(10):2252–2258, Oct 1971.

[28] D. Gloge. **Optical Power Flow in Multimode Fibers**. *The Bell System Technical Journal*, 51(8):1767–1783, Oct 1972.

[29] K. P. Ho and J. M. Kahn. **Statistics of Group Delays in Multimode Fiber With Strong Mode Coupling**. *Journal of Lightwave Technology*, 29(21):3119–3128, Nov 2011.

[30] ITU Telecommunication Standardization Sector. **Characteristics of a Single-Mode Optical Fibre and Cable**. *ITU-T Recommendations, G Series*, 2016.

[31] P. J. Winzer and R. J. Essiambre. **Advanced Optical Modulation Formats**. *Proceedings of the IEEE*, 94(5):952–985, May 2006.

[32] Edited by Ivan Kaminow and Tingye Li. **Optical Fiber Telecommunications - IVB: Systems and Impairments**. *Academic Press*, 2002.

[33] L. Faustini and G. Martini. **Bend Loss in Single-Mode Fibers**. *Journal of Lightwave Technology*, 15(4):671–679, April 1997.

[34] M. Ohashi, K. Shiraki, and K. Tajima. **Optical Loss Property of Silica-Based Single-Mode Fibers**. *Journal of Lightwave Technology*, 10(5):539–543, May 1992.

[35] Wang Zhi, Ren Guobin, Lou Shuqin, and Jian Shuisheng. **Loss Properties Due to Rayleigh Scattering in Different Types of Fiber**. *Opt. Express*, 11(1):39–47, Jan 2003.

[36] T. Miya, Y. Terunuma, T. Hosaka, and T. Miyashita. **Ultimate Low-Loss Single-Mode Fibre at 1.55 μm**. *Electronics Letters*, 15(4):106–108, February 1979.

[37] ITU Telecommunication Standardization Sector. **ITU-T G.Sup39: Optical System Design and Engineering Considerations**. *ITU-T Recommendations, G Series, Supplement 39*, 2016.

[38] M. J. Hamp, J. Wright, M. Hubbard, and B. Brimacombe. **Investigation into the Temperature Dependence of Chromatic Dispersion in Optical Fiber**. *IEEE Photonics Technology Letters*, 14(11):1524–1526, Nov 2002.

[39] Paulo S. André and Armando N. Pinto. **chromatic dispersion fluctuations in optical fibers due to temperature and its effects in high-speed optical communication systems**. *Optics Communications*, 246(4):303 – 311, 2005.

[40] Corning Incorporated. **Corning®SMF-28e+®Optical Fiber - Product Information**, 2018.

[41] B. Jopson and A. Gnauck. **Dispersion Compensation for Optical Fiber Systems**. *IEEE Communications Magazine*, 33(6):96–102, Jun 1995.

[42] A. Hill and D. Payne. **Linear Crosstalk in Wavelength-Division-Multiplexed Optical-Fiber Transmission Systems**. *Journal of Lightwave Technology*, 3(3):643–651, Jun 1985.

[43] P. A. Rosher and A. R. Hunwicks. **The Analysis of Crosstalk in Multichannel Wavelength Division Multiplexed Optical Transmission Systems and its Impact on Multiplexer Design**. *IEEE Journal on Selected Areas in Communications*, 8(6):1108–1114, Aug 1990.

[44] K. P. Ho and J. M. Kahn. **Methods for Crosstalk Measurement and Reduction in Dense WDM Systems**. *Journal of Lightwave Technology*, 14(6):1127–1135, Jun 1996.

[45] J. D. Downie and A. B. Ruffin. **Analysis of Signal Distortion and Crosstalk Penalties Induced by Optical Filters in Optical Networks**. *Journal of Lightwave Technology*, 21(9), Sept 2003.

[46] Maurice O'Sullian and Rongqing Hui. ***Fibre Optic Measurement Techniques***. Elsevier Academic Press, 2009.

[47] Govind P. Agrawal. ***Applications of Nonlinear Fiber Optics (Second Edition)***. Academic Press, Burlington, second edition edition, 2008.

[48] P.M. Becker, A.A. Olsson, and J.R. Simpson. ***Erbium-Doped Fiber Amplifiers: Fundamentals and Technology***. Optics and Photonics. Elsevier Science, 1999.

[49] Carlton M. Caves. **Quantum Limits on Noise in Linear Amplifiers**. *Phys. Rev. D*, 26:1817–1839, Oct 1982.

[50] Govind Agrawal. **Nonlinear Fiber Optics (Fifth Edition)**. *Academic Press*, 2013.

[51] Y. Sasaki and Y. Ohmori. **Phase Matched Sum Frequency Light Generation in Optical Fibers**. *Applied Physics Letters*, 39(6):466–468, 1981.

[52] M. C. Farries. **Efficient Second Harmonic Generation in an Optical Fibre**. In *IEE Colloquium on Non-Linear Optical Waveguides*, pages 20/1–20/4, Jun 1988.

[53] P. D. Maker and R. W. Terhune. **Study of Optical Effects Due to an Induced Polarization Third Order in the Electric Field Strength**. *Phys. Rev.*, 137:A801–A818, Feb 1965.

[54] T. Kato, Y. Suetsugu, M. Takagi, E. Sasaoka, and M. Nishimura. **Measurement of the Nonlinear Refractive Index in Optical Fiber by the Cross-Phase-Modulation Method with depolarized Pump Light**. *Opt. Lett.*, 20(9):988–990, May 1995.

[55] A. R. Chraplyvy. **Limitations on Lightwave Communications Imposed by Optical-Fiber Nonlinearities**. *Journal of Lightwave Technology*, 8(10):1548–1557, Oct 1990.

[56] M. Stern, J. P. Heritage, R. N. Thurston, and S. Tu. **Self-Phase Modulation and Dispersion in High Data Rate Fiber-Optic Transmission Systems**. *Journal of Lightwave Technology*, 8(7):1009–1016, Jul 1990.

[57] R. H. Stolen and Chinlon Lin. **Self-Phase-Modulation in Silica Optical Fibers**. *Phys. Rev. A*, 17:1448–1453, Apr 1978.

[58] M. N. Islam, L. F. Mollenauer, R. H. Stolen, J. R. Simpson, and H. T. Shang. **Cross-Phase Modulation in Optical Fibers**. *Opt. Lett.*, 12(8):625–627, Aug 1987.

[59] L. Rapp. **Experimental Investigation of Signal Distortions Induced by Cross-Phase odulation Combined with Dispersion**. *IEEE Photonics Technology Letters*.

[60] M. Shtaif, M. Eiselt, and L. D. Garrett. **Cross-Phase Modulation Distortion Measurements in Multispan WDM Systems**. *IEEE Photonics Technology Letters*, 12(1):88–90, Jan 2000.

[61] M. Shtaif and M. Eiselt. **Impact of Cross Phase Modulation in WDM Systems**. In *Optical Fiber Communication Conference. Technical Digest Postconference Edition. Trends in Optics and Photonics Vol.37 (IEEE Cat. No. 00CH37079)*, volume 3, pages 192–193 vol.3, March 2000.

[62] D. Marcuse, A. R. Chraplyvy, and R. W. Tkach. **Dependence of Cross-Phase Modulation on Channel Number in Fiber WDM Systems**. *Journal of Lightwave Technology*, 12(5):885–890, May 1994.

[63] N. Kikuchi, K. Sekine, and S. Sasaki. **Analysis of Cross-Phase Modulation (XPM) Effect on WDM Transmission Performance**. *Electronics Letters*, 33(8):653–654, Apr 1997.

[64] N. Shibata, R. Braun, and R. Waarts. **Phase-Mismatch Dependence of Efficiency of Wave Generation Through Four-Wave Mixing in a Single-mode Optical Fiber**. *IEEE Journal of Quantum Electronics*, 23(7):1205–1210, Jul 1987.

[65] S. Song, C. T. Allen, K. R. Demarest, and R. Hui. **Intensity-Dependent Phase-Matching Effects on Four-wave Mixing in Optical Fibers**. *Journal of Lightwave Technology*, 17(11):2285–2290, Nov 1999.

[66] M. Eiselt. **Limits on WDM Systems Due to Four-Wave Mixing: A Statistical Approach**. *Journal of Lightwave Technology*, 17(11):2261–2267, Nov 1999.

[67] Paul D. Townsend, Alistair J. Poustie, P. J. Hardman, and K. J. Blow. **Measurement of the Refractive-Index Modulation Generated by Electrostriction-Induced Acoustic Waves in Optical Fibers**. *Opt. Lett.*, 21(5):333–335, Mar 1996.

[68] R. G. Smith. **Optical Power Handling Capacity of Low Loss Optical Fibers as Determined by Stimulated Raman and Brillouin Scattering**. *Appl. Opt.*, 11(11):2489–2494, Nov 1972.

[69] D. A. Fishman and J. A. Nagel. **Degradations Due to Stimulated Brillouin Scattering in Multigigabit Intensity-Modulated fiber-Optic Systems**. *Journal of Lightwave Technology*, 11(11):1721–1728, Nov 1993.

[70] P. Mitchell, A. Janssen, and J. K. Luo. **High Performance Laser Linewidth Broadening for Stimulated Brillouin Suppression with Zero Parasitic Amplitude Modulation**. *Journal of Applied Physics*, 105(9):093104, 2009.

[71] R. H. Stolen, E. P. Ippen, and A. R. Tynes. **Raman Oscillation in Glass Optical Waveguide**. *Applied Physics Letters*, 20(2):62–64, 1972.

[72] Martin Pfennigbauer, Peter J. Winzer, Martin M. Strasser, and Walter R. Leeb. **Optimum Optical and Electrical Filter Characteristics in Optically Preamplified Direct Detection (N)RZ Receivers**. *Proc.SPIE*, 4272:4272 – 4272 – 10, 2001.

[73] Rene-Jean Essiambre, Peter J. Winzer, and Diego F. Grosz. **Impact of DCF Properties on System Design**. *Journal of Optical and Fiber Communications Reports*, 3(4):221–291, Aug 2006.

[74] W. Schottky. **Über Spontane Stromschwankungen in Verschiedenen Elektrizitätsleitern**. *Annalen der Physik*, 362(23):541–567, 1918.

[75] B. M. Oliver. **Thermal and Quantum Noise**. *Proceedings of the IEEE*, 53(5):436–454, May 1965.

[76] J. B. Johnson. **Thermal Agitation of Electricity in Conductors**. *Phys. Rev.*, 32:97–109, Jul 1928.

[77] H. Nyquist. **Thermal Agitation of Electric Charge in Conductors**. *Phys. Rev.*, 32:110–113, Jul 1928.

[78] N. S. Bergano, F. W. Kerfoot, and C. R. Davidsion. **Margin Measurements in Optical Amplifier Systems**. *IEEE Photonics Technology Letters*, 5(3):304–306, March 1993.

[79] Maxim: Integrated Products. **HFTA-05.0: Statistical Confidence Levels for Estimating Error Probability**. White Paper: notes-application.abcelectronique.com/003/3-5321.pdf. Document Last Accessed: 10/09/2018.

[80] ITU Telecommunication Standardization Sector. **ITU-T G.975: Forward Error Correction for Submarine Systems**. *ITU-T Recommendations, G Series*, 2000.

[81] ITU Telecommunication Standardization Sector. **10-Gigabit-Capable Passive Optical Network (XGPON): Transmission Convergence Layer Specification**. *ITU-T Recommendations, G Series*, 2014.

[82] Federal Communications Commission. **Broadband Speed Guide**, 2017.

[83] Corning Incorporated. **Optical Fibre Innovation**, 2017.

[84] ITU Telecommunication Standardization Sector. **ITU-T G.984.x: Gigabit-Capable Passive Optical Networks (G-PON)**. *ITU-T Recommendations, G Series*, 2008.

[85] IEEE Computer Society. **IEEE 802.3ah: Telecommunications and Information Exchange Between Systems - Local and Metropolitan Area Networks - Specific Requirements - Part 3**. *IEEE Standards Association, 802.3ah*, 2004.

[86] IEEE Standards Association. **IEEE Recommended Practice for Local and Metropolitan Area Networks Coexistence of Fixed Broadband Wireless Access Systems**. *IEEE Std 802.16.2-2004 (Revision of IEEE Std 802.16.2-2001)*, pages 1–166, March 2004.

[87] 3rd Generation Partnership Project (3GPP). **Technical Specifications and Technical Reports for a UTRAN-based 3GPP System**.

[88] ITU Radio Communication Sector. **ITU-R S.2361-0: Broadband Access by Fixed-Satellite Service Systems**. *ITU-R Recommendations, S. Series*, 2015.

[89] European Commission. ***Digital Single Market: Comparison of Broadband Access Technologies***, January 2018.

[90] R. D. Hall, R. A. Betts, and J. P. Moss. **Bidirectional Transmission Over 11 km of Single-Mode Optical Fibre at 34 Mbit/s using 1.3μm LEDs and Directional Couplers**. *Electronics Letters*, 21(14):628–629, July 1985.

[91] J. R. Stern, J. W. Ballance, D. W. Faulkner, S. Hornung, D. B. Payne, and K. Oakley. **Passive Optical Local Networks for Telephony Applications and Beyond**. *Electronics Letters*, 23(24):1255–1256, November 1987.

[92] J. W. Ballance, R. F. Lee, P. H. Rogers, and M. F. Halls. **A B-ISDN Local Distribution System Based on a Passive Optical Network**. In

Global Telecommunications Conference, 1990, and Exhibition. 'Communications: Connecting the Future', GLOBECOM '90., IEEE, pages 206–210 vol.1, Dec 1990.

[93] D. Hincapie, G. Maierbacher, and M. Leibiger. **Rate and Reach Gains of Vectored DSL in the Current Access Network**. In *Broadband Coverage in Germany. 9th ITG Symposium. Proceedings*, pages 1–6, April 2015.

[94] José Salgado et. al. **New FTTH-based Technologies and Applications**. White Paper: www.ftthcouncil.eu, 2014.

[95] ITU Telecommunication Standardization Sector. **ITU-T G.984.x: Gigabit-Capable Passive Optical Networks (G-PON)**. *ITU-T Recommendations, G Series*, 2008.

[96] D.B. Payne and R.P. Davey. **The Future of Fibre Access Systems?** *BT Technology Journal*, 20(4):104–114, Oct 2002.

[97] D.B. Payne and R.P. Davey. **Long-Reach Access Networks - Avoiding the Bandwidth-Price Dilemma**. *Proc. Broadband Europe*, Dec 2004.

[98] D. S. Forrester, A. M. Hill, R. A. Lobbett, R. Wyatt, and S. F. Carter. **39.81 Gbits/s, 43.8 million-way WDM Broadcast Network with 527km Range**. *Electronics Letters*, 27(22):2051–2053, Oct 1991.

[99] R. P. Davey, D. B. Grossman, M. Rasztovits-Wiech, D. B. Payne, D. Nesset, A. E. Kelly, A. Rafel, S. Appathurai, and S. H. Yang. **Long-Reach Passive Optical Networks**. *Journal of Lightwave Technology*, 27(3):273–291, Feb 2009.

[100] ITU Telecommunication Standardization Sector. **ITU-T G.984.6: Gigabit-Capable Passive Optical Networks (G-PON): Reach Extension**. *ITU-T Recommendations, G Series*, 2008.

[101] ITU Telecommunication Standardization Sector. **ITU-T G.984.7: Gigabit-Capable Passive Optical Networks (G-PON): Long Reach**. *ITU-T Recommendations, G Series*, 2010.

[102] R. J. Mears, L. Reekie, I. M. Jauncey, and D. N. Payne. **Low-Noise Erbium-Doped Fibre Amplifier Operating at 1.54um**. *Electronics Letters*, 23(19):1026–1028, September 1987.

[103] Y. Nishida, M. Yamada, T. Kanamori, K. Kobayashi, J. Temmyo, S. Sudo, and Y. Ohishi. **Development of an Efficient Praseodymium-doped Fiber Amplifier**. *IEEE Journal of Quantum Electronics*, 34(8):1332–1339, Aug 1998.

[104] K. P. W. Dissanayakel, S. D. Emami, H. A. Abdul-Rashidi, S. M. Aljamimi, Z. Yusoff, M. I. Zulkifli, S. Z. Muhamad-Yassin, K. A. Mat-Sharif, and N. Tamchek. **Design and Performance of an S-band Thulium Doped Modified Silica Fiber Amplifier**. In *2013 IEEE 4th International Conference on Photonics (ICP)*, pages 288–290, Oct 2013.

[105] Ken-Ichi Suzuki, Youichi Fukada, Derek Nesset, and Russell Davey. **Amplified Gigabit PON Systems [Invited]**. *J. Opt. Netw.*, 6(5):422–433, May 2007.

[106] D. R. Zimmerman and L. H. Spiekman. **Amplifiers for the Masses: EDFA, EDWA, and SOA Amplets for Metro and Access Applications**. *Journal of Lightwave Technology*, 22(1), Jan 2004.

[107] Derek Nesset, Shamil Appathurai, Russell Davey, and Tony Kelly. **Extended Reach GPON Using High Gain Semiconductor Optical Amplifiers**. In *Optical Fiber Communication Conference/National Fiber Optic Engineers Conference*, page JWA107. Optical Society of America, 2008.

[108] S. Porto, C. Antony, P. Ossieur, and P. D. Townsend. **An Upstream Reach-Extender for 10Gb/s PON Applications Based on an Optimised Semiconductor amplifier Cascade**. In *2011 37th European Conference and Exhibition on Optical Communication*, pages 1–3, Sept 2011.

[109] Rong Zhao (Detecon International) José Salgado (PT Inovação) and Nuno Monteiro (PT Inovação). White paper:**New FTTH-based Technologies and Applications**. Technical report, Fibre-to-the-Home (FTTH) Council Europe, 2014.

[110] Huawei Technology Co. Ltd. **Next-Generation PON Evolution**. *ITU-T Recommendations, G Series*, 2010.

[111] IEEE 802.3 Task Force. *Online Report:* **10Gbps PHY for EPON Call for Interest**. Technical report, Institute for Electrical and Electronic Engineers, 2006.

[112] M. Hajduczenia and H. J. A. da Silva. **Next Generation PON Systems - Current Status**. In *2009 11th International Conference on Transparent Optical Networks*, pages 1–8, June 2009.

[113] D. Faulkner, R. Mistry, T. Rowbotham, K. Okada, W. Warzanskyj, A. Zylbersztejn, and Y. Picault. **The Full Services Access Networks Initiative**. *IEEE Communications Magazine*, 35(4):58, 63–68, Apr 1997.

[114] Frank J. Effenberger. **The XG-PON System: Cost Effective 10Gb/s Access**. *J. Lightwave Technol.*, 29:403–409, Feb 2011.

[115] F. J. Effenberger, H. Mukai, S. Park, and T. Pfeiffer. **Next-Generation PON-part II: Candidate Systems for Next-Generation PON**. *IEEE Communications Magazine*, 47(11):50–57, November 2009.

[116] Sameer Ashfaq Malik. *Online Report:* **10G EPON - Unleashing the Bandwidth Potential**. Technical report, ZTE Corporation, 2009.

[117] S. Jain, F. Effenberger, A. Szabo, Z. Feng, A. Forcucci, W. Guo, Y. Luo, R. Mapes, Y. Zhang, and V. O'Byrne. **World's First XG-PON Field Trial**. In *2010 Conference on Optical Fiber Communication (OFC/NFOEC), collocated National Fiber Optic Engineers Conference*, pages 1–3, March 2010.

[118] ITU Telecommunication Standardization Sector. **10-Gigabit-Capable Symmetric Passive Optical Network (XGS-PON)**. *ITU-T Recommendations, G Series*, 2016.

[119] Derek Nesset. **PON Roadmap *Invited***. *J. Opt. Commun. Netw.*, 9(1):A71–A76, Jan 2017.

[120] P. Chanclou, A. Cui, F. Geilhardt, H. Nakamura, and D. Nesset. **Network Operator Requirements for the Next Generation of Optical Access Networks**. *IEEE Network*.

[121] J. i. Kani, F. Bourgart, A. Cui, A. Rafel, M. Campbell, R. Davey, and S. Rodrigues. **Next-Generation PON-part I: Technology Roadmap and General Requirements**. *IEEE Communications Magazine*, 47(11):43–49, November 2009.

[122] D. Nesset. **NG-PON2 Technology and Standards**. *Journal of Lightwave Technology*, 33(5):1136–1143, March 2015.

[123] Huawei Technologies Ltd. **Next Generation PON Evolution**. Technical report, Huawei Technologies Ltd., 2010.

[124] Y. Matsui, W. Li, H. Roberts, H. Bulthuis, H. Deng, L. Lin, and C. Roxlo. **Transceiver for NG-PON2: Wavelength Tunablity for Burst-Mode TWDM and Point-to-Point WDM**. In *2016 Optical Fiber Communications Conference and Exhibition (OFC)*, pages 1–3, March 2016.

[125] P. Ramaswamy, J. O'Callaghan, F. H. Peters, B. Corbett, and B. Roycroft. **Monolithically Integrated Low-Cost 10Gb/s Tuneable Transmitter Using a Slotted Fabry-Pérot Laser**. In *2016 Compound Semiconductor Week (CSW) [Includes 28th International Conference on Indium Phosphide Related Materials (IPRM) 43rd International Symposium on Compound Semiconductors (ISCS)*, pages 1–1, June 2016.

[126] D. A. Khotimsky. **NG-PON2 Transmission Convergence Layer: A Tutorial**. *Journal of Lightwave Technology*, 34(5):1424–1432, March 2016.

[127] Frank Effenberger. **XG-PON1 versus NG-PON2: Which One Will Win?** In *European Conference and Exhibition on Optical Communication*, page Tu.4.B.1. Optical Society of America, 2012.

[128] Frank Effenberger, Lin Huafeng, and Peng Guikai. **Beyond NG-PON2: A More Flexible Future**, November 2013.

[129] Collaborative Integrated Project. **Photonic Integrated Extended Metro and Access Network**. Community Research and Development Information Service (CORDIS), June 2009. Last Accessed: 21-10-2018.

[130] Collaborative Integrated Project. **Scalable Advanced Ring-Based Passive Dense Access Network Architecture.** Community Research and Development Information Service (CORDIS), February 2011. Last Accessed: 21-10-2018.

[131] J. Prat, J. Lazaro, P. Chanclou, R. Soila, A. M. Gallardo, A. Teixeira, G. M. TosiBeleffi, and I. Tomkos. **Results from EU project SARDANA on 10G extended reach WDM PONs**. In *2010 Conference on Optical Fiber Communication (OFC/NFOEC), collocated National Fiber Optic Engineers Conference*, pages 1–3, March 2010.

[132] European Commission. **Broadband Coverage in Europe 2017**. https://ec.europa.eu/digital-single-market/en/news/study-broadband-coverage-europe-2017, 2018.

[133] Climate Action Department of Communications and Environment. **National Broadband Plan**. http://www.dccae.gov.ie/documents/National%20Broadband%20Plan.pdf, 2012.

[134] European Commission. **Digital Agenda for Europe**. https://europa.eu/european-union/topics/digital-economy-society_en, 2014.

[135] EU FP7 Large-Scale Integrating Project. **DISCUS: The DIStributed Core for unlimited bandwidth supply for all Users and Services**. Community Research and Development Information Service (CORDIS), November 2012.

[136] M. Ruffini, D. B. Payne, and L. Doyle. **Protection Strategies for Long-Reach PON**. In *36th European Conference and Exhibition on Optical Communication*, pages 1–3, Sept 2010.

[137] M. Ruffini, D. Mehta, B. O'Sullivan, L. Quesada, L. Doyle, and D. Payne. **Deployment Strategies for Protected Long-Reach PON**. *IEEE/OSA Journal of Optical Communications and Networking*, 4(2):118–129, February 2012.

[138] Transport Innovation) Marco Schiano (Telecom Italia and Core Network Evolution Group) Felipe Jimenez Arribas (Telefonica I+D GCTO. **Optical Transport Networks: Operator's Requirements and ICT DISCUS Concepts**. TI Transport Network Trend, Telecom Italia Group, July 2013.

[139] Kai Shi, Frank Smyth, Douglas Reid, Brendan Roycroft, Brian Corbett, JeongHwan Song, Peter O'Brien, Frank Peters, and Liam Barry. **Characterization of a Novel Three-Section Tunable Slotted Fabry-Perot Laser**. In *Optical Fiber Communication Conference*, page OWU3. Optical Society of America, 2010.

[140] ITU Telecommunication Standardization Sector. **40-Gigabit-Capable Passive Optical Networks (NG-PON2): Physical Media Dependent (PMD) Layer Specification**. *ITU-T Recommendations, G Series*, 2017.

[141] Y. Sun, A. K. Srivastava, J. L. Zyskind, J. W. Sulhoff, C. Wolf, and R. W. Tkach. **Fast Power Transients in WDM Optical Networks with Cascaded EDFAs**. *Electronics Letters*, 33(4):313–314, Feb 1997.

[142] Mitsunori Fukutoku and Masahiko Jinno. **Pump Power Reduction of Optical Feedback Controlled EDFA using Electrical Feedforward Control**. In *Optical Amplifiers and Their Applications*, page AA6. Optical Society of America, 1998.

[143] J. C. R. F. Oliveira, S. M. Rossi, R. F. Silva, J. B. Rosolem, and A. C. Bordonalli. **An EDFA Hybrid Gain Control Technique for Extended Input Power and Dynamic Gain Ranges with Suppressed Transients**. In *2007 SBMO/IEEE MTT-S International Microwave and Optoelectronics Conference*, pages 683–687, Oct 2007.

[144] P. Ossieur, S. Porto, C. Antony, A. Jain, D. Kelly, N. A. Quadir, G. Talli, and P. D. Townsend. **Burst-Mode Electronic Dispersion Compensation**. In *OFC 2014*, pages 1–3, March 2014.

[145] N. Brandonisio, S. Porto, D. Carey, P. Ossieur, G. Talli, N. Parsons, and P. D. Townsend. **Forward Error Correction For 10Gb/s Burst-Mode Transmission in TDM-DWDM PONs**. In *2017 Optical Fiber Communications Conference and Exhibition (OFC)*, pages 1–3, 2017.

[146] P. Ossieur, N. A. Quadir, S. Porto, C. Antony, W. Han, M. Rensing, P. O' Brien, and P. D. Townsend. **A 10 Gb/s Linear Burst-Mode Receiver in 0.25μm SiGe:C BiCMOS**. *IEEE Journal of Solid-State Circuits*, 48(2):381–390, 2013.

[147] N. Brandonisio, D. Carey, S. Porto, G. Talli, and P. D. Townsend. **Burst-Mode FEC Performance for PON Upstream Channels with EDFA Optical Transients**. In *2018 International Conference on Optical Network Design and Modeling (ONDM)*, pages 190–193, May 2018.

[148] Huda Saleh Abbas and Mark A. Gregory. **The Next Generation of Passive Optical Networks: A Review**. *[Journal of Network and Computer Applications*, 67:53 – 74, 2016.

[149] Eugen Lach and Wilfried Idler. **Modulation Formats for 100G and Beyond**. *Optical Fiber Technology*, 17(5):377 – 386, 2011.

[150] Joe Berthold, Jeff Hutchins, Karl Gass, David R Stauffer, Ted Schmidt, Francesco Caggioni, and Torsten Wuth. **100G Ultra Long Haul DWDM Framework Document**. Technical report, Ciena and CoreOptics and Sandia National Laboratories and IBM Microelectronics and Opnext and AMCC and Nokia Siemens Networks, 2009.

[151] Stefano Porto, Daniel Carey, Nicola Brandonisio, Alan Naughton, Cleitus Antony, Peter Ossieur, Nick Parsons, Giuseppe Talli, and Paul D. Townsend. **Point-to-Point overlay of a 100Gb/s DP-QPSK Channel in LR-PONs for Urban and Rural Areas**. *Opt. Express*, 26(3):3303–3319, Feb 2018.

[152] A. Einstein. **Zur Quantentheorie der Strahlung**. *Physikalische Zeitschrift*, 18, 1917.

[153] T. H. Maiman. **Optical and Microwave-Optical Experiments in Ruby**. *Phys. Rev. Lett.*, 4:564–566, Jun 1960.

[154] Z. Alferov. **Effect of the Heterostructure Parameters on the Laser Threshold Current and the Realization of Continuous Generation at Room Temperature**. *Fiz. Tekh. Poluprovodn. (Sov. Phys. Semicond.)*, 4:1826, 1970. cited By 1.

[155] H. Ishikawa, H. Imai, T. Tanahashi, K. Hori, and K. Takahei. **V-grooved Substrate Buried Heterostructure InGaAsP/InP Laser Emitting at 1.3μm Wavelength**. *IEEE Journal of Quantum Electronics*, 18(10):1704–1711, October 1982.

[156] K. Sakai, K. Utaka, S. Akiba, and Y. Matsushima. **1.5 μm Range InGaAsP/InP Distributed Feedback Lasers**. *IEEE Journal of Quantum Electronics*, 18(8):1272–1278, August 1982.

[157] K. Kobayashi and I. Mito. **Single Frequency and Tunable Laser Diodes**. *Journal of Lightwave Technology*, 6(11):1623–1633, Nov 1988.

[158] T. L. Koch and U. Koren. **Semiconductor Lasers for Coherent Optical fiber Communications**. *Journal of Lightwave Technology*, 8(3):274–293, Mar 1990.

[159] G. A. Antypas and R. L. Moon. **Growth and Characterization of InP/lnGaAsP Lattice Matched Heterojunctions**. *Journal of The Electrochemical Society*, 120(11):1574–1577, 1973.

[160] L. A. Coldren, G. A. Fish, Y. Akulova, J. S. Barton, L. Johansson, and C. W. Coldren. **Tunable Semiconductor Lasers: A Tutorial**. *Journal of Lightwave Technology*, 22(1):193–202, Jan 2004.

[161] H. Oohashi, Y. Shibata, H. Ishii, Y. Kawaguchi, Y. Kondo, Y. Yoshikuni, and Y. Tohmori. **46.9-nm Wavelength-Selectable Arrayed DFB Lasers with Integrated MMI Coupler and SOA**. In *Conference Proceedings. 2001 International Conference on Indium Phosphide and Related Materials. 13th IPRM (Cat. No.01CH37198)*, pages 575–578, 2001.

[162] M. Teshima. **Dynamic Wavelength Tuning Characteristics of the 1.5μ/m Three-Section DBR Lasers: Analysis and Experiment**. *IEEE Journal of Quantum Electronics*, 31(8):1389–1400, Aug 1995.

[163] B. Mroziewicz. **External Cavity Wavelength Tunable Semiconductor Lasers - A Review**. *Opto-Electronics Review*, 16(4):347, Sep 2008.

[164] S. Jatta, B. Kogel, M. Maute, K. Zogal, F. Riemenschneider, G. Bohm, M. C. Amann, and P. Meisner. **Bulk-Micromachined VCSEL At 1.55 *mu*m With 76-nm Single-Mode Continuous Tuning Range**. *IEEE Photonics Technology Letters*, 21(24):1822–1824, Dec 2009.

[165] L. Coldren and S. Corzine. **Continuously-Tunable Single-Frequency Semiconductor Lasers**. *IEEE Journal of Quantum Electronics*, 23(6):903–908, Jun 1987.

[166] P. Healey, P. Townsend, C. Ford, L. Johnston, P. Townley, I. Lealman, L. Rivers, S. Perrin, and R. Moore. **Spectral Slicing WDM-PON Using Wavelength-Seeded Reflective SOAs**. *Electronics Letters*, 37(19):1181–1182, Sep 2001.

[167] C. Antony, P. Ossieur, A. M. Clarke, A. Naughton, H. G. Krimmel, Y. Chang, A. Borghesani, D. Moodie, A. Poustie, R. Wyatt, B. Harmon, I. Lealman, G. Maxwell, D. Rogers, D. W. Smith, D. Nesset, R. P. Davey, and P. D. Townsend. **Demonstration of a Carrier Distributed, 8192-split Hybrid DWDM-TDMA PON over 124km Field-Installed Fibers**. In *Optical Fiber Communication (OFC), collocated National Fiber Optic Engineers Conference, 2010 Conference on (OFC/NFOEC)*, pages 1–3, 2010.

[168] G. Talli, D. Cotter, and P. D. Townsend. **Rayleigh Backscattering Impairments in Access Networks with Centralised Light Source**. *Electronics Letters*, 42(15):877–878, July 2006.

[169] Masamichi Fujiwara, Jun ichi Kani, Hiro Suzuki, and Katsumi Iwatsuki. **Impact of Backreflection on Upstream Transmission in WDM Single-Fiber Loopback Access Networks**. *J. Lightwave Technol.*, 24(2):740, Feb 2006.

[170] G. Berrettini, L. Giorgi, F. Ponzini, F. Cavaliere, P. Ghiggino, L. Poti, and A. Bogoni. **Testbed for Experimental Analysis on Seamless Evolution Architectures from GPON to High Capacity WDM-PON**. In *2009 5th International Conference on Testbeds and Research Infrastructures for the Development of Networks Communities and Workshops*, pages 1–9, April 2009.

[171] A. Naughton, G. Talli, S. Porto, C. Antony, P. Ossieur, and P. D. Townsend. **Design Optimization of R-EAM-SOA for Long-Reach Carrier-Distributed Passive Optical Networks**. *Journal of Lightwave Technology*, 32(22):4386–4392, Nov 2014.

[172] ITU Telecommunication Standardization Sector. **40-Gigabit-Capable Passive Optical Networks (NG-PON2): Physical Media Dependent (PMD) Layer Specification: Amendment 2**. *ITU-T Recommendations, G Series*, 2017.

[173] Germán V. Arévalo, Roberto C. Hincapié, and Roberto Gaudino. **Optimization of Multiple PON Deployment Costs and Comparison Between GPON, XGPON, NGPON2 and UDWDM PON**. *Optical Switching and Networking*, 25:80 – 90, 2017.

[174] C. C. Renaud, M. J. Fice, L. Lealman, P. Cannard, L. Rivers, and A. J. Seeds. **100GHz Spaced 10Gbit/s WDM over 10°C to 70°C using an Uncooled DBR Laser**. In *2006 Optical Fiber Communication Conference and the National Fiber Optic Engineers Conference*, pages 3 pp.–, March 2006.

[175] Y. Liu, J. D. Ingham, R. G. S. Plumb, R. V. Penty, I. H. White, D. J. Robbins, N. D. Whitbread, and A. J. Ward. **Directly-Modulated DS-DBR Tunable**

Laser for Uncooled C-band WDM system. In *2006 Optical Fiber Communication Conference and the National Fiber Optic Engineers Conference*, March 2006.

[176] S. Pachnicke, J. Zhu, M. Lawin, A. Wonfor, M. Eiselt, R. V. Penty, R. Cush, R. Turner, P. Firth, M. J. Wale, I. H. White, and J. P. Elbers. **First Demonstration of a Full C-Band Tunable WDM-PON System with Novel High-Temperature DS-DBR Lasers**. In *OFC 2014*, pages 1–3, March 2014.

[177] S. L. Woodward, P. Parayanthal, and U. Koren. **The Effects of Aging on the Bragg Section of a DBR Laser**. *IEEE Photonics Technology Letters*, 5(7):750–752, July 1993.

[178] M. Roppelt, K. Grobe, M. Eiselt, and J. P. Elbers. **Investigation of Wavelength Control Schemes in WDM-PONs**. In *Photonic Networks, 12 . ITG Symposium*, pages 1–5, May 2011.

[179] **SUBTUNE - Widely Tunable VCSEL using Sub Wavelength Gratings**. https://cordis.europa.eu/project/rcn/86598_en.html. Accessed: 25-05-2018.

[180] Y. Qian, Z. H. Zhu, Y. H. Lo, H. Q. Hou, M. C. Wang, and W. Lin. **1.3μm Vertical-Cavity Surface-Emitting Lasers with Double-Bonded GaAs-AlAs Bragg Mirrors**. *IEEE Photonics Technology Letters*, 9(1):8–10, Jan 1997.

[181] W. Hofmann, E. Wong, G. Bohm, M. Ortsiefer, N. H. Zhu, and M. C. Amann. **1.55-*mu*m VCSEL Arrays for High-Bandwidth WDM-PONs**. *IEEE Photonics Technology Letters*, 20(4):291–293, Feb 2008.

[182] A. Bachmann, K. Kashani-Shirazi, S. Arafin, and M. C. Amann. **GaSb-Based VCSEL With Buried Tunnel Junction for Emission Around 2.3*mu*m**. *IEEE Journal of Selected Topics in Quantum Electronics*, 15(3):933–940, May 2009.

[183] C. J. Chang-Hasnain. **Tunable VCSEL**. *IEEE Journal of Selected Topics in Quantum Electronics*, 6(6):978–987, Nov 2000.

[184] T. Yano, H. Saitou, N. Kanbara, R. Noda, S. i. Tezuka, N. Fujimura, M. Ooyama, T. Watanabe, T. Hirata, and N. Nishiyama. **Wavelength Modulation Over 500kHz of Micromechanically Tunable InP-Based VCSELs With Si-MEMS Technology**. *IEEE Journal of Selected Topics in Quantum Electronics*, 15(3):528–534, May 2009.

[185] P. Tayebati, Peidong Wang, D. Vakhshoori, Chih-Cheng Lu, M. Azimi, and R. N. Sacks. **Half-Symmetric Cavity Tunable Microelectromechanical VCSEL with Single Spatial Mode**. *IEEE Photonics Technology Letters*, 10(12):1679–1681, Dec 1998.

[186] B. Kogel, M. Maute, H. Halbritter, F. Riemenschneider, G. Bohm, M. C. Amann, and P. Meissner. **Long-Wavelength MEMS Tunable VCSEL with High Sidemode Suppression**. In *IEEE/LEOS International Conference on Optical MEMS and Their Applications Conference, 2005.*, pages 95–96, Aug 2005.

[187] C. Gierl, T. Gruendl, P. Debernardi, K. Zogal, C. Grasse, H. A. Davani, G. Böhm, S. Jatta, F. Küppers, P. Meißner, and M.C. Amann. **Surface Micromachined Tunable 1.55μm-VCSEL with 102nm Continuous Single-Mode Tuning**. *Opt. Express*, 19(18):17336–17343, Aug 2011.

[188] A. Daly, C. Gierl, T. Grundl, C. Grasse, K. Zogal, D. Carey, P. Townsend, M. C. Amann, P. Meissner, and B. Corbett. **10Gbit/s Transmission Over 50km of SMF using MEMS Tunable VCSEL**. *Electronics Letters*, 48(7):394–396, March 2012.

[189] B. Kogel, K. Zogal, S. Jatta, M. Maute, C. Grasse, M. C. Amann, and P. Meissner. **Small Signal Dynamics of an Electrically-Pumped Long-Wavelength Tunable VCSEL**. In *2008 IEEE 21st International Semiconductor Laser Conference*, pages 85–86, Sept 2008.

[190] B. Kogel, H. Halbritter, M. Maute, G. Bohm, M. C. Amann, and P. Meissner. **Single-mode and Polarization Stable MEMS-VCSEL with Broadband Tuning Characteristics Around 1.55μm**. In *2006 European Conference on Optical Communications*, pages 1–2, Sept 2006.

[191] H. Halbritter, C. Sydlo, B. Kogel, F. Riemenschneider, H. L. Hartnagel, and P. Meissner. **Impact of Micromechanics on the Linewidth and Chirp Performance of MEMS-VCSELs**. *IEEE Journal of Selected Topics in Quantum Electronics*, 13(2):367–373, March 2007.

[192] L. Colace, G. Masini, and G. Assanto. **Wavelength Stabilizer for Telecommunication Lasers: Design and Optimization**. *Journal of Lightwave Technology*, 21(8):1749–1757, Aug 2003.

[193] S. Paul, C. Gierl, J. Cesar, Q. T. Le, M. Malekizandi, B. Kögel, C. Neumeyr, M. Ortsiefer, and F. Küppers. **10-Gb/s Direct Modulation of Widely Tunable 1550-nm MEMS VCSEL**. *IEEE Journal of Selected Topics in Quantum Electronics*, 21(6):436–443, Nov 2015.

[194] S. Paul, N. Heermeier, M. Malekizandi, J. Cesar, M. T. Haidar, C. Gréus, C. Neumeyr, and F. Küppers. **10-Gbps Direct On-Off-Keying Modulation Across 85-nm Continuous Tuning Range Using Telecom MEMS-VCSEL**. In *2017 Conference on Lasers and Electro-Optics Europe European Quantum Electronics Conference (CLEO/Europe-EQEC)*, pages 1–1, June 2017.

[195] B. Mason, G. A. Fish, S. P. DenBaars, and L. A. Coldren. **Widely Tunable Sampled Grating DBR Laser with Integrated Electroabsorption Modulator**. *IEEE Photonics Technology Letters*, 11(6):638–640, June 1999.

[196] H. Ishii, H. Tanobe, F. Kano, Y. Tohmori, Y. Kondo, and Y. Yoshikuni. **Quasicontinuous Wavelength Tuning in Super-Structure-Grating (SSG) DBR Lasers**. *IEEE Journal of Quantum Electronics*, 32(3):433–441, March 1996.

[197] A. J. Ward, D. J. Robbins, G. Busico, E. Barton, L. Ponnampalam, J. P. Duck, N. D. Whitbread, P. J. Williams, D. C. J. Reid, A. C. Carter, and M. J. Wale. **Widely Tunable DS-DBR Laser with Monolithically Integrated SOA: Design and Performance**. *IEEE Journal of Selected Topics in Quantum Electronics*, 11(1):149–156, Jan 2005.

[198] R. Laroy, G. Morthier, T. Mullane, M. Todd, and R. Baets. **Stabilisation and Control of Widely Tunable MG-Y Lasers with Integrated Photodetectors**. *IET Optoelectronics*, 1(1):35–38, February 2007.

[199] W. T. Tsang, N. A. Olsson, R. A. Linke, and R. A. Logan. **1.5 μm Wavelength GaInAsP C3 Lasers: Single-Frequency Operation and Wideband Frequency Tuning**. *Electronics Letters*, 19(11):415–417, May 1983.

[200] O. Hildebrand, D. Baums, W. Idler, K. Dutting, G. Laube, and K. Wunstel. **The Y-Laser: A Multifunctional Device for Optical Communication Systems and Switching Networks**. *Journal of Lightwave Technology*, 11(12):2066–2075, Dec 1993.

[201] R. Phelan, W. Guo, Q. Lu, D. Byrne, B. Roycroft, P. Lambkin, B. Corbett, F. Smyth, L. P. Barry, B. Kelly, J. O'Gorman, and J. F. Donegan. **A Novel Two-Section Tunable Discrete Mode Fabry-Pérot Laser Exhibiting Nanosecond Wavelength Switching**. *IEEE Journal of Quantum Electronics*, 44(4):331–337, April 2008.

[202] D. C. Byrne, J. P. Engelstaedter, W. H. Guo, Q. Y. Lu, B. Corbett, B. Roycroft, J. O'Callaghan, F. H. Peters, and J. F. Donegan. **Discretely Tunable Semiconductor Lasers Suitable for Photonic Integration**. *IEEE Journal of Selected Topics in Quantum Electronics*, 15(3):482–487, May 2009.

[203] J. Zhao, K. Shi, Y. Yu, and L. P. Barry. **Theoretical Analysis of Tunable Three-Section Slotted Fabry Pérot Lasers Based on Time-Domain Traveling-Wave Model**. *IEEE Journal of Selected Topics in Quantum Electronics*, 19(5):1–8, Sept 2013.

[204] K. Shi, F. Smyth, D. Reid, B. Roycroft, B. Corbett, F.H. Peters, and L.P. Barry. **Characterization of a Tunable Three-Section Slotted Fabry–Pérot Laser for Advanced Modulation Format Optical Transmission**. *Optics Communications*, 284(6):1616 – 1621, 2011.

[205] P. Ramaswamy, B. Roycroft, J. OCallaghan, C. L. Janer, F. H. Peters, and B. Corbett. **Wavelength Agile Slotted Fabry-Pérot Lasers**. In *2014 International Semiconductor Laser Conference*, pages 102–103, Sept 2014.

[206] S. Shen, G. Li, Z. Lin, C. Lee, and Y. Chiu. **Power-Enhancement Broadband Cascaded Integration of Electroabsorption Modulator and Semiconductor Optical Amplifier by Local Quantum Well Intermixing**. In *2014 IEEE Photonics Conference*, pages 278–279, Oct 2014.

[207] Y. Cheng, J. Pan, Y. Wang, F. Zhou, B. Wang, L. Zhao, H. Zhu, and W. Wang. **40-Gb/s Low Chirp Electroabsorption Modulator Integrated With DFB Laser**. *IEEE Photonics Technology Letters*, 21(6):356–358, March 2009.

[208] K. Taguchi, K. Asaka, S. Kimura, K. Suzuki, and A. Otaka. **Reverse Bias Voltage Controlled Burst-Mode Booster SOA in λ-Tunable ONU Transmitter for High-Split-Number TWDM-PON**. *IEEE/OSA Journal of Optical Communications and Networking*, 10(4):431–439, April 2018.

[209] D. Marcuse. **Reflection Loss of Laser Mode from Tilted End Mirror**. *Journal of Lightwave Technology*, 7(2):336–339, Feb 1989.

[210] Manfred Mundbrod. **Ridge-Waveguide Lasers with Tilted Facets**, 2003.

[211] I. F. Lealman, L. J. Rivers, M. J. Harlow, and S. D. Perrin. **InGaAsP/InP Tapered Active Layer Multiquantum Well Laser with 1.8dB Coupling Loss to Cleaved Singlemode Fibre**. *Electronics Letters*, 30(20):1685–1687, Sep 1994.

[212] L. D. Westbrook. **Measurements of dg/dN and dn/dN and their Dependence on Photon Energy in λ =1.5μm InGaAsP Laser Diodes**. *IEE Proceedings J - Optoelectronics*, 133(2):135–142, April 1986.

[213] Basil W. Hakki and Thomas L. Paoli. **Gain Spectra in GaAs Double Heterostructure Injection Lasers**. *Journal of Applied Physics*, 46(3):1299–1306, 1975.

[214] Shifu Yuan and Nabeel A. Riza. **General Formula for Coupling-Loss Characterization of Single-Mode Fiber Collimators by use of Gradient-Index Rod Lenses**. *Appl. Opt.*, 38(15):3214–3222, May 1999.

[215] G. Talli, A. Naughton, S. Porto, C. Antony, P. Ossieur, and P. D. Townsend. **Advantageous Effects of Gain Saturation in Semiconductor Optical Amplifier-Based Integrated Reflective Modulators**. *Journal of Lightwave Technology*, 32(3):392–401, Feb 2014.

[216] P. Kozodoy, T. A. Strand, Y. A. Akulova, G. Fish, C. Schow, Ping-Chiek Koh, Zhixi Bian, J. Christofferson, and A. Shakouri. **Thermal Effects in Monolithically Integrated Tunable Laser Transmitters**. *IEEE Transactions on Components and Packaging Technologies*, 28(4):651–657, Dec 2005.

[217] ITU Telecommunication Standardization Sector. **Spectral Grids for WDM Applications: DWDM Frequency Grid**. *ITU-T Recommendations, G Series*, 2012.

[218] Kenji Sato, Shoichiro Kuwahara, and Yutaka Miyamoto. **Chirp Characteristics of 40-Gb/s Directly Modulated Distributed-Feedback Laser Diodes**. *J. Lightwave Technol.*, 23(11):3790, Nov 2005.

[219] F. Dorgeuille and F. Devaux. **On the Transmission Performances and the Chirp Parameter of a Multiple-Quantum-Well Electroabsorption Modulator**. *IEEE Journal of Quantum Electronics*, 30(11):2565–2572, Nov 1994.

[220] M. Y. Jamro and J. M. Senior. **Optimising Negative Chirp of an Electroabsorption Modulator for Use in High-Speed Optical Networks**. *European Transactions on Telecommunications*, 18(4):369–380, 2006.

[221] G. Simon, F. Saliou, P. Chanclou, B. L. Guyader, L. Guillo, J. Konopacki, F. Bourgart, and D. Erasme. **Focus on Time-Dependent Wavelength Drift of DMLs Under Burst-Mode Operation for NG-PON2**. *Journal of Lightwave Technology*, 34(13):3148–3154, July 2016.

[222] ITU Telecommunication Standardization Sector. **40-Gigabit-Capable Passive Optical Networks (NG-PON2): Transmission Convergence Layer Specification**. *ITU-T Recommendations, G Series*, 2017.

[223] Darren P. Shea and John E. Mitchell. **A 10-Gb/s 1024-Way-Split 100-km Long-Reach Optical-Access Network**. *J. Lightwave Technol.*, 25(3):685–693, Mar 2007.

[224] S. Hornung, D. Payne, and R. Davey. **New Architecture for an All-Optical Network.** In *OFC/NFOEC Technical Digest. Optical Fiber Communication Conference, 2005.*, volume 2, pages 3 pp. Vol. 2–, March 2005.

[225] T. Li. **The Impact of Optical Amplifiers on Long-Distance Lightwave Telecommunications**. *Proceedings of the IEEE*, 81(11):1568–1579, Nov 1993.

[226] C. R. Giles, E. Desurvire, and J. R. Simpson. **Transient Gain and Crosstalk in Erbium-Doped Fiber Amplifiers**. *Opt. Lett.*, 14(16):880–882, Aug 1989.

[227] Y. Sun, J. L. Zyskind, and A. K. Srivastava. **Average Inversion Level, Modeling, and Physics of Erbium-doped Fiber Amplifiers**. *IEEE Journal of Selected Topics in Quantum Electronics*, 3(4), Aug 1997.

[228] A. Kaszubowska-Anandarajah, R. Oberland, E. Bravi, A. Surpin, O. Aharoni, U. Ghera, R. Giller, E. Connolly, E. K. MacHale, M. Todd, G. Talli, and D. McDonald. **EDFA Transient Suppression in Optical Burst Switching Systems**. In *2012 14th International Conference on Transparent Optical Networks (ICTON)*, pages 1–4, July 2012.

[229] R. J. Mears, L. Reekie, I. M. Jauncey, and D. N. Payne. **Low-Noise Erbium-doped Fibre Amplifier Operating at 1.54μm**. *Electronics Letters*, 23(19):1026–1028, September 1987.

[230] S. Poole, D. Payne, R. Mears, M. Fermann, and R. Laming. **Fabrication and Characterization of Low-Loss Optical Fibers Containing Rare-Earth Ions**. *Journal of Lightwave Technology*, 4(7):870–876, Jul 1986.

[231] B. J. Ainslie. **A Review of the Fabrication and Properties of Erbium-doped Fibers for Optical Amplifiers**. *Journal of Lightwave Technology*, 9(2):220–227, Feb 1991.

[232] E. Desurvire, C. R. Giles, and J. R. Simpson. **Gain Saturation Effects in High-Speed, Multichannel Erbium-Doped Fiber Amplifiers at $\lambda =$ 1.53μm**. *Journal of Lightwave Technology*, 7(12):2095–2104, Dec 1989.

[233] A. A. M. Saleh, R. M. Jopson, J. D. Evankow, and J. Aspell. **Modeling of Gain in Erbium-doped Fiber Amplifiers**. *IEEE Photonics Technology Letters*, 2(10):714–717, Oct 1990.

[234] A. K. Srivastava, Y. Sun, J. L. Zyskind, and J. W. Sulhoff. **EDFA Transient Response to Channel Loss in WDM Transmission System**. *IEEE Photonics Technology Letters*, 9(3):386–388, March 1997.

[235] C. R. Giles and E. Desurvire. **Modeling Erbium-doped Fiber Amplifiers**. *Journal of Lightwave Technology*, 9(2):271–283, Feb 1991.

[236] Yan Sun, John L. Zyskind, Atul K. Srivastava, and Liyan Zhang. **Analytical Formula for the Transient Response of Erbium-doped Fiber Amplifiers**. *Appl. Opt.*, 38(9):1682–1685, Mar 1999.

[237] L. Tancevski, L. A. Rusch, and A. Bononi. **Gain Control in EDFA's by Pump Compensation**. *IEEE Photonics Technology Letters*, 10(9):1313–1315, Sept 1998.

[238] D. H. Richards, J. L. Jackel, and M. A. Ali. **A Theoretical Investigation of Dynamic All-Optical Automatic Gain Control in Multichannel EDFA's and EDFA Cascades**. *IEEE Journal of Selected Topics in Quantum Electronics*, 3(4):1027–1036, Aug 1997.

[239] T. Shiozaki, M. Fuse, and S. Morikura. **A Study of Gain Dynamics of Erbium-Doped Fiber Amplifiers for Burst Optical Signals**. In *2002 28TH European Conference on Optical Communication*, volume 3, pages 1–2, Sept 2002.

[240] K. Okamura, E. Otani, T. Yoshikawa, T. Uchino, M. Fukushima, and N. Kagi. **Optical Burst Amplification Using EDFA with Fast Feedback Control**. In *OFC/NFOEC Technical Digest. Optical Fiber Communication Conference, 2005.*, volume 2, pages 3 pp. Vol. 2–, March 2005.

[241] E. Otani, T. Okaniwa, K. Okamura, T. Yoshikawa, T. Uchina, M. Fukushima, and N. Kagi. **Amplification of WDM Burst Signals using EDFA with a Fast Feedback Control**. In *2005 IEEE LEOS Annual Meeting Conference Proceedings*, pages 298–299, Oct 2005.

[242] Y. Horiuchi, Y. Tanaka, Y. Oikawa, N. Shiga, H. Nagaeda, R. Sugimoto, H. Miyauchi, K. Himeno K. Shima, and H. Hosoya. **Ultra-Fast Automatic Gain Controlled Optical Fiber Amplifier**. *Fujikura Technical Review,*, 39:4–7, January 2010.

[243] S. Nishihara, S. Kimura, T. Yoshida, M. Nakamura, J. Terada, K. Nishimura, K. Kishine, K. Kato, Y. Ohtomo, N. Yoshimoto, T. Imai, and M. Tsubokawa. **A Burst-Mode 3R Receiver for 10-Gbit/s PON Systems With High Sensitivity, Wide Dynamic Range, and Fast Response**. *Journal of Lightwave Technology*, 26(1):99–107, Jan 2008.

[244] P. Ossieur, T. De Ridder, J. Bauwelinck, C. Melange, B. Baekelandt, Xing-Zhi Qiu, J. Vandewege, G. Talli, C. Antony, P. Townsend, and C. Ford. **A 10 Gb/s Burst-Mode Receiver with Automatic Reset Generation**

and Burst Detection for Extended Reach PONs. In *2009 Conference on Optical Fiber Communication - incudes post deadline papers*, pages 1–3, March 2009.

[245] K. Sugihara, K. Ishii, K. Dohi, K. Kubo, T. Sugihara, and W. Matsumoto. **Scalable SD-FEC for Efficient Next-Generation Optical Networks**. In *ECOC 2016; 42nd European Conference on Optical Communication*, pages 1–3, Sept 2016.

[246] B. Neto, A. Klingler, C. Reis, J. P. Girão, A. Teixeira, and P. S. André. **EDFA Transient Assessment for Bursty Traffic**. In *2009 3rd ICTON Mediterranean Winter Conference (ICTON-MW)*, pages 1–4, Dec 2009.

[247] I. S. Reed and G. Solomon. **Polynomial Codes Over Certain Finite Fields**. *Journal of the Society for Industrial and Applied Mathematics*, 8(2):300–304, 1960.

[248] N. Brandonisio, S. Porto, D. Carey, P. Ossieur, G. Talli, N. Parsons, and P. D. Townsend. **Burst-Mode FPGA Implementation and Error Location Analysis of Forward Error Correction for Passive Optical Networks**. *IEEE/OSA Journal of Optical Communications and Networking*, 10(4):298–308, April 2018.

[249] B. Schrenk, J. A. Lazaro, D. Klonidis, F. Bonada, F. Saliou, V. Polo, E. Lopez, Q. T. Le, P. Chanclou, L. Costa, A. Teixeira, S. Chatzi, I. Tomkos, G. M. T. Beleffi, D. Leino, R. Soila, S. Spirou, G. de Valicourt, R. Brenot, C. Kazmierski, and J. Prat. **Demonstration of a Remotely Dual-Pumped Long-Reach PON for Flexible Deployment**. *Journal of Lightwave Technology*, 30(7):953–961, 2012.

[250] K. Taguchi, K. Asaka, M. Fujiwara, S. Kaneko, T. Yoshida, Y. Fujita, H. Iwamura, M. Kashima, S. Furusawa, M. Sarashina, H. Tamai, A. Suzuki, T. Mukojima, S. Kimura, K. I. Suzuki, and A. Otaka. **Field Trial of Long-Reach and High-Splitting λ-Tunable TWDM-PON**. *Journal of Lightwave Technology*, 34(1):213–221, 2016.

[251] Peter Ossieur, Nasir A. Quadir, Stefano Porto, Marc Rensing, Cleitus Antony, Wei Han, Peter O'Brien, Y. Chang, and Paul D. Townsend. **A 10G Linear Burst-Mode Receiver Supporting Electronic Dispersion Compensation for Extended-Reach Optical Links**. *Optics Express*, 19(26):B604–B610, 2011.

[252] D. Brunina, S. Porto, A. Jain, C. P. Lai, C. Antony, N. Pavarelli, M. Rensing, G. Talli, P. Ossieur, P. O' Brien, and P. D. Townsend. **Analysis of Forward**

Error Correction in the Upstream Channel of 10Gb/s Optically Amplified TDM-PONs. In *2015 Optical Fiber Communications Conference and Exhibition (OFC)*, pages 1–3, 2015.

[253] S. Porto, C. Antony, A. Jain, D. Kelly, D. Carey, G. Talli, P. Ossieur, and P. D. Townsend. **Demonstration of 10 Gbit/s Burst-Mode Transmission Using a Linear Burst-Mode Receiver and Burst-Mode Electronic Equalization [Invited]**. *IEEE/OSA Journal of Optical Communications and Networking*, 7(1):A118–A125, 2015.

[254] D. Carey, P. Ramaswamy, G. Talli, C. Antony, B. Roycroft, B. Corbett, and P. D. Townsend. **Characterization of a Low-Cost, Monolithically Integrated, Tunable 10G Transmitter for Wavelength Agile PONs**. *IEEE Journal of Quantum Electronics*, 54(6):1–12, Dec 2018.

[255] M. Ruffini, D. B. Payne, W. Graudszus, K. Pulverer, A. Di Giglio, R. Wessaely, and G. Talli. **D3.2: Initial White Papers on Regulation/Policy and Multi-Business Model Support**. Community Research and Development Information Service (CORDIS), September 2013.

[256] R. Bonk, H. Schmuck, B. Deppisch, W. Poehlmann, and T. Pfeiffer. **Wavelength-Transparent Long-Reach-High-Split TWsDM-PON Utilized by a Non-Gated Parallel Cascade of Linear SOAs**. In *2014 The European Conference on Optical Communication (ECOC)*, pages 1–3, Sept 2014.

[257] S. Koenig, R. Bonk, H. Schmuck, W. Poehlmann, Th. Pfeiffer, C. Koos, W. Freude, and J. Leuthold. **Amplification of Advanced Modulation Formats with a Semiconductor Optical Amplifier Cascade**. *Opt. Express*, 22(15):17854–17871, Jul 2014.

[258] R. Bonk, T. Vallaitis, J. Guetlein, C. Meuer, H. Schmeckebier, D. Bimberg, C. Koos, W. Freude, and J. Leuthold. **The Input Power Dynamic Range of a Semiconductor Optical Amplifier and Its Relevance for Access Network Applications**. *IEEE Photonics Journal*, 3(6):1039–1053, Dec 2011.

[259] R. Bonk, G. Huber, T. Vallaitis, S. Koenig, R. Schmogrow, D. Hillerkuss, R. Brenot, F. Lelarge, G.-H. Duan, S. Sygletos, C. Koos, W. Freude, and J. Leuthold. **Linear Semiconductor Optical amplifiers for Amplification of Advanced Modulation Formats**. *Opt. Express*, 20(9):9657–9672, Apr 2012.

[260] ITU Telecommunication Standardization Sector. **ITU-T G.671: Transmission Characteristics of Optical Components and Subsystems**. *ITU-T Recommendations, G Series*, 2012.

[261] P. Schulz, M. Matthe, H. Klessig, M. Simsek, G. Fettweis, J. Ansari, S. A. Ashraf, B. Almeroth, J. Voigt, I. Riedel, A. Puschmann, A. Mitschele-Thiel, M. Muller, T. Elste, and M. Windisch. **Latency Critical IoT Applications in 5G: Perspective on the Design of Radio Interface and Network Architecture**. *IEEE Communications Magazine*, 55(2):70–78, February 2017.

[262] Open Networking Foundation. **SDN Architecture**. *ONF TR-502*, 2014.

[263] S. McGettrick, F. Slyne, N. Kitsuwan, D. B. Payne, and M. Ruffini. **Experimental End-to-End Demonstration of Shared N:M Dual-Homed Protection in SDN-Controlled Long-Reach PON and Pan-European Core**. *Journal of Lightwave Technology*, 34(18):4205–4213, Sept 2016.

[264] M. Ruffini, F. Slyne, C. Bluemm, N. Kitsuwan, and S. McGettrick. **Software Defined Networking for Next Generation Converged Metro-Access Networks**. *Optical Fiber Technology*, 26, Part A:31–41, 2015.

[265] G. Talli, S. Porto, D. Carey, N. Brandonisio, A. Naughton, P. Ossieur, F. Slyne, S. McGettrick, C. Blum, M. Ruffini, D. Payne, R. Bonk, T. Pfeiffer, N. Parsons, and P. Townsend. **Demonstration of SDN Enabled Dynamically Reconfigurable High Capacity Optical Access for Converged Services**. In *2016 Optical Fiber Communications Conference and Exhibition (OFC)*, pages 1–3, March 2016.

[266] Jens Buus, Markus-Christian Amann, and Daniel J. Blumenthal. ***Widely Tunable Monolithic Laser Diodes***, pages 390–. Wiley-IEEE Press, 2005.

[267] ITU Telecommunication Standardization Sector. **Multiple-Wavelength Passive Optical Networks (MW-PONs)**. *ITU-T Recommendations, G Series*, 2016.

[268] B. Hammond, Bingzhi Su, J. Mathews, E. Chen, and E. Schwartz. **Integrated Wavelength Locker for Tunable Laser Applications**. In *The 15th Annual Meeting of the IEEE Lasers and Electro-Optics Society*, volume 2, pages 479–480 vol.2, Nov 2002.

[269] G. Sarlet, G. Morthier, and R. Baets. **Control of Widely Tunable SSG-DBR Lasers for Dense Wavelength Division Multiplexing**. *Journal of Lightwave Technology*, 18(8):1128–1138, Aug 2000.

[270] D. A. Ackerman, K. A. Paget, L. F. Schneemeyer, L. J. . Ketelsen, O. Sjolund, J. E. Graebner, A. Kanan, F. W. Warning, V. R. Raju, L. Eng, E. D. Schaeffer, and P. Van Emmerik. **Low-Cost, Athermal Wavelength-Locker Integrated in a Temperature-Tuned Laser Package**. In *OFC 2003 Optical Fiber Communications Conference, 2003.*, pages PD32–P1, March 2003.

[271] S. Pachnicke, J. Zhu, M. Lawin, M. H. Eiselt, S. Mayne, B. Quemeneur, D. Sayles, H. Schwuchow, A. Wonfor, P. Marx, M. Fellhofer, P. Neuber, M. Dietrich, M. J. Wale, R. V. Penty, I. H. White, and J. P. Elbers. **Tunable WDM-PON System with Centralized Wavelength Control**. *Journal of Lightwave Technology*, 34(2):812–818, Jan 2016.

[272] P. Miguelez. **What Applications are Driving Higher Capacity in Access?** In *2018 Optical Fiber Communications Conference and Exposition (OFC)*, pages 1–3, March 2018.

[273] *Visions and Roadmaps*. https://5g-ppp.eu/roadmaps/. [Online; accessed 27-Jan-2018].

[274] Next Generation Mobile Networks Ltd. **NGNM 5G White Paper**, 2015.

[275] G. Talli, S. Porto, D. Carey, N. Brandonisio, P. Ossieur, P. Townsend, R. Bonk, T. Pfeiffer, F. Slyne, S. McGettrick, C. Blümm, M. Ruffini, A. Hill, D. Payne, and N. Parsons. **Technologies and Architectures to Enable SDN in Converged 5G/Optical Access Networks**. In *2017 International Conference on Optical Network Design and Modeling (ONDM)*, pages 1–6, May 2017.

[276] M. Ruffini. **Multidimensional Convergence in Future 5G Networks**. *Journal of Lightwave Technology*, 35(3):535–549, Feb 2017.

[277] ITU Telecommunication Standardization Sector. **ITU-T G.987.4: 10-Gigabit-Capable Passive Optical Networks (XG-PON): Reach** Extension. *ITU-T Recommendations, G Series*, 2012.

[278] IEEE P802.3ca 50G-EPON Task Force. http://web.archive.org/web/20080207010024/http://www.808multimedia.com/winnt/kernel.htm. Accessed: 2018-08-22.

[279] C. Knittle. **IEEE 100Gb/s EPON**. In *2016 Optical Fiber Communications Conference and Exhibition (OFC)*, pages 1–3, March 2016.

[280] V. Houtsma and D. van Veen. **A Study of Options for High-Speed TDM-PON Beyond 10G**. *Journal of Lightwave Technology*, 35(4):1059–1066, Feb 2017.

[281] A. Mecozzi and M. Shtaif. **The Statistics of Polarization-Dependent Loss in Optical Communication Systems**. *IEEE Photonics Technology Letters*, 14(3):313–315, March 2002.